THE UNIVERSITY
of ADELAIDE

Improved Determination of Hadron Matrix Elements using the Variational Method

Jack Dragos

Supervisors:
Assoc. Prof. Ross Young
Dr. James Zanotti

Faculty of Sciences
School of Physical Sciences
Department of Physics

September, 2016

Abstract

Utilising lattice QCD to calculate nucleon matrix elements has had a huge impact on the knowledge of the structure of nucleons. From the comparison to experimental data, to the new insights into the structure of nucleons, the practices of lattice QCD has cemented itself as a fundamental field for particle physics. Some key contributions to the understanding of nucleon structure lattice QCD can provide are parameters needed for the *beyond standard model* (BSM) extensions, understanding the size of the nucleons via the charge radii and the decomposition of the spin and angular momentum of the quarks and gluons within the nucleon.

But the extraction of hadron matrix elements in lattice QCD using the standard two- and three-point correlator functions demands careful attention to systematic uncertainties. Although other systematics including discretisation, renormalisation and chiral extrapolation effects need to be analysed, one of the most recent and emerging sources of systematic error is contamination from excited-states.

This thesis applies the variational method to calculate the axial vector current g_A, the scalar current g_S, the tensor current g_T and the quark momentum fraction $\langle x \rangle$ of the nucleon and we compare the results to the more commonly used summation and two-exponential fit methods. Proceeding with the same comparison of methods, we extend the calculation to non-zero momentum transfer to access the vector form factors for both the proton and neutron, as well as the iso-vector combination of the axial and induced pseudoscalar form factors for the proton. The results demonstrate how excited-states affect the extraction of nucleon matrix elements and in the process discovering that the variational approach offers a more efficient and robust method for the determination of nucleon matrix elements.

Through this demonstration of how excited-states impact lattice QCD calculation and how we can use methods to suppress these excited-states, we can hope to achieve higher and higher precision determinations of nucleon matrix elements form lattice QCD which will aid in our understanding of the structure of nucleons.

I certify that this work contains no material which has been accepted for the award of any other degree or diploma in my name in any university or other tertiary institution and, to the best of my knowledge and belief, contains no material previously published or written by another person, except where due reference has been made in the text. In addition, I certify that no part of this work will, in the future, be used in a submission in my name for any other degree or diploma in any university or other tertiary institution without the prior approval of the University of Adelaide. I give consent to this copy of my thesis, when deposited in the University Library, being made available for loan and photocopying, subject to the provisions of the Copyright Act 1968. The author acknowledges that copyright of published works contained within this thesis resides with the copyright holder(s) of those works. I also give permission for the digital version of my thesis to be made available on the web, via the University's digital research repository, the Library Search and also through web search engines, unless permission has been granted by the University to restrict access for a period of time.

Jack Dragos

Acknowledgements

From the beginning, I thank Waseem Kamleh and Derek Leinweber for starting me off on my road to research through my pre-PhD years. Little did I know what I was getting into when you set me up on this research path, yet over the years you make it quite clear what the motivations and goals in this research topic was. I am grateful for your patience while I staggered over my self numerous times trying to get my head around lattice QCD concepts. None of the things I have achieved in my PhD would have been possible without the two of you.

In this period, I send my deepest gratitude to Ben Owen. Probably one of the best teachers I have ever had, along with his endless patience me, made my honours year and the years to follow the most inspiring and interesting years of my academic life. Never turning me away and always attempting to explain things I had troubles understanding in different and new ways, my understanding of lattice QCD would not be what it is today without his support. I wish him all the best in his life and will always be remembered.

A special thanks to Kaustubh Naik for the friendship we had during our under- and post-graduate years. You made sure I was well fed with lunch at mid day sharp, and I value all the random talks we had about physics, gaming and other topics.

Next in the time line comes James Zanotti. After sitting in on my honours meetings and helping me through this period, it started to come clear that I would eventually be working with James for my PhD. I thank you for this path you have shown to me, from the beginnings of creating the lattice data, to showing me the world of lattice QCD research at the lattice conference and to the patience you had with my bad writing skills for my publications.... Always making time to try to assist in my understanding of lattice QCD, James always made sure I fully understand what I was doing and explaining things in an understandable and relatable way. It always amazed me how much enthusiasm, interest and support he had with the work I was producing, always giving me the confidence to continue.

After working with Ross Young for some time, I started to understand how supportive he is to me and his colleagues as well as how passionate his about particle physics. My fear of showing Ross some writing or some results was a very real thing, as he will pick through every little detail and make sure everything is

exact and correct. I was very honoured to have Ross as my supervisor, someone who was always making sure I was working up to a high standard of research and always made me keep track of the key goals of my work.

To my fellow colleagues, Samuel Thomas, Adrian Kiratidis, Daniel Trewartha, Finn Stokes, Alexander Chambers, Ryan Bignell and Dylan Harries (and others I have talked with over the years). You made my PhD years interesting and insightful (even if it wasn't anything to do with physics) and helped me understand physics in a whole new way. Listening to you guys talking about random stuff made my days somehow. Whether it be listening to seminars at the conference, or just talking about physics and other random stuff at different events, you guys made my time here interesting and enjoyable. Along side this, the research you share and produce is always amassing and inspiring to me, pushing me to always better myself to keep up with your ever increasing standards.

A large thanks to the CSSM and Physical Sciences department. They both have made my PhD years new and exciting, whether it be the CSSM conferences they hosted and sent me to, or the Physical Sciences department showing me the teaching side of being in academia.

To all the people I meet at the international lattice conference in Japan. The conversations and presentations I was a part of gave my work a sense of purpose in the lattice QCD community. Special thanks to Andrea Shindler who I look forward to working with in the future.

To my loving and caring family, I thank whole-heartily. My mother Sophie Wait for supporting and taking care of me throughout my journey, to my brothers James and Jon Dragos for always listening and making me laugh over the years and to all my extended family for the fun gatherings and entertaining times.

Lastly to my fiancèe Sarah Brown, for always being there, always listening, always supporting me, always making me laugh and for all the love you show to me and others.

Dedicated to my grandma (yiayia Marika),
take care of Marie for us up there.

Contents

Chapter 1

Introduction

After the discovery of internal structure of the proton and neutrons, the standard model (SM) was slowly developed to explain what constitutes the inner workings of these composite particles. We describe all observed particles as being built up by elementary particles we call quarks and leptons and they interact via the exchange of gauge bosons.

Whether it be the protons (up up down quarks), neutrons (down down up quarks) and electrons observed from our periodic table, or it be some undetectable exchange of intermediate particles, they can all be described by the standard model. Through the mechanism of the electro-weak theory, quantum electrodynamics (QED) and quantum chromodynamics (QCD), we explain how all the elementary particles in the standard model interact with one another via the exchange of photons, W-bosons, Z-boson and gluons. Along with this, we have the vacuum energy being non-zero which results in particle/anti-particle creation and annihilation. Due to this, any real world observable we want to calculate will always have inherent vacuum interactions present.

This in turn gives rise to all the properties seen in our observable universe. Hence, our understanding of simple physics questions need to be re-evaluated, including once simple questions such as "what is the mass of a proton/neutron?" needs to be re-evaluated to "what is the observed mass of a 3 light quark system in a vacuum, including all their interaction forces?" Further questions that we can inquire about are the spatial, momentum, spin, flavour and gluon structure of the nucleon which can lead to a picture of how the nucleon is put together and how it interacts with itself, the vacuum and other particles.

Although the Standard Model describes the theory, we still need to prescribe the degrees of freedom of the theory. As experimental physics gets pushed further and further to higher energy scales and more exotic detection methods, we begin to constrain these degrees of freedom with reduced experimental uncertainty. Recently, primarily driven by the evidence for the existence of dark matter which

is not predicted from the Standard Model, the physics community has started to explore theories that are beyond the Standard Model (such as Supersymmetric theories). Again, with enough precision, experimental physics will show where the Standard Model breaks down and how it needs to be extended.

Due to the self interactions of the gluons in the theory of QCD, it is difficult to calculate quantities analytically at low-energy scales. We can attempt to apply perturbation theory in certain regimes, where we calculate quantities in the large energy sector or where *asymptotic freedom* occurs and try to extrapolate to the lower energy scales, but it is not possible to extrapolate all the way to hadronic energy scales. The only way currently to calculate observables from first principles in a non-perturbative way is in lattice Quantum Chromodynamics (QCD), where a discretised version of the theory is calculated on supercomputers. Thought to be highly impractical in the past, due to limitations in computing power, has now come to fruition from the massive increase in computing technology over recent years. For observables of the nucleon, we have extended beyond the mass calculations to more exotic observables associated with the structure of the nucleon.

Discretising space-time and calculating observables comes with its own systematics that need to be taken into consideration. The work in this thesis is primarily focused on the systematic error associated with the phenomenon of excited-state removal in the extraction of some selected nucleon observables. Although there are other effects that need to be accounted for, such as the finite lattice spacing in space and time, the finite extent of the spatial and temporal dimensions and the chiral extrapolation of the quark masses to their physical mass, excited-state removal has proven to be a complicated task to undertake and has required the use of specific techniques. This thesis calculates and shows how the excited-states can be suppressed by comparing a naive calculation with the summation method, two-state fit method and the variational method.

Beginning with a brief overview of QCD along with a look at some experimental processes in Chapter 2, the lattice approach to QCD is outlined in Chapter 3. Once we have the foundations laid out for computing QCD on the lattice, some advanced techniques are formalised in Chapter 5 along with some extraction methods in Chapter 6. A detailed comparison of the mentioned techniques for zero-momentum transfer matrix elements are presented in Chapter 7, then a demonstration of excited-state effects in form factor calculations appear in Chapter 8. As these quantities need to be renormalised to be comparable to physical quantities, the theory and a brief demonstration for this process is outlined in Chapter 4.

Chapter 2

Quantum Chromodynamics (QCD)

2.1 Quarks and Interactions

The Standard Model is a theory that explains how all the atoms that we see are made up of quarks, leptons and gluons. The generations of the flavours of quarks in the theory are grouped into pairs, up and down flavour quarks being the lightest, the strange and charm being heavier and the top and bottom being the heaviest. Analogous to these, the leptons are paired off into their generations: the electron and electron neutrino, the muon and muon neutrino and the tau and tau neutrino all from lightest to heaviest generation. We describe the interactions between these particles through the exchange of bosons. In the electro-weak interactions they come in the form of a neutral charged massless photon, a heavy positively and negatively charged W-bosons, and a heavier electrically neutral Z-boson, while for the strong nuclear forces we have a decomposition of 8 gluons. Lastly, the explicit mass parameters in this theory is generated via the interaction with a spin-0 higgs field. A summary of all these properties appear in Figure 2.1.

For this thesis, we focus on QCD theory and interactions for baryons. If we consider the lightest three flavoured quarks (up, down and strange), the baryons are comprised of three quarks that break down into decuplet, octets or singlets:

$$3 \otimes 3 \otimes 3 \rightarrow 10 \oplus 8 \oplus 8 \oplus 1 \tag{2.1}$$

The proton and neutron correspond to the combination that has spin $\frac{1}{2}$, hypercharge 1 and charge +1 for the proton and 0 for the neutron. The only such combination is an up, up, down quark combination for the proton and down, down, up quark combination for the neutron, both with two iso-spins aligned and one iso-spin anti-aligned.

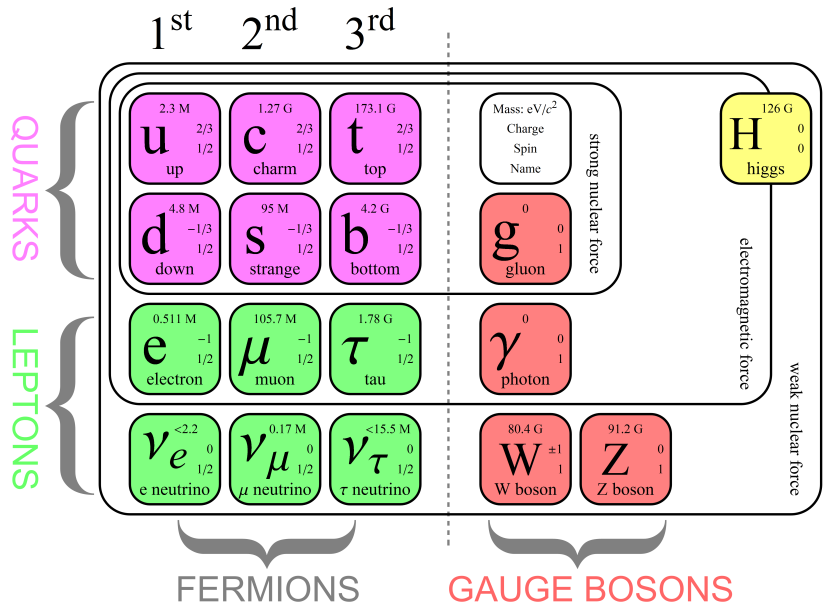

Figure 2.1: Diagram showing the standard model, and how the particles are categorised into their respective groups [1].

Colour charge is introduced into the theory to account for the discovery of the $\Delta^{++}(uuu)$ particle which, due to the Pauli exclusion principle, should not be allowed since it requires 3 up quarks, all with spin-up. We add a colour $SU_c(3)$ charge to the quarks, but since this colour charge is never observed we assume that all objects are "colour neutral" either in the form of a meson having a colour charged quark and a colour charged anti-quark, or a hadron containing 3 colour charges that are anti-symmetrised to form a colour singlet.

2.2 Lagrangian

Using the particles described in the previous section, we can describe how the quarks and gluons interact through a non-abelian gauge field theory. The Lagrangian that describes this interaction in the gauge field is:

$$\mathcal{L}_{QCD} = -\frac{1}{4} F^{(a)}_{\mu\nu} F^{(a)\mu\nu} + \sum_q \overline{\psi}^i_q \left(i\gamma^\mu D^{ij}_\mu - \delta^{ij} m_q \right) \psi^j_q. \tag{2.2}$$

Where we have $F^{(a)}_{\mu\nu}$ defined as the field strength tensor:

$$F^{(a)}_{\mu\nu} \equiv \partial_\mu A^a_\nu - \partial_\nu A^a_\mu + g_s f_{abc} A^b_\mu A^c_\nu, \tag{2.3}$$

and we have the covariant derivative D_μ^{ij} defined as:

$$D_\mu^{ij} \equiv \delta^{ij}\partial_\mu - ig_s \sum_a \frac{\lambda_a^{ij}}{2} A_\mu^a. \tag{2.4}$$

The strong coupling parameter g_s is the only arbitrary parameter of the theory. We denote ψ as the spin-$\frac{1}{2}$ fermion fields in the fundamental representation (which are the quark fields) and A_μ^a corresponds to the spin-1 gauge bosons (which are the gluon fields). Summing over the q variable amounts to summing over all the quark flavours in our theory (up, down, strange etc...). The conventions in the equations above are that the letters $a, b, c = 1, \ldots, 8$ correspond to indices in the adjoint representation of $SU(3)_c$ and $i, j = 1, 2, 3$ correspond to indices in the fundamental representation of $SU(3)_c$. f_{abc} are the $SU(3)$ Lie group structure constants and λ^a are the Gell-Mann matrices which are generators of the $SU(3)_c$ algebra.

Using an independent $SU(3)$ transformation at every point via $V(x) = e^{i\phi^a(x)\frac{\lambda^a}{2}}$

$$\psi(x) \to \psi(x)' = V(x)\psi(x), \tag{2.5}$$

$$A_\mu(x) \to A'_\mu(x) = V(x)A_\mu(x)V^{-1}(x) + \frac{i}{g_s}\left(\partial_\mu V(x)\right)V^{-1}(x), \tag{2.6}$$

and requiring these gauge transformation to be invariant (i.e. $\psi(x) = \psi(x)'$ and $A_\mu(x) = A'_\mu(x)$), along with conditions of renormalisability and the coupling g_s completely specify the theory and impose the Lagrangian.

In the QCD Lagrangian there are terms that allow the gluons to couple to themselves. Due to this effect, we can analyse two regions of different energy. The asymptotic free region which occurs at high-energies where the quarks essentially act as free particles, while the confined region occurs at low-energies, in which the quarks are never observed as free particles but are bound in hadrons. Calculating hadron properties in the low energy region has proven to be highly difficult without the use of lattice QCD.

We can determine experimentally the mass spectrum for mesons and baryons defined in Section 2.1, but since we have confinement at low energies, we cannot directly measure the quark masses from experiments. We can use the masses calculated from experiments along with a quark model to infer a quark mass, but the obvious drawback is that the quark masses calculated are dependant on the type of experiment and quark model used. As a result, a systematic analysis is required to cross-check the different methods.

Features of QCD can be studied in the lab by undergoing measurements which can be used to determine matrix elements. Theoretically, these are difficult in QCD so we use lattice QCD instead. This thesis is interested in the determination

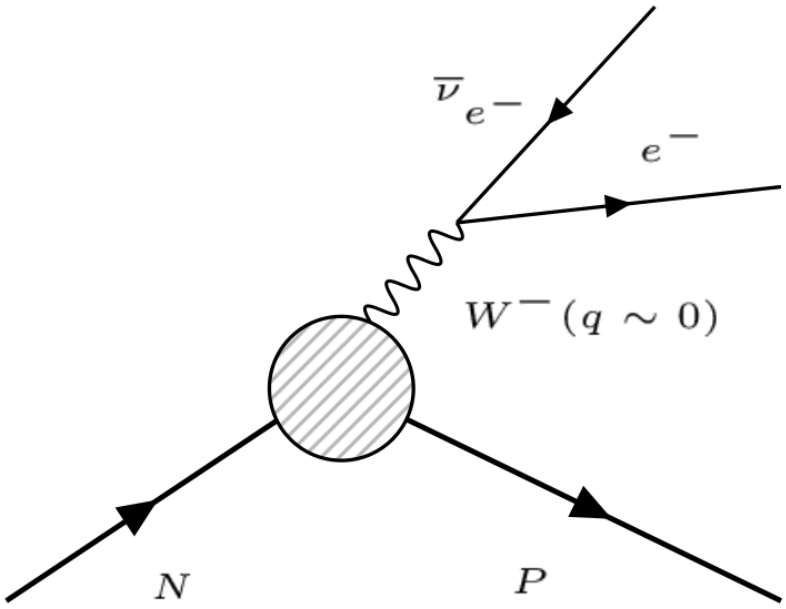

Figure 2.2: Figure showing the β-decay process of a the neutron decaying into a proton and emitting an electron and electron anti-neutrino via a W^- boson.

of nucleon matrix elements, with a theory that only considers the three lightest quarks (up, down and strange).

2.3 Neutron β-Decay

The coupling g_A is related to the rate of neutron β-decay, which is where a neutron decays into a proton and emits a W^- boson which decays into an electron and an electron anti-neutrino. In the language of QCD, a down quark within the neutron changes into an up quark and emits an electron and an electron anti-neutrino.

$$n \to p + e^- + \overline{\nu}_e \qquad d \to u + e^- + \overline{\nu}_e \tag{2.7}$$

From the diagram depicting how the decay occurs in Figure 2.2, we can derive the scattering matrix element T_{fi} as:

$$T_{fi} = (-ig_W)^2 \cos\theta_c \left(\overline{u}_e(\vec{p}_e)\gamma_\mu(1-\gamma_5)\nu_{\nu_e}(\vec{p}_\nu)\right) \frac{i}{m_W^2} \langle p(\vec{p})| J_L^\mu(0) |n(\vec{p})\rangle \,, \tag{2.8}$$

with the weak current $J_L^\mu(0) \equiv \overline{u}\gamma^\mu (1-\gamma_5)\, d$ and with the assumption that the W

boson mass m_W is much larger than the transfer momentum q so that the initial neutron and final proton states have approximately the same momentum p^μ.

To obtain a matrix element between the neutron and proton, we need to define g_A and g_V using the above approximation $q \ll m_W$:

$$\langle p|\, \overline{u}\gamma_\mu d\,|n\rangle = g_V \overline{u}_p \gamma_\mu u_n, \qquad \langle p|\, \overline{u}\gamma_\mu\gamma_5 d\,|n\rangle = g_A \overline{u}_p \gamma_\mu\gamma_5 u_n. \tag{2.9}$$

We know that $g_V = 1$ due to the vector isospin charge ladder operator Q_V^+. Using the relation

$$\left[A_\mu^3, Q_V^+\right] = A_\mu^+, \tag{2.10}$$

where

$$A_\mu^3 = \frac{1}{2}(\overline{u}\gamma_\mu\gamma_5 u - \overline{d}\gamma_\mu\gamma_5 d), \qquad A_\mu^+ = \overline{u}\gamma_\mu\gamma_5 d, \tag{2.11}$$

the value g_A can be related to,

$$\langle p|\, \overline{u}\gamma_\mu\gamma_5 d\,|n\rangle = \langle p(\vec{p}), \vec{s}|\, \overline{u}\gamma_\mu\gamma_5 u - \overline{d}\gamma_\mu\gamma_5 d\,|p(\vec{p}), \vec{s}\rangle = 2 s_\mu g_A. \tag{2.12}$$

This gives a way to relate the g_A of neutron β-decay to a matrix element of the proton.

By using the differential decay rate relation

$$d\Gamma\left(n \to p e^- \overline{\nu}_e\right) \propto \left[1 + \frac{\left|\vec{k_e}\right|(1-g_A)^2}{E_e(1+3g_A)^2}\cos\theta\right] dE_e d\cos\theta, \tag{2.13}$$

with the angle θ between the emitted electron and electron anti-neutrino and utilising momentum conservation, the value of g_A can be extracted.

Experimentally, $\lambda = g_A/g_V = 1.270(3)$ has been observed [2–21], with the newest experiments using "cold polarised neutrons".

2.4 Form Factors

The spatial, charge and magnetisation density of nucleons are encoded in electromagnetic form factors [22]. While these were first studied for the proton and neutron in the 1950's [23, 24], yet we still have much to determine and discover with them [25]. Nowadays we have many precise experimental determinations of many form factors [26–29] and to accompany this, many low energy non-perturbative lattice QCD calculations have been performed [30–46].

Electron-nucleon scattering is one of the most common experiments performed, which involves an electron elastically scattering of a nucleon. Within this colision,

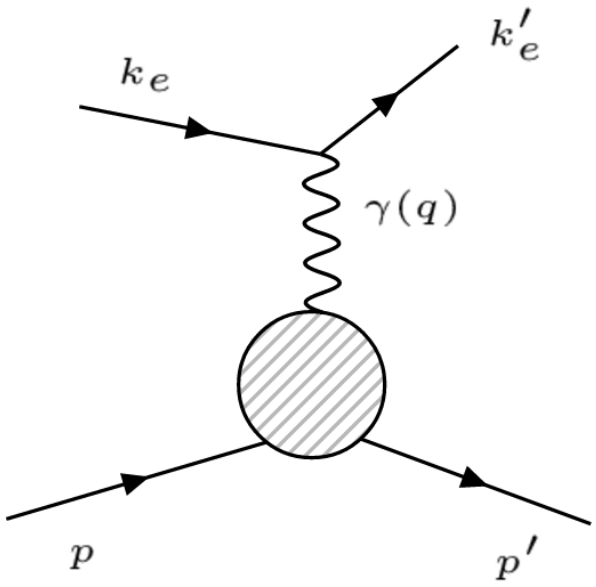

Figure 2.3: Figure showing the nucleon/electron interaction with initial momenta k_e and p and final momenta k'_e and p', respectively.

momentum $-q^2$ is transfered (shown in Figure 2.3) in the ranges of $[0.49, 3.47](GeV)^2$ in [27], $[0.215, 0.474](GeV)^2$ in [28] and $[0.298, 0.695](GeV)^2$ in [29]. Assuming one photon exchange, we can obtain a scattering amplitude of

$$T_{fi} = (-ie)^2 \overline{u}_e(\vec{k'}_e)\gamma_\mu u_e(\vec{k}_e)\frac{-i}{q^2}\left\langle \vec{p'}|J^\mu(\vec{q})|\vec{p}\right\rangle, \tag{2.14}$$

where the vector current J_μ is

$$J_\mu = q_u \overline{u}\gamma_\mu u + q_d \overline{d}\gamma_\mu d + ... \tag{2.15}$$

and q_q is the charge associated with the the quark $q = u, d, s, ...$ We can use the vector form factor to understand how the nucleon is structured, for example, the charge distribution of the nucleon.

Considering all possible unique vector terms, we arrive at the decomposition for the vector matrix element:

$$\left\langle \vec{p'}|J^\mu(\vec{q})|\vec{p}\right\rangle = \overline{u}(\vec{p'})\left[\frac{q_\mu}{2m_N}F_0(q^2) + \gamma_\mu F_1(q^2) + \frac{i\sigma^{\mu\nu}q_\nu}{m_N}F_2(q^2) + \frac{q_\mu\gamma^\nu q_\nu}{4m_N^2}F_3(q^2)\right]u(\vec{p}), \tag{2.16}$$

where m_N is the mass of the nucleon and $F_1(q^2)$ and $F_2(q^2)$ are the electric current and anomalous magnetic moment form factors at momentum transfer $q^2 \equiv q^\mu q_\mu$.

The terms $F_0(q^2)$ and $F_3(q^2)$ do not contribute due to the Ward identity, which tells us

$$\overline{u}_e(\vec{k'}_e)\gamma_\mu u_e(\vec{k}_e)q^\mu = 0. \tag{2.17}$$

It is common practice to define the Sachs electric and magnetic form factors as

$$\begin{aligned} G_E(q^2) &= F_1(q^2) + \frac{q^2}{(2m_N)^2}F_2(q^2), \\ G_M(q^2) &= F_1(q^2) + F_2(q^2), \end{aligned} \tag{2.18}$$

respectively. Two useful quantities are the mean square radius of the nucleon, which in the non-relativistic limit is

$$\langle r^2 \rangle \equiv -6 \left. \frac{dG_E(q^2)}{dq^2} \right|_{q^2=0}, \tag{2.19}$$

and the magnetic moment of the nucleon, which is $\mu = G_M(Q^2 = 0)$.

The next form factor is the non-zero transfer momentum version of β-decay described in Section 2.3. Depending on the transfer of momentum direction, the W^--boson processes are described as

$$\nu_l + n \to l + p, \qquad n \to \overline{\nu}_l + l + p, \tag{2.20}$$

where the lepton $l = e^-, \mu^-, \tau^-$. The matrix element the muon-neutrino, neutron scattering process diagrammatically shown in Figure 2.4, is

$$T_{fi} = (-ig_W)^2 \cos\theta_c \overline{u}_\mu(\vec{k'}_\mu)\gamma_\mu(1-\gamma_5)u_\nu(\vec{k}_\nu)\frac{i}{m_W^2}\left\langle p(\vec{p'})|J_5^\mu(\vec{q})|n(\vec{p})\right\rangle. \tag{2.21}$$

The Lorentz decomposition for the neutron-proton transition matrix element part becomes

$$\left\langle p(\vec{p'})|J_5^\mu(\vec{q})|n(\vec{p})\right\rangle = \overline{u}_p(\vec{p'})\left[\gamma^\mu\gamma^5 G_A(q^2) + \frac{q^\mu}{2m_N}\gamma^5 G_P(q^2)\right]u_n(\vec{p}), \tag{2.22}$$

where we have defined the axial-vector form factor $G_A(q^2)$ and the induced pseudo-scalar form factor $G_P(q^2)$.

Last point, as noted previously, we have the relation:

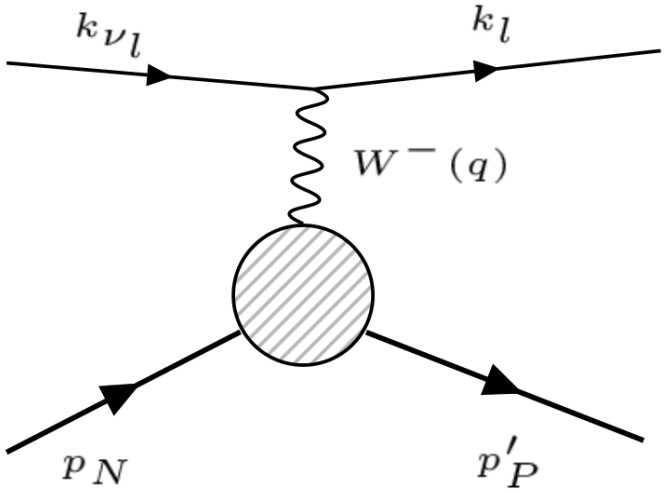

Figure 2.4: Figure showing the analogous non-zero transfer momentum q version β-decay from Figure 2.2.

$$G_A(q^2 = 0) = g_A \tag{2.23}$$

Although these form factors have rich and deep experimental and theoretical importance, this thesis will be more concerned with how we extract the form factors from lattice QCD calculations and systematics associated with these extractions.

2.5 Deep Inelastic Scattering

Another way to describe the structure of hadrons is by understanding the *Parton Distribution Functions* (PDF) which, when analysing the unpolarised PDF, describes how the momentum of the hadron is distributed to the quarks and gluons. The PDF's can be determined experimentally by deep inelastic scattering, which is still a lepton-nucleon collision, but in which transfer momentum q is so large, the target is no longer a nucleon.

Many models have been formulated [47–53] and experiments undertaken [54–57] to understand this field. Lattice QCD has been involved in determining matrix elements that are related to Mellin moments of the parton distribution functions [58–61], and in Chapter 7, we show extracted values for the first moment or momentum fraction $\langle x \rangle$.

For deep inelastic scattering, the process is shown pictorially in Figure 2.5 and is described by the scattering amplitude

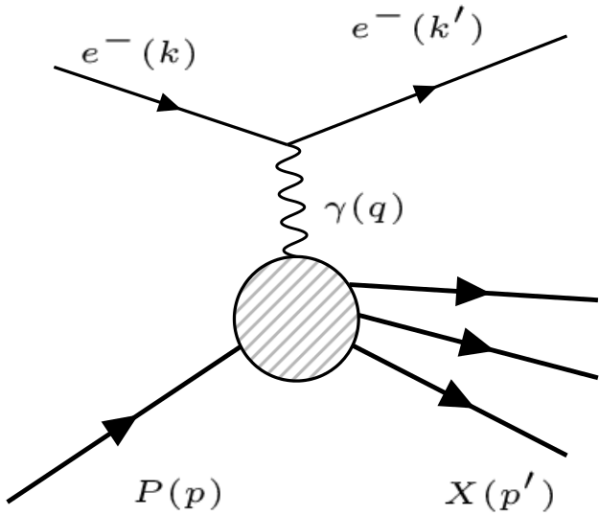

Figure 2.5: Figure demonstrating the deep inelastic scattering process for a nucleon/electron collision producing some final state X.

$$T_{fi} = (-ie)^2 \overline{u}_e(\vec{p}_e')\gamma_\mu u_e(\vec{p}_e)\frac{-i}{q^2}\left\langle X\right| J^\mu(\vec{q})\left|\vec{p}\right\rangle, \tag{2.24}$$

where X is some unknown final state. The usual initial and final momenta of the target are p and p' and initial and final momenta of the lepton $k = (E_e, \vec{k})$ and $k' = (E_e', \vec{k}')$ respectively. To be more precise about the inelastic scattering condition, the invariant mass $M_X^2 = (p+q)^2$ in elastic scattering must be fixed to the final state $M_X^2 = m_N^2$, where as for inelastic scattering, we take $M_X^2 > m_N$. The Bjorken scaling parameter x and its inverse ω are defined as

$$\omega \equiv 1/x \equiv \frac{2m_N\nu}{Q^2} = \frac{-2p\cdot q}{q^2}, \qquad \nu \equiv \frac{p\cdot q}{m_n}. \tag{2.25}$$

Elastic scattering has values $x = \omega = 1$ but for deep inelastic scattering, we have any $x \leq 1$ but require large $Q^2 \equiv -q^2$. The resulting cross section becomes

$$\left.\frac{d^2\sigma}{d\Omega dE_e'}\right|_{\text{N lab. frame}} = \frac{\alpha^2}{m_N Q^4}\frac{E_e'}{E_e}L_{\mu\nu}W^{\mu\nu}, \tag{2.26}$$

where the leptonic tensor is defined as

$$L_{\mu\nu} = k_\mu' k_\nu + k_\nu' k_\mu - g_{\mu\nu}k'\cdot k + i\epsilon_{\mu\nu\sigma\rho}s_e^\rho q^\sigma. \tag{2.27}$$

By considering the *inclusive process* in which the final states X are summed over, the hadronic part of the cross section has the form

$$
\begin{aligned}
W^{\mu\nu} &= \frac{1}{4\pi}\int d^4x e^{-iq\cdot x}\left\langle p\right|\left[J^{\mu}(x), J^{\nu}(0)\right]\left|p\right\rangle, \\
&\equiv W_S^{\mu\nu} + iW_A^{\mu\nu}.
\end{aligned}
\tag{2.28}
$$

We can Lorentz decompose the scalar and axial components of the hadronic cross section term to produce the factors

$$
\begin{aligned}
W_S^{\mu\nu} &= \left(g^{\mu\nu} + \frac{q^\mu q^\nu}{q^2}\right)F_1(x,Q^2) + \frac{1}{m_N\nu}\left(p^\mu - \frac{p\cdot q}{q^2}q^\mu\right)\left(p^\nu - \frac{p\cdot q}{q^2}q^\nu\right)F_2(x,Q^2) \\
W_A^{\mu\nu} &= \frac{1}{m_N\nu}\epsilon^{\mu\nu\rho\sigma}q_\rho s_\sigma g_1(x,Q^2) + \frac{1}{m_N\nu}\epsilon^{\mu\nu\rho\sigma}q_\rho\left(s_\sigma - \frac{q\cdot s}{m_N\nu}p_\sigma\right)g_2(x,Q^2)
\end{aligned}
\tag{2.29}
$$

The unpolarised structure functions F_1 and F_2 carry information about the longitudinal parton structure and g_1 and g_2 encode the corresponding longitudinal spin distributions. For the present thesis, we focus on the quark momentum fraction $\langle x\rangle$ which is related to the structure functions F_1 and F_2. Although the axial-vector current g_A can be related to g_1 by the Bjorken sum rule, it is not explored in this thesis.

To gain physical intuition, we can employ Feynman's *parton model* of the nucleon, in which in the Bjorken limit of high transfer energy $Q^2 \to \infty$ at some fixed Bjorken scale x, the nucleon is considered to be three free on-shell particles or "partons". We can define the Bjorken limit structure functions as

$$
F_1(x) = \lim_{Q^2\to\infty} F_1(x,Q^2), \quad F_2(x) = \lim_{Q^2\to\infty}\frac{\nu}{M_X}F_2(x,Q^2),
\tag{2.30}
$$

where the previously defined ν in Eq.(2.25) is the energy transferred to the nucleon by the scattering electron.

By continuing Feynman's parton view of the nucleon, the total structure function is related to a sum of the individual quark or "parton" densities constituting the proton

$$
F_1(x) = \frac{1}{2}\sum_i e_i^2 f_i(x), \qquad F_2(x) = x\sum_i e_i^2 f_i(x),
\tag{2.31}
$$

utilising the parton distribution function $f_i(x)$ which describes the probability that the probed quark i carries a fraction, x, of the proton's momentum.

To relate the parton interpretation to the structure functions, we define the first moment of the structure functions as

$$
\begin{aligned}
2\int_0^1 dx x F_1(x,Q^2) &= E^{\mathcal{S}}_{F_1;v_2}(\mu, g^{\mathcal{S}}) v_2^{\mathcal{S}}(\mu) + \mathcal{O}(1/Q^2), \\
\int_0^1 dx F_2(x,Q^2) &= E^{\mathcal{S}}_{F_2;v_2}(\mu, g^{\mathcal{S}}) v_2^{\mathcal{S}}(\mu) + \mathcal{O}(1/Q^2),
\end{aligned}
\tag{2.32}
$$

involving the Wilson coefficients $E^{\mathcal{S}}_{F_2;v_2}(\mu, g^{\mathcal{S}})$ calculated in perturbation theory for some scheme $\mathcal{S}$ at some momentum scale μ, and the proton (forward) matrix elements $v_n^{\mathcal{S}}$ which will be calculated using lattice QCD renormalised at the same scheeme $\mathcal{S}$.

Utilising the *operator product expansion* (OPE) which tells us that for some current operator $O^{(q)}$ acting on quark (q), in limit where now the position vector $x \to 0$ (or $q \to \infty$), the product of two operators can be reduced to one

$$
\lim_{x\to 0} O_i^{(q)}(x) O_j^{(q)}(0) = \sum_k E_{ijk}(x) O_{ijk}^{(q)}(0), \tag{2.33}
$$

where E_{ijk} are the appropriate Wilson coefficients which can be calculated perturbatively for small distances. All allowable operators for the right hand side of Eq.(2.33) have the form

$$
\begin{aligned}
O^{(q)}_{\mu_1\ldots\mu_n} &= i^{n-1}\overline{q}\gamma_{\mu_1}\overleftrightarrow{D}_{\mu_2}\ldots\overleftrightarrow{D}_{\mu_n}q, \\
O^{(5q)}_{\mu_1\ldots\mu_n} &= i^{n-1}\overline{q}\gamma_{\mu_1}\gamma_5\overleftrightarrow{D}_{\mu_2}\ldots\overleftrightarrow{D}_{\mu_n}q,
\end{aligned}
\tag{2.34}
$$

using the standard left/right derivative definition $\overleftrightarrow{D} \equiv \frac{1}{2}(\overrightarrow{D} - \overleftarrow{D})$. For this thesis, we will only consider the $n = 2$ case, which reduces down to

$$
\begin{aligned}
O^{(q)}_{\mu\nu} &= i\overline{q}\gamma_\mu\overleftrightarrow{D}_\nu q, \\
O^{(5q)}_{\mu\nu} &= i\overline{q}\gamma_\mu\gamma_5\overleftrightarrow{D}_\nu q.
\end{aligned}
\tag{2.35}
$$

The symmetrised traceless part of the operator $O^{(q)}_{\mu\nu}$ is defined as

$$
\mathcal{S}O^{(q)}_{\mu\nu} = i\overline{q}\left[\gamma_{\{\mu}\overleftrightarrow{D}_{\nu\}} - \frac{1}{4}\eta_{\mu\nu}\gamma_\omega\overleftrightarrow{D}^\omega\right]q. \tag{2.36}
$$

$$
\langle\vec{p},\vec{s}|\, i\overline{q}\left[\gamma_{\{\mu}\overleftrightarrow{D}_{\nu\}} - \frac{1}{4}\eta_{\mu\nu}\gamma_\omega\overleftrightarrow{D}^\omega\right]q\,|\vec{p},\vec{s}\rangle = v_2^f\overline{u}(\vec{p},\vec{s})\left(\gamma_{\{\mu}p_{\nu\}} - \frac{1}{4}\eta_{\mu\nu}\gamma_\omega p^\omega\right)u(\vec{p},\vec{s}). \tag{2.37}
$$

The simplest of choice for lattice QCD calculations is to consider the combination

$$O^{(q)}_{v_{2,b}} \equiv \overline{q}\left[\gamma_4 \overleftrightarrow{D}_4 - \frac{1}{3}\sum_{i=1}^{3}\gamma_i \overleftrightarrow{D}_i\right] q, \tag{2.38}$$

which when calculated in lattice QCD in sections to come, will be proportional to v_2. The last remark is that in the parton model, v_2 can be related to the quark momentum fraction $\langle x \rangle$ at some scale μ. The quark momentum fraction $\langle x \rangle$ is defined as the average value of the momentum fraction probability function q_P of quark $q = up, down, strange, etc...$

$$v_2^q(\mu) = \langle x \rangle^q(\mu) \equiv \int_0^1 dx x[q_P(x,\mu) + \overline{q}_P(x,\mu)] \tag{2.39}$$

This is why v_2 and $\langle x \rangle$ are used interchangeably throughout the thesis.

Chapter 3

Quantum Chromodynamics on the Lattice

To calculate non-perturbative properties in QCD from first principles we follow the Lattice gauge theory formulation of the Feynman path integral. A general overview can be found in [62–64]

The first step is to work in Euclidean space, which is achieved by rotating the time dimension by 90° in the complex plane

$$t \to it \qquad , \qquad it \to -t. \tag{3.1}$$

For dealing with fermions in the later Section 3.2, the γ matrices in Euclidean space satisfy hermiticity $\gamma = \gamma^\dagger$ and the anticommutator has the relation $\{\gamma_\mu, \gamma_\nu\} = 2\delta_{\mu\nu}$. For this thesis, the Sakurai representation for the γ matrices, which can be seen in Appendix A.1, were used.

The notion of a Lattice implies that a finite set of points in space-time will be used as a substitute for the continuous space-time we live in. This requires that the formalism for QCD including the Feynman path integral need analogous Lattice QCD versions. Assuming we have a uniform lattice of points, these quantities will depend on the separation between each of the points (denoted by a) and the length of the lattice in each space-time direction (denoted (L_x, L_y, L_z, L_t)). So our continuous space-time vectors x^μ now are restricted to only take values that are points on our lattice (Lat).

To introduce functions onto our lattice, we restrict the function to reflect our discretised lattice domain:

$$\psi(x) \to \psi(an) \ : \ n \in \mathbb{N}^{n_x} \times \mathbb{N}^{n_y} \times \mathbb{N}^{n_z} \times \mathbb{N}^{n_t}, \tag{3.2}$$

where n_x, n_y, n_z, n_t are the number of points in the (x, y, z, t) directions respectively and a is the lattice spacing used. The labelling an is usually dropped for the lattice

restricted space-time point x.

3.1 Gluon Action

The continuum gauge fields are replaced with a set of links $U_\mu(x)$ which now allows a gauge invariant method of transporting a quantity from $x \to x+\hat{\mu}$ where $\hat{\mu}$ is an adjacent lattice site corresponding to which direction is chosen for $(\mu = 1, 2, 3, 4)$. This gauge link can be related to the gluon fields $A_\mu(x)$ via

$$U_\mu(x) = \mathcal{P} e^{ig\int_0^a A_\mu(x+b\hat{\mu}/a)db}, \tag{3.3}$$

where $\mathcal{P}$ orders the integration on the path from x to $x+\hat{\mu}$.

We still impose the same gauge invariance on the lattice as in the continuous version, and require our gauge links $U_\mu(x)$ which belong in the gauge group $SU(3)$ rather than continuum gauge field algebra $su(3)$, to have the transformation

$$U'_\mu(x) = V(x)U_\mu(x)V(x+\hat{\mu})^{-1}, \tag{3.4}$$

using $V(x)$ described in Eq.(2.5).

With this transformation, it is easy to see that any traced loop of gauge links that have a common start and end point (for example, Eq.(3.5)) will be gauge invariant.

Naturally, the first quantity to note is the plaquette, which is the smallest loop of gauge links that start and end at a common space-time position. The Figure 3.1 shows how the gauge links are arranged to form the loop. We define it as

$$P_{\mu\nu}(x) = \frac{1}{3}\mathcal{R}e\mathrm{Tr}U_{sq}, \tag{3.5}$$

where,

$$U_{sq} \equiv U_\mu(x)U_\nu(x+\hat{\mu})U^\dagger_\mu(x+\hat{\nu})U^\dagger_\nu(x). \tag{3.6}$$

Rewriting as an integration around a closed loop and Taylor expanding, Eq.(3.5) becomes,

$$\begin{aligned} P_{\mu\nu}(x) &= \frac{1}{3}\mathcal{R}e\mathrm{Tr}\mathcal{P}e^{ig\oint_\Box A.dx} \\ &= \frac{1}{3}\mathcal{R}e\mathrm{Tr}\mathcal{P}\left[1 + ig\oint_\Box A.dx - \frac{1}{2}\left(g\oint_\Box A.dx\right)^2 + \mathcal{O}(A^3)\right]. \end{aligned} \tag{3.7}$$

Working in the Abelian theory, Stokes's Theorem tells us that,

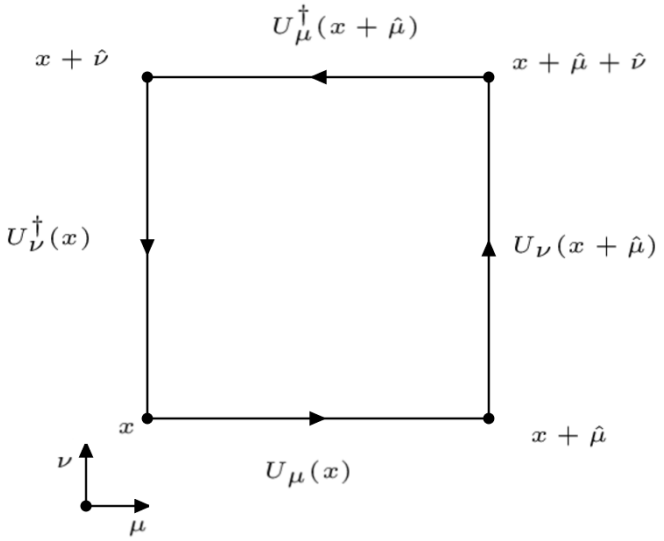

Figure 3.1: Diagram showing the arrangement of the gauge links U to form the smallest loop on the lattice in the μ, ν plane.

$$\begin{aligned}\oint_{\square} A.dx &= \int_{-\frac{a}{2}}^{\frac{a}{2}} dx_\mu dx_\nu \left[\partial_\mu A_\nu(x_0+x) - \partial_\nu A_\mu(x_0+x)\right] \\ &= \int_{-\frac{a}{2}}^{\frac{a}{2}} dx_\mu dx_\nu F_{\mu\nu}(x_0+x) \\ &= a^2 F_{\mu\nu}(x_0) + \frac{a^4}{24}(\partial_\mu^2 + \partial_\nu^2)F_{\mu\nu}(x_0) + \mathcal{O}(a^6, A^2),\end{aligned} \tag{3.8}$$

where $F_{\mu\nu} = \partial_\mu A_\nu - \partial_\nu A_\mu$ is the abelian field strength tensor and x_0 is the centre of the integration loop. The final line is the Taylor expansion of $F_{\mu\nu}(x_0+x)$ about the origin x_0. By inserting Eq.(3.8) into Eq.(3.7) and extracting the real component, we get,

$$P_{\mu\nu} = 1 - \frac{1}{2}g^2 a^4 \mathrm{Tr} F_{\mu\nu}^2 + \mathcal{O}(g^2 a^6, a^8, g^4 a^6) \tag{3.9}$$

The Wilson action for gluons on the lattice is written in terms of our plaquette operator,

$$S_{Wil} = \frac{2}{g^2}\sum_{x,\mu>\nu}(1 - P_{\mu\nu}(x)) = \frac{a^4}{2g^2}\sum_{x,\mu>\nu}\mathrm{Tr}\left[F_{\mu\nu}(x)^2\right] + \mathcal{O}(a^2, a^2 g^2). \tag{3.10}$$

The Wilson action of this kind agrees with the continuum gluon action (the first term in Eq.(2.2)) up until terms of order $\mathcal{O}(a^2)$. Since we can calculate not only squares, but rectangles and parallelograms on the lattice, we can improve on our action by incorporating rectangular terms $R_{\mu\nu}$ and parallelogram-shaped terms $L_{\mu\nu}$ to correct the $\mathcal{O}(a^2)$ effects [65].

Then added in a way to improve the action up to $\mathcal{O}(a^4)$ at tree level and $\mathcal{O}(g^2a^2)$

$$\begin{aligned} S_{Imp} &= \frac{2}{g^2}\sum_{x,\mu>\nu}\left[c_0(1-P_{\mu\nu}(x)) + c_1(1-R_{\mu\nu}(x)) + c_2(1-L_{\nu\mu}(x))\right], \\ & c_0 + 8c_1 + 8c_2 = 1 \end{aligned} \tag{3.11}$$

where the coefficients c_i which are generally functions of g^2 and are selected to remove tree level $\mathcal{O}(a^4)$ effects. A choice of $c_0 = 20/12$, $c_1 = -1/12$ and $c_2 = 0$ corresponds to the tree-level improved action [66] and $c_0 = 3.648$, $c_1 = -0.331$ and $c_2 = 0$ corresponds to the Iwasaki gauge action [67].

3.1.1 Gauge Field Mean-Field Improvement

Taylor expanding the gauge links with respect to the gluon fields, we can see,

$$U_\mu(x) \approx 1 + iagA_\mu(x) - \frac{1}{2}a^2g^2A_\mu^2(x) + \dots. \tag{3.12}$$

It can be noted that the terms $\mathcal{O}(a^2g^2)$ and larger are lattice artefacts which give rise to quark-gluon vertices with two or more gluons. The tadpole diagram can be constructed by contracting the two gluons in the term $\frac{1}{2}a^2g^2A_\mu^2(x)$. Lepage and Mackenzie [68] noted that for quantum fields, contracting the A_μ terms can create divergence factors of $1/a^2$ that counteract the increasing power of a. This means that the trailing terms are $\mathcal{O}(g^2)$ which results in large renormalisations that spoil naive perturbative lattice expansions. We can take account for this by modifying the lattice gauge fields by applying the mean-field improvement (or tadpole improvement).

This is done by separating the quark fields into a high energy UV component and the useful low energy IR component,

$$e^{iagA_\mu(x)} = e^{iag(A_\mu^{IR}(x)+A_\mu^{UV}(x))} \sim u_0 e^{iagA_\mu^{IR}(x)} \equiv u_0\tilde{U}_\mu(x). \tag{3.13}$$

As long as $u_0 \leq 1$, the new gauge fields $\tilde{U}_\mu(x)$, when replacing the old gauge fields $U_\mu(x)$, will retain the same transformation properties. Generally, the *mean-field improved gauge links* are constructed with the u_0 parameter set to

$$u_0 = \left(\frac{1}{3}\mathcal{R}e\mathrm{Tr}\left\langle U_{sq}\right\rangle\right). \tag{3.14}$$

3.2 Fermion Action

Although the gauge fields themselves can provide much information about the structure of our vacuum, introducing fermions into lattice QCD provides a way to analyse how fermionic particles are structured and how they interact with the rest of QCD. Starting with the Dirac action for a fermion:

$$\int d^4x\overline{\psi}(x)(\not{D}+m)\psi(x). \tag{3.15}$$

Derivatives on the lattice are reduced to finite differences. The two nearest neighbour prescriptions are

$$\begin{aligned} D^{(f)}_\mu\psi(x) =& \frac{1}{a}\left[U_\mu(x)\psi(x+\hat{\mu})-\psi(x)\right], \\ D^{(b)}_\mu\psi(x) =& \frac{1}{a}\left[U^\dagger_\mu(x-\hat{\mu})\psi(x-\hat{\mu})-\psi(x)\right], \end{aligned} \tag{3.16}$$

where the gauge links U have been constructed in Section 3.1, and a is the lattice spacing. The symmetric nearest neighbour derivative is constructed via the following,

$$D_\mu\psi(x) = \frac{1}{2}\left[D^{(f)}_\mu\psi(x) - D^{(b)}_\mu\psi(x)\right] = \frac{1}{2a}\left[U_\mu(x)\psi(x+\hat{\mu}) - U^\dagger_\mu(x-\hat{\mu})\psi(x-\hat{\mu})\right] \tag{3.17}$$

A first candidate for the fermion action on the lattice S^N_F can be derived by naively discretising the free fermion action

$$\begin{aligned} S^N_F[U,\psi,\overline{\psi}] = &\sum_{x\in Lat}\overline{\psi}(x)\sum_{\mu=1}^{4}\frac{1}{2a}\gamma_\mu\left[U_\mu(x)\psi(x+\hat{\mu}) - U^\dagger_\mu(x-\hat{\mu})\psi(x-\hat{\mu})\right] + \\ &\sum_{x\in Lat} m\overline{\psi}(x)\psi(x). \end{aligned} \tag{3.18}$$

The above can be rewritten in terms of an interaction matrix $M^N_{xy}[U]$ by inserting delta functions and summing over the lattice variables x, y

$$S_F^N[U,\psi,\overline{\psi}] = \sum_{x,y\in Lat} \overline{\psi}(x) M_{xy}^N[U]\psi(y), \tag{3.19}$$

where

$$M_{xy}^N[U] = m\delta_{xy} + \frac{1}{2a}\sum_{\mu=1}^{4}\gamma_\mu\left[U_\mu(x)\delta_{x(y-\hat{\mu})} - U_\mu^\dagger(x-\hat{\mu})\delta_{x(y+\hat{\mu})}\right]. \tag{3.20}$$

We define the free field propagator as the propagator in momentum space in which we set $U_\mu = 1$ for all points over the lattice. This fermion action suffers from the fermion doubling problem, which occurs when we look at the roots to the inverse of the free field propagator with respect to its momentum:

$$S^{-1}(p) = m_q + \frac{i}{a}\sum_\mu \gamma_\mu \sin(p_\mu a). \tag{3.21}$$

Taking a limit in which our quark masses $m_q \to 0$ we see this vanishes for multiple momenta solutions for $-\pi/a < p_\mu < \pi/a$, $\mu = 1,2,3,4$, obtaining more than 1 type of fermion.

3.2.1 Improving the Action

There are two methods used to resolve this problem, the first method involves staggering the degrees of freedom of the quarks on the lattice which results in reducing the number of momenta solutions from 16 to 16/4 [69].

Another method involves adding a Wilson term [70, 71] which is a five-dimensional scalar operator which would be added to the naive fermion action in Eq.(3.18) which breaks chiral symmetry at $\mathcal{O}(a)$

$$S_W = \sum_{x\in Lat}\overline{\psi}(x)\left[\sum_\mu\left(\gamma_\mu D_\mu - \frac{r(D_\mu^f + D_\mu^b)}{2}\right) + m\right]\psi(x), \tag{3.22}$$

where D_μ is defined in Eq.(3.17) and D_μ^f and D_μ^b are defined in Eq.(3.16) respectively.

A mass proportional to r/a is given to the 15 doublers which removes the doubler solutions in Eq.(3.18). Using the D definitions, we can write the action in full:

$$
\begin{aligned}
S_W = &\left(m + \frac{4r}{a}\right) \sum_{x \in Lat} \overline{\psi}(x)\psi(x) + \\
&\frac{1}{2a} \sum_{x \in Lat} \sum_{\mu=1}^{4} \overline{\psi}(x) \left[(\gamma_\mu - r) U_\mu(x) \psi(x + \hat{\mu}) - (\gamma_\mu + r) U_\mu^\dagger(x - \hat{\mu}) \psi(x - \hat{\mu})\right], \\
&\equiv \sum_{x,y \in Lat} \overline{\psi}_x^L M_{xy}^W \psi_y^L.
\end{aligned}
\tag{3.23}
$$

Again, our interacting matrix is pulled out as:

$$
M_{n.m}^W[U]a = \delta_{n,m} - \kappa \sum_\mu \left[(r - \gamma_\mu) U_\mu(x) \delta_{n,m-\mu} + (r + \gamma_\mu) U_\mu^\dagger(x - \mu) \delta_{n,m+\mu}\right],
\tag{3.24}
$$

and we have renormalised our quark fields and introduced our κ parameter by

$$
\psi^L = \psi/\sqrt{2\kappa}, \qquad \kappa = (2m_q a + 8r)^{-1}. \tag{3.25}
$$

When taking the standard value $r = 1$, the quark mass becomes

$$
m_q = \frac{1}{2}\left(\frac{1}{\kappa} - \frac{1}{\kappa_c}\right). \tag{3.26}
$$

The parameter κ_c is the critical kappa value which describes where the quark masses vanish. In the free theory, this is at $\kappa_c = 1/8r$, but when we have an interacting theory, additive and multiplicative renormalisations are needed due to explicit chiral symmetry breaking by the Wilson term.

Rewriting the Wilson action in the continuum limit

$$
S_W = \int d^4 \overline{\psi}(x) \left(\not{D} + m - \frac{ar \not{D}^2}{2}\right) \psi(x) + \mathcal{O}(a^2), \tag{3.27}
$$

we see a term an $\mathcal{O}(a)$ difference between the Wilson action in Eq.(3.27) and the naive action in Eq.(3.18).

3.2.2 Further Improving the Action

Since the Wilson action has $\mathcal{O}(a)$ errors, for this action to be reliable, simulations need to be undertaken at very fine lattice spacings which in turn requires more computational time. An improvement to the scaling properties of the action can

be obtained by adding operators of increasing dimension which all vanish in the continuum limit. Through many works [72–74], the clover term improved Wilson fermion action has been developed, which is also employed in this thesis and has the form

$$S_{SW} = S_W - \frac{iaC_{SW}r}{4}\overline{\psi}(x)\sigma_{\mu\nu}F_{\mu\nu}\psi(x), \tag{3.28}$$

in the process, scaling out the parameters of the theory by b_q, c_q, b_g and b_m

$$\begin{aligned} \psi \to \psi' = (1 + b_q am)(1 - c_q a \overrightarrow{\not{D}})\psi \qquad & \overline{\psi} \to \overline{\psi}' = (1 + b_q am)\overline{\psi}(1 + c_q a \overleftarrow{\not{D}}), \\ g^2 \to g^2(1 + b_g ma), \qquad & m \to m(1 + b_m ma). \end{aligned} \tag{3.29}$$

The parameter C_{SW} is tuned depending on the situation to remove the $\mathcal{O}(a)$ errors

$$C_{SW} = \begin{cases} 1 & \text{at tree level,} \\ 1/u_0^3 & \text{mean-field improved ,} \\ C_{SW}^{Lat} & \text{non-perturbatively lattice QCD calculated.} \end{cases} \tag{3.30}$$

where u_0 corrects for the quantum renormalisation of the operators. Improvements to the tuning can be done by using the Ward identity to tune C_{SW} which also improves the coupling g^2, quark mass m_q and the currents. Selecting $C_{SW} = C_{SW}^{Lat}$ is referred to as the non-perturbative (NP) improved clover fermion action, which is demonstrated by Chapter 4 [74].

3.3 Gauge Field and Propagator Generating

Just like in statistical mechanics systems, the partition function is where one generally begins to extract useful quantities. In lattice QCD, the partition function is defined as

$$Z = \int DU_\mu D\psi D\overline{\psi} e^{-S} \qquad S = S_G + S_F = S_G + \sum \overline{\psi} M \psi, \tag{3.31}$$

where S is the total QCD action, which encodes the systems particles and interactions. S is broken up into the gauge part S_G and the fermion part S_F which can be written in terms of an interaction matrix M as described in the previous section.

We can separate and integrate out the Grassmann fermion fields ψ and $\overline{\psi}$ to simplify the expression to

$$Z = \int DU_\mu \det[M] e^{-S_G}. \tag{3.32}$$

Physical observables in lattice QCD correspond to expectation values

$$\langle O \rangle = \frac{1}{Z} \int DU_\mu \det[M] O e^{-S_G}, \tag{3.33}$$

where $\langle O \rangle$ is the expectation value of the operator O which corresponds to the average value of the physical observable.

In Eq.(3.33), we have a dependency on the the background gauge field $U[A]$ which is being integrated over via $\int DU_\mu$. Since we cannot integrate over a continuous range, we must approximate the integral by a finite sum over some set of N gauge fields $\mathcal{U}[N] = \left\{U^i | i = 1, 2, ..., N\right\}$,

$$\langle O \rangle \approx \frac{1}{N} \sum_{i=1}^{N} O[U^{[i]}], \tag{3.34}$$

where $O[U^{[i]}]$ represents a measurement of O on a background gauge field "configuration" $U^{[i]}$. A Markov chain is used to generate $\mathcal{U}[N]$ via the accept/reject prescription to take us from the $U^{[i-1]}$ to $U^{[i]}$

$$P[U^{[i-1]}] P(U^{[i-1]} \to U^{[i]}) = P[U^{[i]}] P(U^{[i]} \to U^{[i-1]}), \tag{3.35}$$

where

$$P[U] = \left(\frac{1}{Z} \det[M] e^{-S_G}\right)[U], \tag{3.36}$$

is the probability weighting factor for proposing configuration U and $P(U \to U^{'})$ is the probability for the transfer of U to U'.

Starting from some initial gauge field $U^{[0]}$, which can be chosen to be "cold" which corresponds to the identity matrix, or "hot" where we choose a random SU(3) matrix, the Markov chain needs to thermalise which is decided by some thermalisation condition for $U^{[i=n]}$. Once thermalised, our set of gauge fields becomes

$$\mathcal{U}[N] = \left\{U^{[i]} | i = n, ..., N + n\right\}, \tag{3.37}$$

where n is the number of iterations before the gauge fields have thermalised in the Markov chain.

Since we require more than just the gauge fields to probe quarks and their interactions, we introduce quarks via the *quark propagator*. The goal of introducing the quark propagator is to remove the dependence of the quark operators on the

quark fields by performing Wick contractions. The quark propagators can be obtained by inverting the the Dirac operator on a particular gauge field U

$$S_{ab}^{\alpha\beta}(x, y, U, m_q) = (M_{ab}^{\alpha\beta})^{-1}(x, y, U, m_q), \tag{3.38}$$

where α, a, y are the spin, colour and lattice site of the annihilation "sink" operator respectively and β, b, x are the spin, colour and lattice site of the quark creation "source" operator respectively. Each propagator is calculated on a single gauge field U for a particular quark mass m_q.

Propagators are the building blocks for any hadronic lattice QCD calculation as we can combine propagators in different ways to analyse the particle system in question. To calculate anything we desire would require propagators from $y \to x$ for all x and y on the lattice, which is very computationally expensive. As we will see in the coming sections, we mitigate this problem by reducing the propagators to go from $y \to x$ for all x on the lattice, but some fixed space-time point y.

3.4 Correlation Functions

From this point onwards in this thesis, there will be a set of conventions used. Upper indices in English characters will represent the colour indices, lower indices in Greek will represent spin indices and any other subscripts/superscripts will be used for labelling. Using the split space-time notation $x = x^\mu = (\vec{x}, t)$, the source will be represented at the space-time position $x_0 = (\vec{x}_0, t_0)$ (set to $0 = (\vec{0}, 0)$ for the theory), the sink space-time position will be at $x = (\vec{x}, t)$. When a spatial Fourier transform is applied, the sink time-momentum will be $p' = (\vec{p}', t)$. The later defined three-point correlation function in Section 3.4.2 has an intermediate space-time point which will be denoted $y = (\vec{y}, \tau)$ or when spatial transformed to momentum space will be $q = (\vec{q}, \tau)$.

If summing over a primed vector variable (e.g. $\vec{x}'$), it is implied that the time variable is the same as the unprimed time variable (e.g. $x' = (\vec{x}', t)$ as $x = (\vec{x}, t)$).

The spin matrix Γ is a spin projector which is utilised to pick out components when traced with a spin matrix. When taking the trace $\mathrm{Tr}\{\}$, it will imply tracing both over spin matrices and colour matrices.

3.4.1 Two-Point Functions

Although gauge fields and quark propagators in position and momentum space can be studied in great depth, this thesis works on the calculations of nucleon masses and matrix elements. These require the construction of two-point and three-point correlation functions. For general interpolating fields χ_1 and χ_2 which correspond

to annihilation and creation operators at the sink and source respectively, the (forward) two-point correlation function on the lattice is defined as

$$G_2(\Gamma;\vec{p},t-t_0) \equiv \sum_{\vec{x}-\vec{x}_0} e^{-i\vec{p}\cdot(\vec{x}-\vec{x}_0)}\mathrm{Tr}\left\{\Gamma\left\langle\Omega\right|\chi_1(\vec{x},t)\overline{\chi}_2(\vec{x}_0,t_0)\left|\Omega\right\rangle\right\}. \tag{3.39}$$

The spin matrix Γ is used with the trace to project out particular spin components, $\vec{p}$ is the momentum of the system and t_0 and t are the times in which the particle is created and annihilated on the lattice, respectively. The correlator is taken to momentum space with momentum $\vec{p}$ by a spatial Fourier transform since we are interested in systems with momentum $\vec{p}$ rather than systems that travel from $\vec{x}_0$ to $\vec{x}$.

Although practically $(\vec{x}_0,t_0)$ will most likely be non-zero to avoid boundary condition effects, theoretically we set it to zero since we can translate our lattice in space-time to create an equally valid gauge field for our statistics (in Eq.(3.37)).

The usefulness of the two-point correlator can be seen once we reduce Eq.(3.39). Although in general, the source and sink interpolating fields can be different (which will be the case in Section 5.2), we set $\chi_1=\chi_2=\chi$ for this derivation. First we translate the operator $\chi(\vec{x},t)$, noting that we are working in Euclidean time

$$\begin{aligned}\chi(\vec{x},t) &= e^{\hat{H}t}e^{-i\hat{\vec{p}}\cdot\vec{x}}\chi(\vec{0},0)e^{-\hat{H}t}e^{i\hat{\vec{p}}\cdot\vec{x}}\\ G_2(\Gamma;\vec{p},t) &= \sum_{\vec{x}} e^{-i\vec{p}\cdot\vec{x}}\mathrm{Tr}\left\{\Gamma\left\langle\Omega\right|e^{\hat{H}t}e^{-i\hat{\vec{p}}\cdot\vec{x}}\chi(\vec{0},0)e^{-\hat{H}t}e^{i\hat{\vec{p}}\cdot\vec{x}}\overline{\chi}(\vec{0},0)\left|\Omega\right\rangle\right\},\end{aligned} \tag{3.40}$$

where the Hamiltonian and momentum operators are $\hat{H}$ and $\hat{\vec{p}}$ respectively. Next step is to insert a complete set of states,

$$\begin{aligned}G_2(\Gamma;\vec{p},t) &= \sum_{\vec{x}} e^{-i\vec{p}\cdot\vec{x}}\mathrm{Tr}\left\{\Gamma\left\langle\Omega\right|e^{\hat{H}t}e^{-i\hat{\vec{p}}\cdot\vec{x}}\chi(\vec{0},0)e^{-\hat{H}t}e^{i\hat{\vec{p}}\cdot\vec{x}}\hat{I}\ \overline{\chi}(\vec{0},0)\left|\Omega\right\rangle\right\}.\\ \hat{I} &= \sum_{N_s}\frac{\left|N_s\right\rangle\left\langle N_s\right|}{E_{p_s}} + \left|\Omega\right\rangle\left\langle\Omega\right|\end{aligned} \tag{3.41}$$

The index N_s is summed over all eigenstates, with each state having energy E_{p_s}, momentum $\vec{p}_s$ and spin s. The operators acting on $\left|N_s\right\rangle$ give

$$\hat{H}\left|N_s\right\rangle = E_{p_s}\left|N_s\right\rangle \qquad \hat{\vec{p}}\left|N_s\right\rangle = \vec{p}_s\left|N_s\right\rangle, \tag{3.42}$$

hence

$$G_2(\Gamma;\vec{p},t) = \sum_{\vec{x},N_s}\frac{1}{E_{p_s}}e^{-i(\vec{p}-\vec{p}_s)\cdot\vec{x}}e^{-E_{p_s}t}\mathrm{Tr}\left\{\Gamma\left\langle\Omega\right|\chi(\vec{0},0)\left|N_s\right\rangle\left\langle N_s\right|\overline{\chi}(\vec{0},0)\left|\Omega\right\rangle\right\}. \tag{3.43}$$

Breaking the sum over eigenstates into energy, momenta and spin $N_s = E_{p_s}, \vec{p}_s, s$ we can sum over $\vec{x}$, giving a δ-function and hence can be summed over $\vec{p}_s$

$$\sum_{\vec{p}_s,\vec{x}} = e^{-i\vec{x}\cdot(\vec{p}-\vec{p}_s)}F(\vec{p}_s) = \sum_{\vec{p}_s}\delta^3(\vec{p}-\vec{p}_s)F(\vec{p}_s) = F(\vec{p}), \tag{3.44}$$

which amounts to replacing $\vec{p}_s \to \vec{p}$

$$G_2(\Gamma;\vec{p},t) = \sum_{E_p,s}\frac{1}{E_p}e^{-E_p t}\mathrm{Tr}\left\{\Gamma\left\langle\Omega\right|\chi(\vec{0},0)\left|E_p,\vec{p},s\right\rangle\left\langle E_p,\vec{p},s\right|\overline{\chi}(\vec{0},0)\left|\Omega\right\rangle\right\}. \tag{3.45}$$

Next we evaluate the overlaps with the interpolating fields

$$\begin{aligned}\left\langle\Omega\right|\chi(\vec{0},0)\left|E_p,\vec{p},s\right\rangle &= \mathcal{Z}(E_p,\vec{p})\sqrt{E_p}u(\vec{p},s)\\ \left\langle E_p,\vec{p},s\right|\overline{\chi}(\vec{0},0)\left|\Omega\right\rangle &= \overline{\mathcal{Z}}(E_p,\vec{p})\sqrt{E_p}\overline{u}(\vec{p},s),\end{aligned} \tag{3.46}$$

where $u(\vec{p},s)$ is a spinor and $\mathcal{Z}(E_p,\vec{p})$ is the coupling strength of operator χ to the state with energy/momentum $(E_p,\vec{p})$

$$G_2(\Gamma;\vec{p},t) = \sum_{\vec{x},E_p,s}(\overline{\mathcal{Z}}\mathcal{Z})(E_p,\vec{p})e^{-E_p t}\mathrm{Tr}\left\{\Gamma u(\vec{p},s)\overline{u}(\vec{p},s)\right\}. \tag{3.47}$$

For baryons we must consider the anti-baryon contribution as well, which is achieved by changing $\chi \to \overline{\chi}$ and $\overline{\chi} \to \chi$. We denote the anti-particle energy/spinnors/correlator with a prime. The total contribution to the two-point correlation function is

$$\begin{aligned}G_2(\Gamma;\vec{p},t) =& G_2(\Gamma;\vec{p},t) + G_2'(\Gamma;\vec{p},t) =\\ &\sum_{E_p,s}(\overline{\mathcal{Z}}\mathcal{Z})(E_p,\vec{p})\mathrm{Tr}\left\{\Gamma\left(e^{-E_p t}u(\vec{p},s)\overline{u}(\vec{p},s)\right)\right\} +\\ &\sum_{E_p',s}(\overline{\mathcal{Z}}\mathcal{Z})(E_p',\vec{p})\mathrm{Tr}\left\{\Gamma\left(e^{-E_p' t}v'(\vec{p},s)\overline{v}'(\vec{p},s)\right)\right\}.\end{aligned} \tag{3.48}$$

If we can satisfy $(0 \ll t)$ on our lattice and we assume the lowest lying energy state is not the anti-particle version of the baryon (e.g. anti-proton), Eq.(3.48) can be reduced to just a ground state energy term of

$$G_2(\Gamma;\vec{p},t) = (\overline{\mathcal{Z}}\mathcal{Z})(E_p^{[0]},\vec{p})e^{-E_p^{[0]}t}\sum_s \mathrm{Tr}\left\{\Gamma u(\vec{p},s)\overline{u}(\vec{p},s)\right\}, \tag{3.49}$$

where $E_p^{[0]}$ is the ground state energy of the baryon. Summing over s, we have

$$\begin{aligned}\sum_s u(\vec{p},s)\overline{u}(\vec{p},s) =& -i\not{p}+m \\ G_2(\Gamma;\vec{p},t) =& (\overline{\mathcal{Z}}\mathcal{Z})(E_p^{[0]},\vec{p})e^{-E_p^{[0]}t}A(\Gamma,\vec{p},m^{[0]}),\end{aligned} \tag{3.50}$$

where we have defined the kinematical constant

$$A(\Gamma,\vec{p},m^{[0]}) \equiv \mathrm{Tr}\left\{\Gamma(-i\not{p}+m^{[0]})\right\}. \tag{3.51}$$

The most common projector used is the "unpolarised" projector $\Gamma = \Gamma_4 \equiv (I+\gamma_4)/2$ which gives rise to

$$G_2(\vec{p},t) \equiv G_2(\Gamma_4;\vec{p},t) = (\overline{\mathcal{Z}}\mathcal{Z})(E_p^{[0]},\vec{p})e^{-E_p^{[0]}t}, \tag{3.52}$$

with the relabelling of $(\overline{\mathcal{Z}}\mathcal{Z})(E_p^{[0]},\vec{p})A(\Gamma_4,\vec{p},m^{[0]}) \to (\overline{\mathcal{Z}}\mathcal{Z})(E_p^{[0]},\vec{p})$. The main focus of this thesis is fundamentally on the question *"when can we be justified in the approximation, $(0 \ll t)$?"* The results in Chapter 7 is a detailed analysis on the importance of this approximation and when we can be justified in this approximation for the two-point correlation functions and three-point correlation functions (defined in Section 3.4.2).

Using the propagators described in Section 3.3, we create two-point correlators on the lattice by combining different quark propagators to create the system we want to analyse. For a baryon that consists of two different types of quarks (e.g. up and down quark for proton/neutron), we can write down their interpolating fields for a proton.

$$\chi_\alpha(x) = \epsilon^{abc}u_\alpha^a(x)u_\beta^b(x)\widetilde{C}_{\beta\gamma}d_\gamma^c(x) \qquad \overline{\chi}_\alpha(x) = \epsilon^{a'b'c'}\overline{u}_\alpha^a(x)\overline{d}_\beta^b(x)\widetilde{C}_{\beta\gamma}\overline{u}_\gamma^c(x). \tag{3.53}$$

The quark fields u and d refer to the "doubly" or the "singly" -represented up and down quark in the proton which correspond to the quark occurring twice or once in the baryon respectively (and the convention q refers to any quark). The spin matrix $\widetilde{C} = C\gamma_5$ where C is the charge conjugation matrix. In Sakurai representation, we have $C = \gamma_4\gamma_2\gamma_5 = \gamma_3\gamma_1$.

The forward propagating two-point correlator can be expressed in terms of quark fields

$$G_2(\Gamma;\vec{p},t) \equiv \sum_{\vec{x}} e^{-i\vec{p}\cdot\vec{x}}\epsilon^{abc}\epsilon^{a'b'c'}\widetilde{C}_{\beta\gamma}\widetilde{C}_{\beta'\gamma'}\Gamma_{\alpha'\alpha}\left\langle u_\alpha^a(x)u_\beta^b(x)d_\gamma^c(x)\overline{u}_{\alpha'}^{a'}(0)\overline{d}_{\beta'}^{b'}(0)\overline{u}_{\gamma'}^{c'}(0)\right\rangle. \tag{3.54}$$

Next we perform Wick contractions for all possible combinations. The standard Wick contraction of two quark fields we define as the propagator in Eq.(3.38), dropping the (U, m_q) for ease of notation

$$S^{(q)aa'}_{\alpha\alpha'}(x,y) \equiv \overbrace{q^a_\alpha(x)\bar{q}^{a'}_{\alpha'}}(y), \tag{3.55}$$

where q represents the quark flavour used in the contraction, which is either the doubly/singly quark in the baryon, or in general could correspond to a disconnected quark (e.g. strange quark in the proton). In Eq.(3.54) we can write down two different ways to contact all the quark fields

$$\begin{aligned} G_2(\Gamma;\vec{p},t) = &\sum_{\vec{x}} e^{-i\vec{p}\cdot\vec{x}}\epsilon^{abc}\epsilon^{a'b'c'}\widetilde{C}_{\beta\gamma}\widetilde{C}_{\beta'\gamma'}\Gamma_{\alpha'\alpha} \\ &\langle S^{(d)cb'}_{\gamma\beta'}(x,0)\left(S^{(u)aa'}_{\alpha\alpha'}(x,0)S^{(u)bc'}_{\beta\gamma'}(x,0) + S^{(u)ac'}_{\alpha\gamma'}(x,0)S^{(u)ba'}_{\beta\alpha'}(x,0)\right)\rangle\,. \end{aligned} \tag{3.56}$$

For simplicity, we define the quantity

$$\underline{S^{(q)cb'}_{\gamma'\beta}}(x,0) \equiv \widetilde{C}_{\beta\gamma}S^{(q)cb'}_{\gamma\beta'}(x,0)\widetilde{C}_{\beta'\gamma'}, \tag{3.57}$$

which simplifies the expression to

$$\begin{aligned} G_2(\Gamma;\vec{p},t) = &\sum_{\vec{x}} e^{-i\vec{p}\cdot\vec{x}}\epsilon^{abc}\epsilon^{a'b'c'} \\ &\left[\left\langle \mathrm{Tr}\left\{\Gamma S^{(u)aa'}(x,0)\right\}\mathrm{Tr}\left\{\underline{S^{(d)cb'}}(x,0)S^{(u)bc'}(x,0)\right\}\right\rangle + \right. \\ &\left.\left\langle \mathrm{Tr}\left\{\Gamma S^{(u)ac'}(x,0)\underline{S^{(d)cb'}}(x,0)S^{(u)ba'}(x,0)\right\}\right\rangle\right]. \end{aligned} \tag{3.58}$$

So once we have constructed the propagators S and $\underline{S}$ on each of the gauge field, we can take traces of the combinations above to give the two-point correlation function G_2.

3.4.2 Three-Point Functions

To investigate the internal structure of the hadron (in this case, baryon), we must create a three-point correlation function. The three-point correlation function is analogous to the two-point correlator with the added current insertion operator

$O^{(q)}$ at some intermediate position $(\vec{y},\tau)$ on some quark $q = up, down, strange, ...$ Again we assume the creation operators are at the origin

$$G_3(\Gamma;\vec{p}',t;\vec{q},\tau;O^{(q)}) = \sum_{\vec{x},\vec{y}} e^{-i\vec{p}'\cdot\vec{x}} e^{i\vec{q}\cdot\vec{y}} \mathrm{Tr}\left\{\Gamma \langle\Omega| \chi(\vec{x},t) O^{(q)}(\vec{y},\tau)\overline{\chi}(\vec{0},0) |\Omega\rangle\right\}. \tag{3.59}$$

This time, we have two independent momenta $\vec{q}$ and $\vec{p}'$ which correspond to the momenta at the current insertion space-time point $(\vec{y},\tau)$ and sink $(\vec{x},t)$. For ease of notation, we refer to the source momentum $p^\mu = p'^\mu - q^\mu$. We follow the same procedure for the two-point correlation function, starting with time invariance from Eq.(3.40)

$$\begin{aligned} G_3(\Gamma;\vec{p}',t;\vec{q},\tau;O^{(q)}) = &\sum_{\vec{x},\vec{y}} e^{-i\vec{p}'\cdot\vec{x}} e^{i\vec{q}\cdot\vec{y}} \\ &\mathrm{Tr}\left\{\Gamma \langle\Omega| e^{\hat{H}t} e^{-i\hat{\vec{p}}\cdot\vec{x}} \chi(\vec{0},0) e^{-\hat{H}t} e^{i\hat{\vec{p}}\cdot\vec{x}} \times \right. \\ &\left. e^{\hat{H}\tau} e^{-i\hat{\vec{p}}\cdot\vec{y}} O^{(q)}(\vec{0},0) e^{-\hat{H}\tau} e^{i\hat{\vec{p}}\cdot\vec{y}} \overline{\chi}(\vec{0},0) |\Omega\rangle\right\}. \end{aligned} \tag{3.60}$$

Inserting the complete set of states from Eq.(3.41)

$$\begin{aligned} G_3(\Gamma;\vec{p}',t;\vec{q},\tau;O^{(q)}) = &\sum_{\vec{x},\vec{y}} \sum_{N_1,N_2} \frac{1}{E_{N_1} E_{N_2}} e^{-i\vec{p}'\cdot\vec{x}} e^{i\vec{q}\cdot\vec{y}} \\ &\mathrm{Tr}\left\{\Gamma \langle\Omega| e^{\hat{H}t} e^{-i\hat{\vec{p}}\cdot\vec{x}} \chi(\vec{0},0) e^{-\hat{H}t} e^{i\hat{\vec{p}}\cdot\vec{x}} |N_1\rangle \right. \\ &\left. \langle N_1| e^{\hat{H}\tau} e^{-i\hat{\vec{p}}\cdot\vec{y}} O^{(q)}(0) e^{-\hat{H}\tau} e^{i\hat{\vec{p}}\cdot\vec{y}} |N_2\rangle \langle N_2| \overline{\chi}(\vec{0},0) |\Omega\rangle\right\}, \end{aligned} \tag{3.61}$$

with the state $N_i, i = 1,2$ being decomposed into energy E_{p_i}, momentum $\vec{p}_i$ and spin s_i. Using the eigenvalues in Eq.(3.42) with the notation change of $s \to s_1$ or s_2, we have

$$\begin{aligned} G_3(\Gamma;\vec{p}',t;\vec{q},\tau;O^{(q)}) = &\sum_{N_1,N_2} \sum_{\vec{x},\vec{y}} e^{-i\vec{p}'\cdot\vec{x}} e^{i\vec{q}\cdot\vec{y}} \frac{1}{E_{N_1} E_{N_2}} \\ &\mathrm{Tr}\left\{\Gamma \langle\Omega| \chi(\vec{0},0) e^{-E_{p_1}t} e^{i\vec{p}_1\cdot\vec{x}} |N_1\rangle \langle N_1| e^{E_{p_1}\tau} e^{-i\vec{p}_1\cdot\vec{y}} \right. \\ &\left. O^{(q)}(0) e^{-E_{p_2}\tau} e^{i\vec{p}_2\cdot\vec{y}} |N_2\rangle \langle N_2| \overline{\chi}(\vec{0},0) |\Omega\rangle\right\}. \end{aligned} \tag{3.62}$$

Next we have the prescription $\vec{p}_1 \to \vec{p}'$ and $\vec{p}_2 \to \vec{p} = \vec{p}' - \vec{q}$ due to the two delta sums over $\vec{x}$ and $\vec{y}$ demonstrated in Eq.(3.44)

$$G_3(\Gamma; \vec{p}', t; \vec{q}, \tau; O^{(q)}) = \sum_{N_1, N_2} \frac{1}{E_{N_1} E_{N_2}} e^{-E_{p'}t} e^{-(E_p - E_{p'})\tau} \\ \mathrm{Tr}\left\{ \Gamma \langle \Omega | \chi(\vec{0}, 0) | N_1 \rangle \langle N_1 | O^{(q)}(0) | N_2 \rangle \langle N_2 | \overline{\chi}(\vec{0}, 0) | \Omega \rangle \right\}. \tag{3.63}$$

Utilising the spin sum in Eq.(3.46) along with

$$\langle E_{p'}, \vec{p}', s_1 | O^{(q)}(0) | E_q, \vec{p}, s_2 \rangle = \overline{u}(\vec{p}', s_1) \mathcal{J}_{O^{(q)}}(q^2) u(\vec{p}, s_2), \tag{3.64}$$

where $\mathcal{J}_{O^{(q)}}(q^2)$ is an appropriate form factor combination for the operator O described in Sections 2.4 and 2.5. Substituting all the overlaps gives us expressions

$$G_3(\Gamma; \vec{p}', t; \vec{q}, \tau; O^{(q)}) = \sum_{E_{p'}, E_p} \sum_{s_1, s_2} \frac{1}{E_p E_{p'}} e^{-E_{p'}t} e^{-(E_p - E_{p'})\tau} \\ \mathrm{Tr}\left\{ \Gamma \sqrt{E_{p'}} \mathcal{Z}(E_{p'}, \vec{p}') u(\vec{p}', s_1) \overline{u}(\vec{p}', s_1) \mathcal{J}_{O^{(q)}}(q^2) \right. \\ \left. u(\vec{p}, s_2) \sqrt{E_p} \overline{\mathcal{Z}}(E_p, \vec{p}) \overline{u}(\vec{p}, s_2) \right\}, \tag{3.65}$$

then summing over the spin s_1 and s_2 as shown in Eq.(3.50), we have

$$G_3(\Gamma; \vec{p}', t; \vec{q}, \tau; O^{(q)}) = \sum_{E_{p'}, E_p} e^{-E_{p'}t} e^{-(E_p - E_{p'})\tau} \mathcal{Z}(E_{p'}, \vec{p}') \overline{\mathcal{Z}}(E_p, \vec{p}) \\ \frac{1}{\sqrt{E_{p'} E_p}} \mathrm{Tr}\left\{ \Gamma(-i\not{p}' + m_{si}) \mathcal{J}_{O^{(q)}}(q^2) (-i\not{p} + m_{so}) \right\}, \tag{3.66}$$

where we have defined m_{si} and m_{so} as the source and sink ground state masses, which will generally be $m = m_{so} = m_{si}$. For convenience, we define the quantity

$$FF(E_p \to E_{p'}, \Gamma, O^{(q)}) \equiv \mathrm{Tr}\left\{ \Gamma(-i\not{p}' + m_{si}) \mathcal{J}_{O^{(q)}}(q^2) (-i\not{p} + m_{so}) \right\}. \tag{3.67}$$

Looking at the bare two- and three-point correlators individually, you cannot access the form factor $\mathcal{J}_{O^{(q)}}(q^2)$ due to the $\mathcal{Z}(E_{p'}, \vec{p}')$ and $\overline{\mathcal{Z}}(E_p, \vec{p})$ terms. To remove these, there are one of two combinations we take depending on which momenta we have access to

$$R(\Gamma;\vec{p}',t;\vec{q},\tau;O^{(q)}) \equiv \frac{G_3(\Gamma;\vec{p}',t;\vec{q},\tau;O^{(q)})}{G_2(\vec{p}',t)}\sqrt{\frac{G_2(\vec{p}',\tau)G_2(\vec{p}',t)G_2(\vec{p},t-\tau)}{G_2(\vec{p},\tau)G_2(\vec{p},t)G_2(\vec{p}',t-\tau)}}, \tag{3.68}$$

$$R_2(\Gamma;\vec{p}',t;\vec{q},\tau;O^{(q)}) \equiv \sqrt{\frac{G_3(\Gamma;\vec{p}',t;\vec{q},\tau;O^{(q)})G_3(\Gamma;\vec{p},t;-\vec{q},\tau;O^{(q)})}{G_2(\vec{p}',t)G_2(\vec{p},t)}}, \tag{3.69}$$

where we have omitted $\Gamma = \Gamma_4$ as our projector for the two-point correlation function for notational convenience. With these ratios, we have already made the assumption that $m = m_{so} = m_{si}$ so that the same interpolating fields are used for the two- and three-point correlators.

When we look at Eq.(3.68), we can break it into analysing the "energy and time dependence", the "$\mathcal{Z}$ dependence" and everything else that is left over. Since we know a priori that we need to under go a large current insertion and sink time approximation $t \gg \tau \gg 0$, we assume this for the derivation below.

The energy and time dependence for the ratio function Eq.(3.68) is

$$\begin{aligned} R(\Gamma;\vec{p}',t;\vec{q},\tau;O^{(q)})_{time} = e^{-E^{[0]}_{p'}t}e^{-\left(E^{[0]}_{p}-E^{[0]}_{p'}\right)\tau}e^{E^{[0]}_{p'}t}\times \\ \sqrt{e^{-E^{[0]}_{p'}\tau}e^{-E^{[0]}_{p'}t}e^{-E^{[0]}_{p}(t-\tau)}e^{-E^{[0]}_{p}\tau}e^{-E^{[0]}_{p}t}e^{-E^{[0]}_{p'}(t-\tau)}}, \end{aligned} \tag{3.70}$$

which reduces to

$$R(\Gamma;\vec{p}',t;\vec{q},\tau;O^{(q)})_{time} = e^{-\left(E^{[0]}_{p}-E^{[0]}_{p'}\right)\tau}\sqrt{e^{-2\left(E^{[0]}_{p'}-E^{[0]}_{p}\right)\tau}} = 1. \tag{3.71}$$

So we see that taking this combination removes all time dependence from our correlation function at the large time approximation. Next we look at the $\mathcal{Z}$ term

$$\begin{aligned} R(\Gamma;\vec{p}',t;\vec{q},\tau;O^{(q)})_{\mathcal{Z}} &= \frac{\mathcal{Z}(E^{[0]}_{p'},\vec{p}')\overline{\mathcal{Z}}(E^{[0]}_{p},\vec{p})}{\mathcal{Z}(E^{[0]}_{p'},\vec{p}')\overline{\mathcal{Z}}(E^{[0]}_{p'},\vec{p}')}\sqrt{\frac{\mathcal{Z}(E^{[0]}_{p'},\vec{p}')\overline{\mathcal{Z}}(E^{[0]}_{p'},\vec{p}')}{\mathcal{Z}(E^{[0]}_{p},\vec{p})\overline{\mathcal{Z}}(E^{[0]}_{p},\vec{p})}} \\ R(\Gamma;\vec{p}',t;\vec{q},\tau;O^{(q)})_{\mathcal{Z}} &= \sqrt{\frac{\mathcal{Z}(E^{[0]}_{p'},\vec{p}')\overline{\mathcal{Z}}(E^{[0]}_{p},\vec{p})}{\mathcal{Z}(E^{[0]}_{p},\vec{p})\overline{\mathcal{Z}}(E^{[0]}_{p'},\vec{p}')}}. \end{aligned} \tag{3.72}$$

Lastly, we can remove the $\mathcal{Z}$ dependence if we assume $\mathcal{Z}(E^{[0]}_{p'},\vec{p}')\overline{\mathcal{Z}}(E^{[0]}_{p},\vec{p})$ is real.

Using the definition in Eq.(3.67), the left-over becomes the whole ratio function (as the other terms become 1)

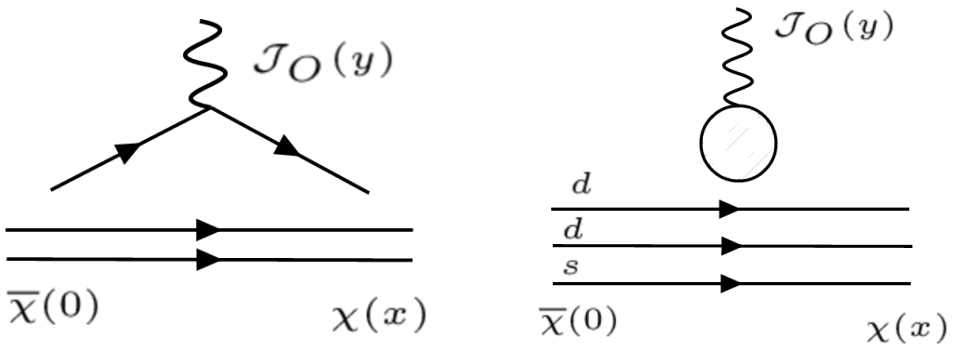

Figure 3.2: A pictorial representation of the connected (left) and disconnected (right) contributions to the three-point correlation function depending on the how we Wick contract Eq.(3.76).

$$R(\Gamma;\vec{p}',t;\vec{q},\tau;O^{(q)}) = \frac{1}{\sqrt{E_p^{[0]}E_{p'}^{[0]}}}\left(\frac{E_{p'}^{[0]}}{E_{p'}^{[0]}+m}\right)\sqrt{\left(\frac{E_{p'}^{[0]}+m}{E_{p'}^{[0]}}\right)\left(\frac{E_p^{[0]}}{E_p^{[0]}+m}\right)}\times FF(E_p^{[0]}\to E_{p'}^{[0]},\Gamma,O^{(q)}), \tag{3.73}$$

which, when reduced down, becomes

$$R(\Gamma;\vec{p}',t;\vec{q},\tau;O^{(q)}) = FF(E_p^{[0]}\to E_{p'}^{[0]},\Gamma,O^{(q)})\frac{1}{\sqrt{(E_{p'}^{[0]}+m^{[0]})(E_p^{[0]}+m^{[0]})}}, \tag{3.74}$$

which we can substitute the defined A kinematical function from Eq.(3.51)

$$R(\Gamma;\vec{p}',t;\vec{q},\tau;O^{(q)}) = FF(E_p^{[0]}\to E_{p'}^{[0]},\Gamma,O^{(q)})\frac{1}{\sqrt{E_p^{[0]}E_{p'}^{[0]}}}\left(A(\Gamma_4,\vec{p},m^{[0]})A(\Gamma_4,\vec{p}',m^{[0]})\right)^{-\frac{1}{2}}. \tag{3.75}$$

Following the same process for the two-point correlation function construction, we class the Wick contracted terms into *disconnected* and *connected* terms which correspond to whether the current insertion quarks are contracted with themselves or not respectively (pictorially demonstrated in Figure 3.2)

$$G_3^{dis}(\Gamma;\vec{p}',t;\vec{q},\tau;O^{(q)}) = \sum_{\vec{x},\vec{y}} e^{-i\vec{p}\cdot\vec{x}} e^{i\vec{q}\cdot\vec{y}} \epsilon^{abc}\epsilon^{a'b'c'} \widetilde{C}_{\beta\gamma}\widetilde{C}_{\beta'\gamma'}\Gamma_{\alpha'\alpha} \times \\ \langle u^a_\alpha(x) u^b_\beta(x) d^c_\gamma(x) \overline{q}^d_\delta(y) O^{de}_{\delta\epsilon} q^e_\epsilon(y) \overline{u}^{a'}_{\alpha'}(0) \overline{d}^{b'}_{\beta'}(0) \overline{u}^{c'}_{\gamma'}(0)\rangle, \tag{3.76}$$

where $q = up, down, strange, ...$ is a quark chosen to obtain the total current contribution for the current acting on the selected quark (which includes both disconnected and connected contributions).

The disconnected contribution has the Wick contracted form of

$$G_3^{dis}(\Gamma;\vec{p}',t;\vec{q},\tau;O^{(q)}) = \sum_{\vec{x},\vec{y}} e^{-i\vec{p}\cdot\vec{x}} e^{i\vec{q}\cdot\vec{y}} \epsilon^{abc}\epsilon^{a'b'c'} \\ \left\langle \left[\mathrm{Tr}\left\{\Gamma S^{(u)aa'}(0,x)\right\} \mathrm{Tr}\left\{ \underline{S^{(d)cb'}}(0,x) S^{(u)bc'}(0,x)\right\} + \right.\right. \\ \left.\left. \mathrm{Tr}\left\{\Gamma S^{(u)ac'}(0,x) \underline{S^{(d)cb'}}(0,x) S^{(u)ba'}(0,x)\right\}\right] \times \right. \\ \left. \mathrm{Tr}\left[S^{(q)ef}(y,y) O^{fe}(y)\right] \right\rangle, \tag{3.77}$$

which is the same calculation for the two-point correlation function with the added *disconnected* term

$$S^{dis} \equiv \mathrm{Tr}\left[S^{(q)ef}(y,y) O^{fe}(y)\right] \tag{3.78}$$

This extra term is difficult to calculate as we need to construct propagators from all source to sink space-time locations. While not discussed in this thesis, this has been looked at for nucleons [75–77].

At this point, we branch off into two common techniques for calculating the three-point correlation functions. The first method is the sequential source *through the operator* (TTO) technique in which we firstly construct a special TTO propagator, then construct the three-point correlator utilising the TTO and regular propagator. This propagator is defined as

$$\hat{S}^{(q)ab}_{\alpha\beta}(x;\vec{q},\tau;0,O) \equiv \sum_{\vec{y}} e^{i\vec{q}\cdot\vec{y}} S^{(q)ad}_{\alpha\delta}(x,y) O^{de}_{\delta\epsilon} S^{(q)eb}_{\epsilon\beta}(y,0), \tag{3.79}$$

where we have introduced the "hat" $\hat{}$ notation to denote the sequential propagator. To construct this propagator on the lattice, we rearrange the correlator as follows

$$\sum_{x} M^{(q)za}_{\omega\alpha}(x',x)\hat{S}^{(q)ab}_{\alpha\beta}(x;\vec{q},\tau;0,O) = \sum_{\vec{y},x} e^{i\vec{q}\cdot\vec{y}} M^{(q)za}_{\omega\delta}(x',x) S^{(q)ad}_{\alpha\delta}(x,y) O^{de}_{\delta\epsilon} S^{(q)eb}_{\epsilon\beta}(y,0), \tag{3.80}$$

the inverse propagator M is defined in Eq.(3.38). Reducing the equation down, we have the matrix inverse equation

$$\sum_{\vec{x}} M^{(q)za}_{\omega\alpha}(x',x)\hat{S}^{(q)ab}_{\alpha\beta}(x;\vec{q},\tau;0,O) = e^{i\vec{q}\cdot\vec{x}\,'} O^{ze}_{\omega\epsilon} S^{(q)eb}_{\epsilon\beta}(x',0), \tag{3.81}$$

where it is noted that $x' = (\vec{x}', t)$.

So in the same way as inverting the equation in Eq.(3.38), we can invert the above to create the TTO propagator. The TTO method of calculating the three-point correlator requires a chosen operator and current time-momentum $(\vec{q},\tau)$ since the TTO propagator involves O and $\vec{q}$ (as seen in Table 3.1).

Now we have the definition for the TTO propagator, we can utilise them in the quark level analysis of the three-point correlators. The Wick contracted three-point correlators for the current insertion on the doubly and singly -represented quarks are as follows

$$\begin{aligned} G_3(\Gamma;\vec{p}\,',t;\vec{q},\tau;O^{(u)}) = &\sum_{\vec{x}} e^{-i\vec{p}\cdot\vec{x}} \epsilon^{abc}\epsilon^{a'b'c'}\Gamma_{\alpha'\alpha} \\ &\left\langle \underline{S^{(d)cb'}_{\gamma'\beta}}(x,0) \left[\hat{S}^{(u)aa'}_{\alpha\alpha'}(x;\vec{q},\tau;0,O) S^{(u)bc'}_{\beta\gamma'}(x,0) + \right.\right. \\ &\qquad \hat{S}^{(u)ac'}_{\alpha\gamma'}(x;\vec{q},\tau;0,O) S^{(u)ba'}_{\beta\alpha'}(x,0) + \\ &\qquad \hat{S}^{(u)ba'}_{\beta\alpha'}(x;\vec{q},\tau;0,O) S^{(u)ac'}_{\alpha\gamma'}(x,0) + \\ &\qquad \left.\left. \hat{S}^{(u)bc'}_{\beta\gamma'}(x;\vec{q},\tau;0,O) S^{(u)aa'}_{\alpha\alpha'}(x,0) \right] \right\rangle, \end{aligned} \tag{3.82}$$

and

$$\begin{aligned} G_3(\Gamma;\vec{p}\,',t;\vec{q},\tau;O^{(d)}) = &\sum_{\vec{x}} e^{-i\vec{p}\cdot\vec{x}} \epsilon^{abc}\epsilon^{a'b'c'}\Gamma_{\alpha'\alpha} \\ &\left\langle \underline{\hat{S}^{(d)cb'}_{\gamma'\beta}}(x;\vec{q},\tau;0,O) \left[S^{(u)aa'}_{\alpha\alpha'}(x,0) S^{(u)bc'}_{\beta\gamma'}(x,0) + \right.\right. \\ &\qquad \left.\left. S^{(u)ac'}_{\alpha\gamma'}(x,0) S^{(u)ba'}_{\beta\alpha'}(x,0) \right] \right\rangle, \end{aligned} \tag{3.83}$$

using the underline notation defined in Eq.(3.57). This method was not employed in this thesis and only included for completeness.

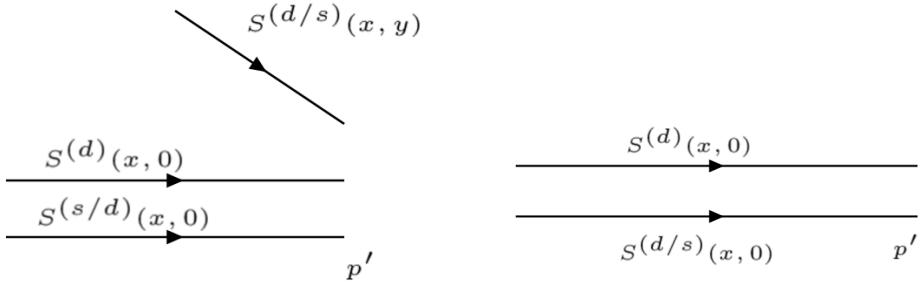

Figure 3.3: Diagram showing (left) the fixed sink propagator section of the three-point correlation function used in the sequential source fixed sink method and (right) the source used in the inversion to create the fixed sink propagator. The label (d/s) refers to a doubly or singly represented quark flavor propagator. For example, the proton we have $(d/s) = (u/d)$ for the up and down quarks.

The second method, named the *fixed sink* (FS) propagator construction method, starts by rewriting the three-point correlator in three terms

$$G_3(\Gamma;\vec{p}',t;\vec{q},\tau;O^{(q)}) = \sum_{\vec{y}} e^{i\vec{q}\cdot\vec{y}} \left\langle \Sigma^{(q)}(\vec{p}',t;y;0;\Gamma) O(y) S^{(q)}(y,0) \right\rangle , \tag{3.84}$$

where we define the *fixed sink* propagator Σ as

$$\Sigma^{(q)}(\vec{p}',t;y;0;\Gamma) \equiv \sum_{\vec{x}} e^{-i\vec{p}'\cdot\vec{x}} S^{(q)}_{(C)}(x,0,\Gamma) S^{(q)}(x,y), \tag{3.85}$$

and the source for the inversion $S^{(q)}_{(C)}$ is represented by all the quark lines excluding the one with a current vertex. The source is defined individually for the doubly-represented quark vertex

$$\begin{aligned} S^{(u)cb'}_{(C)\beta\gamma'}(x,y,0,\Gamma) \equiv & \epsilon^{abc}\epsilon^{a'b'c'} \times \\ & \left[\Gamma_{\alpha'\alpha} S^{(d)aa'}_{\alpha\alpha'}(x,0) \underline{S^{(d)bc'}_{\beta\gamma'}}(x,0) + \underline{\Gamma_{\alpha'\alpha}} \underline{S^{(d)ac'}_{\alpha\gamma'}}(x,0) \underline{S^{(d)ba'}_{\beta\alpha'}}(x,0) \right], \end{aligned} \tag{3.86}$$

and the singly-represented quark vertex

$$\begin{aligned} S^{(d)bc'}_{(C)\beta\gamma'}(x,y,0,\Gamma) \equiv & \epsilon^{abc}\epsilon^{a'b'c'} \times \\ & \Big[\Gamma_{\alpha'\alpha} \underline{S^{(d)cb'}_{\beta\gamma'}}(x,0) S^{(u)aa'}_{\alpha\alpha'}(x,0) + \Gamma_{\beta\alpha} \underline{S^{(d)ca'}_{\gamma\delta'}}(x,0) S^{(u)ab'}_{\alpha\delta'}(x,0) + \\ & \Gamma_{\alpha'\beta} \underline{S^{(d)ab'}_{\delta\gamma'}}(x,0) S^{(u)ca'}_{\delta\alpha'}(x,0) + \Gamma_{\beta\gamma'} \underline{S^{(d)aa'}_{\alpha\delta'}}(x,0) S^{(u)cb'}_{\alpha\delta'}(x,0) \Big]. \end{aligned} \tag{3.87}$$

Fixed Sink Method

Fixed before inversion	Fixed Symbol	Free after inversion	Free Symbol
interpolating fields	χ	current insertion operator	O
spin projector matrix	Γ	current insertion time	τ
sink momentum	$\vec{p}'$	current/source momentum	$\vec{p}$ or $\vec{q}$
sink annihilation time	t		
current quark flavour	u/d		

Through the Operator Method

Fixed before inversion	Fixed Symbol	Free after inversion	Free Symbol
current insertion operator	O	interpolating fields	χ
current insertion time	τ	spin projector matrix	Γ
current/source momentum	$\vec{p}$ or $\vec{q}$	sink momentum	$\vec{p}'$
		sink annihilation time	t
		current quark flavour	u/d

Table 3.1: Table describing what variables are fixed before the second inversion (left) or free to be varied post-inversion for both the fixed sink method (top) and through the operator method (bottom) for the three-point correlation function creation.

The diagrams that demonstrate the propagators used to construct the fixed sink propagator, as well as the source used in the construction of the FS propagator, are shown in Figure 3.3. Analogous to the TTO propagator, the fixed sink propagator is created via the inversion equation

$$\sum_{y} M^{(q)za}_{\omega\alpha}(x', y) \left(\gamma_5 \Sigma^{(q)\dagger}(\vec{p}', t; y; 0; \Gamma)\gamma_5\right)^{ab}_{\alpha\beta} = e^{-i\vec{p}'\cdot\vec{x}'} \left(\gamma_5 S^{(q)\dagger}_{(C)}\gamma_5\right)^{zb}_{\omega\beta}(x', 0, \Gamma), \tag{3.88}$$

where we have used the summed space-time point $y = (\vec{y}, \tau)$.

For the fixed sink method of creating the three-point correlation function, the baryon interpolating field χ, the spin projector Γ and the sink momentum $\vec{p}'$ must be decided before creating the fixed sink propagator. For this reason, generally the ratio function Eq.(3.68) is used since access to the three-point correlation function with $\vec{p}' \leftrightarrow \vec{p}$ requires additional computational time to create.

In Table 3.1 for the fixed sink method and the through the operator method, we show what quantities must be set before the second inversion and what quantities are free to be varied after the second inversion.

Chapter 4

Renormalisation

Since in continuum QCD, calculating the Feynman path integral leads to divergent integrals, we must cut off the integral to remove these divergences. When moving to non-perturbative lattice QCD, we introduce a lattice spacing a, which acts as a regulator by cutting off the high frequency modes of the integral. Calculating correlation functions and extracting values (e.g. in Chapter 6) using the cutoff provided by a is not sufficient to give values that are comparable with experimental results. The general approach to renormalising a lattice operator $O(a)$ (defined in Eq.(3.33)) for observables which depend on the choice of regulator is

$$O^{\mathcal{S}}(M) = Z_O^{\mathcal{S}}(M, g_0(a))O(a), \tag{4.1}$$

where we have renormalised using some particular scheme $\mathcal{S}$ for removing divergences, at some scale M and at a coupling strength $g_0(a)$.

4.1 Vector Form Factor Renormalisation

At finite lattice spacing, the local vector current $O^{(q)} = \overline{q}\gamma_\mu q$ is not conserved. By utilising the Ward identity, the conserved vector current for Wilson-style fermions has the form

$$O_\mu^{a(c)}(x) \equiv \frac{1}{2}\left[\bar{q}(x)(\gamma_\mu - I)t^a U_\mu(x)q(x+\mu) + \bar{q}(x+\mu)(\gamma_\mu + I)t^a U_\mu^\dagger(x)q(x)\right], \tag{4.2}$$

where t^a is a hermitian group generator of $SU(n_f)$ (n_f being the number of flavours). So by taking the combination using the conserved vector current, we can renormalise the local vector current by constructing the ratio of lattice three-point functions Eq.(3.66)

$$\frac{G_3(\Gamma_4;\vec{0},t;\vec{0},\tau;O_\mu^{(c)})}{G_3(\Gamma_4;\vec{0},t;\vec{0},\tau;O_\mu)} \xrightarrow{t\gg 0} \frac{Z_V}{Z_V^{(c)}} = Z_V, \tag{4.3}$$

where Z_V is the renormalisation constant for the local vector current. Since the conserved vector current was not calculated for this thesis, we can renormalise the vector form factor by using charge conservation with the fact that the ratio factor defined in Eq.(3.68), when applied to the vector current operator, produces

$$R(\Gamma;\vec{0},t;\vec{0},\tau;O_4) \xrightarrow{t\gg 0} \frac{1}{\sqrt{2}Z_V} FF(m\to m,\Gamma_4,O_4) = \frac{1}{Z_V}. \tag{4.4}$$

4.2 General Non-Perturbative Renormalisation

This section follows closely the work and method done in [78] and [79] to calculate the renormalisation values. There are other methods available, for example the Schrödinger functional method [80–84], but for this thesis we use the Rome-Southampton approach to calculating the renormalisation values.

To compute general renormalisation factors for all the current types, we start by constructing Greens functions on the lattice with source four-momentum p and sink four-momentum p'.

$$\begin{aligned} G_{\alpha\beta}(p,p',O) \equiv& \frac{a^{12}}{V}\sum_{x,y,z} e^{-ip'\cdot(x-z)}e^{-ip\cdot(z-y)} \left\langle O_{\alpha\beta}(x,y,z)\right\rangle, \\ O_{\alpha\beta}(x,y,z) \equiv& q_\alpha(x)O(z)\overline{q}_\beta(y) \end{aligned} \tag{4.5}$$

where V is the volume of the lattice and q is an up/down/strange quark. Next we define the *amputated Greens function* as

$$\Gamma(p,p',O) = S^{-1}(p)G(p,p',O)S^{-1}(p'), \tag{4.6}$$

with the definition of a quark propagator being

$$S(p) \equiv \frac{a^8}{V}\sum_{x,z} e^{-ip\cdot(x-y)} \left\langle q_\alpha(x)\overline{q}_\beta(y)\right\rangle, \tag{4.7}$$

4.2.1 Zero Transfer Momentum

The simplest case, which was calculated in this thesis, occurs when $p = p'$. For this case, we can impose the renormalisation condition on the vertex function [85–87] as

$$\Gamma_R(p) = Z_q^{-1} Z \Gamma(p), \tag{4.8}$$

where Z_q is the renormalisation for the fermion field (e.g. $q_R = Z_q q$), and Z is the renormalisation value required. The renormalisation value Z_q can be equated to the projection of the propagator onto the Born (or tree level) massless quark

$$Z_q = \Lambda_q(p)|_{p^2=\mu^2}, \qquad \Lambda_q(p) = \frac{\mathrm{Tr}(-i\sum_\mu \sin(ap_\mu) a S^{-1}(p))}{12\sum_\mu \sin^2(ap_\mu)}. \tag{4.9}$$

We fix Z by the renormalisation condition

$$\frac{1}{12}\mathrm{Tr}\left[\Gamma_R(p,p,O)\Gamma^{-1}_{Born}(p,p,O)\right]_{p^2=\mu^2} = 1, \tag{4.10}$$

with the renormalisation scale set to $p^2 = \mu^2$ for some μ^2. Utilising the Born term for the vertex function as Γ_{Born}, with some rearranging, we can write an expression for the renormalisation constant Z

$$Z = 12 Z_q \mathrm{Tr}\left[\Gamma(p,p,O)\Gamma^{-1}_{Born}(p,p,O)\right]^{-1}_{p^2=\mu^2}. \tag{4.11}$$

The Born term $\Gamma_{Born}(p,p',O)$ is dependent on which O is selected, the momentum p and the momentum transfer $p'-p$ (if non-zero)

$$\begin{aligned} \Gamma_{Born}(p,p,\gamma_\mu) &= -i\gamma_\mu, & \Gamma_{Born}(p,p,\gamma_\mu\gamma_5) &= -i\gamma_\mu\gamma_5, \\ \Gamma_{Born}(p,p,I) &= -iI, & \Gamma_{Born}(p,p,\gamma_\mu\gamma_\nu) &= -i\gamma_\mu\gamma_\nu, \end{aligned} \tag{4.12}$$

and the Born term for the momentum fraction $\langle x \rangle$ shown in Eq.(2.38) has the form

$$\Gamma_{Born}\left(p,p,\gamma_4 \overleftrightarrow{D}_4 - \frac{1}{3}\sum_{i=1}^{3}\gamma_i \overleftrightarrow{D}_i\right) = \gamma_4 p_4 - \frac{1}{3}\sum_{i=1}^{3}\gamma_i p_i. \tag{4.13}$$

The lattice momentum p must be chosen to avoid the energy scales

$$\Lambda^2_{QCD} \ll p^2 \leq \left(\frac{\pi}{a}\right)^2, \tag{4.14}$$

which avoids the QCD scale Λ^2_{QCD}, and lattice size effects from $\left(\frac{\pi}{a}\right)^2$.

We denote the result from this renormalisation calculation as a variant of the Regularisation Independent Momentum scheme (denoted $RI' - MOM$).

4.2.2 Lattice Greens Function Calculation

Firstly, the Fourier transformed quark propagator in Eq.(4.7) can be calculated by first calculating the inverse of the Dirac matrix Eq.(3.38), then taking the Fourier transform (we omit the conventional tilde used for Fourier transforms)

$$S(p) = \sum_x e^{-ip\cdot x} S(x,0), \tag{4.15}$$

making mention to this being a space-time Fourier transform, opposed to the spatial Fourier transform used for correlation functions in Chapters 3, 5 and 6. Then for the Greens function defined in Eq.(4.5), the total construction is

$$\begin{aligned} G(p,p',O) &= \sum_z e^{-i(p'-p)\cdot z} S(p',z) O(z) S(z,p), \\ S(z,p) &\equiv \sum_y S(z,y) e^{ip\cdot y}, \\ S(p,z) &\equiv \sum_y S(y,z) e^{ip\cdot y}, \end{aligned} \tag{4.16}$$

where we have utilised the "momentum source" propagator $S(p,z)$ or $S(z,p)$ that propagates from a position z to some momentum p (or vice-versa). We construct such a propagator via the inversion

$$\sum_\omega M(z,\omega) S(\omega,p) = e^{ip\cdot z}. \tag{4.17}$$

I.e. Inverting the above equation will produce a momentum source propagator $S(z,p)$.

4.2.3 Moving to the $\overline{MS}$ Scheme

The most commonly used scheme is named the *Modified Minimal Subtraction* scheme (denoted $\overline{MS}$) usually taken at the energy scale $\mu = 2\ GeV$. The first attempt to convert to this scheme would be to use Eq.(4.1) and convert directly to $\overline{MS}$

$$Z^{\overline{MS}}(2GeV) = \Delta Z^{\overline{MS}}_{RI'-MOM}(\mu) Z^{RI'-MOM}(\mu). \tag{4.18}$$

We first move to the Renormalisation Group Invariant (RGI) scheme, resulting in

$$Z^{\overline{MS}}(2GeV) = \Delta Z^{\overline{MS}}_{RGI}(2GeV) \Delta Z^{RGI}_{RI'-MOM}(\mu) Z^{RI'-MOM}(\mu). \tag{4.19}$$

We now perturbatively calculate the conversion factors ΔZ by starting with the three loop approximation to the coupling constant $g^{\mathcal{S}}(\mu)$ in some scheme $\mathcal{S}$

$$\frac{g^{\mathcal{S}}(\mu)^2}{16\pi^2} = \frac{1}{\beta_0 L} - \frac{\beta_1}{\beta_0^3}\frac{\log L}{L^2} + \frac{1}{\beta_0^5}\frac{\beta_1^2\log^2 L - \beta_1^2 \log L + \beta_2\beta_0 - \beta_1^2}{L^3}, \\ L \equiv \log\frac{\mu^2}{\Lambda^2_{\overline{MS}}}, \tag{4.20}$$

where the $\beta^{\mathcal{S}}$ function defined in Appendix B along with the perturbative expansion of said quantity. Once the coupling strengths g have been calculated, the conversion factor can be solved by the relation

$$\Delta Z^{\mathcal{S}}(\mu) = \left(2\beta_1\frac{g^{\mathcal{S}}(\mu)^2}{16\pi^2}\right)^{-\frac{\gamma_1^{\mathcal{S}}}{2\beta_1}} \exp\left[\int_0^{g^{\mathcal{S}}(\mu)} dg' \left(\frac{\gamma^{\mathcal{S}}(g')}{\beta^{\mathcal{S}}(g')} + \frac{\gamma_0}{\beta_0 g'}\right)\right], \tag{4.21}$$

which, up to three-loop approximation, is

$$\Delta Z^{\mathcal{S}}(\mu) = \left(2\beta_1\frac{g^{\mathcal{S}}(\mu)^2}{16\pi^2}\right)^{-\frac{\gamma_1^{\mathcal{S}}}{2\beta_1}} \left[1 + \frac{g^{\mathcal{S}}(\mu)^2}{16\pi^2}\frac{\beta_1\gamma_0 - \beta_0\gamma_1^{\mathcal{S}}}{2\beta_1^2} + \frac{g^{\mathcal{S}}(\mu)^4}{(16\pi^2)^2}\times \right. \\ \left. \frac{-2\beta_0^3\gamma_2^{\mathcal{S}} + \beta_0^2(\gamma_1^{\mathcal{S}}(2\beta_1+\gamma_1^{\mathcal{S}}) + 2\beta_2\beta_0) - 2\beta_0\beta_1\gamma_0(\beta_1+\gamma_1^{\mathcal{S}}) + \beta_1^2\gamma_0^2}{8\beta_0^4}\right]. \tag{4.22}$$

Again, the $\gamma^{\mathcal{S}}$ function is also defined in Appendix B along with the perturbative expansion of said quantity.

Lastly, we note that each calculation at $p = \mu$ in the RI'-MOM scheme is a momentum dependent result, where-as the renormalisation value we require is at zero momentum. So the process is to use the acceptable momentum range in Eq.(4.14) in the RGI scheme, chirally extrapolate back to zero momentum and then lastly convert to the $\overline{MS}$ scheme at $\mu = 2GeV$.

4.3 Calculation

In this section, we undertake a calculation in the $RI' - MOM$ scheme for the renormalisation constant $Z_{\langle x\rangle}$, as well as demonstrating how we transform this quantity to the $\overline{MS}$ scheme.

4.3.1 Lattice Parameters

These results presented were undertaken on a $32^3 \times 64$ lattice with $\beta = 5.50$ using the SLiNC action. Working with a lattice spacing $a = 0.074$ fm, we set the clover parameter $c_{sw} = 2.65$ and the stout parameter $\omega = 0.1$ [66, 74]. To try to remove quark mass dependence, multiple quark masses were calculated and chirally extrapolated back to the physical quark mass. The κ and corresponding pion masses are displayed in the right of Table 4.1. Here we present the results for the renormalisations undertaken for the five operators, which correspond to five renormalisation constants displayed in the left of Table 4.1.

Operator O	Renormalising Constant
γ_4	Z_V
$\gamma_3\gamma_5$	Z_A
$\gamma_1\gamma_2$	$Z_T^{\overline{MS}}$
I	$Z_S^{\overline{MS}}$
$D_4\gamma_4 - \frac{1}{3}(\sum_{i=1}^{3} D_i\gamma_i)$	$Z_{\langle x\rangle}^{\overline{MS}}$

$\kappa_u = \kappa_d = \kappa_s$	am_π
0.120900	0.1757(10)
0.120920	0.1647(4)
0.120950	0.1508(4)
0.120990	0.1285(7)
0.121021	0.1089(21)

Table 4.1: Two tables showing on the left, the different renormalising constants calculated along with which operators they derive from and on the right, the κ values along with the corresponding pion masses used in the linear extrapolation to the physical pion mass.

The resolution of the momenta allowable in standard lattice QCD can be improved by introducing a twist to the boundary condition [88]. The allowable momenta on a periodic boundary conditional lattice (in lattice units of momentum) is

$$p = \frac{2\pi}{L}(n_x + \theta_x, n_y + \theta_y, n_z + \theta_z, \frac{1}{2}(n_t + \theta_t)), \tag{4.23}$$

for some set of integers n_x, n_y, n_z, n_t and twist angles $\theta_x, \theta_y, \theta_z, \theta_t$. We have made the assumption with the number of lattice points in each dimension to be $L_x = L_y = L_z = \frac{1}{2}L_t = L$. The optimal choice to reduce the number of perturbative corrections needed is to choose momentum diagonally in four-dimensional space [66]. Table 4.2 summarises the momenta used in the calculation.

$\theta = (0,0,0,0)$		$\theta = (\frac{1}{2},\frac{1}{2},\frac{1}{2},0)$		$\theta = (\frac{1}{4},\frac{1}{4},\frac{1}{4},\frac{1}{2})$	
$n_{xyzt} + \theta_{xyzt}$	$(ap)^2$	$n_{xyzt} + \theta_{xyzt}$	$(ap)^2$	$n_{xyzt} + \theta_{xyzt}$	$(ap)^2$
(1, 1, 1, 1)	0.15421	$(0\frac{1}{2}, 0\frac{1}{2}, 0\frac{1}{2}, 0\frac{1}{2})$	0.03855	$(0\frac{1}{4}, 0\frac{1}{4}, 0\frac{1}{4}, 0\frac{1}{4})$	0.00964
(2, 2, 2, 2)	0.61685	$(1\frac{1}{2}, 1\frac{1}{2}, 1\frac{1}{2}, 1\frac{1}{2})$	0.34698	$(1\frac{1}{4}, 1\frac{1}{4}, 1\frac{1}{4}, 1\frac{1}{4})$	0.24096
(3, 3, 3, 3)	1.38791	$(2\frac{1}{2}, 2\frac{1}{2}, 2\frac{1}{2}, 2\frac{1}{2})$	0.96383	$(2\frac{1}{4}, 2\frac{1}{4}, 2\frac{1}{4}, 2\frac{1}{4})$	0.78070
(4, 4, 4, 4)	2.46740	$(3\frac{1}{2}, 3\frac{1}{2}, 3\frac{1}{2}, 3\frac{1}{2})$	1.88910	$(3\frac{1}{4}, 3\frac{1}{4}, 3\frac{1}{4}, 3\frac{1}{4})$	1.62887
(5, 5, 5, 5)	3.85531	$(4\frac{1}{2}, 4\frac{1}{2}, 4\frac{1}{2}, 4\frac{1}{2})$	3.12280	$(4\frac{1}{4}, 4\frac{1}{4}, 4\frac{1}{4}, 4\frac{1}{4})$	2.78546
(6, 6, 6, 6)	5.55165	$(5\frac{1}{2}, 5\frac{1}{2}, 5\frac{1}{2}, 5\frac{1}{2})$	4.66493	$(5\frac{1}{4}, 5\frac{1}{4}, 5\frac{1}{4}, 5\frac{1}{4})$	4.25048
(7, 7, 7, 7)	7.55642	$(6\frac{1}{2}, 6\frac{1}{2}, 6\frac{1}{2}, 6\frac{1}{2})$	6.51548	$(6\frac{1}{4}, 6\frac{1}{4}, 6\frac{1}{4}, 6\frac{1}{4})$	62393
(8, 8, 8, 8)	9.86960	$(7\frac{1}{2}, 7\frac{1}{2}, 7\frac{1}{2}, 7\frac{1}{2})$	8.67446	$(7\frac{1}{4}, 7\frac{1}{4}, 7\frac{1}{4}, 7\frac{1}{4})$	8.10580

Table 4.2: Table showing the different momenta calculated, utilising 3 different twist angles for more resolution. The first column corresponding to $\theta = (0,0,0,0)$ corresponds to the standard, non-twisted boundary condition.

4.3.2 Results

We begin by analysing the renormalisation constants in the $RI' - MOM$ scheme calculated over multiple p^2. The green points plotted in Figures 4.2, 4.3 and 4.1 represent the renormalisation constant $Z^{RI'-MOM}$ for the scalar, tensor and momentum fraction operators respectively. In this scheme, we can see a non-linear dependence on the momentum scale p^2.

Next, by utilising the scheme transformation value $\Delta Z^{RGI}_{RI'-MOM}$ found in Eq.(4.19), we can plot the renormalisation constant in the RGI scheme. The red shaded area in Figures 4.2, 4.3 and 4.1 correspond to an area that encapsulates the errors associated with fitting $p^2 \in [5, 10]$ and $p^2 \in [2, 10]$ (satisfying Eq.(4.14)). This encapsulation is done to take into account any deviations from a linear set of points in the data.

Lastly, we convert to the $\overline{MS}$ scheme at 2 GeV for every scale p^2 as demonstrated by the blue points in Figures 4.2, 4.3 and 4.1. The linear fit is the same undertaken in RGI scheme, only multiplied by $\Delta Z^{\overline{MS}}_{RGI}$ to coincide with the $\overline{MS}$ scheme.

Up to third order, the vector and axial vector renormalisation constants Z_V and Z_A have the same coefficients in the $\overline{MS}$ and $RI' - MOM$ schemes (shown in Appendix B). This means $\Delta Z^{\overline{MS}}_{RI'-MOM} = 1$ in Eq.(4.18) and is why the vector (red) and axial vector (blue) values in Figure 4.4 show the renormalisation values in the $\overline{MS}$ scheme, and equivalently the $RI' - MOM$ scheme.

The final result in the $\overline{MS}$ scheme at $\mu = 2$ GeV for the momentum fraction

renormalisation constant is

$$Z_{\langle x\rangle}^{\overline{MS}} = 1.104(23). \tag{4.24}$$

For error analysis and improved renormalisation values (besides $\langle x\rangle$), see [78].

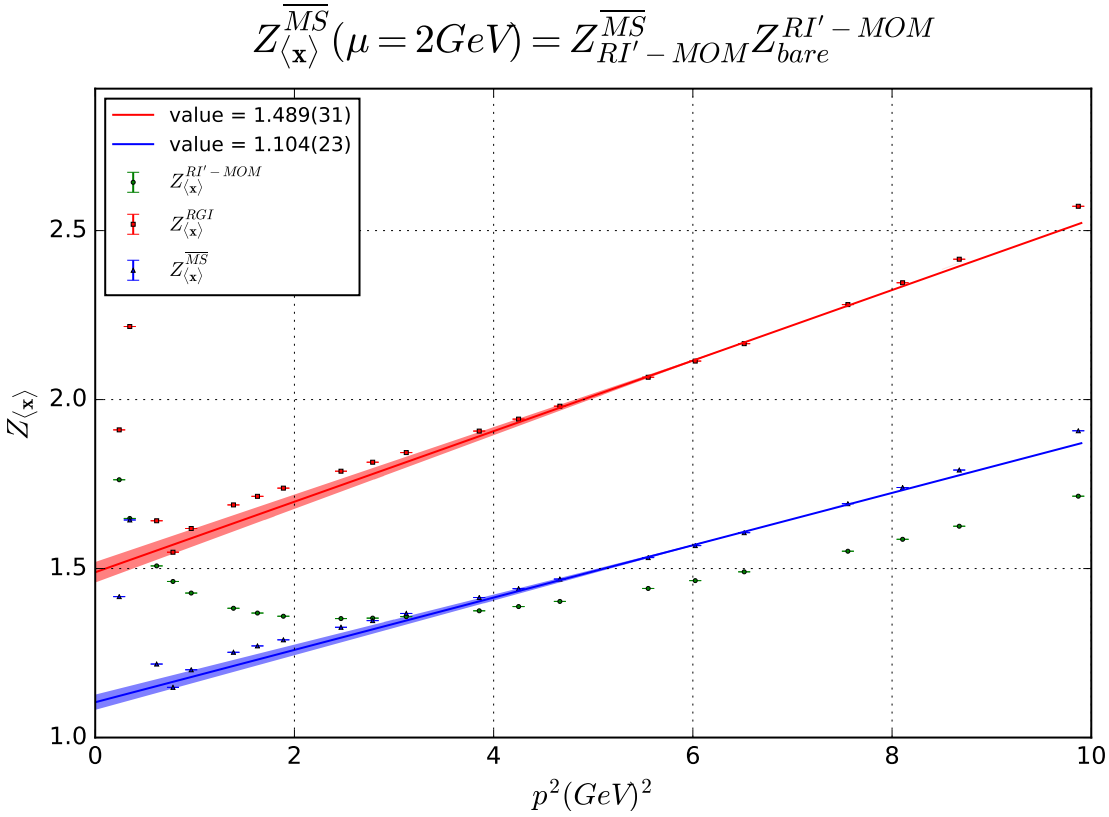

Figure 4.1: Graph showing the momentum fraction renormalisation constant $Z_{\langle x\rangle}^{\mathcal{S}}$ plotted over p^2 in $RI' - MOM$, RGI and $\overline{MS}$ schemes. The lines are linear fit functions fitted to p^2 values that appropriately satisfy Eq.(4.14), which are used to extrapolate to $p^2 = 0$.

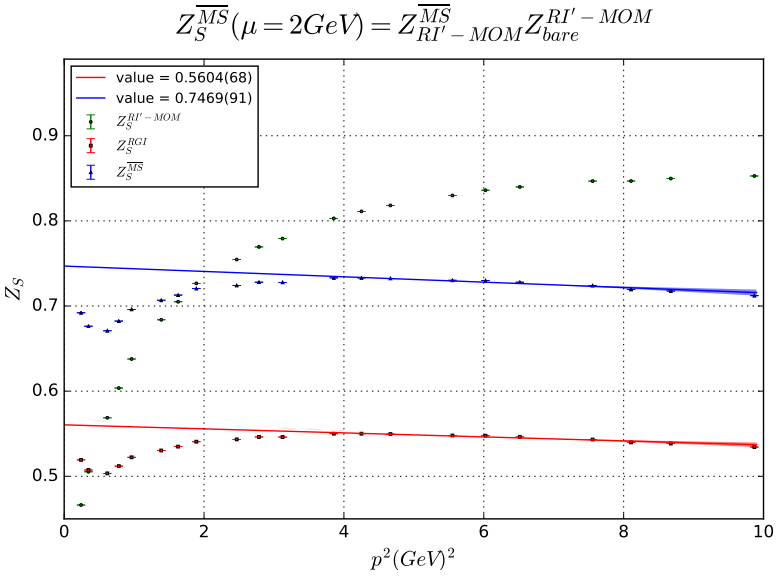

Figure 4.2: Graph showing the scalar renormalisation constant Z_I^S plotted over p^2 in $RI'-MOM$, RGI and $\overline{MS}$ schemes. The lines are linear fit functions fitted to p^2 values that appropriately satisfy Eq.(4.14), which are used to extrapolate to $p^2 = 0$.

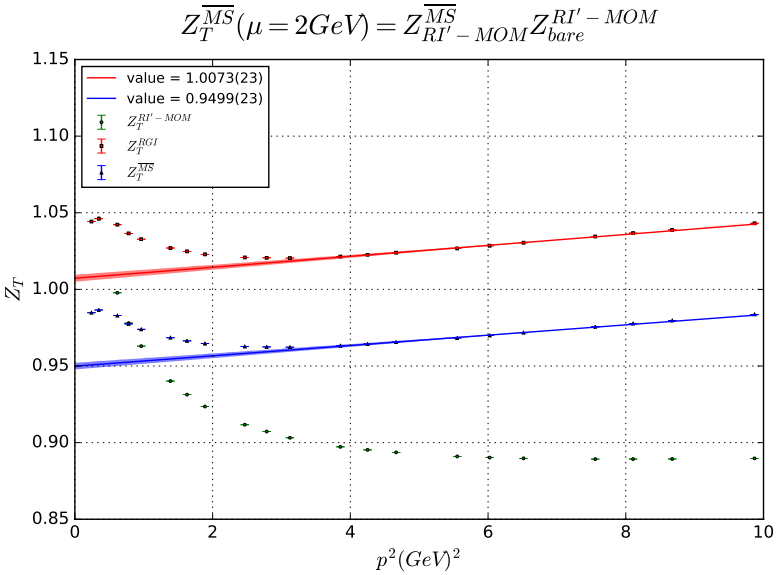

Figure 4.3: Graph showing the tensor renormalisation constant Z_T^S plotted over p^2 in $RI'-MOM$, RGI and $\overline{MS}$ schemes. The lines are linear fit functions fitted to p^2 values that appropriately satisfy Eq.(4.14), which are used to extrapolate to $p^2 = 0$.

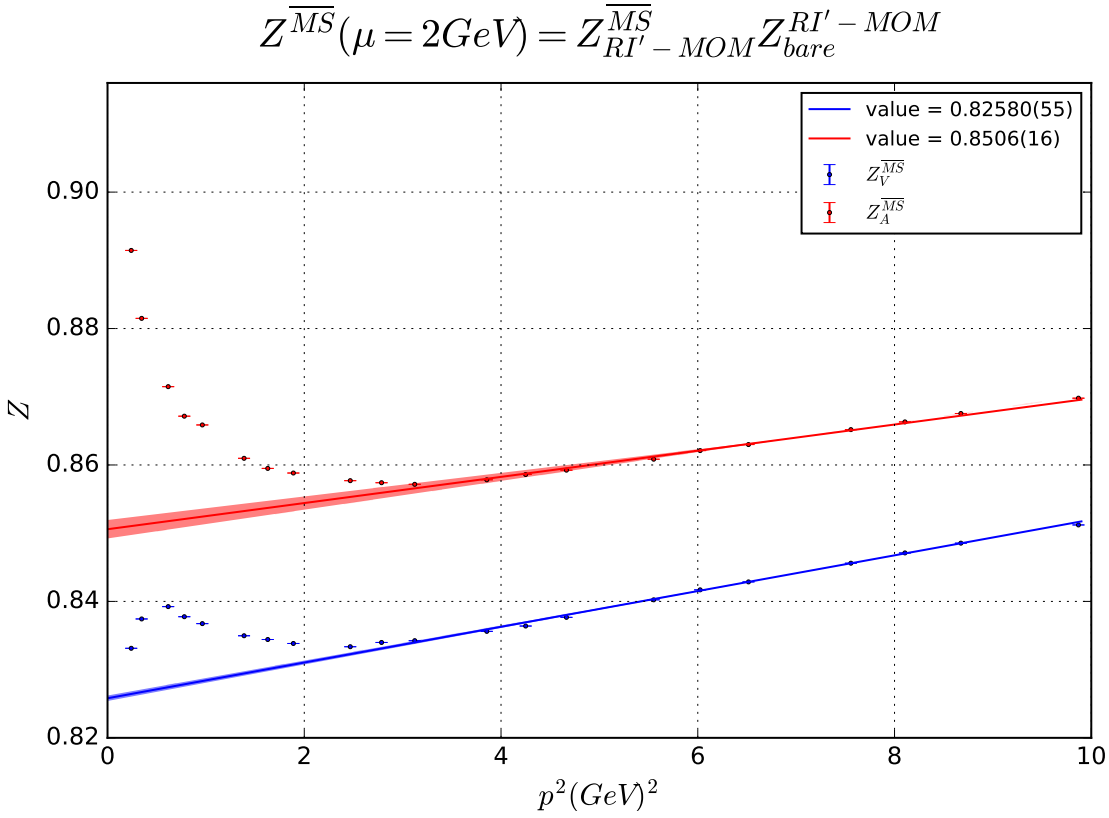

Figure 4.4: Graph showing the vector and axial vector renormalisation constants Z_V and Z_A plotted over p^2. The lines are linear fit functions fitted to p^2 values that appropriately satisfy Eq.(4.14), which are used to extrapolate to $p^2 = 0$.

Chapter 5

Advanced Correlation Functions

5.1 Smearing the Quark Fields

One of the first ideas to improve the overlap of the correlation functions with observable states was to "smear" the quark fields to resemble a quark field that is closest to the state required for the analysis [89]. The general method for achieving this is

$$\begin{aligned} q^a_{(1)\alpha}(x) &= \sum_{\vec{x}'} H^{ab}(\vec{x},\vec{x}')q^b_\alpha(x'), \\ q^a_{(n)\alpha}(x) &= \sum_{\vec{x}'} H^{ab}(\vec{x},\vec{x}')q^b_{(n-1)\alpha}(x'), \end{aligned} \tag{5.1}$$

where $H^{ab}(\vec{x},\vec{x}')$ is a smearing matrix which "smears" out the quark operator around x. Repeated applications of this smearing operator will create different levels of smearing for the quark operator.

Any type of smearing matrix can be used for H, but for this thesis, the Gaussian gauge invariant smearing operator is used [89], which is defined as

$$H\left(\vec{x},\vec{x}'\right) = (1-\alpha)\,\delta_{\vec{x}'\vec{x}} + \frac{\alpha}{6}\sum_{\hat{i}}\left\{\delta_{\vec{x}'\left(\vec{x}-\hat{i}\right)}U_{\hat{i}}\left(\vec{x}'\right) + \delta_{\vec{x}'\left(\vec{x}+\hat{i}\right)}U^\dagger_{\hat{i}}\left(\vec{x}'-\hat{i}\right)\right\}, \tag{5.2}$$

where α is a smearing parameter usually taken to be $\alpha = 0.7$. Generally this operator is repeatedly applied to the quark field on the order of 20-150 times to produce an improved correlator with higher suppression of excited-state contamination.

Pushing this through to propagators, we have the notation

$$S^{(q)aa'}_{(mn)\alpha\alpha'}(x,y) \equiv \overbrace{q^a_{(m)\alpha}(x)\overline{q}}^{}{}^{a'}_{(n)\alpha'}(y), \tag{5.3}$$

using the level of smearing indices (mn) to represent how many applications of the smearing operator H have been applied to the sink and source quark fields respectively.

5.1.1 Fixed Sink Propagator Smearing

When constructing the fixed sink propagator for the fixed sink three-point correlation function, there is no direct access to the sink of the propagator $S^{(q)}(x,y)$ in Eq.(3.84) since we are inverting Eq.(3.88) to construct $\Sigma^{(q)}(\vec{p}',t;y;0;\Gamma)$ directly. To overcome this problem, we look at the smeared version of Eq.(3.85)

$$\Sigma^{(q)}_{(mn)}(\vec{p}',t;y;0;\Gamma) = \sum_{\vec{x}} e^{-i\vec{p}'\cdot\vec{x}} S^{(q)}_{(C)(mn)}(x,0,\Gamma) S^{(q)}_{(m0)}(x,y), \tag{5.4}$$

noting that smearing is not to be done on the source of the quark propagator $S^{(q)}_{(m0)}$ beginning at the current $y=(\vec{y},\tau)$. For simplicity, we start the with $m=1$ case

$$\Sigma^{(q)}_{(1n)}(\vec{p}',t;y;0;\Gamma) = \sum_{\vec{x},\vec{x}'} e^{-i\vec{p}'\cdot\vec{x}} S^{(q)}_{(C)(1n)}(x,0,\Gamma) H(\vec{x},\vec{x}') S^{(q)}(x',y), \tag{5.5}$$

simply by switching the sum variables $\vec{x} \leftrightarrow \vec{x}'$ we have exact same equation with a modified source propagator

$$\begin{aligned} S^{(q)}_{(C_1)(1n)}(x,0,\Gamma) &\equiv \sum_{\vec{x}'} e^{-i\vec{p}'\cdot(\vec{x}'-\vec{x})} S^{(q)}_{(C)(1n)}(x',0,\Gamma) H(\vec{x}',\vec{x}), \\ \Sigma^{(q)}_{(1n)}(\vec{p}',t;y;0;\Gamma) &= \sum_{\vec{x}} e^{-i\vec{p}'\cdot\vec{x}} S^{(q)}_{(C_1)(1n)}(x,0,\Gamma) S^{(q)}(x,y), \end{aligned} \tag{5.6}$$

and then iteratively apply the procedure m times, to show by induction

$$\begin{aligned} S^{(q)}_{(C_m)(mn)}(x,0,\Gamma) &= \sum_{\vec{x}'} e^{-i\vec{p}'\cdot(\vec{x}'-\vec{x})} S^{(q)}_{(C_{m-1})((m-1)n)}(x',0,\Gamma) H(\vec{x}',\vec{x}), \\ \Sigma^{(q)}_{(mn)}(\vec{p}',t;y;0;\Gamma) &= \sum_{\vec{x}} e^{-i\vec{p}'\cdot\vec{x}} S^{(q)}_{(C_m)(mn)}(x,0,\Gamma) S^{(q)}(x,y). \end{aligned} \tag{5.7}$$

The index m on C_m must be the same as the index m for the sink of $S^{(q)}_{(C_m)(mn)}$ or else the sink smearing for the quark with the current insertion will be of different size to the spectator quarks.

5.2 Variational Method for Correlation Functions

The variational method has proven to be a robust and useful tool for studying two-point correlators [90–96]. The conceptual basis for the variational method is to create a correlator that is a combination of multiple source and sink smearing amounts which is optimised to extract the state desired. The process starts by inferring the existence of an optimised operator for the state β, which is then used to construct an optimised two-point correlation function

$$G_2^{\beta}(\vec{p},t;\Gamma) \equiv \sum_{\vec{x}} e^{-i\vec{p}\cdot\vec{x}} \mathrm{Tr}\left\{\Gamma \left\langle \Omega \right| \phi^{\beta}(x) \overline{\phi}^{\beta}(0) \left| \Omega \right\rangle\right\}, \tag{5.8}$$

where we have the overlaps

$$\begin{aligned} \left\langle \Omega \right| \phi^{\beta}(x) \left| E_p^{\alpha}, \vec{p}, s \right\rangle &= \sqrt{E_p^{\beta}} \mathcal{Z}(E_{\vec{p}}^{\beta}, \vec{p}) \delta_{\alpha\beta} u(\vec{p}, s), \\ \left\langle E_p^{\alpha}, \vec{p}, s \right| \overline{\phi}^{\beta}(0) \left| \Omega \right\rangle &= \sqrt{E_p^{\beta}} \overline{\mathcal{Z}}(E_{\vec{p}}^{\beta}, \vec{p}) \delta_{\alpha\beta} \overline{u}(\vec{p}, s). \end{aligned} \tag{5.9}$$

Inserting this into Eq.(3.48)

$$G_2^{\beta}(\vec{p},t;\Gamma) = (\overline{\mathcal{Z}}\mathcal{Z})(E_{\vec{p}}^{\beta}, \vec{p}) e^{-E_{\vec{p}}^{\beta} t} \mathrm{Tr}\left\{\Gamma V(\vec{p})\right\}, \tag{5.10}$$

where we have defined

$$V(\vec{p}) \equiv \begin{cases} \sum_s u(\vec{p},s)\overline{u}(\vec{p},s) & \text{for } \beta = \text{particle state.} \\ \sum_s v(\vec{p},s)\overline{v}(\vec{p},s) & \text{for } \beta = \text{antiparticle state.} \end{cases}, \tag{5.11}$$

where for the above equation, u and v are spinors. We obtain the ground state when $\beta = 0$ and $\Gamma = \Gamma_4$

$$G_2^{\beta=0}(\vec{p},t) = (\overline{\mathcal{Z}}\mathcal{Z})(E_p^{[0]}, \vec{p}) e^{-E_p^{[0]} t}. \tag{5.12}$$

We can approximate the ideal interpolating fields ϕ by creating a linear combination of N interpolating fields denoted with a tilde $\widetilde{\phi}$

$$\begin{aligned} \phi^{\beta}(x) &\approx \widetilde{\phi}^{\beta}(x,\vec{p}) \equiv \sum_{i=1}^{N} v_i^{\beta}(\vec{p}) \chi_i(x), \\ \overline{\phi}^{\beta}(0) &\approx \widetilde{\overline{\phi}}^{\beta}(0,\vec{p}) \equiv \sum_{i=1}^{N} u_i^{\beta}(\vec{p}) \overline{\chi}_i(0). \end{aligned} \tag{5.13}$$

If we express the correlators G_2 created over some basis of source and sink interpolating fields $\chi_i, \overline{\chi}_j$ as a matrix of correlators $(G_2)_{ij}$, we can construct an improved two-point correlation function as

$$\widetilde{G}_2^\beta(\vec{p},t;\Gamma) = v_i^\beta(\vec{p})\,(G_2)_{ij}\,(\Gamma;\vec{p},t)u_j^\beta(\vec{p}), \tag{5.14}$$

which constructs a new two-point correlator that has a stronger coupling to state β. By selecting two sink times $t = t_0$ and $t = t_0 + \Delta_v t$, u and v can be found via the solution to the following eigenvalue equations:

$$v_i^\beta(\vec{p})\left[G_2(\Gamma;\vec{p},t_0+\Delta t)G_2(\Gamma;\vec{p},t_0)^{-1}\right]_{ij} = v_j^\beta(\vec{p})\lambda^\beta, \tag{5.15}$$

$$\left[G_2(\Gamma;\vec{p},t_0)^{-1}G_2(\Gamma;\vec{p},t_0+\Delta t)\right]_{ij}u_j^\beta(\vec{p}) = u_i^\beta(\vec{p})\lambda^\beta. \tag{5.16}$$

Using this construction, it can be shown [96] that in theory the uncertainty should be

$$G_2^\beta(\vec{p},t) = \widetilde{G}_2^\beta(\vec{p},t) + \mathcal{O}(e^{-(E^{N+1}-E^\beta)t_0}), \tag{5.17}$$

i.e. excited states have been numerically removed. Recently, this approach has been extended to three-point correlators, specifically aiming to reduce the effect of excited-state contamination in matrix elements [45, 46, 97–102].

The estimation for the optimised three-point correlation function of state β has the form

$$\begin{aligned}\widetilde{G}_3^\beta(\Gamma;\vec{p}',t;\vec{q},\tau;O^{(q)}) &= \sum_{\vec{x},\vec{y}} e^{-i\vec{p}'\cdot\vec{x}}e^{i\vec{q}\cdot\vec{y}}\mathrm{Tr}\left\{\Gamma\,\langle\Omega|\,\widetilde{\phi}^\beta(x)O^{(q)}(y)\overline{\widetilde{\phi}}^{\,\beta}(0)\,|\Omega\rangle\right\},\\ \approx G_3^\beta(\Gamma;\vec{p}',t;\vec{q},\tau;O^{(q)}) &= \sum_{\vec{x},\vec{y}} e^{-i\vec{p}'\cdot\vec{x}}e^{i\vec{q}\cdot\vec{y}}\mathrm{Tr}\left\{\Gamma\,\langle\Omega|\,\phi^\beta(x,\vec{p}')O^{(q)}(y)\overline{\phi}^{\,\beta}(0,\vec{p})\,|\Omega\rangle\right\}.\end{aligned} \tag{5.18}$$

or rewritten over ij, utilising the same u and v found for the two-point correlators at a particular momentum

$$\widetilde{G}_3^\beta(\Gamma;\vec{p}',t;\vec{q},\tau;O^{(q)}) = v_i^\beta(\vec{p}')\,(G_3)_{ij}\,(\Gamma;\vec{p}',t;\vec{q},\tau;O^{(q)})u_j^\beta(\vec{p}). \tag{5.19}$$

Lastly, we construct the same ratio as previously described in Eq.(3.68):

$$\widetilde{R}^\beta(\Gamma;\vec{p}',t;\vec{q},\tau;O^{(q)}) \equiv \frac{\widetilde{G}_3^\beta(\Gamma;\vec{p}',t;\vec{q},\tau;O^{(q)})}{\widetilde{G}_2^\beta(\vec{p}',t)}\sqrt{\frac{\widetilde{G}_2^\beta(\vec{p}',\tau)\widetilde{G}_2^\beta(\vec{p}',t)\widetilde{G}_2^\beta(\vec{p},t-\tau)}{\widetilde{G}_2^\beta(\vec{p},\tau)\widetilde{G}_2^\beta(\vec{p},t)\widetilde{G}_2^\beta(\vec{p}',t-\tau)}}. \tag{5.20}$$

It is general convention to omit the tilde, and consider G_2^β, G_3^β and R^β as the variational method optimised functions for state β.

5.2.1 Bases for the Variational Analysis

Although the main calculation of this thesis only considers different levels of smearing of the source and sink propagators as the basis of the matrix of correlators, other operators with the same quantum numbers [103] and even shifts in time can be used to construct the basis.

The general matrix of correlation functions has the form

$$(G_2)_{ij}\left(\Gamma;\vec{p},t\right)=\sum_{\vec{x}}e^{-i\vec{p}\cdot\vec{x}}\mathrm{Tr}\left\{\Gamma\left\langle\Omega\right|\chi_i(\vec{x},t)\overline{\chi}_j(\vec{0},0)\left|\Omega\right\rangle\right\}. \tag{5.21}$$

The usual candidates for χ_i for the proton being the two creation interpolating fields

$$\begin{aligned}(\chi_1)_\alpha(x)&=\epsilon^{abc}u^a_\alpha(x)u^b_\beta(x)\widetilde{C}_{\beta\gamma}d^c_\gamma(x),\\(\chi_2)_\alpha(x)&=\epsilon^{abc}(\gamma_5)_{\alpha\delta}u^a_\delta(x)u^b_\beta(x)C_{\beta\gamma}d^c_\gamma(x),\end{aligned} \tag{5.22}$$

and their corresponding annihilation interpolating fields

$$\begin{aligned}(\overline{\chi}_1)_\alpha(x)&=\epsilon^{a'b'c'}\overline{u}^a_\alpha(x)\overline{d}^b_\beta(x)\widetilde{C}_{\beta\gamma}\overline{u}^c_\gamma(x),\\(\overline{\chi}_2)_\alpha(x)&=\epsilon^{a'b'c'}\overline{u}^a_\delta(x)(\gamma_5)_{\alpha\delta}\overline{d}^b_\beta(x)C_{\beta\gamma}\overline{u}^c_\gamma(x).\end{aligned} \tag{5.23}$$

Commonly in ground state analysis, χ_2 is omitted since it is well known to have weak coupling to the ground state [93, 104].

As shown in Section 5.1, we can smear the quark fields to create a smeared interpolating field. Hence we have more candidates for our basis

$$\begin{aligned}(\chi_{m_i})_\alpha(x)&=\epsilon^{abc}u^a_{(m_i)\alpha}(x)u^b_{(m_i)\beta}(x)\widetilde{C}_{\beta\gamma}d^c_{(m_i)\gamma}(x),\\(\overline{\chi}_{m_i})_\alpha(x)&=\epsilon^{a'b'c'}\overline{u}^a_{(m_i)\alpha}(x)\overline{d}^b_{(m_i)\beta}(x)\widetilde{C}_{\beta\gamma}\overline{u}^c_{(m_i)\gamma}(x).\end{aligned} \tag{5.24}$$

We use the convention where the quark fields are smeared m_i times for each of the basis indices i (for example, $m_1 = 32$ times, $m_2 = 64$ times and $m_3 = 128$ times).

It is important to note that the basis of operators can be the outer product of any of the bases described here or in the "Pencil of Function" method described in the next section. In practice, selecting the basis of operators is difficult as with no knowledge of the overlap depenance of the operators, we need to calculate a large number of interpolating fields identify an optimal basis for the variational method.

5.2.2 Pencil of Function Basis

Although there are many other construction methods (e.g. locally split sink interpolating fields [105]), the final one discussed in this thesis is called the "Pencil of Function" method [106–110].

We begin by defining interpolating fields that have been shifted in time by δ,

$$\begin{aligned}\chi^{\delta}(\vec{x},t) &\equiv e^{\hat{H}\delta}\chi(\vec{x},t)\,e^{-\hat{H}\delta} = \chi(\vec{x},t+\delta)\,,\\ \overline{\chi}^{\delta}(\vec{x},t) &\equiv e^{-\hat{H}\delta}\overline{\chi}(\vec{x},t)\,e^{\hat{H}\delta} = \overline{\chi}(\vec{x},t-\delta)\,,\end{aligned} \tag{5.25}$$

where δ is usually chosen to be 1 or 2. The $ij = 2\times 2$ matrix of correlators is now defined as shifts in time on the source and sink interpolating fields by δ

$$\begin{aligned}(G_2)_{ij}(\Gamma;\vec{p},t) \equiv \sum_{\vec{x}} e^{-i\vec{p}\cdot\vec{x}}\times \\ \mathrm{Tr}\left\{\Gamma\begin{bmatrix}\langle\Omega|\,\chi(\vec{x},t)\overline{\chi}(\vec{0},0)\,|\Omega\rangle & \langle\Omega|\,\chi^{\delta}(\vec{x},t)\overline{\chi}(\vec{0},0)\,|\Omega\rangle\\ \langle\Omega|\,\chi(\vec{x},t)\overline{\chi}^{\delta}(\vec{0},0)\,|\Omega\rangle & \langle\Omega|\,\chi^{\delta}(\vec{x},t)\overline{\chi}^{\delta}(\vec{0},0)\,|\Omega\rangle\end{bmatrix}_{ij}\right\}.\end{aligned} \tag{5.26}$$

Due to transnational invariance, we note that

$$\langle\Omega|\,\chi(\vec{x},t)\overline{\chi}^{\delta}(\vec{0},0)\,|\Omega\rangle = \langle\Omega|\,\chi(\vec{x},t)\overline{\chi}(\vec{0},-\delta)\,|\Omega\rangle \to \langle\Omega|\,\chi(\vec{x},t+\delta)\overline{\chi}(\vec{0},0)\,|\Omega\rangle\,, \tag{5.27}$$

and as a result, we can rewrite Eq.(5.26) to

$$\begin{aligned}(G_2)_{ij}(\Gamma;\vec{p},t) \equiv \sum_{\vec{x}} e^{-i\vec{p}\cdot\vec{x}}\times \\ \mathrm{Tr}\left\{\Gamma\begin{bmatrix}\langle\Omega|\,\chi(\vec{x},t)\overline{\chi}(\vec{0},0)\,|\Omega\rangle & \langle\Omega|\,\chi(\vec{x},t+\delta)\overline{\chi}(\vec{0},0)\,|\Omega\rangle\\ \langle\Omega|\,\chi(\vec{x},t+\delta)\overline{\chi}(\vec{0},0)\,|\Omega\rangle & \langle\Omega|\,\chi(\vec{x},t+2\delta)\overline{\chi}(\vec{0},0)\,|\Omega\rangle\end{bmatrix}_{ij}\right\},\end{aligned} \tag{5.28}$$

which with some substitution becomes

$$(G_2)_{ij}(\Gamma;\vec{p},t) = \begin{bmatrix}G_2(\Gamma;\vec{p},t) & G_2(\Gamma;\vec{p},t+\delta)\\ G_2(\Gamma;\vec{p},t+\delta) & G_2(\Gamma;\vec{p},t+2\delta)\end{bmatrix}_{ij}. \tag{5.29}$$

A strong recommendation is that we avoid $\delta = \Delta_v t$ since the solution to the eigenvalue problem in Eq.(5.15) will have a degeneracy.

The corresponding three-point correlation function basis is derived by

$$\begin{aligned}(G_3)_{ij}\left(\Gamma;\vec{p}',t;\vec{q},\tau;O^{(q)}\right) = &\sum_{\vec{x},\vec{y}} e^{-i\vec{p}'\cdot\vec{x}}e^{i\vec{q}\cdot\vec{y}} \\ &\mathrm{Tr}\left\{\Gamma\begin{bmatrix}\langle\Omega|\,\chi(\vec{x},t)O^{(q)}(\vec{y},\tau)\overline{\chi}(\vec{0},0)\,|\Omega\rangle\ldots \\ \langle\Omega|\,\chi(\vec{x},t)O^{(q)}(\vec{y},\tau)\overline{\chi}^{\delta}(\vec{0},0)\,|\Omega\rangle\ldots \\ \langle\Omega|\,\chi^{\delta}(\vec{x},t)O^{(q)}(\vec{y},\tau)\overline{\chi}(\vec{0},0)\,|\Omega\rangle \\ \langle\Omega|\,\chi^{\delta}(\vec{x},t)O^{(q)}(\vec{y},\tau)\overline{\chi}^{\delta}(\vec{0},0)\,|\Omega\rangle\end{bmatrix}_{ij}\right\}.\end{aligned} \tag{5.30}$$

Again, with the same trick from Eq.(5.27), we have

$$\begin{aligned}(G_3)_{ij}\left(\Gamma;\vec{p}',t;\vec{q},\tau;O^{(q)}\right) = &\sum_{\vec{x},\vec{y}} e^{-i\vec{p}'\cdot\vec{x}}e^{i\vec{q}\cdot\vec{y}} \\ &\mathrm{Tr}\left\{\Gamma\begin{bmatrix}\langle\Omega|\,\chi(\vec{x},t)O^{(q)}(\vec{y},\tau)\overline{\chi}(\vec{0},0)\,|\Omega\rangle\ldots \\ \langle\Omega|\,\chi(\vec{x},t+\delta)O^{(q)}(\vec{y},\tau+\delta)\overline{\chi}(\vec{0},0)\,|\Omega\rangle\ldots \\ \langle\Omega|\,\chi(\vec{x},t+\delta)O^{(q)}(\vec{y},\tau)\overline{\chi}(\vec{0},0)\,|\Omega\rangle \\ \langle\Omega|\,\chi(\vec{x},t+2\delta)O^{(q)}(\vec{y},\tau+\delta)\overline{\chi}(\vec{0},0)\,|\Omega\rangle\end{bmatrix}_{ij}\right\},\end{aligned} \tag{5.31}$$

and lastly, substituting in the three-point correlation function, we have (omitting Γ and $O^{(q)}$ for brevity)

$$(G_3)_{ij}\left(\vec{p}',t;\vec{q},\tau\right) = \begin{bmatrix}G_3(\vec{p}',t;\vec{q},\tau) & G_3(\vec{p}',t+\delta;\vec{q},\tau) \\ G_3(\vec{p}',t+\delta;\vec{q},\tau+\delta) & G_3(\vec{p}',t+2\delta;\vec{q},\tau+\delta)\end{bmatrix}_{ij}. \tag{5.32}$$

5.2.3 Variational Method Optimised Fixed Sink Propagator

Since in most cases, a single sink momentum $\vec{p}'$ is chosen (usually $\vec{p}' = \vec{0}$), we can reduce the computation time for the three-point correlator from n^2 to n where n is the basis size in the variational method. This is achieved by constructing a three-point correlator as a combination of sink interpolating fields with weights v created from the variational method on the two-point correlators:

$$(G_3^{\beta})_j(\Gamma;\vec{p}',t;\vec{q},\tau;O^{(q)}) \equiv v_i^{\beta}(\vec{p}')\,(G_3)_{ij}\,(\Gamma;\vec{p}',t;\vec{q},\tau;O^{(q)}). \tag{5.33}$$

Now when we create the fixed sink propagator Σ, we can solve Eq.(3.88) with a substitution of:

$$e^{-i\vec{p}'\cdot\vec{x}'}\,S^{(q)}_{(C_m)mn}\left(\vec{p}';x';0,\Gamma\right) \Rightarrow \sum_i e^{-i\vec{p}'\cdot\vec{x}'}\,S^{(q)}_{(C_i)m_in_j}\left(x';0,\Gamma\right)v_i^{\beta}(\vec{p}'), \tag{5.34}$$

where $v_i^{\beta}(\vec{p}')$ are the weightings obtained from the variational method applied to the two-point correlators, and $S^{(q)}_{(C_i)m_in_j}$ are the i,j'th source propagator for the fixed sink inversion. That is, if $S^{(q)}_{(C_i)m_in_j}$ was to be used as the source propagator in the fixed sink inversion, it could eventually be used to create $(G_3)_{ij}$

An important point to note here is that a single combination of t_0 and $\Delta_v t$ must be chosen from the two-point correlator as $v_i^{\beta}(\vec{p}')$ is now used in the matrix inversion calculation to create the fixed sink propagator/correlator and is dependent on these parameters.

One additional advantage of this source propagator combination, is for the pencil of function method. If we decide to run the analysis over two such sink times t_1 and $t_2 = t_1 + \delta$, we have

$$\begin{bmatrix} G_3^{\beta}(\vec{p}',t_1;\vec{q},\tau) \\ G_3^{\beta}(\vec{p}',t_1+\delta;\vec{q},\tau) \end{bmatrix} = \begin{bmatrix} v_1^{\beta}(\vec{p}') & v_2^{\beta}(\vec{p}') \end{bmatrix} \begin{bmatrix} G_3(\vec{p}',t_1;\vec{q},\tau) & G_3(\vec{p}',t_1+\delta;\vec{q},\tau) \\ G_3(\vec{p}',t_1+\delta;\vec{q},\tau+\delta) & G_3(\vec{p}',t_1+2\delta;\vec{q},\tau+\delta) \end{bmatrix}, \tag{5.35}$$

$$\begin{bmatrix} G_3^{\beta}(\vec{p}',t_2;\vec{q},\tau) \\ G_3^{\beta}(\vec{p}',t_2+\delta;\vec{q},\tau) \end{bmatrix} = \begin{bmatrix} v_1^{\beta}(\vec{p}') & v_2^{\beta}(\vec{p}') \end{bmatrix} \begin{bmatrix} G_3(\vec{p}',t_2;\vec{q},\tau) & G_3(\vec{p}',t_2+\delta;\vec{q},\tau) \\ G_3(\vec{p}',t_2+\delta;\vec{q},\tau+\delta) & G_3(\vec{p}',t_2+2\delta;\vec{q},\tau+\delta) \end{bmatrix}, \tag{5.36}$$

we notice that

$$G_3^{\beta}(\vec{p}',t_2;\vec{q},\tau+\delta) = G_3^{\beta}(\vec{p}',t_1+\delta;\vec{q},\tau). \tag{5.37}$$

Hence we get a "*three sink times for the price of two*" effect in terms of computation time for creating the fixed sink propagator. Repetitions of this can create 5 sink times with 3 inversions, 7 for 5 etc..

Chapter 6

Analysis of Correlation Functions

Analysing two- and three-point correlation functions has proven to be a difficult task due to limitations arising from limited computational resources. The effects include finite lattice spacing effects, effects from determining the renormalisation constants, continuum extrapolation complications and effects due to contamination from excited-states.

Since we have a lattice spacing a when we calculate quantities on the lattice, this induces errors in our calculations (for example, $\mathcal{O}(a^n)$ errors in any fermion and gauge actions we choose). Although you could quantify these errors and any other discretisation effects, a common technique is to calculate the same quantity over multiple lattice spacings a and fit to extrapolate to the continuum ($a \to 0$) limit. The results in this thesis does not analyse this effect.

The process of calculating the renormalisation factors is described in Chapter 4.

Generally, calculations involving correlation functions are greatly more cost effective to perform at heavier pion (quark) masses. But this incurs an error when we decide to chirally extrapolate to the physical pion (quark) mass. Recently with the recent increase in computational power, there have been calculations at the physical pion (quark) mass [111]. In this thesis we have selected the pion mass to be $m_\pi = 470$ MeV.

The term *excited-state contamination* is used to describe when a correlator has not satisfied a large enough time to suppress terms that have different contributions from states of higher energies (excited-states). The classic example is in the two-point correlation function starting from Eq.(3.52), with out implying the approximation $t \gg 1$

$$G_2(\vec{p}, t) = (\overline{\mathcal{Z}}\mathcal{Z})(E_p^{[0]}, \vec{p})e^{-E_p^{[0]}t} + (\overline{\mathcal{Z}}\mathcal{Z})(E_p^{[1]}, \vec{p})e^{-E_p^{[1]}t} + ..., \tag{6.1}$$

where generally we only want a single term out of all the terms being summed, for example $\left((\overline{\mathcal{Z}}\mathcal{Z})(E_p^{[0]}, \vec{p})e^{-E_p^{[0]}t}\right)$ for ground state analysis. The reason why the

large time approximation is difficult to satisfy is because the signal to noise ratio of the correlation function is dependent on the source-sink separation. Too small a t and the excited-states start to contaminate the signal, yet too large a t turns the correlation function into noise.

The contamination from excited-states is starting to emerge as the largest and most difficult effect to analyse and control for baryons. The work in this thesis is a systematic analysis of many efforts to analyse and reduce this effect.

6.1 Two-Point Function Analysis

Although extraction of energy states of hadrons is a large and very important field in lattice QCD, it is not what this thesis is focused on. Nevertheless the two-point correlation functions are being created in the process for hadron matrix elements, we can conceptually understand the excited-state contamination through the extraction of the energies. The process is outlined in this section.

Using a two-point correlation function, the most common method to identify the ground-state dominance is via the *effective mass* which is defined by combination

$$\log\left(\frac{G_2(\Gamma_4;\vec{p},t)}{G_2(\Gamma_4;\vec{p},t+\Delta t)}\right) \xrightarrow{t\gg 0} E_p^{[0]}\Delta t, \tag{6.2}$$

which when plotted will "plateau" to a constant value for some large enough value of t which is then considered the region in which $t \gg 0$.

An example of the effective mass defined in Eq.(6.2) can be found in Figure 6.1, where we see at smaller source-sink separations t, the effective mass has not achieved ground-state saturation.

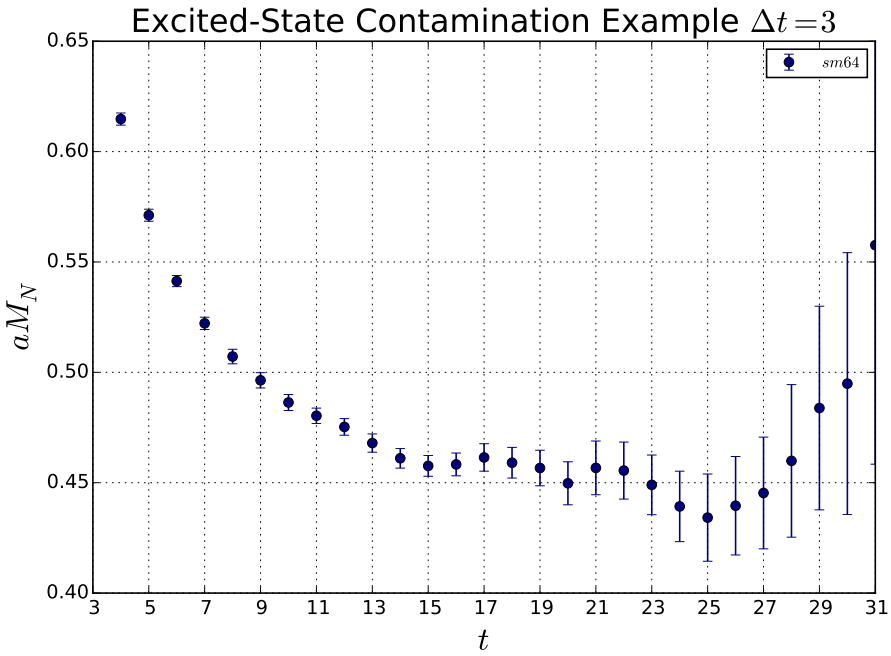

Figure 6.1: Effective mass plot defined in Eq.(6.2) demonstrating the effect of excited-state contamination at smaller source-sink separations t. We chose the time shift parameter $\Delta t = 3$ defined in Eq.(6.2), and 64 sweeps of smearing applied to the quark fields as described in Section 5.1.

This effective mass construction is only used as a guide to help constrain the fit range and instead, the following fit parametrisation should be utilised.

Since we know the functional form of the two-point correlator in the region $t \gg 0$, we can fit a function directly to these points. The fit function for the *one-exponential fit* is parameterised by the following

$$G_2(\Gamma_4; \vec{p}, t) = A_{E_p^{[0]}} e^{-E_p^{[0]} t}, \tag{6.3}$$

where we have the two fit parameters $A_{E_p^{[0]}}$ and $E_p^{[0]}$. To employ this fit, we find a region where $t \gg 0$ to fit to, then extract the $E_p^{[0]}$ as a fit parameter. Although in principal we can select two sink times t to extract a fit parameter, it is common practice to use as many sink times that are still considered statistically significant to help remove gauge field fluctuations.

This fitting procedure can be taken one step further, considering the next predominant state $E_p^{[1]}$ in a region where we are dominated by the first two-states. The fit function for the *two-exponential fit* can have one of the two forms (depending on preference)

$$
\begin{aligned}
G_2(\Gamma_4;\vec{p},t) =& A_{E_p^{[0]}} e^{-E_p^{[0]}t} + A_{E_p^{[1]}} e^{-(E_p^{[0]}+\Delta E_p^{[0,1]})t}, \\
G_2(\Gamma_4;\vec{p},t) =& A_{E_p^{[0]}} e^{-E_p^{[0]}t}(1 + A'_{E_p^{[1]}} e^{-\Delta E_p^{[0,1]}t}), \qquad A'_{E_p^{[1]}} \equiv \frac{A_{E_p^{[1]}}}{A_{E_p^{[0]}}},
\end{aligned}
\tag{6.4}
$$

where we have defined the energy difference $\Delta E_p^{[0,1]} \equiv E_p^{[1]} - E_p^{[0]}$. Now we have four fit parameters $A_{E_p^{[0]}}, A_{E_p^{[1]}}, E_p^{[0]}, \Delta E_p^{[0,1]}$. The benefit of fitting the first excited-state and the ground-state together is the fitting window can be relaxed to earlier sink times. Another reason for fitting both states is that they can be determined from the two-point correlation function before fitting to the three point correlation function since the same parameters appear in both the two- and three-point correlators.

Although theoretically more states can be fitted to the correlation function, it is usually unfeasible due to the statistical precision of the correlation functions and the number of fit parameters that are needing to be constrained.

One interesting extension to fitting the states of the two-point correlator is to consider a class of differently smeared correlation functions, and fit one- or two-states to the correlation functions. The one-exponential fit has the form

$$
(G_2)_{ij}(\Gamma_4;\vec{p},t) = A^{ij}_{E_p^{[0]}} e^{-E_p^{[0]}t}, \quad i,j = 1,...,n \tag{6.5}
$$

where we have individual fit parameters $A^{ij}_{E_p^{[0]}}$ for each correlation function, but a single parameter $E_p^{[0]}$. Not much extra will be gained from a single exponential fit, as each correlation function must satisfy the large sink time approximation $t \gg 0$ which will depend on the smearing.

The two-exponential fit has the form

$$
(G_2)_{ij}(\Gamma_4;\vec{p},t) = A^{ij}_{E_p^{[0]}} e^{-E_p^{[0]}t}(1 + A'^{ij}_{E_p^{[1]}} e^{-\Delta E_p^{[0,1]}t}), \tag{6.6}
$$

where again, we have individual fit parameters $A^{ij}_{E_p^{[0]}}$ and $A^{ij}_{E_p^{[1]}}$ for each correlation function, but two shared parameters $E_p^{[0]}$ and $\Delta E_p^{[0,1]}$. The two-exponential fit may provide an improvement, but again multiple fit ranges will be needed to find regions in which two-states are dominant for each individually smeared correlator $(G_2)_{ij}(\Gamma_4;\vec{p},t)$.

6.2 Three-Point and Ratio Function Analysis

Utilising the two- and three-point correlation functions to construct the ratio function in Eq.(3.68) (or Eq.(3.69)), we can extract the desired FF function for the ground-state defined in Eq.(3.67) by rearranging Eq.(3.75)

$$FF(E_p^{[0]} \to E_{p'}^{[0]}, \Gamma, O^{(q)}) = R(\Gamma; \vec{p}', t; \vec{q}, \tau; O^{(q)}) \left(A(\Gamma_4, \vec{p}, m^{[0]}) A(\Gamma_4, \vec{p}', m^{[0]}) \right)^{-\frac{1}{2}}, \tag{6.7}$$

as long as we satisfy $t \gg \tau \gg 0$.

The satisfaction of the large time approximation is more difficult to identify than the two-point correlator case (in Section 6.1), since either τ is fixed when using the "through the operator" method or t is fixed when using the "fixed sink propagator" method for creating the three-point correlation function (described in Section 3.4.2). Fixing τ requires you to have knowledge that the condition $\tau \gg 0$ is satisfied for the particular operator being studied, whereas fixing t requires you have the knowledge that $t \gg \tau$ when $\tau \gg 0$, otherwise some sort of excited-state contamination will be in effect.

For the "fixed sink propagator" method, we look at variations of the ratio function with respect to τ. Although picking $\tau = t/2$ would be the "optimal" choice for the extraction of FF, we can re-assure ourselves that there is no excited-state contamination from transition matrix elements by fitting over a plateaued region where $t \gg \tau$ and $\tau \gg 0$. For the example for g_A in Figure 6.2, we see no clear plateau over the centre region for τ, which means we cannot draw any conclusions for the value of g_A from this calculation.

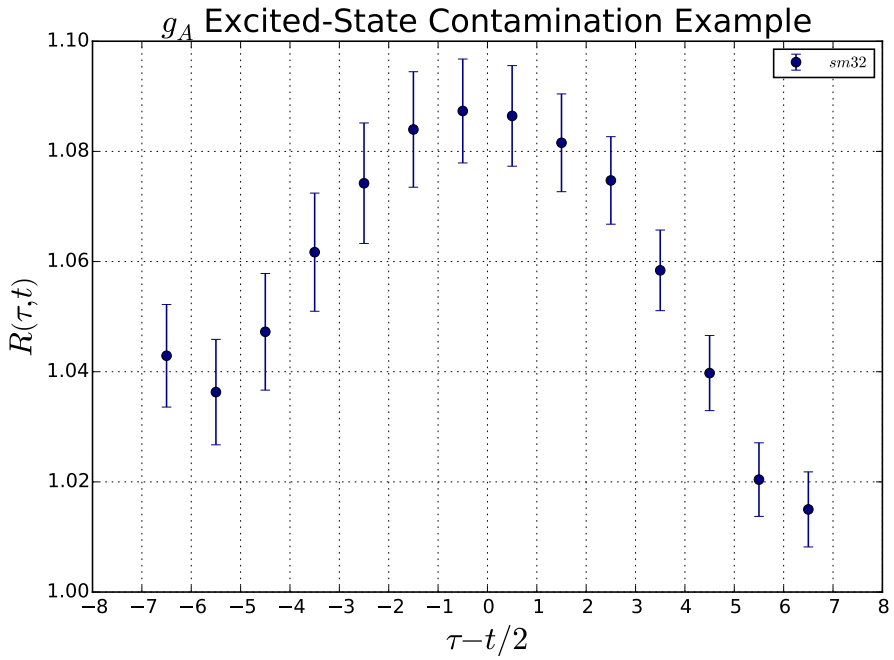

Figure 6.2: Graph for g_A extracted from the R function defined in Eq.(3.68) plotted over the current insertion time τ which has been centred about zero via the construction $\tau - t/2$. We have selected the 32 sweeps of smearing for the quark fields described in Section 5.1 and the fixed sink calculation was undertaken at a source-sink separation of $t = 13$.

Knowing the functional form of the three-point correlation function, as well as noting some of the parameters are shared with the two-point correlation function, we can fit directly to the three-point correlator. The parametrisation of the first state of the three-point correlation function is

$$G_3(\Gamma;\vec{p}',t;\vec{q},\tau;O^{(q)}) = B_{00}\sqrt{A_{E_p^{[0]}}A_{E_{p'}^{[0]}}}e^{-E_{p'}^{[0]}t}e^{-\left(E_p^{[0]}-E_{p'}^{[0]}\right)\tau}, \tag{6.8}$$

where $A_{E_p^{[0]}}$, $A_{E_{p'}^{[0]}}$, $E_p^{[0]}$ and $E_{p'}^{[0]}$ are all fit parameters extracted from a single state fit to the two-point correlators with momentum p and p'. The resulting parameter out of the fit is

$$B_{00} = FF\left(E_p^{[0]} \to E_{p'}^{[0]},\Gamma,O^{(q)}\right)\left(A(\Gamma_4,\vec{p},m^{[0]})A(\Gamma_4,\vec{p}',m^{[0]})\right)^{-\frac{1}{2}}. \tag{6.9}$$

It is worth noting, that this method is very similar to the construction of the ratio function Eq.(3.68), but instead of utilising the two-point correlation functions

at τ and t, we use fitted versions of the two-point correlation function at τ and t. It is possible that using the fitted values might help remove statistical fluctuations, especially at larger sink times, t.

To extend this fitting method to two-states, we arrive at the commonly named *two-state fit* method [77, 111–114] which has the functional form

$$\begin{aligned} G_3(\Gamma;\vec{0},t;\vec{q},\tau;O^{(q)}) = &\sqrt{A_{E_p^{[0]}}A_{E_{p'}^{[0]}}}e^{-E_{p'}^{[0]}t}e^{-\left(E_p^{[0]}-E_{p'}^{[0]}\right)\tau}\times \\ &\Big\{B_{00}+B_{10}e^{-\Delta E_p^{[0,1]}\tau}+B_{01}e^{-\Delta E_{p'}^{[0,1]}(t-\tau)}+ \\ &\quad B_{11}e^{-\Delta E_{p'}^{[0,1]}t}e^{-\left(\Delta E_p^{[0,1]}-\Delta E_{p'}^{[0,1]}\right)\tau}\Big\}, \end{aligned} \tag{6.10}$$

in which $A_{E_p^{[0]}}$, $A_{E_{p'}^{[0]}}$, $E_p^{[0]}$, $E_{p'}^{[0]}$, $\Delta E_p^{[0,1]}$ and $\Delta E_{p'}^{[0,1]}$ are all calculated from the two-exponential fit to the two-point correlator. The four remaining fit parameters are B_{00}, B_{10}, B_{01} and B_{11} which correspond to

$$\begin{aligned} B_{00} &= FF\left(E_p^{[0]}\to E_{p'}^{[0]},\Gamma,O^{(q)}\right)\left(A(\Gamma_4,\vec{p},m^{[0]})A(\Gamma_4,\vec{p}',m^{[0]})\right)^{-\frac{1}{2}}, \\ B_{10} &= \sqrt{\frac{A_{E_p^{[1]}}}{A_{E_p^{[0]}}}}FF\left(E_p^{[1]}\to E_{p'}^{[0]},\Gamma,O^{(q)}\right)\left(A(\Gamma_4,\vec{p},m^{[1]})A(\Gamma_4,\vec{p}',m^{[0]})\right)^{-\frac{1}{2}}, \\ B_{01} &= \sqrt{\frac{A_{E_{p'}^{[1]}}}{A_{E_{p'}^{[0]}}}}FF\left(E_p^{[0]}\to E_{p'}^{[1]},\Gamma,O^{(q)}\right)\left(A(\Gamma_4,\vec{p},m^{[0]})A(\Gamma_4,\vec{p}',m^{[1]})\right)^{-\frac{1}{2}}, \\ B_{11} &= \sqrt{\frac{A_{E_p^{[1]}}A_{E_{p'}^{[1]}}}{A_{E_p^{[0]}}A_{E_{p'}^{[0]}}}}FF\left(E_p^{[1]}\to E_{p'}^{[1]},\Gamma,O^{(q)}\right)\left(A(\Gamma_4,\vec{p},m^{[1]})A(\Gamma_4,\vec{p}',m^{[1]})\right)^{-\frac{1}{2}}. \end{aligned} \tag{6.11}$$

Since when using the *fixed sink* method, the sink momentum is often fixed to $\vec{p}'=\vec{0}$, we can use the replacement $E_{p'}\to m$ in Eq.(6.8) and Eq.(6.10). When analysing zero momentum transfer matrix elements, we also set $\vec{p}=\vec{0}$, which reduces Eq.(6.8) and Eq.(6.10) to

$$G_3(\Gamma;\vec{p}',t;\vec{q},\tau;O^{(q)}) = B_{00}A_{m^{[0]}}e^{-m^{[0]}t}, \tag{6.12}$$

and

$$G_3(\Gamma;\vec{0},t;\vec{0},\tau;O^{(q)}) = A_{m^{[0]}}e^{-m^{[0]}t}\times \left\{B_{00} + B_{10}\left(e^{-\Delta m^{[0,1]}\tau} + e^{-\Delta m^{[0,1]}(t-\tau)}\right) + B_{11}e^{-\Delta m^{[0,1]}t}\right\}. \tag{6.13}$$

Once again, the parameters B_{00}, B_{10}, B_{01} and B_{11} correspond to

$$\begin{aligned} B_{00} &= FF\left(m^{[0]} \to m^{[0]},\Gamma,O^{(q)}\right)\left(A(\Gamma_4,\vec{p},m^{[0]})A(\Gamma_4,\vec{0},m^{[0]})\right)^{-\frac{1}{2}}, \\ B_{10} = B_{01} &= \sqrt{\frac{A_{m^{[1]}}}{A_{m^{[0]}}}}FF\left(m^{[1]} \to m^{[0]},\Gamma,O^{(q)}\right)\left(A(\Gamma_4,\vec{p},m^{[1]})A(\Gamma_4,\vec{0},m^{[0]})\right)^{-\frac{1}{2}}, \\ B_{11} &= \frac{A_{m^{[1]}}}{A_{m^{[0]}}}FF\left(m^{[1]} \to m^{[1]},\Gamma,O^{(q)}\right)\left(A(\Gamma_4,\vec{p},m^{[1]})A(\Gamma_4,\vec{0},m^{[1]})\right)^{-\frac{1}{2}}. \end{aligned} \tag{6.14}$$

We have the relation $B_{10} = B_{01}$ as a result of the transition FF function being time-reversal invariant

$$FF\left(m^{[1]} \to m^{[0]},\Gamma,O^{(q)}\right) = FF\left(m^{[0]} \to m^{[1]},\Gamma,O^{(q)}\right). \tag{6.15}$$

One important fact to keep in consideration is that the specific function used to fit the correlator must be dominated by the one- or two-states. This gives the fitting a great deal of sensitivity to the fit ranges over sink and current times, which can result in skewed results.

Given the experience in spectroscopy studies, we emphasise that the fit parameter $\Delta E_p^{[0,1]}$ should not be taken too literally in terms of the energy gap to the first excited-state as the exponential behaviour is merely acting to mock up the sum of all excited-states over the range of fit considered. It is for this reason we prefer the nomenclature *two-exponential fit* instead of *two-state fit*.

Analogous to the ratio function described in Section 3.4.2, we can construct a one- or two-exponential fitted ratio function by utilising the one- or two-exponential fitted function instead of the actual two-point correlation function. These ratio functions play no part in the extraction of the matrix elements and are merely for illustrative purposes only. For the one-exponential fit, it is defined as

$$R_{OSF}(\Gamma;\vec{p}',t;\vec{q},\tau;O^{(q)}) \equiv \frac{G_3(\Gamma;\vec{p}',t;\vec{q},\tau;O^{(q)})}{\sqrt{A_{E_p^{[0]}}A_{E_{p'}^{[0]}}}e^{-E_{p'}^{[0]}t}e^{-\left(E_p^{[0]}-E_{p'}^{[0]}\right)\tau}}, \tag{6.16}$$

and for the two-exponential fit function it is defined at $\vec{p}=0$ as

$$R_{TSF}(\Gamma;\vec{0},t;\vec{0},\tau;O^{(q)}) \equiv \frac{G_3(\Gamma;\vec{0},t;\vec{0},\tau;O^{(q)})}{A_{m^{[0]}}e^{-m^{[0]}t} + A_{m^{[1]}}e^{-(m^{[0]}+\Delta m^{[0,1]})t}}, \tag{6.17}$$

where the parameters in the numerators have been predetermined by fits to the two-point correlation functions.

6.3 Summing the Ratio Function

As has been used many times in the past and in recent works [109, 112, 113, 115], a summation method can be employed in this calculation to reduce the excited-state contamination. The process proceeds by summing the ratio $R(\Gamma;\vec{p}',t;\vec{q},\tau;O^{(q)})$ over operator insertion times, τ:

$$\begin{aligned} S\left(\Gamma;\vec{p}',t;\vec{q};\mathcal{O}\right) = &\sum_{\tau=\delta t}^{t-\delta t} R(\Gamma;\vec{p}',t;\vec{q},\tau;O^{(q)}) \rightarrow \\ &c + t\left\{FF(E_p^{[0]} \rightarrow E_{p'}^{[0]},\Gamma,O^{(q)}) + \mathcal{O}\left(e^{-min\left(\Delta E_p^{[0,1]},\Delta E_{p'}^{[0,1]}\right)t}\right)\right\}, \end{aligned} \tag{6.18}$$

where $\Delta E_p^{[0,1]}$ is the energy difference between the ground and first excited-state energies with momentum $\vec{p}$. The (apparent) advantage of this technique is that the correction to the matrix element is suppressed by an exponential in t, the full source–sink separation time. This is in contrast to the conventional method where the parametric suppression of excited-states in given by a similar exponential of time $t-\tau$ (or τ), which is $\sim t/2$ in the plateau region. We allow for the slight generalisation of Eq.(6.18) including a δt parameter, also considered in [113] which describes the number of current insertion results of the summation of R which have been removed closest to both the source and sink. This region has the strongest statistical signal, yet provides minimal information on the ground-state matrix element. In most instances, we find the results to be largely insensitive to δt, as one might expect. But the summation method results shown later for $\langle x \rangle$ in Figure 7.44 is an example where we see a statistically significant change when we vary the δt parameter.

After performing simulations at multiple source-sink separation times, t, one performs a linear fit to determine $FF(E_p^{[0]} \rightarrow E_{p'}^{[0]},\Gamma,O^{(q)})$.

6.4 Form Factor Extractions

Once the "FF" function is extracted from the two- and three-point correlation functions, we can proceed to extracting charges and form factors. As a reminder, the "FF" function is defined in Eq.(3.67) as

$$FF(E_p \to E_{p'}, \Gamma, O^{(q)}) \equiv \mathrm{Tr}\left\{\Gamma(-i\not{p}' + m)\mathcal{J}_{O^{(q)}}(q^2)(-i\not{p} + m)\right\}, \tag{3.67}$$

or alternatively, we can express the above as

$$FF(E_p \to E_{p'}, \Gamma, O^{(q)}) \equiv \mathrm{Tr}\left\{\Gamma(E_{p'}\gamma_4 - i\vec{p}' \cdot \vec{\gamma} + m)\mathcal{J}_{O^{(q)}}(q^2)(E_p\gamma_4 - i\vec{p} \cdot \vec{\gamma} + m)\right\}. \tag{6.19}$$

The quantity $\mathcal{J}_{O^{(q)}}(q^2)$ is defined and explained in Sections 2.4 and 2.5 with the label (q) referring to the selection of either the doubly or singly represented quark contribution(i.e. up or down quark in the proton, respectively).

Generally, we utilise different combinations of these quark contributions depending on the situation. The most common example is the iso-vector combination for the proton in which the difference between the up and down quarks ($(q) = doub - sing = up - down$) is taken. The benefit of the iso-vector combination is the disconnected quark loop contributions in Eq.(3.77) cancel out in the isospin limit and hence, are not needed in the calculation. Most commonly for the vector form factors, as demonstrated for the vector current in Eq.(2.15), the sum of the quark charges multiplied by the contribution from that quark is taken.

For a lattice calculation using operator $O^{(q)}$, the result is proportional to $\mathcal{J}_{O^{(q)}}(q^2)$ which, depending on what $O^{(q)}$ is used, is defined in Sections 2.4 and 2.5.

For example, if dealing with the vector current using $O^{(q)} = \overline{q}\gamma_4 q$, the unpolarised projector $\Gamma = \Gamma_4$ and fixing the sink momentum $\vec{p}' = \vec{0}$, we have

$$FF(E_p^{[0]} \to m, \Gamma_4, \overline{q}\gamma_4 q) = (E_p^{[0]} + m)mF_1^{(q)}(q^2). \tag{6.20}$$

For this case, we can extract the form factor $F_1^{(q)}(q^2)$ for the quark contribution (q) by a simple rearrangement and substitution of Eq.(6.7) to give

$$F_1^{(q)}(q^2) = R(\Gamma; \vec{p}', t; \vec{q}, \tau; O^{(q)})\frac{1}{m}\sqrt{\frac{2}{(E_p^{[0]} + m)E_p^{[0]}}}. \tag{6.21}$$

This is one of the most simplest extractions for a form factor. In general, assuming the general fixed sink condition of $\vec{p}' = \vec{0}$, we will have an equation of the form

$$\sum_{i=1}^{N_{FF}} a_i F_i^{(q)}(q^2) = R(\Gamma; \vec{p}', t; \vec{q}, \tau; O^{(q)})\left(A(\Gamma_4, \vec{p}, m^{[0]})A(\Gamma_4, \vec{0}, m^{[0]})\right)^{-\frac{1}{2}}, \tag{6.22}$$

remembering to take into consideration excited-state contamination effects in the ratio function R. The sum variable i is summed over the number of form factors for the particular type of from factor

$$\begin{aligned} \text{Scalar and Pseudo Scalar } N_{FF} &= 1, \\ \text{Vector and Pseudo Vector } N_{FF} &= 2, \\ \text{Tensor } N_{FF} &= 3. \end{aligned} \tag{6.23}$$

The parameter a_i will depend on the specific matrix selected for $O^{(q)}$ and Γ and typically is calculated numerically in real time.

When utilising the fixed sink method for creating three-point correlation functions, the free variables in Table 3.1 are generally calculated over as many different values as possible as they are free to calculate (compared to the inversion times). For this thesis, the operator basis calculated was

$$O^{(q)} = \overline{q}\left(I, \gamma_\mu, \gamma_5, \gamma_5\gamma_\mu, \sigma_{\mu\nu}, \overleftrightarrow{D}^\mu, \gamma_\mu\overleftrightarrow{D}^\nu, \gamma_5\overleftrightarrow{D}^\mu, \gamma_5\gamma_\mu\overleftrightarrow{D}^\nu, \sigma_{\mu\nu}\overleftrightarrow{D}^\delta\right) q. \tag{6.24}$$

All current insertion times from $\tau = 0$ to $\tau = t$ along with all current insertion momenta in the range of $0 \leq \vec{q}^{\,2} < 9\left(\frac{2\pi}{a}\right)^2$ in lattice units (assuming isotropic spatial lattice dimensions $L = L_x = L_y = L_z$).

Utilising all the data, we can construct an over-determined set of linear equations to be solved. For a set of solutions $j = (O_j^{(q)}, \vec{q}_j)$ which iterate over every combination of $O^{(q)}$ and $\vec{q} \in \vec{q}^{\,2}$ calculated, we have the set of equations

$$a_{ji}F_i^{(q)}(q_j^2) = R(\Gamma; 0, t; \vec{q}_j, \tau; O_j^{(q)})\left(A(\Gamma_4, \vec{p}_j, m^{[0]})A(\Gamma_4, \vec{0}, m^{[0]})\right)^{-\frac{1}{2}}, \tag{6.25}$$

or with a rearrangement

$$\mathcal{A}_{ji}F_i^{(q)}(q_j^2) = R(\Gamma; 0, t; \vec{q}_j, \tau; O_j^{(q)}), \qquad \mathcal{A}_{ji} \equiv a_{ji}\sqrt{A(\Gamma_4, \vec{p}_j, m^{[0]})A(\Gamma_4, \vec{0}, m^{[0]})}. \tag{6.26}$$

Solving this over determined system of equations achieves both an averaging over different momentum solutions for a particular q^2, as well as decomposing of the individual form factor terms resulting from each operator $O^{(q)}$, all in one calculation. As discussed previously, the individual quark contributions (q) for $F_i^{(q)}$ can be arranged in any way to obtained the desired iso-vector, proton, neutron or any other contribution.

Chapter 7

Zero Momentum Transfer Results

The majority of this chapter will consist of the key findings from a set of calculations of two- and three-point correlation functions and have been published in [116]. The renormalisation factors used to renormalise the operators in this section are discussed in Chapter 4.

7.1 Lattice Details

Simulations were performed on a $32^3 \times 64$ lattice with a pion mass of 460 MeV and a lattice spacing of 0.074 fm [66, 117, 118]. This ensemble corresponds to the SU(3)-symmetric point, where $m_u = m_d = m_s$ with $\kappa = 0.120900$, and has been tuned to be close to the physical, average light-quark mass $\overline{m} = \frac{1}{3}(m_u + m_d + m_s)$ [66]. The simulation uses a clover action defined in Eq.(3.28) comprising of a stout smeared fermion action along with a tree-level Symanzik improved gluon action defined in 3. We perform $\mathcal{O}(1000)$ measurements on $\mathcal{O}(1800)$ trajectories, with multiple source locations to remove autocorrelations. The renormalisation constants $Z_A = 0.8728(6)(27)$, $Z_S^{\overline{MS}} = 0.682(6)(18)$ and $Z_T^{\overline{MS}} = 0.9945(010)(035)$ at 2 GeV have been reported in [78], and $Z_{\langle x \rangle}^{\overline{MS}} = 1.067$ is calculated in Chapter 4.

A fixed (zero) boundary condition in Euclidean time dimension and periodic boundary conditions in the spatial dimensions are chosen for this calculation. To avoid the temporal boundary conditions as discussed in the beginning of Section 3.4, a source time of $t_0 = 16$ as selected. This results in the source-sink separation $t = t_{sink} - t_0$ being the time separation away from $t_0 = 16$. As outlined in Section 3.4.2, we employ the sequential source through the sink method or the named *fixed sink* method to compute three-point function. Hence we are required to fixed the sink momentum $\vec{p}'$ for which we set $\vec{p}' = \vec{0}$.

The smearings undertaken in later sections are a gauge-invariant Gaussian smearing defined in Eq.(5.2) with $\alpha = 0.7$ and is applied iteratively to the source

N_{smear} \ t	10	11	13	16	19	22
32	$\star$		$\star$	$\star$	$\star$	$\star$
64			$\star$			
128			$\star$			
variational			$\star$	$\star$		
pencil of function	$\star$	$\star$				

Table 7.1: Table showing all smearing and source-sink separations undertaken in this paper.

and sink quark field N_{smear} times as described in Section 5.1.

To form our variational basis we solve our quark propagators for 32, 64 and 128 sweeps of smearing which correspond to root mean square radii of 0.248 fm, 0.351 fm and 0.496 fm respectively. This basis was selected after the initial calculation of two-point correlation functions over a larger basis consisting of 8, 16, 32, 64, 128, 256 sweeps of smearing. Due to the smaller 8 and 16 sweeps of smearing two-point correlators having minimal effect on the variational method and the largest 256 sweeps of smearing result having poor signal to noise ratio, we removed these smearing amounts when constructing the three-point correlation function basis. Then once the basis was selected, the three-point correlation functions were calculated at a source-sink separation of $t = 13, 16$ (in physical units, $t = 0.74$ fm, 1.184 fm).

To get an extensive range of source-sink separation times for the study of the summation and two-exponential fit methods, we have performed the sequential-source inversions at source-sink separations of 10, 13, 16, 19 and 22 time slices. In physical units, this corresponds to the range 0.74-1.63 fm. This extended range is primarily at our reference source smearing of $N_{smear} = 32$.

The final study was a pencil of function calculation which was performed over the same sweeps of smearings as the variational method but a new set of sequential-source inversions were undertaken at a source-sink time separation of 10 and 11. The delta time shift parameter used to construct a pencil of function basis described in Section 5.2.2 was set to $\delta = 1$. The full ensemble of inversions performed in this study are indicated in Table 7.1.

For illustrative purposes in the following graph legends and axis labels, we denote the variational method interchangeably as CM or $REvec$, with the following Δt in $(CM\ t_0\#\Delta t\#)$ referring to our variational method eigenvalue solving parameter $\Delta_v t$ from Eq.(5.15).

7.2 Mass Extraction from Two-Point Correlation Function

The starting point for any lattice QCD calculation involving any nucleon matrix element is an analysis of its ground state mass $m^{[0]}$. Using the construction and theory of the two-point correlation function described in Section 3.4.1, we can start by plotting the *effective mass* in Eq.(6.2) which for zero momentum is

$$\log\left(\frac{G_2(\Gamma_4;\vec{0},t)}{G_2(\Gamma_4;\vec{0},t+\Delta t)}\right) \xrightarrow{t\gg 0} m^{[0]}\Delta t, \tag{6.2}$$

for which we select $\Delta t = 3$ for the subsequent plots.

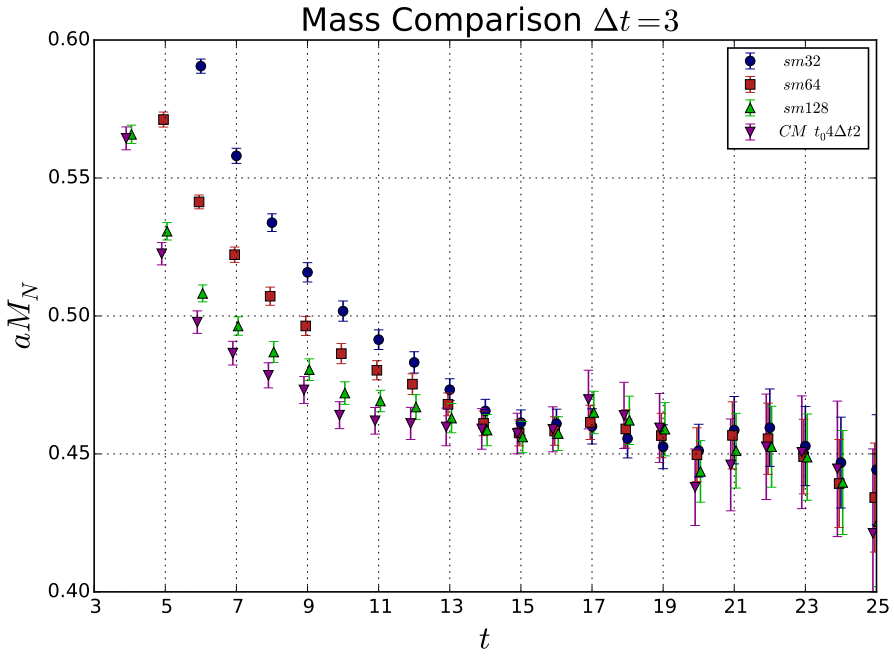

Figure 7.1: Effective mass plots defined in Eq.(6.2) over sink time comparing the different smearings and the variational method labelled by $t_0 = 4,\ \Delta_v t = 2$. We chose the time shift parameter $\Delta t = 3$ defined in Eq.(6.2).

To begin with, we plot the effective mass combinations of the three individually smeared and variational method two-point functions calculated in Figure 7.1. By plotting this, the excited-state contamination can clearly be seen to be altering the effective mass from source-sink separations of $t < 10$. We can also highlight how the excited-states are affecting the correlators more for the less source-sink smeared interpolating fields. The effectiveness of the variational method is clear

in this figure, as we see a further improvement over the three individually smeared effective masses.

When constructing the variational method, we are required to select two source-sink separations t_0 and $\Delta_v t$ to solve the eigenvalue equation in Eq.(5.15). By varying the parameters individually in Figure 7.2, we shows there is minimal change when altering t_0 for fixed $\Delta_v t$ and $\Delta_v t$ for fixed t_0.

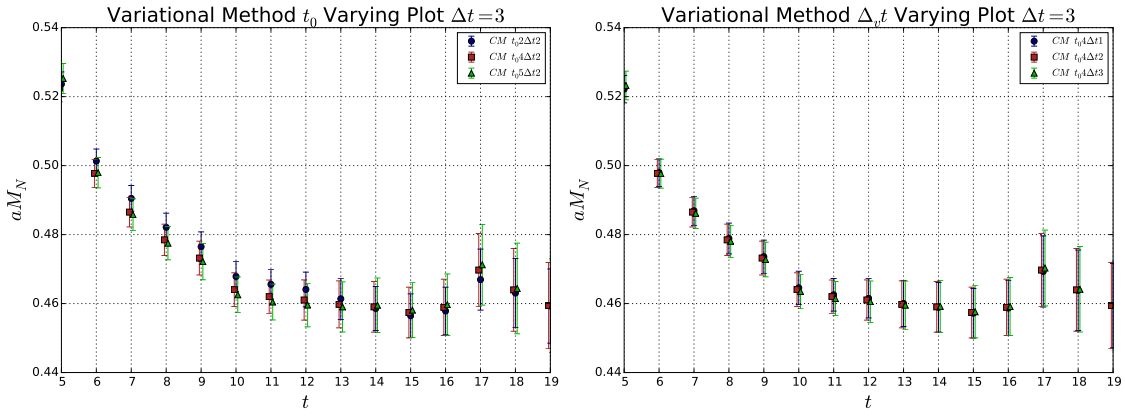

Figure 7.2: Effective mass plots defined in Eq.(6.2) over sink time comparing different t_0 parameters for a fixed $\Delta_v t = 2$ on the left and comparing different $\Delta_v t$ parameters for a fixed $t_0 = 4$ for the figure on the right. We chose the time shift parameter $\Delta t = 3$ defined in Eq.(6.2).

Although plotting effective masses is useful for understanding the excited-state contamination effects in the two-point correlation functions, eventually we need to extract the mass $m^{[0]}$. To achieve this, an appropriate source-sink separated time window is needed, where we are satisfied with the χ^2_{PDF} defined in Eq.(A.8). The one-exponential fit ranges illustrated in Figure 7.3 for the smeared two-point correlators began at the same source-sink separation, even though the different smeared results have different exited-state contamination effects. In the following Figure 7.4, the one-exponential fit ranges for the variational method and pencil of function methods are shown. We see similar values and uncertainties between both mass parameters $m^{[0]}$, despite the fact that the pencil of function methods effective mass points over the source-sink separations are wildly varying and have large uncertainties.

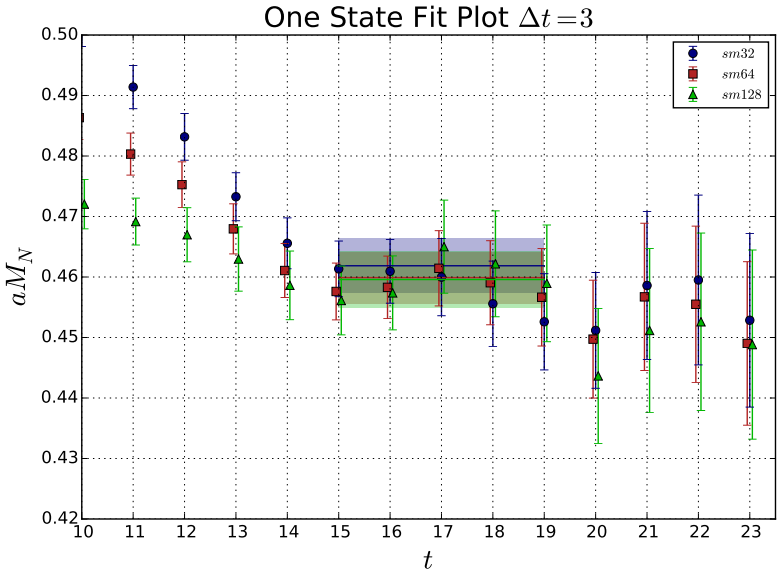

Figure 7.3: Effective mass plots defined in Eq.(6.2) over sink time for differently smeared two-point correlators, shown in conjuncture with lines and shaded uncertainties that represent the one-exponential fit parameter $m^{[0]}$.

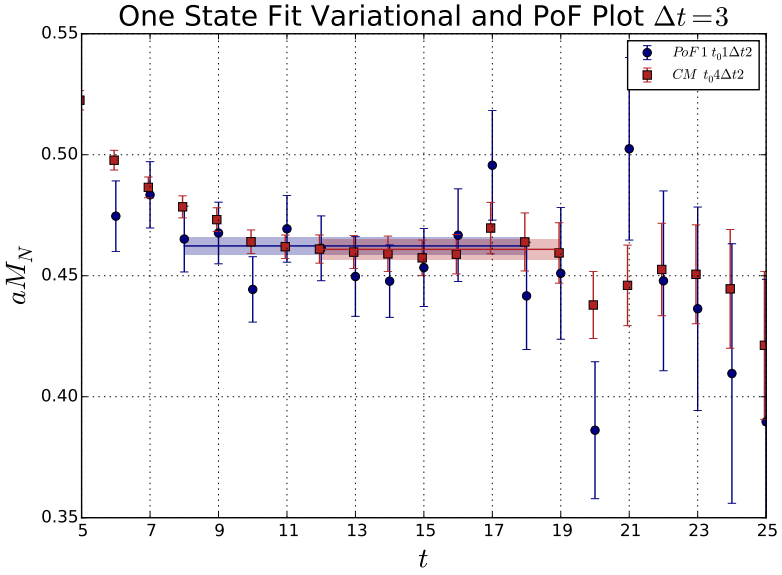

Figure 7.4: Effective mass plots defined in Eq.(6.2) over sink time, for the pencil of function and variational method two-point correlators, shown in conjuncture with lines and shaded uncertainties that represent the one-exponential fit parameter $m^{[0]}$.

The proposed two-exponential fit, in which a ground and first excited state functional form is fitted to the two-point correlation functions, is not displayed individually for each individual two-point correlation function. Instead, we demonstrate the combine fit

$$G_2(\Gamma_4;\vec{0},t) = A^i e^{-m^{[0]}t}(1 + A'^i e^{-\Delta m^{[0,1]}t}), \tag{6.6}$$

where we have multiple coupling parameters A^i, A'^i for each smearing index i, but common mass parameters $m^{[0]}$ and $\Delta m^{[0,1]} = m^{[1]} - m^{[0]}$. Figure 7.5 illustrates this fitting method over the three smeared two-point functions. Opposed to the previous one-exponential fit, we see the effective mass combination of the fit function being non-constant. The difference between the three coloured lines at smaller source-sink separated results shows how the different correlation functions have different couplings to the first excited state, i.e. different values for $A'^{ii}_{m^{[0]}}$ in Eq.(6.6). But when moving to the largest source-sink separated points, a common $m^{[0]}$ parameter is the only contribution in the effective mass construction. The variational and pencil of function methods are omitted from the fit, since these methods have already removed a large amount of excited states.

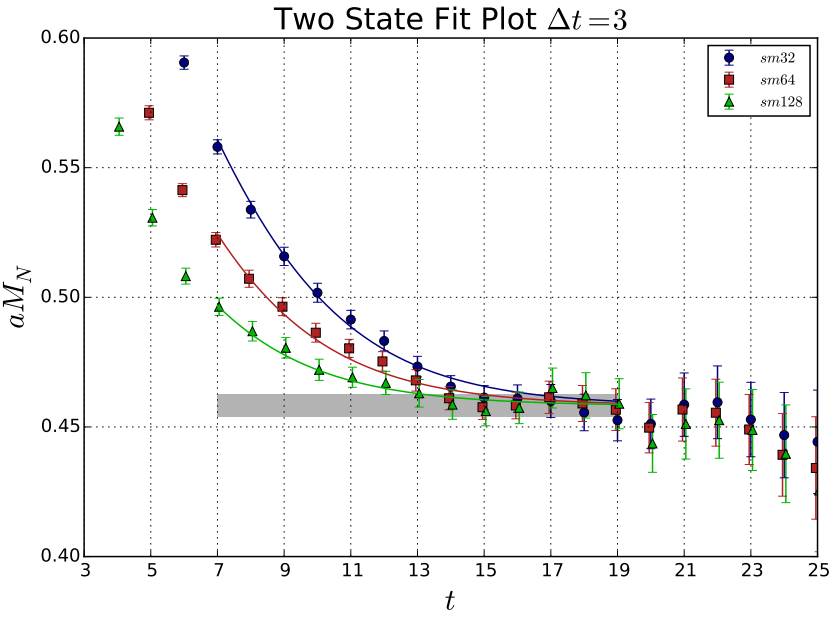

Figure 7.5: Effective mass plots defined in Eq.(6.2) over sink time shown in conjuncture with the two-exponential fit method extracted from all the three smearing sweeps of 32, 64 and 128 as one inclusive fit shown in Eq.(6.6). The lines represent the fit function used in place of the two-point correlator in the mass extraction function Eq.(6.2) and the grey band represents the mass parameter $m^{[0]}$ extracted from the combine two-exponential fit.

The extracted values for $m^{[0]}$ from the one- and two-exponential fits are summarised in Table C.1.

7.3 Zero Momentum Proton Iso-Vector Matrix Elements

The first quantity selected for analysis was the nucleon axial charge g_A, which has been quite an important benchmark for the validity of lattice QCD calculations. It can be calculated by looking at the operator/iso-vector combination

$$O^{(q)} = O^{(u)} - O^{(d)} = \overline{u} i\gamma_3\gamma_5 u - \overline{d} i\gamma_3\gamma_5 d, \tag{7.1}$$

while using a spin projector which corresponds to $\Gamma = \Gamma_3 \equiv \left(\frac{I+\gamma_4}{2}\right)\gamma_3\gamma_5$.

Next, we selected the scalar current, which has been notorious for its large excited-state contamination [102, 119]. For reference, some experimental determinations of the scalar charge can be seen in [120–124]. It can be calculated by looking at the identity operator with the iso-vector combination

$$O^{(q)} = O^{(u)} - O^{(d)} = \overline{u} I u - \overline{d} I d, \tag{7.2}$$

while using a spin projector $\Gamma = \Gamma_4 \equiv \frac{I+\gamma_4}{2}$ which corresponds to an unpolarised nucleon.

Deep inelastic scattering experiments as described in Section 2.5, are our primary method for understanding the nucleon and QCD in general. At the physical quark mass, it is predicted that from the fitted global MRST2001 parton anaysis [125], $\langle x \rangle^{MRST} = 0.157(9)$ whereas the lattice determination of $\langle x \rangle$ at many quark masses has consistently over estimated the quantity over the years [60, 102, 126]. One possible explanation could be due to the contamination from excited-state effecting the results.

This is why we have selected the momentum fraction $\langle x \rangle$, which can be calculated by looking at the operator defined in Eq.(2.38) and the iso-vector quark contribution

$$O^{(q)} = O^{(u)} - O^{(d)} = \overline{u}\left[\gamma_4 \overleftrightarrow{D}_4 - \frac{1}{3}\left(\sum_{i=1}^{3}\gamma_i \overleftrightarrow{D}_i\right)\right] u - \overline{d}\left[\gamma_4 \overleftrightarrow{D}_4 - \frac{1}{3}\left(\sum_{i=1}^{3}\gamma_i \overleftrightarrow{D}_i\right)\right] d, \tag{7.3}$$

while using a spin projector which corresponds to $\Gamma = \Gamma_4$. At zero momentum, the resulting ratio function R for this operator/spin projector combination (assuming large time approximation $t \gg \tau \gg 0$) is

$$R(\Gamma_4; 0, t; 0, \tau; O^{(q)}) = -m_N v_{2,b} = -m_N \langle x \rangle . \tag{7.4}$$

Lastly, beyond the standard model (BSM) extensions to neutron beta-decay requires tensor charge g_T (as well as g_S) corrections, so the extraction of g_T has been of great interest as well. Experimentally, we have seen results using semi-inclusive deep inelastic scattering (SIDIS) from [127–129] which can be combine with Bell e^+e^- scattering experiments to extract g_T [127, 130]. This charge has shown to be less affected by excited-state contamination as shown in [102, 113, 119].

Hence, the the tensor charge was selected also, which can be calculated by looking at the operator/iso-vector combination

$$O^{(q)} = O^{(u)} - O^{(d)} = \overline{u}\gamma_1\gamma_2 u - \overline{d}\gamma_1\gamma_2 d, \tag{7.5}$$

while using a spin projector which corresponds to $\Gamma = \Gamma_3 \equiv \left(\frac{I+\gamma_4}{2}\right)\gamma_3\gamma_5$.

The following subsection will consist of each of the key methods and analysis techniques discussed in the previous chapters, for the nucleon axial charge g_A, scalar charge g_S, the tensor charge g_T and the quark momentum fraction $\langle x \rangle$.

7.4 Analysing the Variational Method Data

In this section, we look at the set of data calculated for a fixed source-sink separation $t = 13$ over 32, 64 and 128 sweeps of smearing at the source and sink. Along with this, the variational method over the 32, 64 and 128 sweeps of smearing was undertaken at a source-sink separation of $t = 13$ and 16. Lastly, the pencil of function method was attempted at source-sink separations of $t = 10$ and 11.

7.4.1 Plateau Smearing/Variational comparison

We start our analysis of zero momentum transfer matrix elements by extending the variational method to the three-point correlation function in Section 5.2. As a reminder, the resulting ratio factor ratio for the *fixed sink* sequential source method of constructing the three-point correlation function is

$$R(\Gamma; 0, t; 0, \tau; O^{(q)}) \equiv \frac{G_3(\Gamma; \vec{0}, t; \vec{0}, \tau; O^{(q)})}{G_2(\vec{0}, t)}, \tag{3.68}$$

and the variational method optimised ratio function is constructed as

$$\widetilde{R}^{\beta}(\Gamma; \vec{0}, t; \vec{0}, \tau; O^{(q)}) \equiv \frac{\widetilde{G}_3^{\beta}(\Gamma; \vec{0}, t; \vec{0}, \tau; O^{(q)})}{\widetilde{G}_2^{\beta}(\vec{0}, t)}, \tag{5.20}$$

where $\beta = 0$ corresponds to a variational method optimised ratio function for the ground state. In this section, we analyse the first equation for the 32, 64 and 128 sweeps of smeared results, and the second equation using the variational method over the basis of 32, 64 and 128 sweeps of smearing all at a source-sink separation of $t = 13$. The general technique in analysing these plots is to refer to the large time approximation $t \gg \tau$ and $\tau \gg 0$ that is required to reach the ground state solution. In analysing the graph, we can note that the centre point $\tau = t/2$ is considered the point in which the excited-state contamination is minimised for a particular source-sink separation t. Furthermore, if around this point a plateau is formed, we can say that the excited-state effects from the transitional matrix elements, for which the first dominate state is $\propto FF(m^{[0]} \to m^{[1]})$, has been suppressed within statistical uncertainty. A detailed discussion can be seen in Section 6.2.

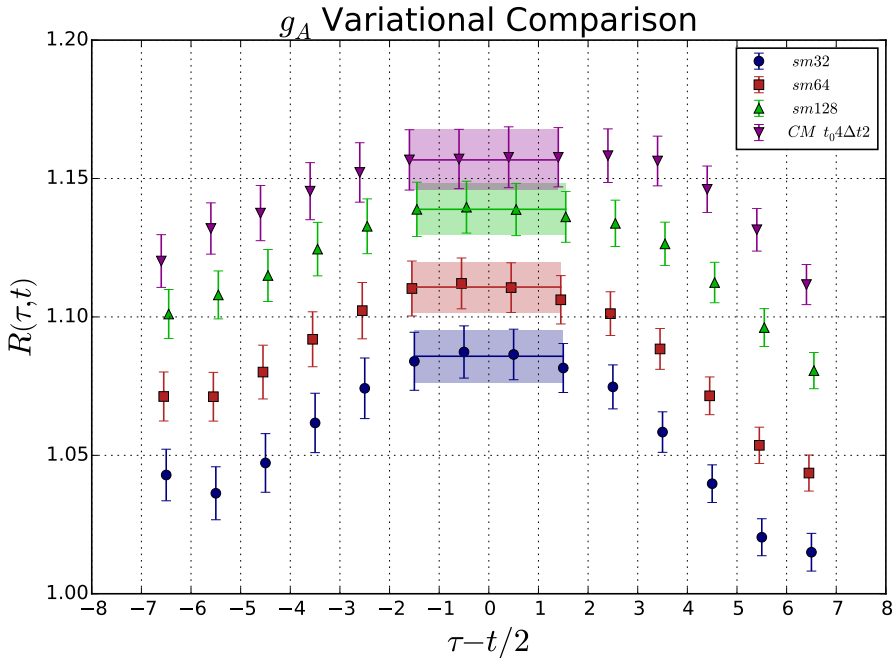

Figure 7.6: Graph for g_A extracted from the R function defined in Eq.(3.68). The lines indicate the constant fit value extracted from each set of data used in Figure 7.42. All subsequent R function graphs are plotted over the current insertion time τ which has been centred about zero via the construction $\tau - t/2$. This and the following three plots compares different diagonally smeared values to the variational method with a source-sink separation of $t = 13$.

In Figure 7.6 for the smeared results, we see that no clear plateau is revealed around the central current insertion point. In contrast, we can see that the variational method seems to have removed the majority of the contamination from

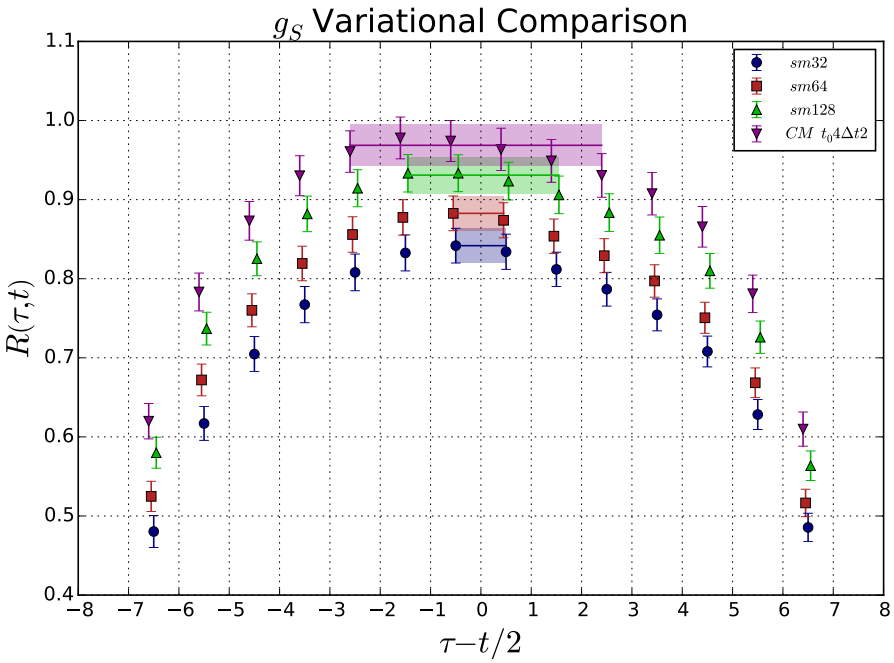

Figure 7.7: Graph for g_S extracted from the R function defined in Eq.(3.68). The lines indicate the constant fit value extracted from each set of data used in Figure 7.43.

transition matrix elements as it looks to plateau from current insertion time 5 to 11 (or on the graph, -1.5 to 1.5). Furthermore, the value produced is statistically larger than any of the smeared results indicating that a poor choice of source and sink operators and/or short source-sink separation times can lead to excited-state contamination which acts to suppress g_A. This is in agreement with other findings [102, 113].

In Figure 7.7, we see a similar picture for g_S. The variational method produces a flatter ratio as a function over τ compared to the individually smeared correlators. We note that in this case, we see that the transition matrix elements are much larger than in g_A as there is a larger curvature with respect to current time insertion τ.

A similar improvement as observed in the previous two quantities has been achieved by the variational method for $\langle x \rangle$ shown in Figure 7.8. For this operator we see there is even more excited-state contamination compared to the precision of the calculation of the current insertion time τ.

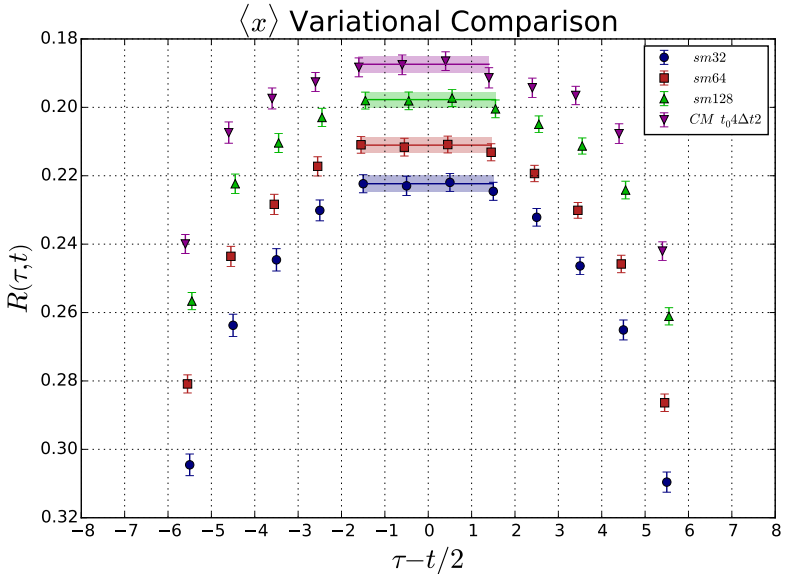

Figure 7.8: Graph for $\langle x \rangle$ extracted from the R function defined in Eq.(3.68). The lines indicate the constant fit value extracted from each set of data used in Figure 7.44.

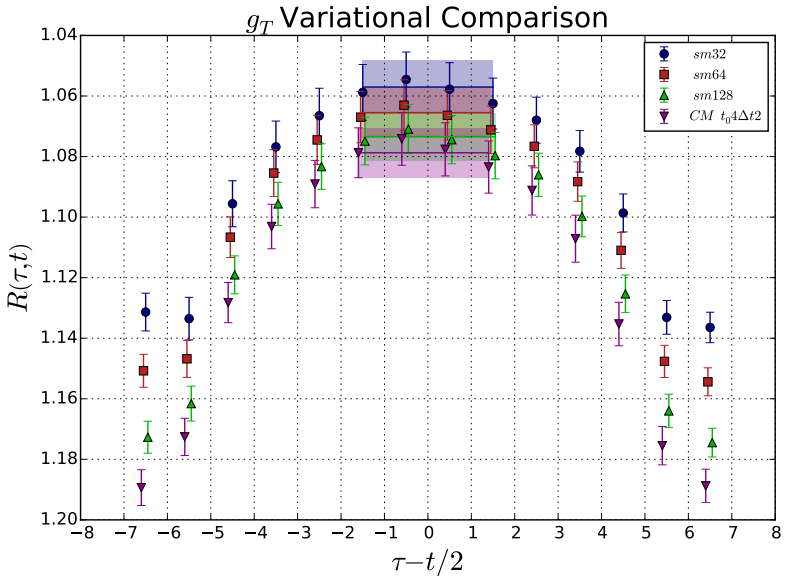

Figure 7.9: Graph for g_T extracted from the R function defined in Eq.(3.68). The lines indicate the constant fit value extracted from each set of data used in Figure 7.45.

We see a completely different picture in the variational method result for g_T shown in Figure 7.9. The removal of excited-state contamination due to varying the current insertion time τ causes the results to decrease, where as increasing the sweeps of smearing causes the results to increase.

7.4.2 One-Exponential Comparison

As we did in the previous section, we again analyse the 32, 64 and 128 smearing sweeps results, along with the variational method over the basis of 32, 64 and 128 sweeps of smearing all at a source-sink separation of $t = 13$. But instead of using the ratio function, we utilise the *one-exponential fit* ratio discussed in Section 6.2

$$R_{OSF}(\Gamma; \vec{0}, t; \vec{0}, \tau; O^{(q)}) \equiv \frac{G_3(\Gamma; \vec{0}, t; \vec{0}, \tau; O^{(q)})}{A_{m^{[0]}} e^{-m^{[0]} t}}, \tag{6.16}$$

where, $m^{[0]}$ and $A_{m^{[0]}}$ are fit parameters from fitting to the two-point correlation function. The aim of this section is to see if there is any slight deviations of the ratio functions and the extracted values from the normal ratio function utilised in the previous section.

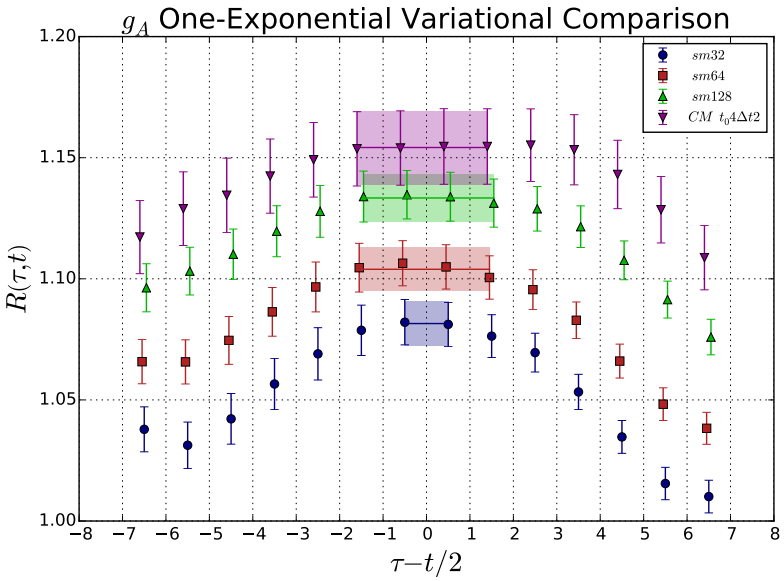

Figure 7.10: A graph utilising the construction defined in Eq.(6.16) along with a line and shaded area for each calculation corresponding to the one-exponential fit parameter g_S on each set. All results in this section have a source-sink separation of $t = 13$ for the 32, 64 and 128 sweeps of smearing and the variational method calculations.

For g_A, the one-exponential fit results Figure 7.10 shows a slight shift downwards in the variational method results to make a small overlap with the 128 sweeps of smearing result. The three smeared results show unnoticeable deviations from their ratio function counterparts.

A similar conclusion is found for g_S and $\langle x \rangle$ in Figures 7.11 and 7.12. We see essentially zero shift when comparing the two plots, which indicates that extracting g_S and $\langle x \rangle$ are not sensitive to the fitting procedure.

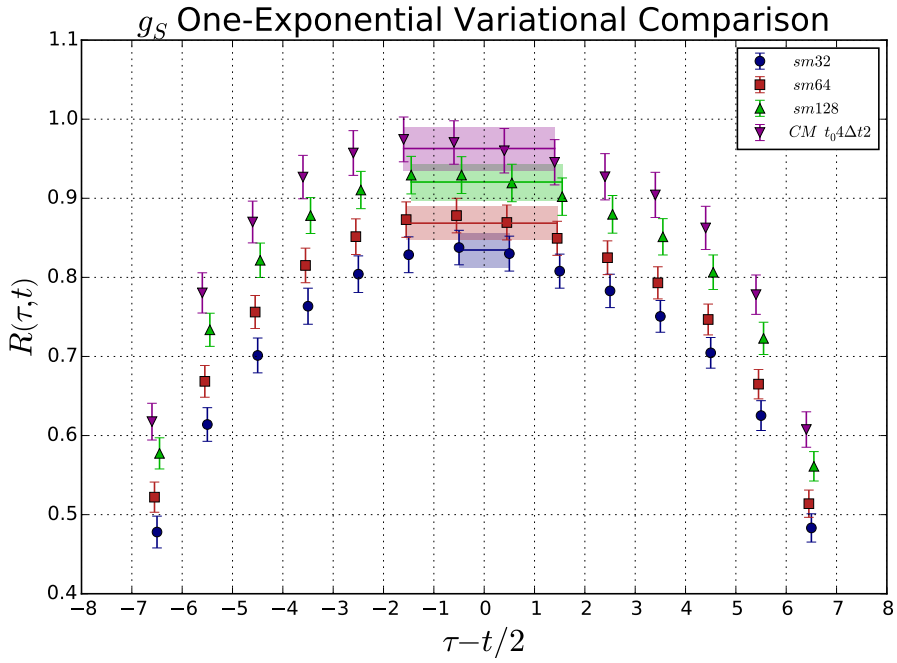

Figure 7.11: A graph utilising the construction defined in Eq.(6.16) along with a one-exponential fit parameter (and uncertainty) corresponding to g_S on each set.

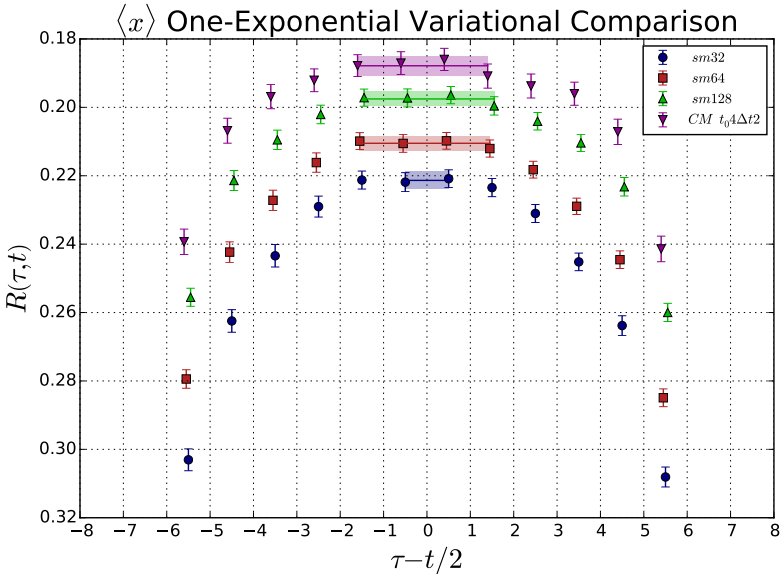

Figure 7.12: A graph utilising the construction defined in Eq.(6.16) along with a one-exponential fit parameter (and uncertainty) corresponding to $\langle x \rangle$ on each set.

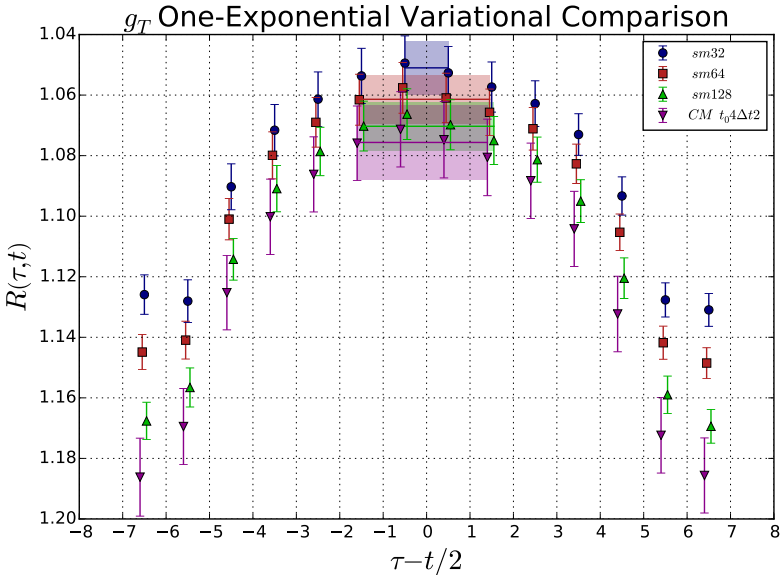

Figure 7.13: A graph utilising the construction defined in Eq.(6.16) along with a one-exponential fit parameter (and uncertainty) corresponding to g_T on each set.

Although being hard to distinguish between the different results for the tensor charge g_T in Figure 7.13, there is a slight shift up in the smaller smeared results.

7.4.3 Source-Sink Separation Dependence

Finding a plateau of the ratio function over current insertion time τ in Section 7.4.1 indicates to us that the transitional matrix elements, for which the dominant first state is $\propto FF(m^{[0]} \to m^{[1]})$, are all being sufficiently suppressed. But it does not tell us any information about the excited to excited state matrix elements, for which the dominant first state is $\propto FF(m^{[1]} \to m^{[1]})$. This is indicated to us when analysing the two-exponential fit function for the three-point correlation function, where the two-state approximation to a three-point correlator is

$$G_3(\Gamma;\vec{0},t;\vec{q},\tau;O^{(q)}) = A_{m^{[0]}} e^{-m^{[0]}t} \times \left\{ B_{00} + B_{10}\left(e^{-\Delta m^{[0,1]}\tau} + e^{-\Delta m^{[0,1]}(t-\tau)}\right) + B_{11} e^{-\Delta m^{[0,1]}t} \right\}. \tag{6.13}$$

The term B_{10}, which is $\propto FF(m^{[0]} \to m^{[1]})$, is dependant on the current time and source-sink time separation τ and t respectively, where as the term B_{11}, which is $\propto FF(m^{[1]} \to m^{[1]})$, is only dependant on the source-sink separation t.

This motivates the study of three-point correlation functions at multiple source-sink separation times, as it is the only way to justify, via the analysis of plateaus, that the three-point correlation function is dominated by the ground state matrix element (which is $\propto FF(m^{[0]} \to m^{[0]})$).

As a result, the strategy in this section is to accredit excited state suppressed three-point correlation functions as those with no shift in value between different source-sink separated results, as well as a plateau forming over current insertion points τ. To execute this strategy, we begin in this section with selecting the 32 sweeps of smearing results along with the variational method results at source-sink separations of 13 and 16.

Beginning with g_A in Figure 7.14 we see sufficiently suppressed excited-states removed as the results did not shift up when moving from a source-sink separation of 13 to 16. Compared to the smallest smeared operators, we see excited-states being removed in the change from a source-sink separation of 13 to 16.

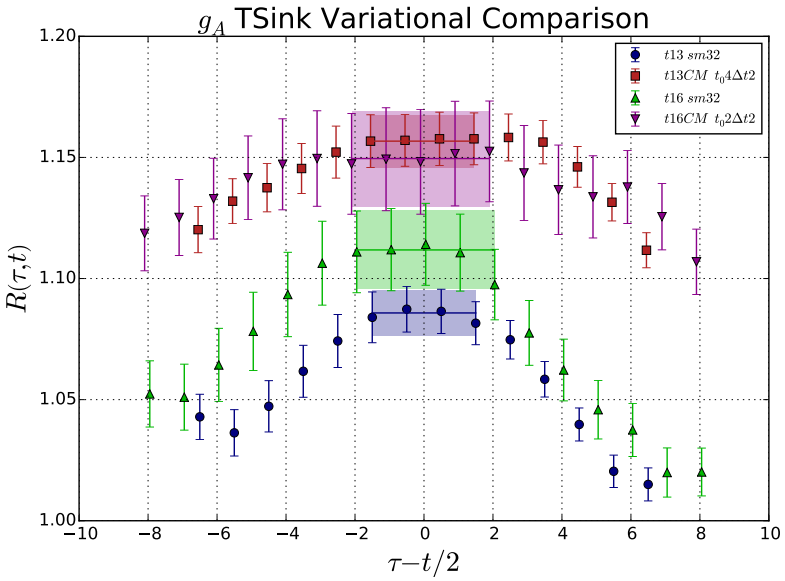

Figure 7.14: Graph for g_A extracted at each current time τ comparing different variational results for different source-sink separations. This is overlaid with the same source-sink separated results, but for the 32 sweeps of smearing.

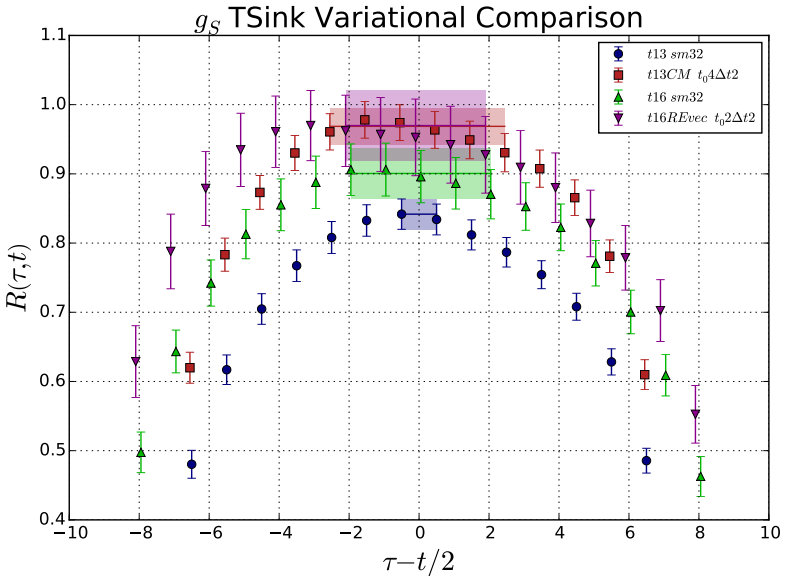

Figure 7.15: Graph for g_S extracted at each current time τ comparing different variational results for different source-sink separations. This is overlaid with the same source-sink separated results, but for the 32 sweeps of smearing.

Once again for g_S in Figure 7.15, which has been established to have larger excited-state effects than g_A, increasing the source-sink separation for the variational method shows no more statistically significant removal of excited-states which cannot be said about the smallest smeared result.

In the case of $\langle x \rangle$, as displayed in Figure 7.16, we see no statistically significant difference between the variational method for the two source-sink separations which implies the variational method has dramatically reduced the amount of excited-state contamination. The 32 sweeps of smearing result seems to be even more effected by excited state effects as the previous two values.

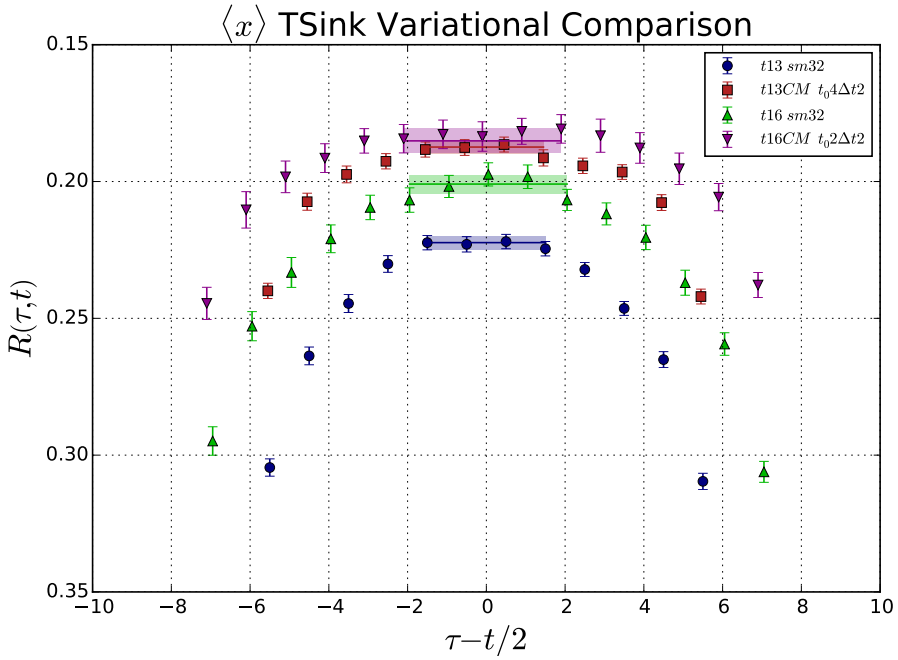

Figure 7.16: Graph for $\langle x \rangle$ extracted at each current time τ comparing different variational results for different source-sink separations. This is overlaid with the same source-sink separated results, but for the 32 sweeps of smearing.

In the case of g_T, as displayed in Figure 7.17, we see no statistically significant difference between the variational method for the two source-sink separations which implies the variational method has dramatically reduced the amount of excited-state contamination. But curiously, the same can be said for the 32 sweeps of smearing result which has a statistically significant signal. The question arises, which smearing operator is correct?

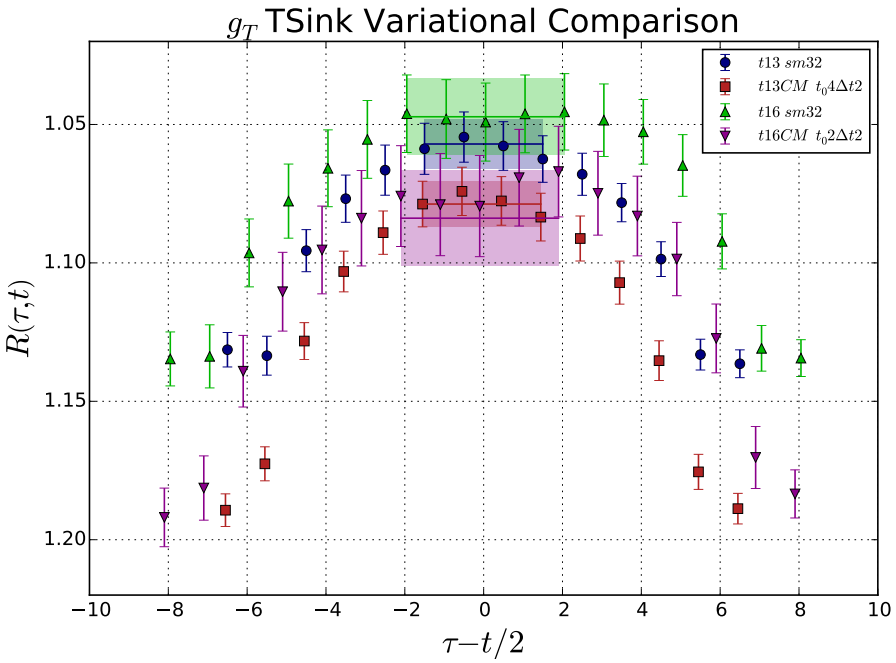

Figure 7.17: Graph for g_T extracted at each current time τ comparing different variational results for different source-sink separations. This is overlaid with the same source-sink separated results, but for the 32 sweeps of smearing.

7.4.4 Two-Exponential Comparison

A two-exponential fit can be applied to the differently smeared three-point correlation functions. By doing this, we can attempt to remove the ground to excited transition matrix element contribution. Since our data set has a single source-sink separation of $t = 13$, the two-exponential fit function will have the form

$$G_3(\Gamma;\vec{0},t;\vec{q},\tau;O^{(q)}) = A_{m^{[0]}} e^{-m^{[0]}t} \times \left\{ B_{00} + B_{10}\left(e^{-\Delta m^{[0,1]}\tau} + e^{-\Delta m^{[0,1]}(t-\tau)} \right) \right\}. \tag{6.13}$$

The term B_{10}, which is $\propto FF(m^{[0]} \to m^{[1]})$, is what we hope remove from the three-point correlation function, to leave us with the term B_{00} which may still be contaminated with the B_{11} term. To help visualise the two-exponential fit, we plot the two-exponential ratio function

$$R_{TSF}(\Gamma;\vec{0},t;\vec{0},\tau;O^{(q)}) \equiv \frac{G_3(\Gamma;\vec{0},t;\vec{0},\tau;O^{(q)})}{A_{m^{[0]}} e^{-m^{[0]}t} + A_{m^{[1]}} e^{-(m^{[0]}+\Delta m^{[0,1]})t}}, \tag{6.17}$$

where the denominator consists of parameters extracted from the two-point correlator.

The two-exponential fit method is not applied to the variational method two- and three-point correlation functions as the two-exponential fit method will have a hard time trying to parameterise the highly suppressed excited states.

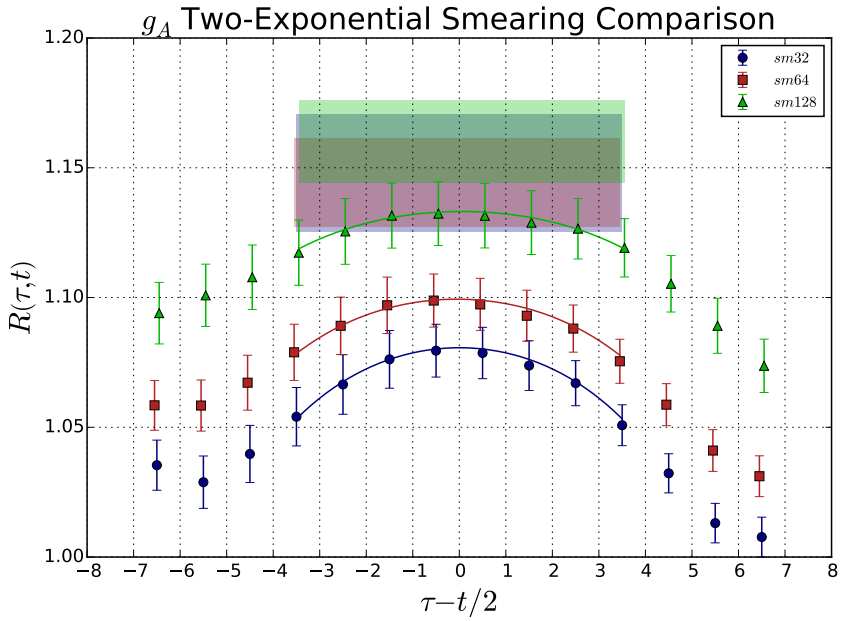

Figure 7.18: Graph of Figure 7.6 utilising the construction defined in Eq.(6.17), overlaid with a two-exponential fit calculation on each set. For all subsequent graphs in this section, the lines are the corresponding fit function and the shaded areas corresponds to g_A value extracted from the fit parameters. Since there is no variation in sink time t, no B_{11} was calculated in Eq.(6.13) as discussed in the end of Section 6.2.

In applying the two-exponential fit for g_A to the different smearing results in Figure 7.18, we observe that all three smearing fits coincide with one another. It is also clear that the determination of the ground state matrix elements have a larger relative error compared to the data points fitted to and being statistically consistent with a constant fit to the largest smeared (sm128) result.

Now applying the two-exponential fit for the smeared results to g_S in Figure 7.19, leads to an improvement to all 3 smeared results. Furthermore, uncertainties on the parameter extracted has increased compared to the uncertainties associated with the ratio factor for each current insertion τ points.

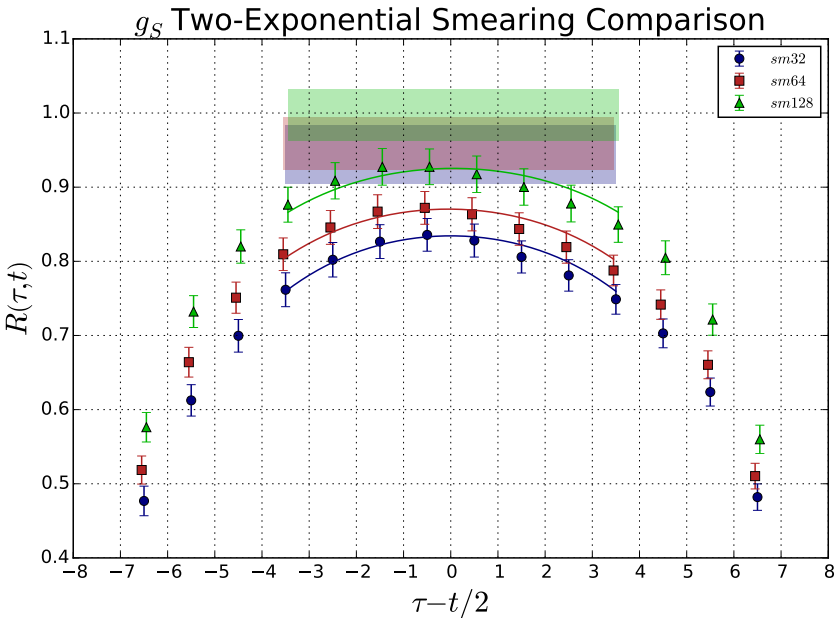

Figure 7.19: Graph of Figure 7.7 utilising the construction defined in Eq.(6.17), overlaid with a two-exponential fit calculation on each set.

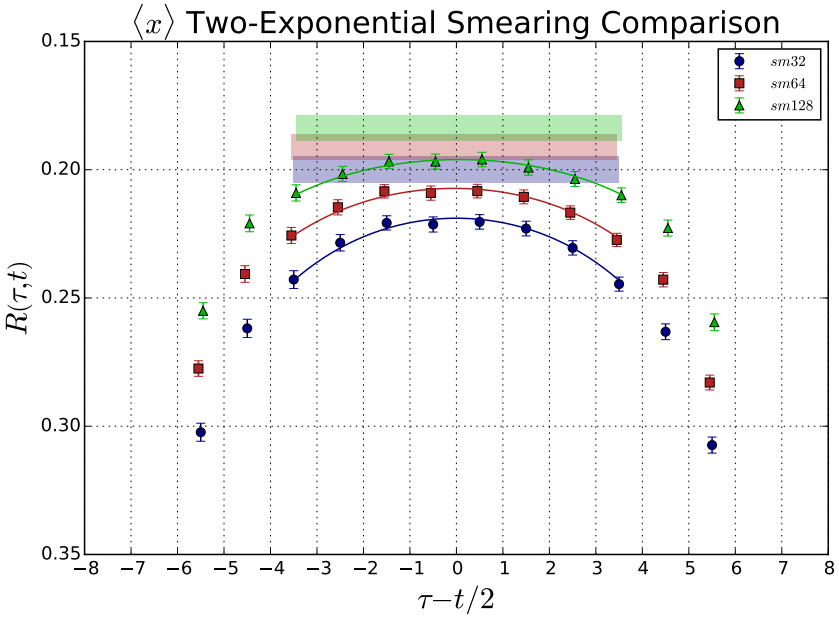

Figure 7.20: Graph of Figure 7.8 utilising the construction defined in Eq.(6.17), overlaid with a two-exponential fit calculation on each set.

Next, we apply the two-exponential fit to $\langle x \rangle$ for the smeared results in Figure 7.20, which looks to have made an improvement to all 3 smeared results. The errors on the parameter extracted has increased compared to the error from a ratio function points, but for $\langle x \rangle$ it seems that the two-exponential fit was more successful due to the relative size of the excited-state contamination to the precision of the ratio function points.

Lastly, applying the two-exponential fit to g_T for the smeared results in Figure 7.21, it has shifted the 64 and 128 sweeps of smearing result to a common extracted value, but the 32 sweeps of smearing has extracted a value larger than the others. The errors on the parameter extracted has increased compared to the error from a ratio function points. For g_T it seems that the two-exponential fit has produced some interesting extractions due to the unexpected excited-state contamination effect.

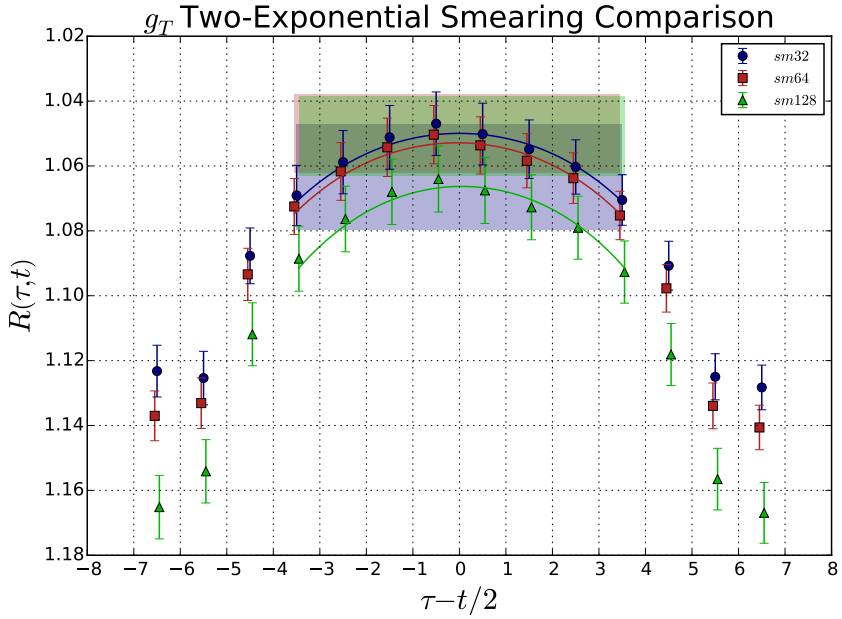

Figure 7.21: Graph of Figure 7.9 utilising the construction defined in Eq.(6.17), overlaid with a two-exponential fit calculation on each set.

7.4.5 Pencil of Function Analysis

Lastly, the pencil of function method is used with a 6×6 basis being the outer product of the 32, 64 and 128 sweeps of smearing with a pencil of function time shift of $\delta t = 1$. A detailed discussion of this process was presented in Section 5.2.2. We jump straight to the one-exponential fit method, as it can average out noisy correlation functions. For comparison, we select the standard variational method

result at a source-sink separation of $t = 13$ as it is considered to have highly suppressed excited-state contamination, along with the 32 sweeps of smearing result as it is considered to be affected substantially by excited-state contamination .

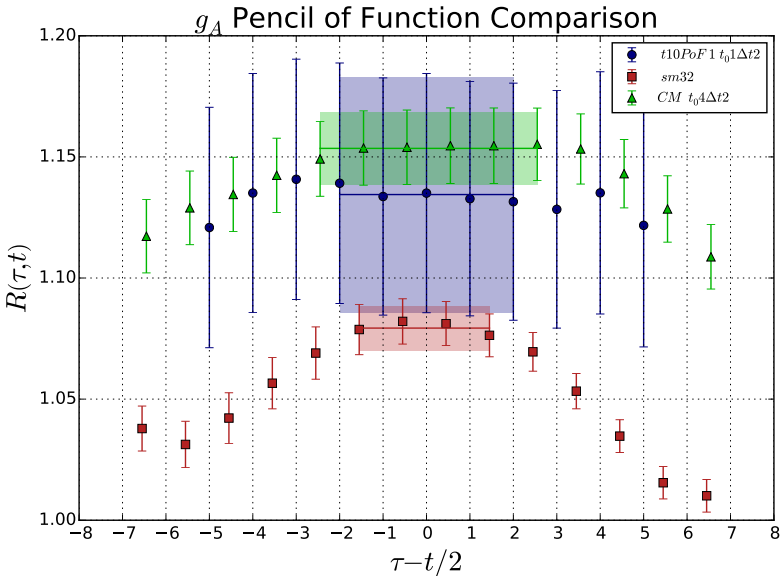

Figure 7.22: Graph for g_A extracted using the one-exponential fit method comparing the pencil of function method to the variational result and a 32 sweeps of smearing result. For all graphs in this section, source-sink separation for the pencil of function method is at $t = 10$ and the rest are at $t = 13$.

The pencil of function results in Figure 7.22 show how the method's statistical uncertainties are much larger than all the other calculations, even with such a short source-sink separation. Since the R function for the pencil of function has minimal variation with respect to τ, and the value is comparable with the variational method, give us a glimpse into the large excited-state removal potential of the pencil of function method as it is able to isolate the ground-state even at a source-sink separation of $t = 10$.

Again, for g_S in Figure 7.23, we have large statistical uncertainties compared to the other methods, but we do start to see a highly optimised correlation function with minimal excited-state contamination over a large time window. This is more prevalent in Figure 7.23, as the excited-state contamination has a greater effect then it did for g_A in Figure 7.22.

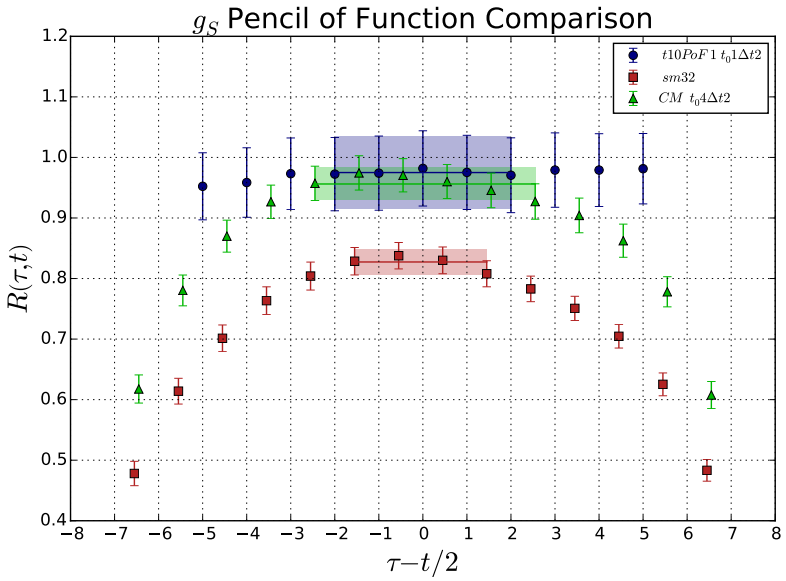

Figure 7.23: Graph for g_S extracted using the one-exponential fit method comparing the pencil of function method to the variational result and a 32 sweeps of smearing result.

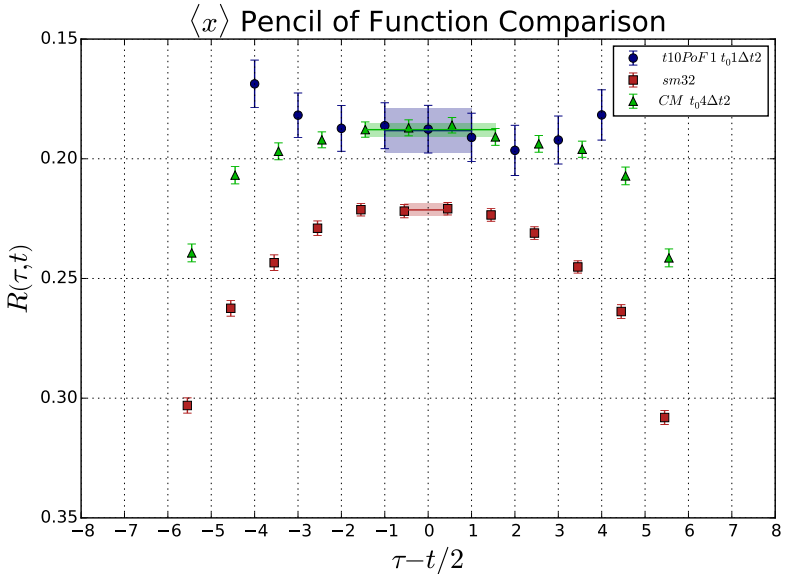

Figure 7.24: Graph for $\langle x \rangle$ extracted using the one-exponential fit method comparing the pencil of function method to the variational result and a 32 sweeps of smearing result.

The same large statistical uncertainty is repeated for $\langle x \rangle$ in Figure 7.24. We do see very promising excited-state removal potential, with a curious trend over the current insertion time $\tau - t/2$ which is in the opposite direction to regular excited-state contamination.

The pencil of function results in Figure 7.25 show no meaningful results, as the statistical uncertainty encapsulates both the variational method and 32 sweeps of smearing results.

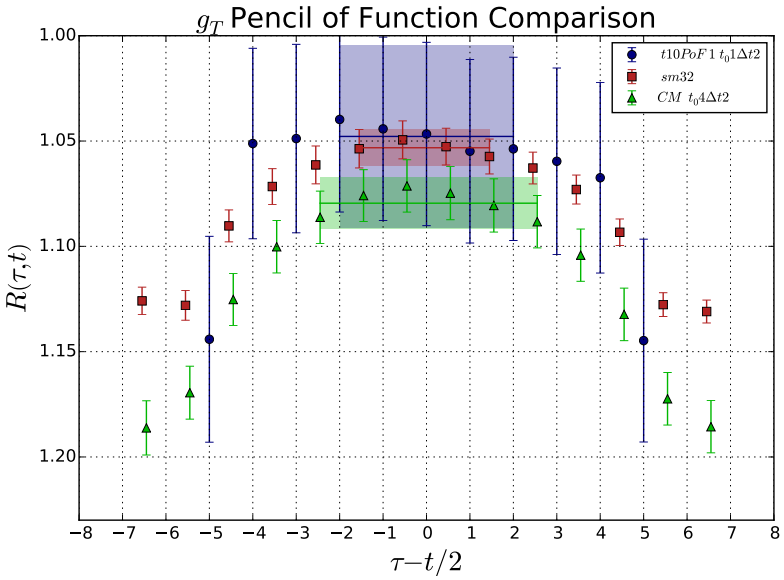

Figure 7.25: Graph for g_T extracted using the one-exponential fit method comparing the pencil of function method to the variational result and a 32 sweeps of smearing result.

7.5 Source-Sink Analysis

In this section, we apply the more commonly utilised summation, one-exponential fit and two-exponential fit methods to the set of data that consists of 32 sweeps of smearing at the source and sink, but with source-sink separations of $t = 10, 13, 16, 19$ and 22.

7.5.1 Summing the Ratio Function

To begin the summation method, we analyse the summed ratio function, for which the definition is

$$S\left(\Gamma;\vec{p}',t;\vec{q};\mathcal{O}\right)=\sum_{\tau=\delta t}^{t-\delta t}R(\Gamma;\vec{p}',t;\vec{q},\tau;O^{(q)})\rightarrow$$
$$c+t\left\{FF(E_p^{[0]}\rightarrow E_{p'}^{[0]},\Gamma,O^{(q)})+\mathcal{O}\left(e^{-min\left(\Delta E_p^{[0,1]},\Delta E_{p'}^{[0,1]}\right)t}\right)\right\}, \tag{6.18}$$

which amounts to summing the ratio function over the current insertion points. After summing, we undergo a linear line of best fit to the summed ratio function over the source-sink separated points t, for which the slope parameter is the quantity of interest (g_A, etc...). As discussed further in Section 6.3, we can additionally vary the number of points excluded at either end of the source-sink time window δt as well as the resulting source-sink separation points selected to fit a linear function to. For the subsequent plots, the colours/symbols blue/circle, red/square, green/triangle and pink/up-side-down triangle let us see the change in the line of best fit when we vary $\delta t = 0, 1, 2, 3$ respectively in Eq.(6.18). Results with small source-sink separations are likely to have the most contamination from higher excitations. They also have smallest statistical error and so can dominate in a weighted fit. By fitting only to the largest 3 source-sink separated results, we can extend the lines back to compare with the smaller source-sink separated results. Any significant deviation indicates that those smaller source-sink separated results should be excluded from the final fit.

In the plots in Figure 7.26 we have the summation function defined in Eq.(6.18) for g_A plotted over the source-sink separation times (in which we have summed over the current insertion times). The top plot shows that the summation fits show no statistically significant change in slope for the different δt value results and the line of best fit seems to satisfy the points well to extract a value. For g_A in the bottom plot in Figure 7.26, we have excluded the two smallest source-sink separated points from the linear fit and we see that the projected errors do encapsulate the smaller source-sink separated results. We can also see that the errors on the results drastically increase when compared to the top figure.

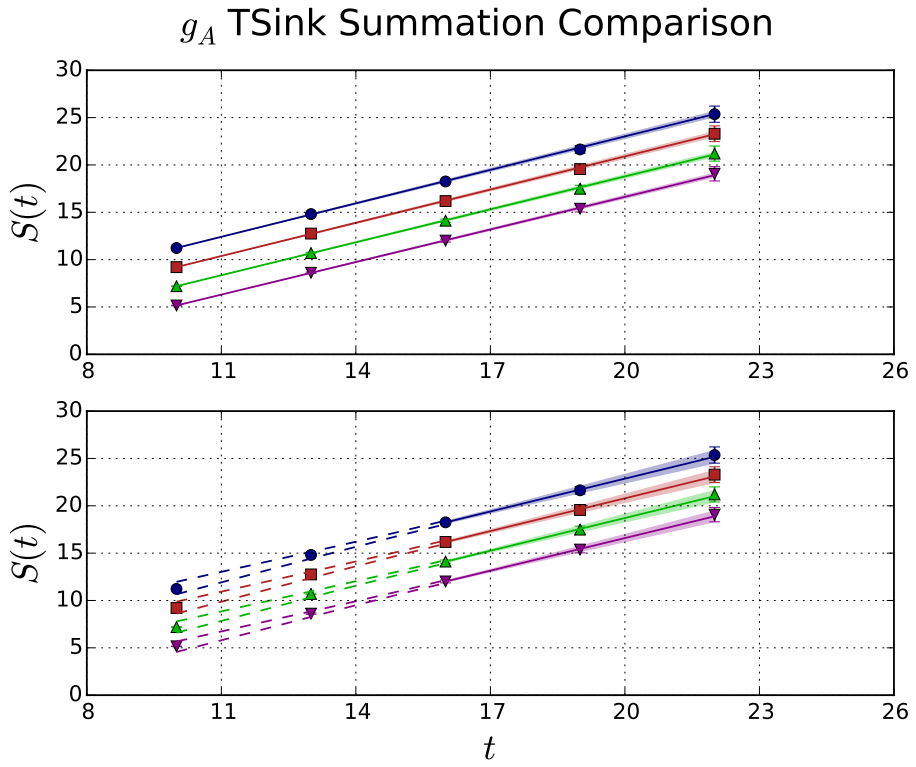

Figure 7.26: Summed ratio factor values for multiple source-sink times defined in Eq.(6.18) used to extract g_A. For all the subsequent plots in this section, the different colours/symbols (blue/circle, red/square, green/triangle and pink/up-side-down triangle respectively) correspond to $\delta t = 0, 1, 2, 3$ where δt is defined in Eq.(6.18). The linear line of best fit, which has initial points of $t = 10$ for the upper plot and $t = 16$ for the lower plot, is used to extract a slope which corresponds to g_A (or g_S, $\langle x \rangle$, g_T). The dashed lines correspond to the projected error ranges to smaller source-sink summed results.

In the summation method results for g_S, comparing the 4 coloured slopes passing through the 4 colours/symbols in the top of Figure 7.27 shows that the $\delta t = 0, 1, 2, 3$ parameter variation is not statistically significant. However, as the fit is a weighted fit and the smallest source-sink separated points have the smallest errors and the set of points are not linear, the smallest points are forcing the linear function to underestimate the slope of the larger source-sink separated values. Fitting over the larger source-sink separated points in the bottom of Figure 7.27 and projecting the fit backwards to smaller times reveals a tension between the results at small and large source-sink separations as the projected errors do not encapsulate the smaller source-sink separated results. This suggests that the error term in Eq.(6.18) is starting to be statistically significant.

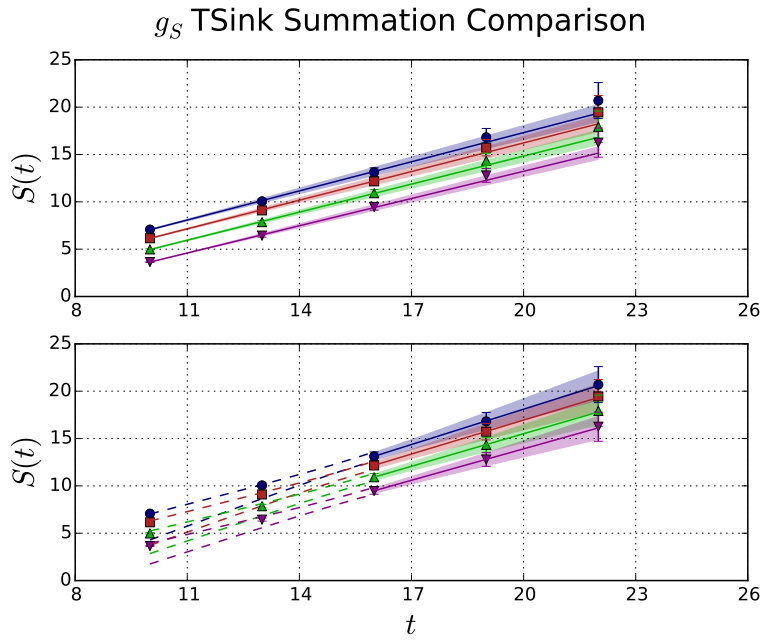

Figure 7.27: Summed ratio factor values for multiple source-sink times defined in Eq.(6.18) used to extract g_S.

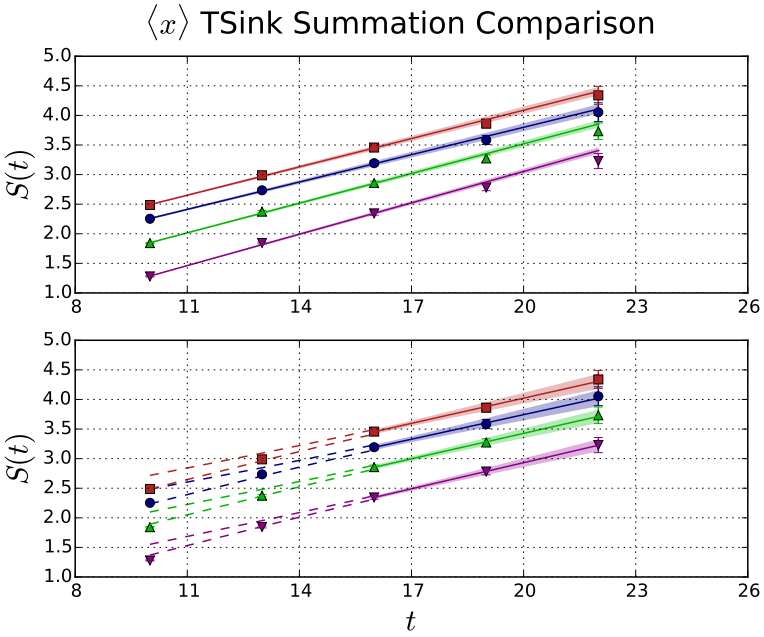

Figure 7.28: Summed ratio factor values for multiple source-sink times defined in Eq.(6.18) used to extract $\langle x \rangle$.

Now the summation method fit undertaken in the top of Figure 7.28 for $\langle x \rangle$ does show a variation on the δt parameter that is statistically significant. We can see for $\langle x \rangle$ the linear fit function is not sufficient to approximate the summed R function values. Again, fitting over larger source-sink separated points in the bottom of Figure 7.28 and projecting the errors to smaller times shows that there is an inconsistency as the smaller source-sink separated result do not lie within the fit errors projected to smaller times. This tells us that the two-state approximation used in the summation method has broken down.

The top plot of Figure 7.29 in which we have summed the ratio function to determine g_T, the summation fits show no statistically significant change in slope for the different δt value results and the line of best fit seems to satisfy the points well to extract a value. For g_T in the bottom plot in Figure 7.29, we have excluded the two smallest source-sink separated points from the linear fit and we see that the projected errors do encapsulate the smaller source-sink separated results. We can also see that the errors on the results increase when compared to the top figure.

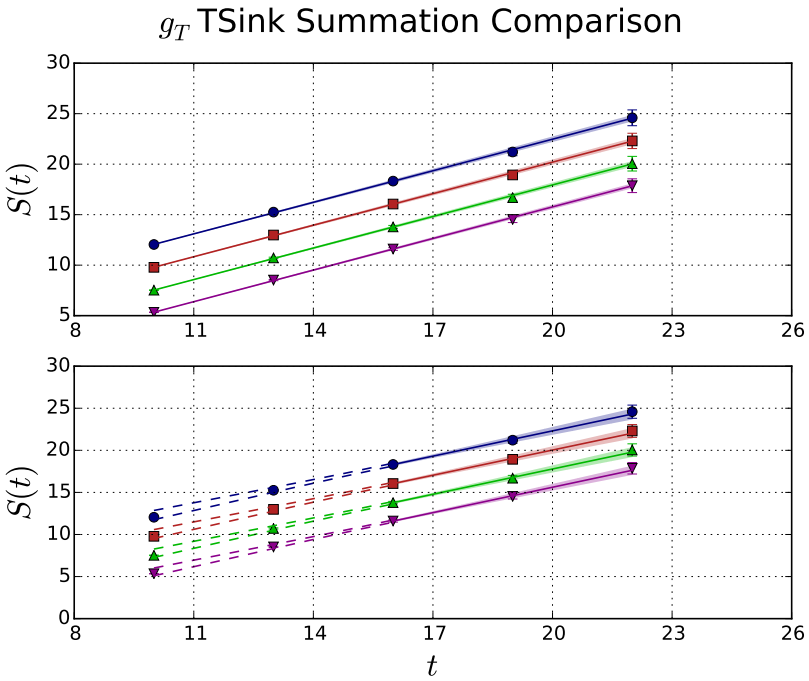

Figure 7.29: Summed ratio factor values for multiple source-sink times defined in Eq.(6.18) used to extract g_T.

7.5.2 Comparing Summation Method to the Correlators

Once the slope of the summed ratio function has been extracted, we can show a comparison between the extracted value and the different ratio functions at source-sink separated points $t = 10, 13, 16, 19$ and 22 at 32 sweeps of smearing (which was used in the summation method fit). For the demonstration, we have selected a summation exclusion parameter $\delta t = 3$ as it is the least susceptible to the effect arising from the problematic boundary of $\tau = t$ and $\tau = 0$. The summation value results for g_A, g_S, $\langle x \rangle$ and g_T used in this section correspond to the purple line in the top graph of Figures 7.26, 7.27, 7.28 and 7.29 respectively.

The extracted summation method result for both g_A and g_S compared to their respective source sink separated results in Figures 7.30 and 7.31 produces results comparable to the largest source-sink separated result, but with less statistical uncertainty.

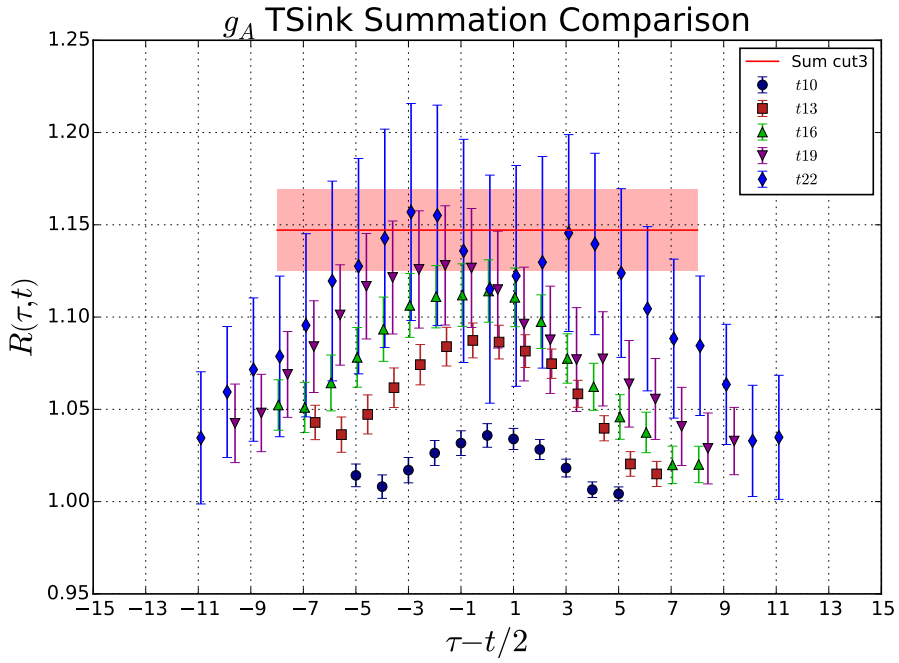

Figure 7.30: Graph for g_A extracted from the R function defined in Eq.(3.68) for different source-sink separated results compared to a summation method result. For all subsequent graphs in this section, the ratio function is plotted for a fixed smearing of 32 sweeps along side a single summation result of $\delta t = 3$ fitting over all the source-sink separated results.

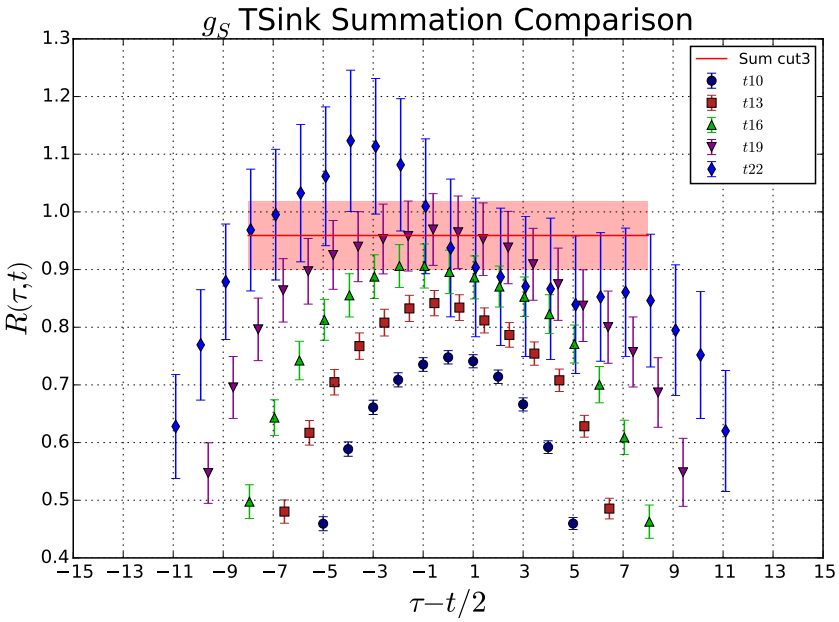

Figure 7.31: Graph for g_S extracted from the R function defined in Eq.(3.68) for different source-sink separated results compared to a summation method result.

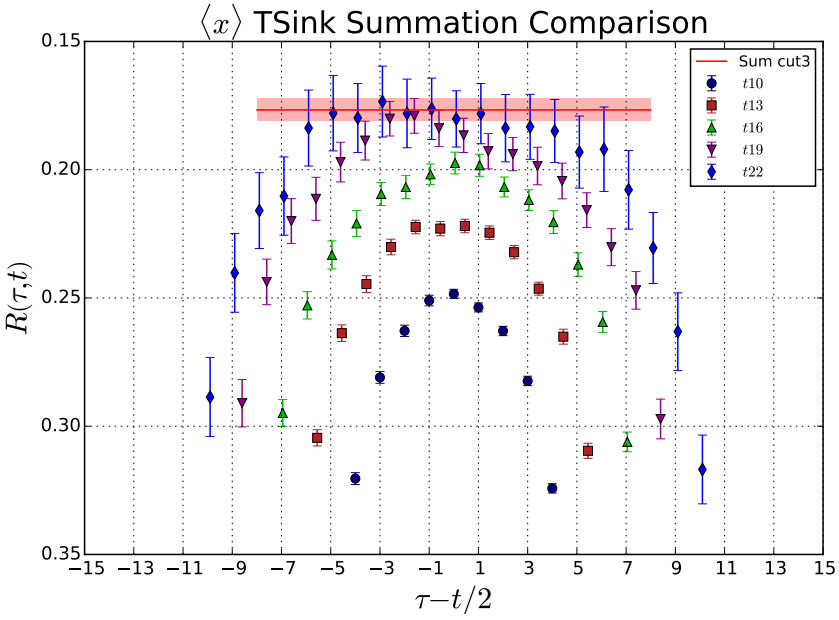

Figure 7.32: Graph for $\langle x \rangle$ extracted from the R function defined in Eq.(3.68) for different source-sink separated results compared to a summation method result.

The summation value extracted for $\langle x \rangle$ compared to the source sink separated results in Figure 7.31, gives a bold claim of a value which is comparable to the largest source-sink separated result, but with greatly reduced uncertainty. Refer to the previous section for a discussion on the validity of the extraction method and the effects of including insufficient source-sink separated results at $t = 10, 13$.

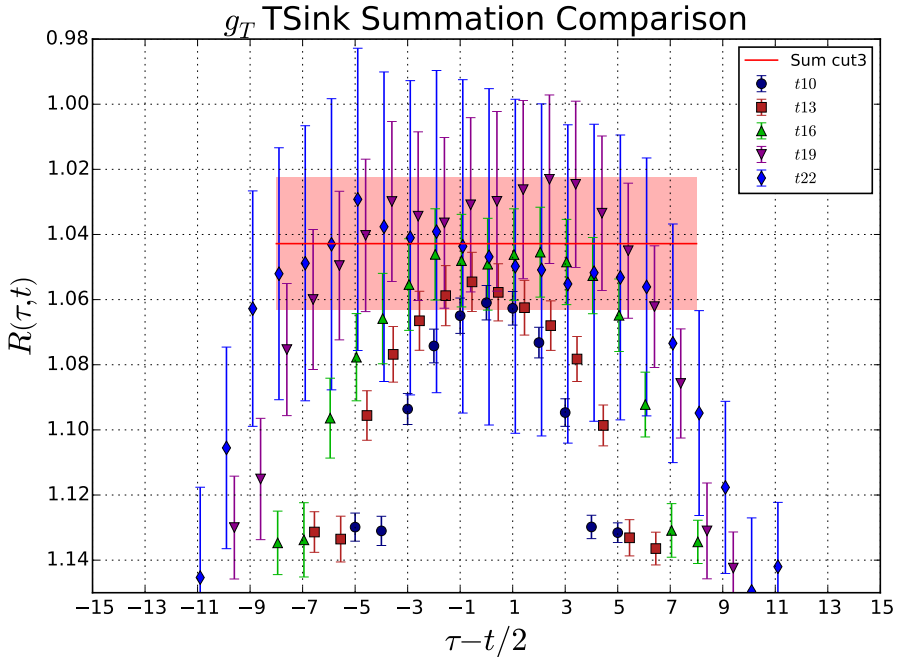

Figure 7.33: Graph for g_T extracted from the R function defined in Eq.(3.68) for different source-sink separated results compared to a summation method result.

We compare an extracted summation method result for g_T to the source sink separated results in Figure 7.33. We start to see a peculiarity in the excited-state contamination as increasing the source-sink separation seems to have minimal improvement. Along with Figure 7.9, we might need to start distinguishing the difference between the transition matrix element contamination and excited- to excited-state contamination and how smearing the interpolating fields effects these quantities.

7.5.3 One-Exponential Comparison

As we did with the variational method comparison in Section 7.4.2, we apply the one-exponential fit equation to the two- and three-point correlation functions, but now over the different source-sink separations $t = 10, 13, 16, 19, 22$ for a fixed

smearing of 32 sweeps (as described above). Again, we utilise the *one-exponential fit* ratio discussed in Section 6.2

$$R_{OSF}(\Gamma;\vec{0},t;\vec{0},\tau;O^{(q)}) \equiv \frac{G_3(\Gamma;\vec{0},t;\vec{0},\tau;O^{(q)})}{A_{m^{[0]}}e^{-m^{[0]}t}}, \tag{6.16}$$

where, $m^{[0]}$ and $A_{m^{[0]}}$ are fit parameters from fitting to the two-point correlation function. The aim of this section is to see if there is any slight deviations of the ratio functions and the extracted values from the normal ratio function demonstrated in the previous section.

All four Figures 7.34, 7.35, 7.36 and 7.37 show the one-exponential fit results over the same smearing results as in Figure 7.30. We see slight shifts when comparing the one-exponential figures in this section with the ratio function values in the previous section. The shifting effect for the smallest source-sink separation is showing a large deviation from the ratio function in all four cases, which might be due to excited-states affecting the two-point correlation function at the small source-sink separation.

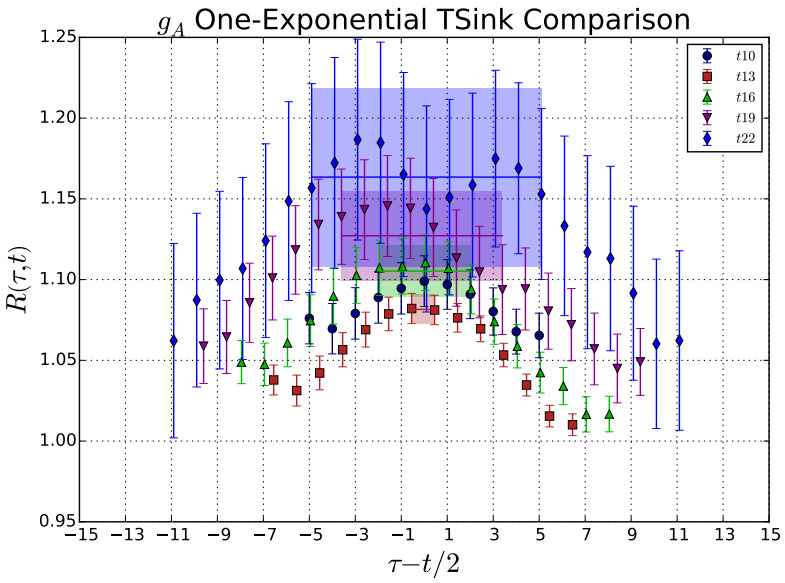

Figure 7.34: Graph for g_A over different source-sink separated results, utilising the one-exponential fit construction defined in Eq.(6.16) along with a one-exponential fit calculation on each set. For all subsequent graphs in this section, the lines and shaded areas corresponds to g_A value extracted from the fit parameters and all results are calculated at 32 sweeps of smearing.

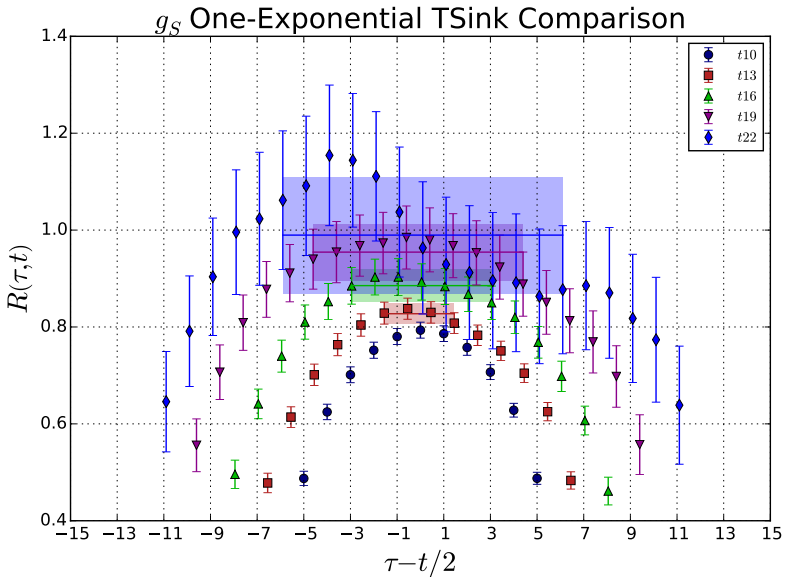

Figure 7.35: Graph for g_S over different source-sink separated results, utilising the one-exponential fit construction defined in Eq.(6.16) along with a one-exponential fit calculation on each set.

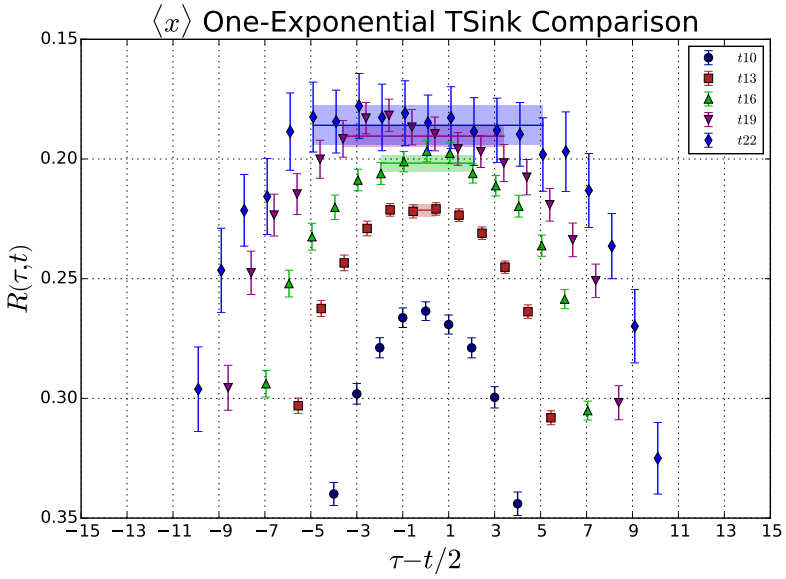

Figure 7.36: Graph for $\langle x \rangle$ over different source-sink separated results, utilising the one-exponential fit construction defined in Eq.(6.16) along with a one-exponential fit calculation on each set.

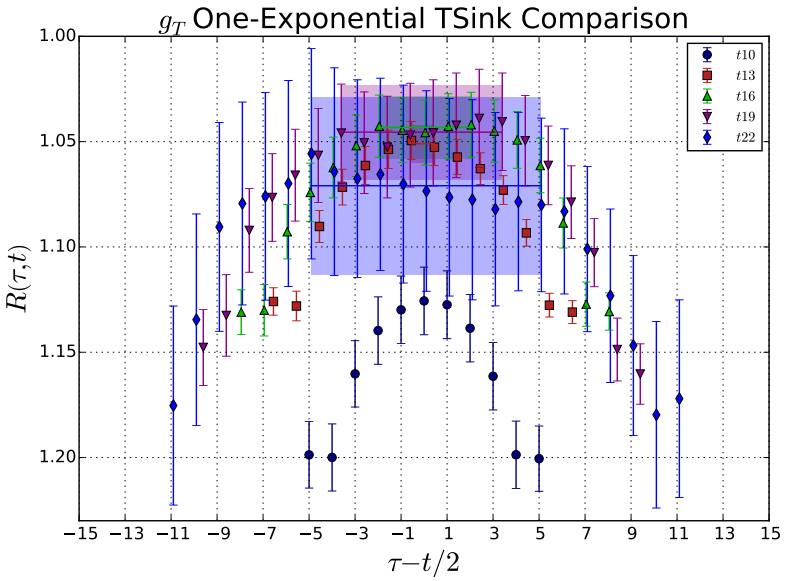

Figure 7.37: Graph for g_T over different source-sink separated results, utilising the one-exponential fit construction defined in Eq.(6.16) along with a one-exponential fit calculation on each set.

7.5.4 Two-Exponential Comparison

Here we present, what is considered the current "standard" technique to remove excited-state contamination. Although the two-exponential fit was applied to the single source-sink separation for varying smearing in Section 7.4.4, the intended way for the two-exponential fit to be applied is through the use of multiple source-sink separated three-point correlation functions. The benefit of this approach is that a single two-exponential fit function is fitted to both the source-sink separation t and the current insertion time τ to extract the three fit parameters B_{00}, B_{10} and B_{11}. The fit function is

$$G_3(\Gamma;\vec{0},t;\vec{q},\tau;O^{(q)}) = A_{m^{[0]}}e^{-m^{[0]}t}\times \left\{B_{00} + B_{10}\left(e^{-\Delta m^{[0,1]}\tau} + e^{-\Delta m^{[0,1]}(t-\tau)}\right) + B_{11}e^{-\Delta m^{[0,1]}t}\right\}, \tag{6.13}$$

and once again, for visualisation purposes, we plot the two-exponential ratio function

$$R_{TSF}(\Gamma;\vec{0},t;\vec{0},\tau;O^{(q)}) \equiv \frac{G_3(\Gamma;\vec{0},t;\vec{0},\tau;O^{(q)})}{A_{m^{[0]}}e^{-m^{[0]}t} + A_{m^{[1]}}e^{-(m^{[0]}+\Delta m^{[0,1]})t}}, \tag{6.17}$$

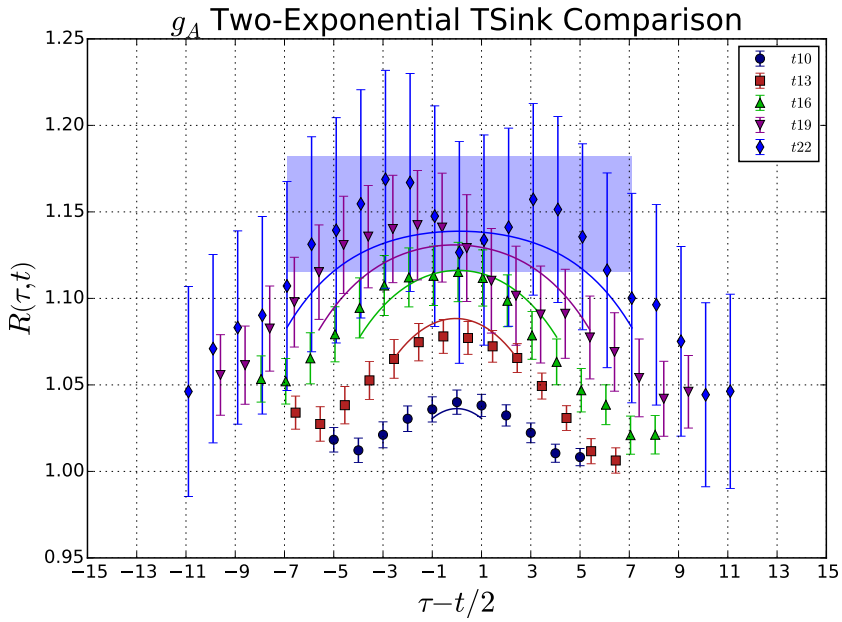

Figure 7.38: Graph for g_A utilising the two-exponential fit ratio (Eq.(6.17)), overlaid with a two-exponential fit over both current and sink times (Eq.(6.13)). For all the graphs in this section, the lines correspond to the two-exponential fit function constructed and the blue shaded area corresponds to the g_A parameter extracted from the two-exponential fit. All results are calculated with 32 multiples of smearing at the source and sink.

where the numerator consists of parameters extracted from the two-point correlator.

For g_A, doing a combined fit to all the source-sink separated data as in Figure 7.38 leads to a result that is very similar to a constant fit for the largest source-sink separated result. Similar to the summation method, the two-exponential method is heavily weighted by the smallest source-sink separated values which can be problematic as these values are most susceptible to excited-state contamination. To ensure that the extracted results are free from such contamination, we repeat the fit excluding $t = 10, 13$ results, which are included in the summary Figure 7.42. Comparing a two-exponential fit to all the data to the exclusion of $t = 10, 13$, we find consistency in uncertainties when the smallest fit range (corresponding to a cut parameter $\delta t = 5$) is implemented, but some increase in uncertainties for the smaller $\delta = 3, 4$, which is also replicated for the following calculations of g_S, $\langle x \rangle$ and g_T.

The two-exponential fit to g_S in Figure 7.39 again raises a lot of concern over the inclusion of small source-sink separations into the fit. Since the fit is weighted

heavily to the smaller source-sink separated results, due to their statistical error the larger source-sink separated results are almost ignored.

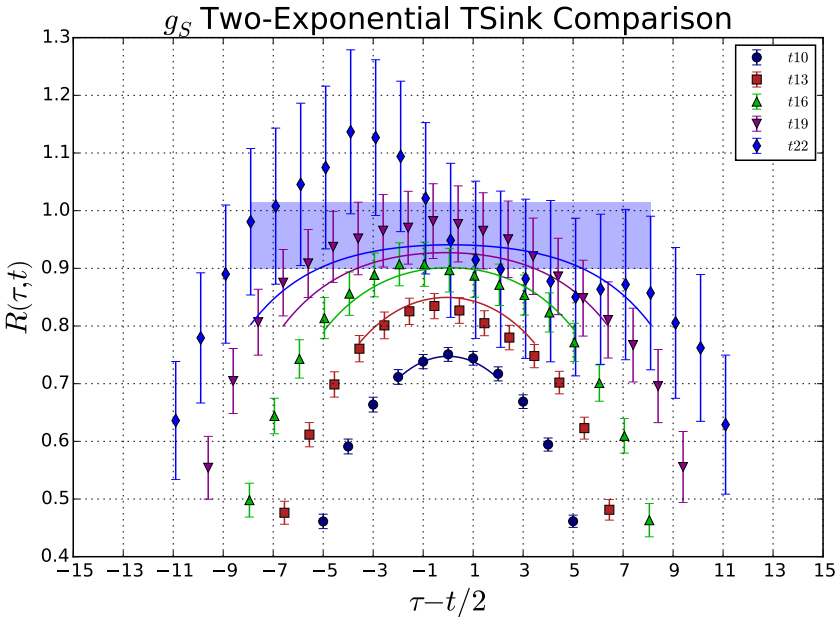

Figure 7.39: Graph for g_S utilising the two-exponential fit ratio (Eq.(6.17)), overlaid with a two-exponential fit over both current and sink times (Eq.(6.13)).

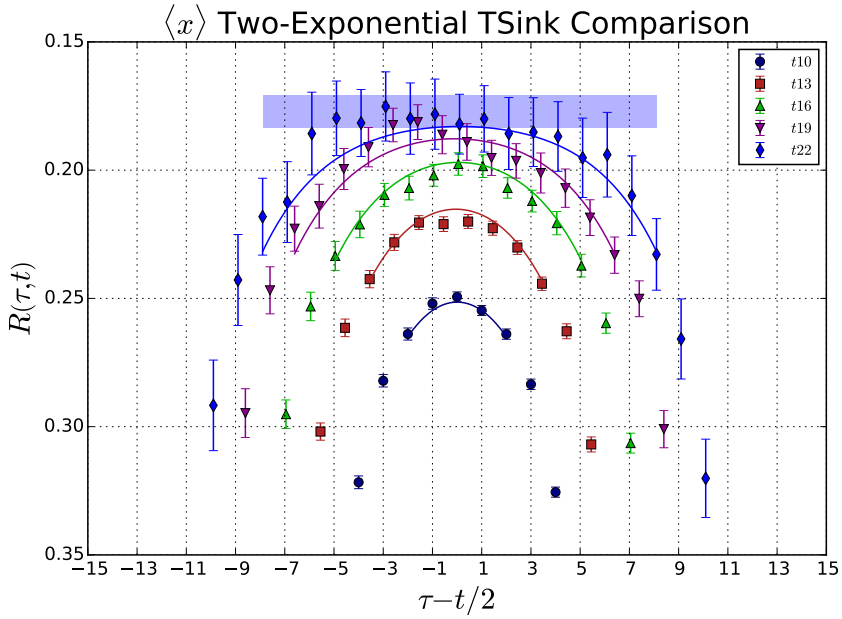

Figure 7.40: Graph for $\langle x \rangle$ utilising the two-exponential fit ratio (Eq.(6.17)), overlaid with a two-exponential fit over both current and sink times (Eq.(6.13)).

The two-exponential fit to all five source-sink time separations for $\langle x \rangle$ in Figure 7.40 has been more successful relative to the previous two quantities. We see the fit function being approximated appropriately for all current time and source-sink data sets. But as discussed in the summation method, we must be sure that the two-state approximation is satisfied, especially as the excited-state contamination is so large for $\langle x \rangle$.

The two-exponential fit to all five source-sink time separations for g_T in Figure 7.41 produced a result which is comparable to the four largest source-sink separated fitted results. We see the fit function being approximated appropriately for all current time and source-sink data sets.

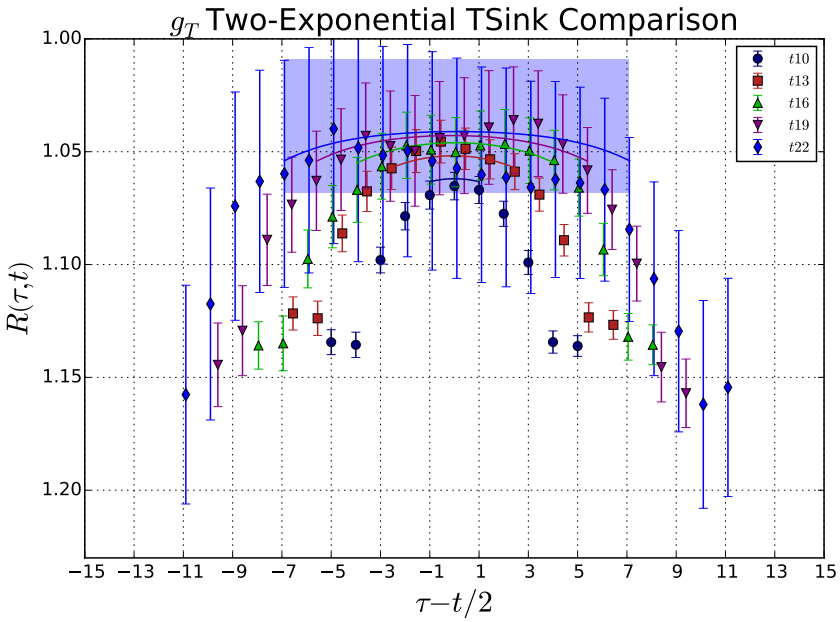

Figure 7.41: Graph for g_T utilising the two-exponential fit ratio (Eq.(6.17)), overlaid with a two-exponential fit over both current and sink times (Eq.(6.13)).

7.6 Summary

Here we display summary plots, which summarise every value that has been extracted from all the methods in the previous sections for the quantities g_A, g_S, $\langle x \rangle$ and g_T. We define the labels in the x-axis of all the following summary graphs in this section in Table 7.2.

Key	Description	More Information
Fits	Plateau fit to the data	Section 6.2
sm##	## sweeps of smearing results	Section 5.1
t#	source-sink separation of #	Section 3.4.2
Var/CM	correlation matrix method, or variational method result	Section 5.2
t_0#δt#	variational method eigenvalue solver parameters	Eq.(5.15)
PoF	pencil of function method result	Section 5.2.2
1SF	one-exponential fit method result	Eq.(6.12)
2SF	two-exponential fit method result	Eq.(6.13)
All	using all source-sink separated results $t = 10, \ldots, 22$	
Lrg	using large source-sink separated results $t = 16, 19, 22$	
Sml	using small source-sink separated results $t = 10, 13$	
fr2	summed ratio function ignoring $t = 10, 13$ results	Section 6.3

Table 7.2: Table explaining all the labels used in the summary plots Figures 7.42, 7.43, 7.44 and 7.45.

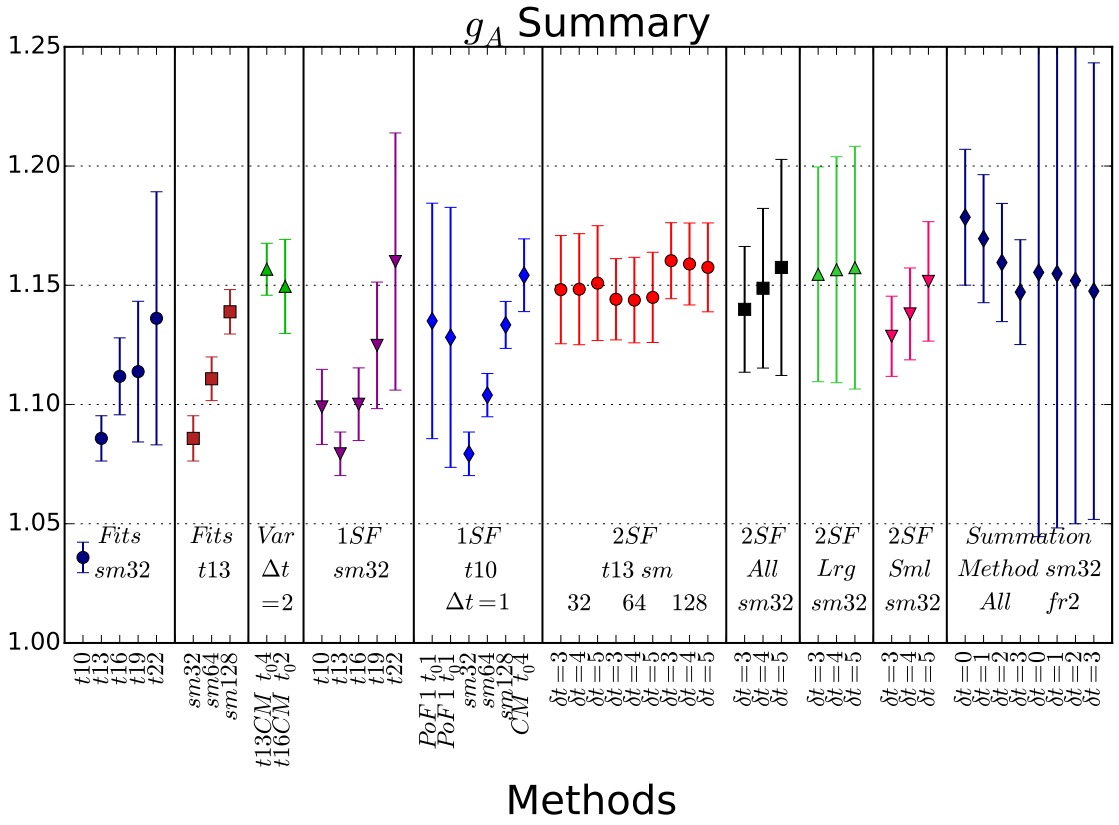

Figure 7.42: Summary of all the extracted values for g_A over the different methods. See Table 7.2 for information on labels.

In the final summary plot for g_A containing all the extracted values from all the different methods calculated (Figure 7.42), we see that the variational method demonstrates reliability and robustness as it produces a value that improves on the results that alter the smearing amounts and small source-sink separated results by removing excited-states. The variational method also improves on the summation and two-exponential fit method by producing a much more precise result. We note that there is no noticeable difference between the "Fits" and "Var" results compared with the "1SF" results (barring the $t = 10$ result).

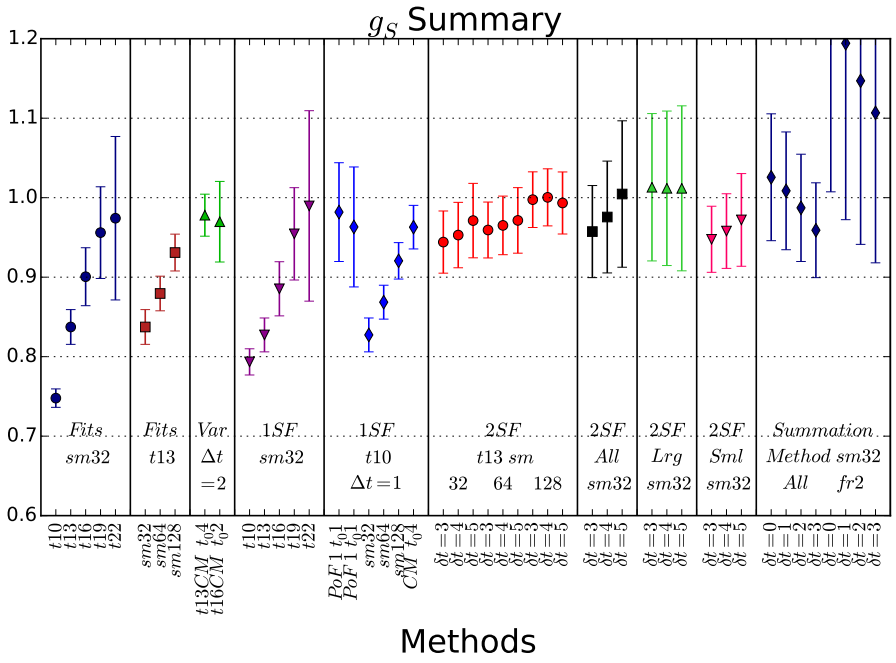

Figure 7.43: Summary of all the extracted values for g_S over the different methods. See Table 7.2 for information on labels.

Similarly for the summary for g_A, g_S in summary (Figure 7.43) shows that the variational method has sufficiently suppressed the excited-states and provides far more precise results compared to the summation and two-exponential fit methods. In addition, while not statistically significant, we observe an undesired δt dependence for each of the summation method results. We also observe no difference between the "Fits" and "Var" results compared with the "1SF" results (barring the $t = 10$ result) which indicates that the extraction of g_S is not sensitive to the fitting the two-point correlation function.

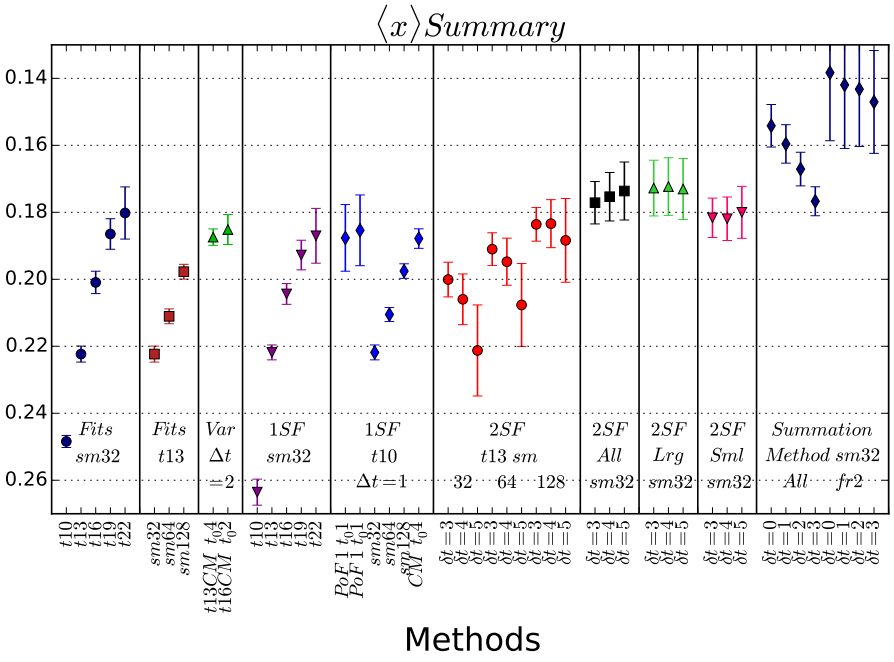

Figure 7.44: Summary of all the extracted values for $\langle x \rangle$ over the different methods. See Table 7.2 for information on labels.

In summary for $\langle x \rangle$ (Figure 7.44) we see that the amount of excited-state contamination removed by the variational method is at the point where the statistical precision has become a larger factor. This puts into question the validity of the summation method and the two-exponential fit results as they show a large disagreement to the variational method. This could be due to insufficient source-sink separated values skewing the results as is indicated by the summation method having a δt dependence when it should not. The larger uncertainties due to using very large source-sink separated results could also contribute to the disagreement. Once again, there is undetectable sensitivity of the fitting method as "Fits" and "Var" is indistinguishable to "1SF" over $t > 10$.

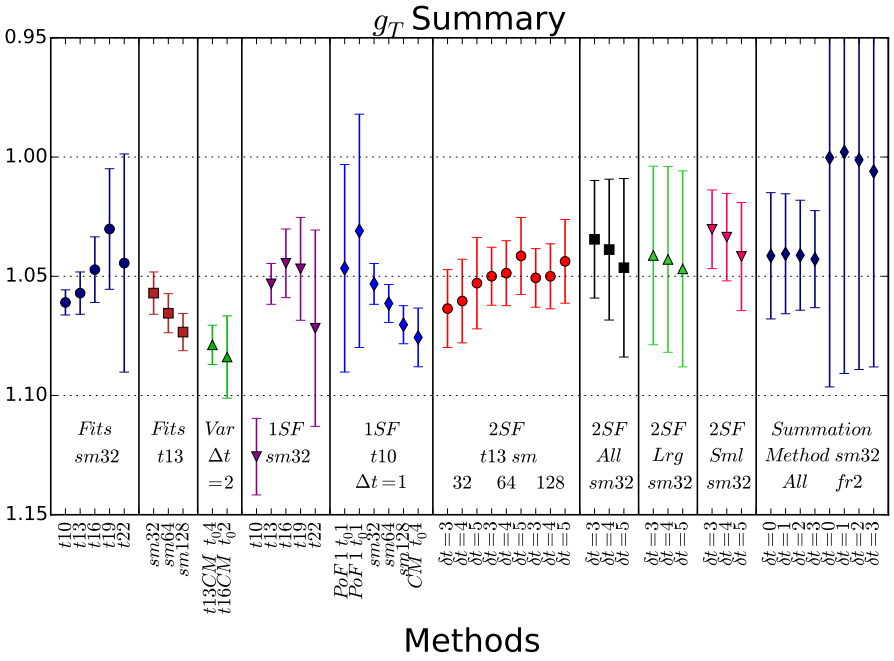

Figure 7.45: Summary of all the extracted values for g_T over the different methods. See Table 7.2 for information on labels.

As we had for $\langle x \rangle$ in Figure 7.44, the summary for g_T (Figure 7.45) shows that the amount of excited-state contamination removed by the variational method is at the point where the statistical precision has become a larger factor. Once again, this puts into question the validity of the summation method and the two-exponential fit results as they show a disagreement to the variational method. This time, we cannot attribute this effect to insufficient source-sink separated values skewing the results as past the source-sink separation $t > 10$, we have statistical agreement. My speculation would be that the transitional excited state contaminants are different in sign or in magnitude to the excited- to excited-state contaminants in the three-point correlation function.

The summary plots in this section for g_A, g_S, $\langle x \rangle$ and g_T are tabulated in Appendix C.1. In the following we summarise our findings.

7.6.1 Summation Results

In Figures 7.38, 7.39, 7.40, we observe that the summation method looks as if it is improving the result. However, when looking at g_S and R for $\langle x \rangle$ extracted values in their respective summary plots (Figures 7.43, 7.44) we can see a dependence in the δt value when, if our two-state ansatz were satisfied, it should have no or minimal effect.

This is seen more clearly when considering summation fits excluding smaller source sink separations (g_A in Figure 7.26, g_S in Figure 7.27 and $\langle x \rangle$ in Figure 7.28). When we exclude the smaller source-sink separated results, we can see that the two-state ansatz is breaking down for g_S and $\langle x \rangle$ as the data points do not lie within the errors projected to earlier source-sink separated time values.

7.6.2 One-Exponential Fit Results

The one-exponential fit discrepancies can be best distinguished from the regular plateau fit method by analysing the summary figures Figures 7.42, 7.43, 7.44 and 7.45. A large discrepancy between the one-exponential fit and the plateau fit for the smallest source-sink separation $t = 10$ (32 sweeps of smearing) arises in all four quantities calculated. This can be accredited to the two-point correlation function at $t = 10$ still being effected by excited-state contamination effects.

The only other slight discrepancy that was observable was at the largest source-sink separation $t = 22$, in which a non-statistically significant shift was observed in all four quantities calculated. This may be attributed to the large source-sink separation causing statistical fluctuation in the two-point correlation function at $t = 22$. The one-exponential fit method result at $t = 22$ is a value extracted from a fit using more constrained earlier source-sink separated results, which may have the effect of "averaging" over the fluctuations at larger t.

7.6.3 Two-Exponential Fit Results

The "Two Exponential Variational Comparison" plots seem to show minimal improvement for g_A in Figure 7.18 and g_T in Figure 7.18, some improvements for g_S (Figure 7.19) and the most improvement for $\langle x \rangle$ (Figure 7.20). Poor determination would be attributed to not being able to distinguish excited-state contamination from our error within a fit range in which a two-state ansatz is justified. These results give a good demonstration of using fitting functions to remove transitional matrix elements. In all cases, the smaller smeared results (with larger excited-state contamination) extract a value closer to the larger smeared results. From the summary plots (Figures 7.42, 7.43, 7.44, 7.45), we see minimal effect on the δt fit parameter for the two-exponential fit method.

Extending to the full source-sink separated set of results in "Two Exponential Fit Comparison" for 32 sweeps of smearing (Figures 7.38, 7.39, 7.40, 7.41), we see that the fit is weighted predominately by the smallest source-sink separations. Furthermore, we see how poorly the larger source-sink separated results are in terms of symmetry about the middle current insertion time, as well as deformations to the expected curved fit lines. Although using the two-exponential fit method controls the excited-states better than using a single source-sink separation, we

found there was no improvement to a constant fit over the largest source-sink separation for g_A, g_S and g_T and a questionable improvement for $\langle x \rangle$.

7.6.4 Variational Results

Beginning with the effective mass plots in Figure 7.1 where the effective masses for the three different smearing results were compared to the variational method, the variational method allows us to extract the mass from the two-point correlator beginning from an earlier time slice compared to the individually smeared results. The improvement is due to the excited-states being suppressed when constructing the optimal correlator in Eq.5.14.

In Figures 7.6, 7.7, 7.8, 7.9 we compare the ratio functions (Eq.3.68) for the three different smearing results to the variational method in which the functions are varied over the current insertion time τ for a fixed source-sink separation $t = 13$. The figures show how applying the variational method improves the suppression of excited-state contamination. The ability to fit a plateau over a much larger current insertion time τ shows how the transition matrix elements are being sufficiently suppressed compared to the individually smeared results. The shift in each of the ratio values for each particular τ shows how the variational method is suppressing all types of excited-state contamination ("transition" and "excited to excited-state" matrix elements).

The final collection of graphs "TSink Variational Comparison" (Figures 7.14, 7.15, 7.16, 7.17) compares the variational method to the 32 sweeps of smearing results over the current insertion times τ and the source-sink separation of 13 and 16. All four quantities calculated with the variational method show no statistically significant difference between the two source-sink separations. This shows us that choosing a source-sink separation of 16 for the variational method gives us a result where the residual excited-state contamination is smaller than the statistical error. Besides the curious case of the tensor charge g_T, a much larger source-sink separation in the 32 sweeps of smearing case is needed to remove the remaining excited-state contamination.

7.6.5 Pencil of Function Results

Although only a proof of concept at this state, the pencil of function shown in "Pencil of Function Comparison" being compared to the variational method and 32 sweeps of smearing result demonstrated potential as, within statistical uncertainty, there is zero excited-state contamination with respect to current insertion time τ for all charges calculated.

There is a possibility that the gauge field correlations have been lost due to the "time trick" defined in Eq.(5.27), which is the cause of such high uncertainties

Create	Standard	2exp & SM (over n_t)	CM (over n_{basis})	PoF
C_2	1	1	n_{basis}	n_{basis}
C_3	4	$4n_t$	$4n_{basis}$	$(n_t+1)4n_{basis}$
Total	5	$1+4n_t$	$5n_{basis}$	$(4n_t+5)n_{basis}$
This Thesis	5	21	15	39

Table 7.3: Comparative computational times for each method for two-point and three-point correlators as well as the total. n_t is the number or source-sink time separations used, n_{basis} is the number of basis interpolating fields used.

relative to all the other methods. A discussion of this is shown in Appendix A.3.

7.7 Cost Benefit Analysis

One run of calculations was undertaken to produce all the data for Sections 7 and 8, so in this section, we discuss the computational costs associated with each method of calculation. Assuming we have an equal number of gauge fields for our particular κ value (or pion mass), we can model the efficiency as to how many inversions we undertake per gauge field. One inversion is required for calculating the two-point correlator, then a second inversion is required for each specific three-point correlator we want to calculate. The fixed sink method requires that we choose a sink time, sink momentum, spin projector and which quark the current acts on for a fixed hadron before the three-point correlator is calculated (Table 3.1).

The variational method requires n_{basis} inversions to create the two-point correlators, where n_{basis} is the number of basis interpolating fields used (e.g. 3 smearings for this work). Then a further n_{basis} is required to create a particular fixed sink resulting correlator as shown in Section 5.2.3.

The two-exponential fit and summation methods are identical to the standard way, but creating n_t multiples of the three-point correlator, where n_t is the number or source-sink time separations.

Lastly the pencil of function method requires the same basis of two-point correlators to be calculated as the variational method, due to the time translation being readily available. The three-point correlation function requires a calculation for two source-sink separated values t and $t+\delta$, but increasing the sink to $t+\delta$ and $t+2\delta$ we notice the same result $t+\delta$ can be utilised in both calculations (also indicated in Section 5.2.3). This results in $(n_t+1)n_{basis}$ inversion per gauge field for the three-point correlator.

For this analysis, simulations were performed with zero sink momentum and two different spin projectors for both up and down quark contributions to the proton. This results in four times the number of inversions for each three-point

correlator required. The inversion numbers are outlined in Table 7.3.

Chapter 8

Form Factor Results

In this chapter, we move onwards from calculating charges at zero transfer momentum to extracting form factors at finite Q^2. The lattice data and parameters used to extract the form factors are the same as described in Section 7.1.

Since form factors are more difficult to extract from the data due to the non-zero momenta $\vec{p}$ at the source, we focus on the key sets of calculations from the "plateau" fit method as well as the one- and two-exponential fit methods. We omit the pencil of function due to the large statistical uncertainty and the summation method due to the problems outlined in the previous Chapter 7. The full list can be found in Table 8.1 and the formalism as to how the form factors are extracted from the lattice data is described in Chapter 6.4.

Note that each individual method in the following figures have had their Q^2 slightly shifted to help distinguish different methods with similar extracted values.

Method	Sets	Cut Range
Fit	$t = 13$ sm32	$\delta t = 5$
1SF	$t = 13$ sm32	$\delta t = 5$
Fit	$t = 13$ variational method $t_0 = 4$, $\Delta_v t = 2$	$\delta t = 5$
1SF	$t = 13$ variational method $t_0 = 4$, $\Delta_v t = 2$	$\delta t = 5$
2SF	$t = 10, 13, 16, 19, 22$ sm32	$\delta t = 4$

Table 8.1: Table showing the specific calculations and extraction methods used for all the form factor plots.

8.1 Vector Form Factors

The vector form factor is defined as

$$\left\langle \vec{p}' \middle| J^{\mu}(\vec{q}) \middle| \vec{p} \right\rangle = \overline{u}(\vec{p}') \left[\gamma_{\mu} F_1(Q^2) + \frac{i\sigma^{\mu\nu} q_{\nu}}{m_N} F_2(Q^2) \right] u(\vec{p}), \tag{2.16}$$

where $F_1(Q^2)$ and $F_2(Q^2)$ are the Dirac and Pauli form factors at momentum transfer Q^2. To access these form factors on the lattice, we look at all operators of the form

$$O^{(q)} = q_u O^{(u)} + q_d O^{(d)} = q_u \overline{u} \gamma_{\mu} u + q_d \overline{d} \gamma_{\mu} d, \tag{8.1}$$

with q_q being the total charge contribution from quark(s) q in the proton or neutron. This implies that the form factors are actually the combination

$$F_i = q_u F_i^{(u)} + q_d F_i^{(d)}, \tag{8.2}$$

with the individual quark contributing form factors $F_i^{(q)}$ being defined in Eq.(6.21). Due to the extra computational cost, which is discussed in Section 3.4.2, we do not consider the disconnected quark loops in this calculation.

In the previous Chapter 7, the calculation of the zero-momentum values utilising 32 sweeps of smearings at a source-sink separation $t = 13$ demonstrated a substantial excited-state contamination effect. Along with this, we demonstrated that the variational method was an effective method in suppressing excited-state contamination and the two-exponential fit method showing some minimal excited-state suppression. In Figures 8.1 and 8.2, we have shown how suppressing excited-states, which is equivalent to moving from the 32 sweeps of smearing results to the variational method results, affects the determination of the vector form factors F_1 and F_2.

Specifically, the excited-state contamination is larger at larger Q^2 for F_1 in Figure 8.1 but is larger at smaller Q^2 for F_2 in Figure 8.2. The two-exponential fit method attempts to remove some excited-state contamination but resulting in a larger uncertainty. In addition, the lowest Q^2 for F_2 shows the two-exponential fit method disagreeing with the variational method, which may indicate that the two-exponential fit may be insufficient at suppressing excited-state contamination.

As also explored in Chapter 7 for zero-momentum quantities, we can test the sensitivity of the fitting procedure by looking at differences between the plateau and one-exponential fit extraction methods. There seems to be no statistically significant disagreement between plateau and the one-exponential fit results over both F_1 and F_2 from Figures 8.1 and 8.2 over all Q^2 calculated, which would suggest the ratio function R is not being affected by lattice fluctuations over source-sink separations t at all Q^2 shown.

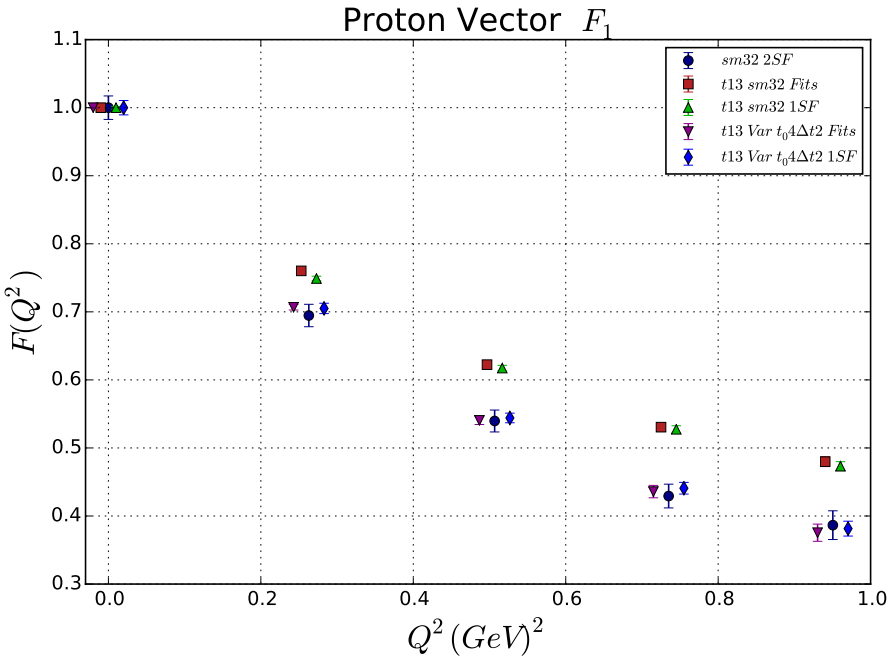

Figure 8.1: First vector form factor F_1 for the proton plotted as a function of the physical transfer momentum Q^2. For all subsequent graphs, the red square and green triangle points are the plateau and one-exponential fit results for the 32 sweeps of smearing result respectively, the blue diamond and purple up-side-down triangle points are the plateau and one-exponential fit results for the variational method respectively and the dark blue circle points are for the two-state fit results using the 32 sweeps of smearing correlators. the points labelled "*1SF*" and "*2SF*" refer to the one-exponential fit and two-exponential fit methods, "*Fits*" refers to using a plateau method and "*Var*" indicates the use of the variational method.

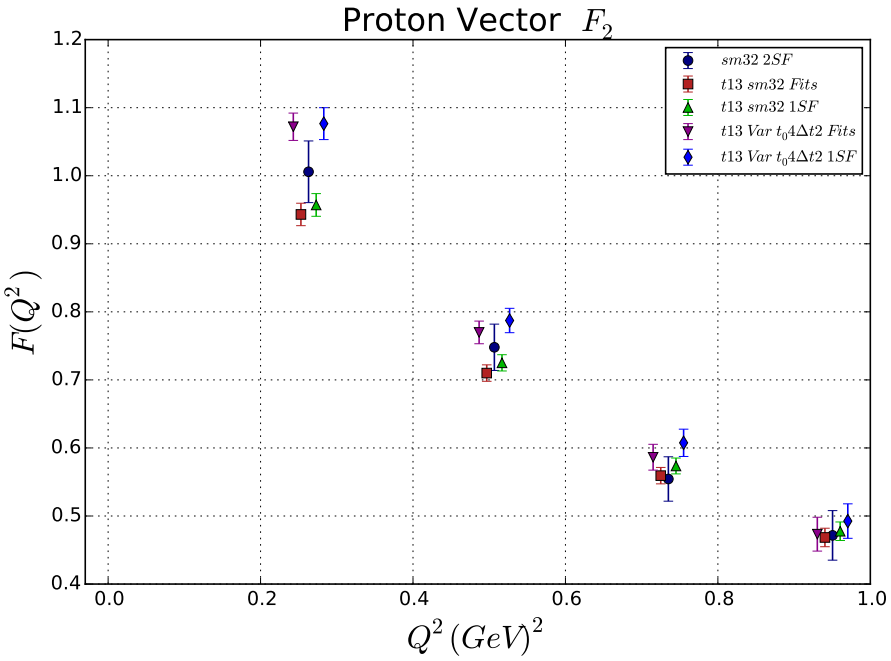

Figure 8.2: Second vector form factor F_2 for the proton plotted as a function of the physical transfer momentum Q^2.

In Figures 8.3 and 8.4 showing F_1 and F_2 for the neutron respectively, we see a similar excited-state effect as we did for the proton in Figures 8.1 and 8.2. This is as to be expected, since both the proton and neutron are constructed as linear combinations of the individual quark contributions to the form factor. As the first form factor F_1 is close to zero, we see much larger relative uncertainties. One peculiarity, in Figure 8.3 is the two-exponential fit method showing a larger deviation away from the 32 sweeps of smearing result compared to the variational method which is primarily observed at the lowest Q^2 values. Again, it is hard to draw any conclusions from this, due to the such small quantities calculated.

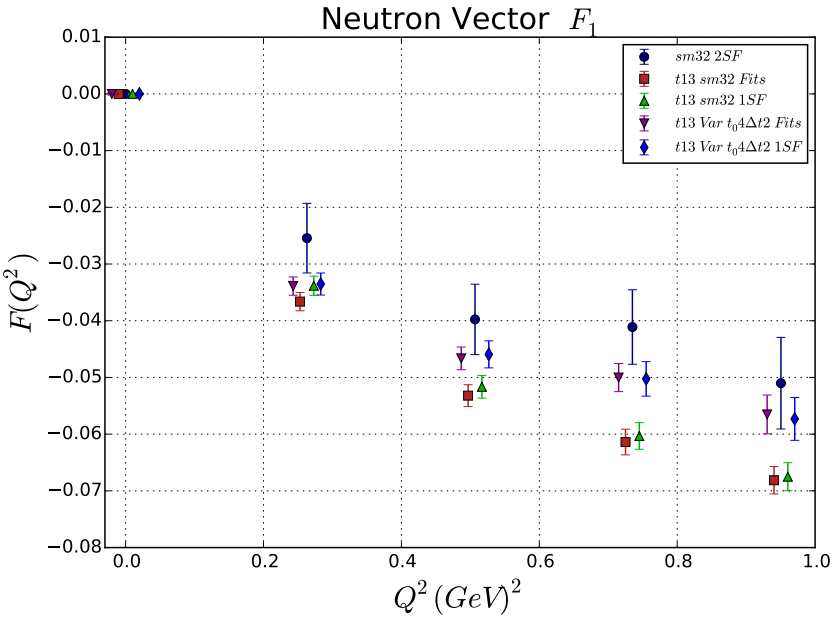

Figure 8.3: First vector form factor F_1 for the neutron plotted as a function of the physical transfer momentum Q^2.

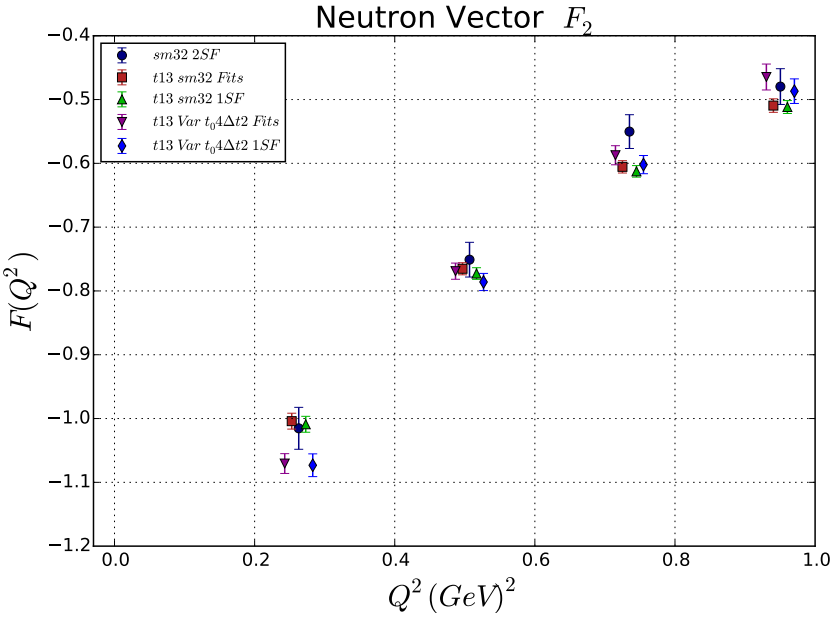

Figure 8.4: Second vector form factor F_2 for the neutron plotted as a function of the physical transfer momentum Q^2.

The Sachs electric and magnetic form factors, which can be constructed by combining F_1 and F_2

$$\begin{aligned} G_E(Q^2) &= F_1(Q^2) + \frac{Q^2}{(2m_N)^2} F_2(Q^2), \\ G_M(Q^2) &= F_1(Q^2) + F_2(Q^2), \end{aligned} \tag{2.18}$$

give us more insights into the structure of the proton and neutron. The charge radius of the nucleon can be calculated by

$$\langle r^2 \rangle \equiv -6 \left. \frac{dG_E(Q^2)}{dQ^2} \right|_{Q^2=0}, \tag{2.19}$$

i.e. The slope of the form factor at $Q^2 = 0$. Along with this, the magnetic moment of the proton or neutron is $\mu = G_M(Q^2 = 0)$.

To obtain both the radius and magnetic moment, we apply a dipole fit of the general form

$$F_i(Q^2) = \frac{F_i(0)}{\left(1 + \frac{Q^2}{m_\tau^2}\right)^2} \tag{8.3}$$

utilising a weighted bootstrap level fit to extract the parameter m_τ. The value for $F_i(0) = G_E(0)$ is set to the charge of the proton (1) or neutron (0) when analysing the Sachs electric form factor, where as the magnetic moment of the proton/neutron $F_i(0) = G_M(0) = \mu$ is considered as a second fit parameter in the dipole fit to the Sachs magnetic form factor.

We demonstrate the excited-state contamination effect in the extraction of G_E for the proton in Figure 8.5, which is almost analogous to F_1 since only low Q^2 has been calculated. Nonetheless, we see the same shift downwards when removing excited-state contamination (which is analogous to moving from 32 sweeps of smearing to the variational method). We can see from the figure that there is clearly a large effect on the slope of G_E at $Q^2 = 0$ when we suppress excited-state contamination effects, which is confirmed by the charge radii shown in Table 8.2. Since the charge radius is such a fundamental quantity, it is crucial that G_E be free from excited-state as it is determined by this mentioned slope.

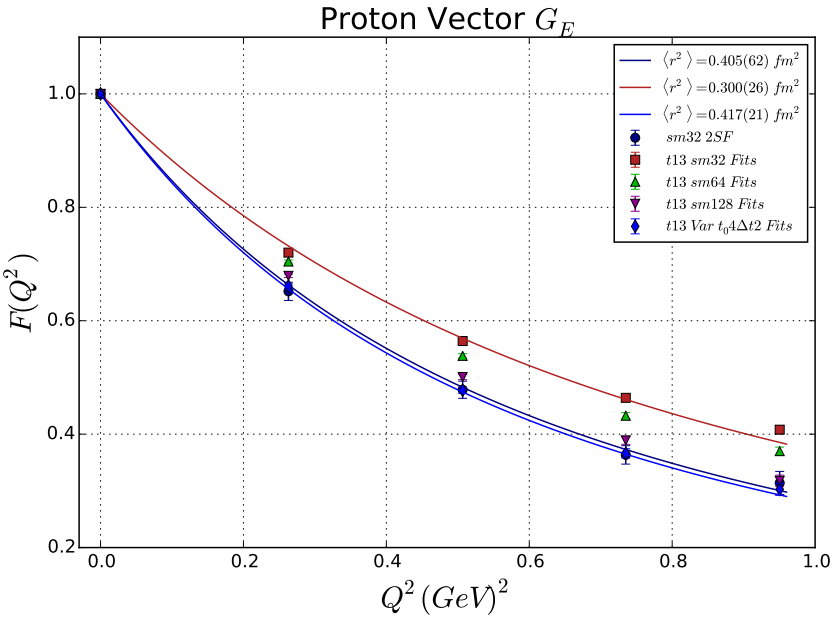

Figure 8.5: Electric Sachs form factor G_E for the proton plotted as a function of the physical transfer momentum Q^2. The coloured lines for the 32 sweeps of smearing, variational method and two-exponential fit method results correspond to dipole fits used to extract a charge radius for the proton $\langle r^2 \rangle$.

The Sachs magnetic form factor G_M, gives us insights into the magnetic field properties (or current distributions) within the nucleon. The excited-state contamination effects demonstrated in Figure 8.6 are just the combination of F_1 and F_2. This produces an interesting "crossing over" effect, where the excited-state suppression increases the value at the lowest Q^2 and decreasing the value at higher Q^2. Overall, this results in a more concentrated magnetic form factor distribution at lower Q^2 when we suppress excited-state contamination. We also see that the magnetic moment μ of the proton, which is extracted by the extrapolation of the dipole fit to $Q^2 = 0$, is very sensitive to excited-state contamination effects. The "crossing over" effect observed in the figure causes the dipole fit to drastically increase when moving from the 32 sweeps of smearing result to the variational method result. The values extracted for the magnetic moment μ as well as the magnetic charge radius $\langle r_M^2 \rangle$ are shown in Table 8.2

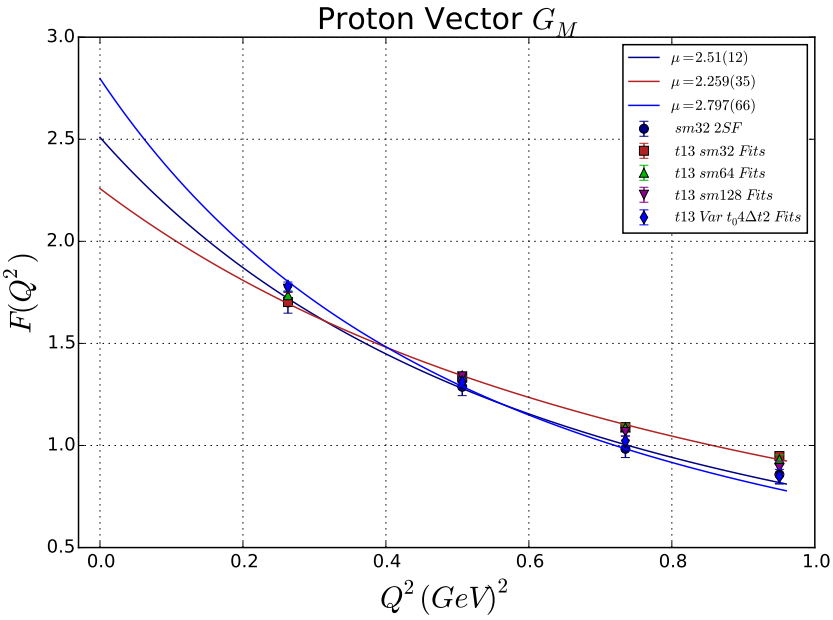

Figure 8.6: Magnetic Sachs form factor G_M for the proton plotted as a function of the physical transfer momentum Q^2. The coloured lines correspond to dipole fits used to extrapolate back to $Q^2 = 0$ to extract the magnetic moment μ for the proton.

The neutron is a difficult quantity to analyse the Sachs electric form factor G_E due to the neutron having no net charge from the constituent quarks and as well the absence of disconnected quark loop contributions. Still, we can attempt to analyse the excited-state effects on G_E for the neutron in Figure 8.7, which shows how a more pronounced curvature for the excited-state suppressed variational method results plotted as a function of the 32 sweeps of smearing result. This feature is important when attempting to compare with phenomenology, where we see a "hump" in the neutron G_E form factor which has a particular amplitude and centre (see [131]).

The neutron Sachs magnetic form factor G_M is expected to have a similar shape and excited-state contamination effect to the proton G_M [131]. We confirm this with the neutron Figure 8.8 in comparison to the proton Figure 8.6 as the variational method results "cross over" the 32 sweeps of smearing results which results in a larger incline. The neutron values for the magnetic moment μ as well as the $\langle r_M^2 \rangle$ are shown in Table 8.2.

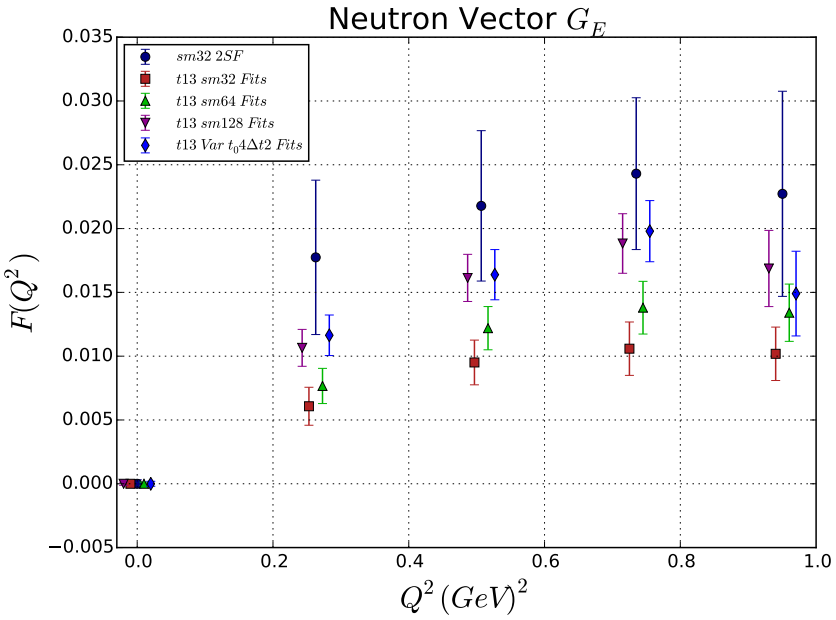

Figure 8.7: Electric Sachs form factor G_E for the neutron plotted as a function of the physical transfer momentum Q^2.

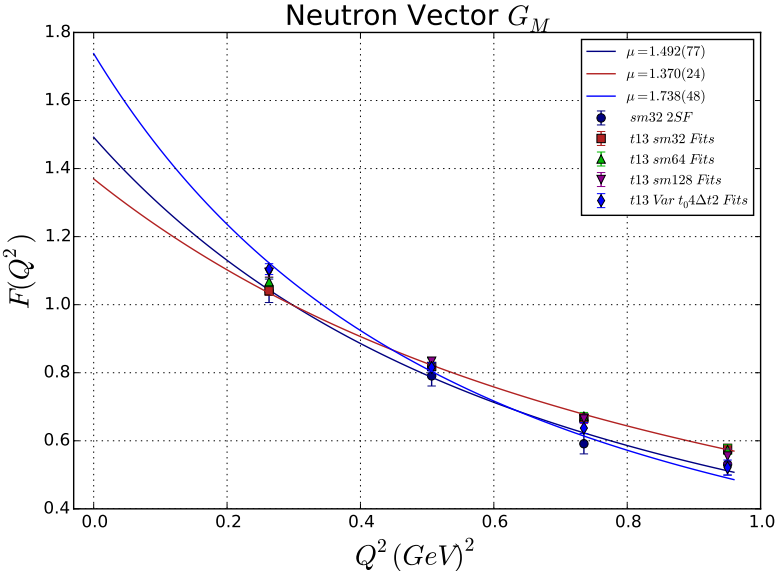

Figure 8.8: Magnetic Sachs form factors G_M for the neutron plotted as a function of the physical transfer momentum Q^2. The coloured lines correspond to dipole fits used to extrapolate back to $Q^2 = 0$ to extract the magnetic moment μ for the neutron.

A common combination studied in the literature is the ratio of the electric to magnetic Sachs form factors G_E/G_M [28]. Although the general interest is in the large Q^2 region to determine if there is a crossing over to negative values, understanding the excited-state contamination effects at lower Q^2 helps us understand the excited-state dependence on Q^2. The ratio G_E/G_M for the proton, in Figure 8.9, displays a substantial effect to excited-state contamination as the 32 sweeps of smearing results are marginally larger than the variational and two-exponential fit results. This indicates to us that the excited-state effects from G_E and G_M are amplified when constructing the ratio, which is something to be mindful for when undergoing precise lattice determination of G_E/G_M for the proton. When looking at the plateau vs one-exponential fit results for the 32 sweeps of smearing results, we start to see a statistically significant difference. This indicates to us that the ratio G_E/G_M for the proton is susceptible to the fitting method used.

The neutron G_E/G_M combination can also be constructed to analyse the excited-state contamination effects. When the comparison is plotted in Figure 8.10, we see a small excited-state contamination effect at low Q^2, but a more pronounced excited-state contamination effect when moving to higher Q^2. This would indicate to us that the removal of excited-states causes the value to increase, as well as the slope at the lowest Q^2 to increase as well.

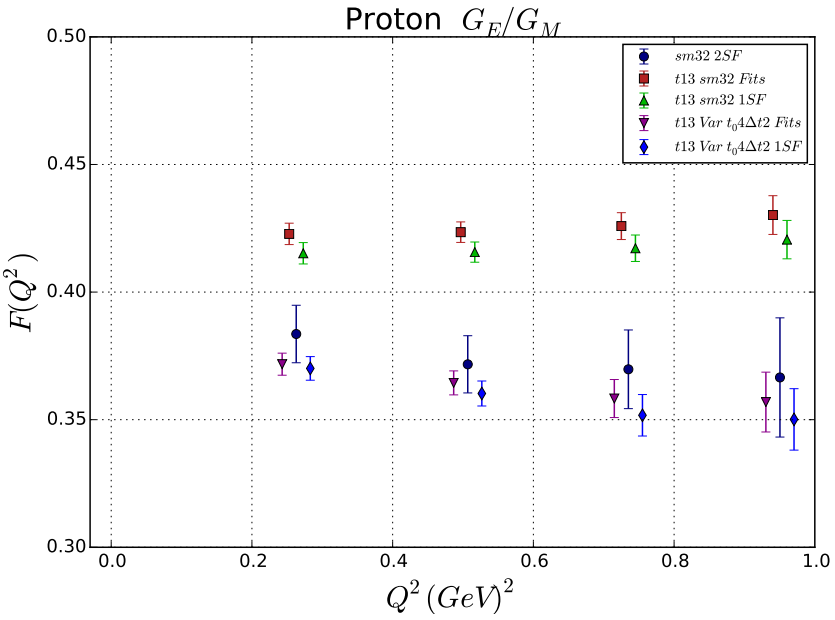

Figure 8.9: Sachs form factor ratio G_E/G_M for the proton plotted as a function of the physical transfer momentum Q^2.

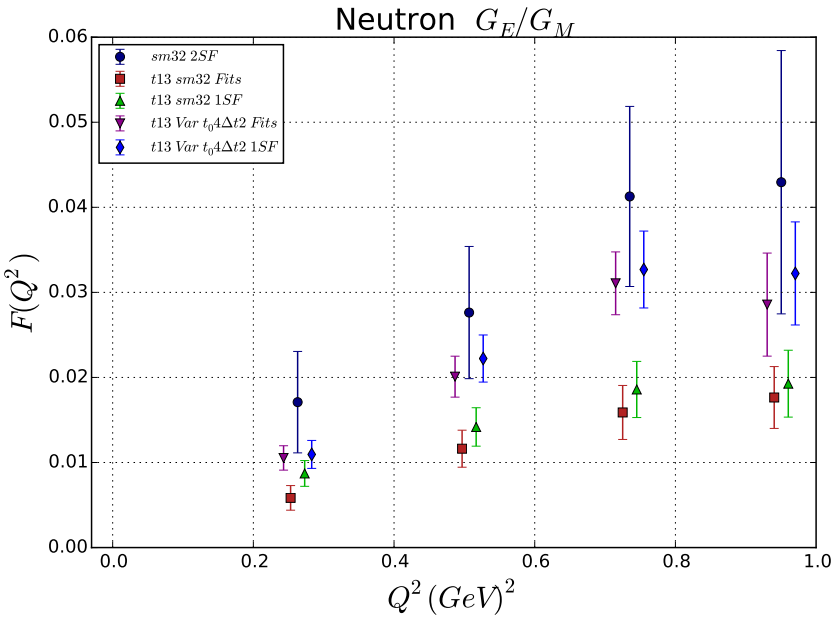

Figure 8.10: Sachs form factor ratio G_E/G_M for the neutron plotted as a function of the physical transfer momentum Q^2.

8.2 Axial G_A and G_P

To understand the axial-charge distribution within nucleons, we can study the axial form factors G_A and G_P, as these form factors involve a flavor changing current insertion which involve a weak interaction. The axial form factor defined as

$$\left\langle p(\vec{p}')|J_5^\mu(\vec{q})|n(\vec{p})\right\rangle = \overline{u}_p(\vec{p}')\left[\gamma^\mu\gamma^5 G_A(Q^2) + \frac{q^\mu}{2m_N}\gamma^5 G_P(Q^2)\right]u_n(\vec{p}), \qquad (2.22)$$

which the isovector combination can be accessed by looking at all operators of the form

$$O^{(q)} = O^{(u)} - O^{(d)} = \overline{u}\gamma_\mu\gamma_5 u - \overline{d}\gamma_\mu\gamma_5 d, \qquad (8.4)$$

since Eq.(2.12) demonstrates how it is equivalent to a flavor changing current. This implies that the form factors are actually the combination

$$G_A = G_A^{(u)} - G_A^{(d)}, \qquad G_P = G_P^{(u)} - G_P^{(d)}, \qquad (8.5)$$

with the individual quark contributing form factors $F_i^{(q)}$, in this case are $G_A^{(q)}$ and $G_P^{(q)}$, being defined in Eq.(6.21).

Lastly, from analysing the axial form factors, we can understand the axial charge radius of the proton by looking at the slope of the axial vector current form factor as a function of Q^2

$$\langle r_A^2 \rangle \equiv -6 \left. \frac{dG_A(Q^2)}{dQ^2} \right|_{Q^2=0}, \tag{8.6}$$

where again, we have employed a dipole fit from Eq.(8.3) to extract the slope at $Q^2 = 0$. The parameter $G_A(Q^2 = 0) = g_A$ in the dipole fit has previously been calculated in Chapter 7.

For the axial form factor G_A in Figure 8.11, we see that suppressing excited states produces the same interesting trend as we observed in the proton and neutron Sachs magnetic form factor G_M in Figures 8.6 and 8.8. For small Q^2, as previously seen for $g_A = G_A(Q^2 = 0)$, suppressing the excited-states results in decreasing the value, whereas for high Q^2 suppressing excited-states increases the value, resulting in a "crossing over" effect. This results for the axial charge radius $\langle r_A^2 \rangle$ shown in Table 8.2 demonstrate the susceptiblity to excited-state contamination, which is due to the slope at $Q^2 = 0$ being severely impacted by the "crossing over" effect.

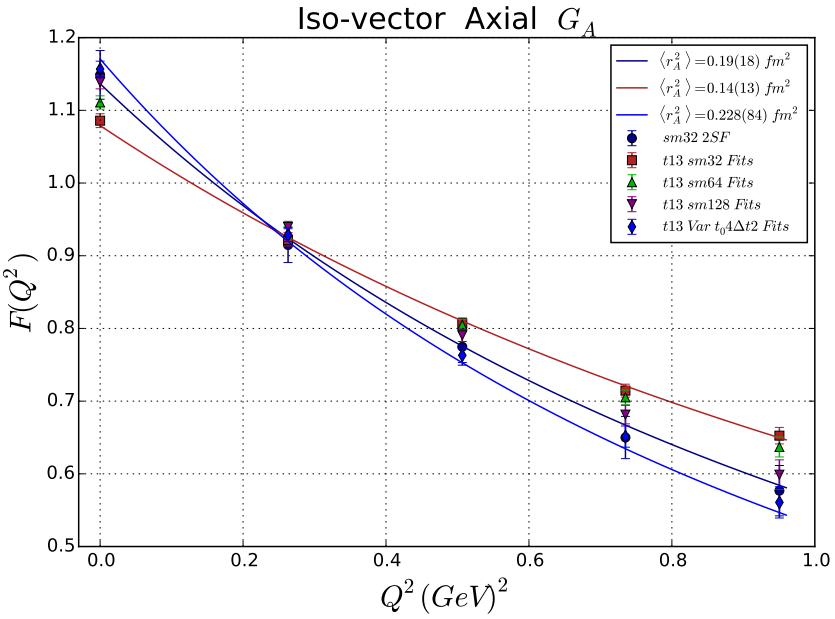

Figure 8.11: Axial vector form factor G_A plotted as a function of the physical transfer momentum Q^2.

Although the induced pseudoscalar form factor G_P in Figure 8.12 shows less

significant excited-state effects at low Q^2, we do see an excited-state contamination effect at low Q^2 which results in a steeper decent.

Both plots show an agreement between the two-exponential fit and variational method, as well as showing no sensitivity between utilising the one-exponential fit or the plateau method.

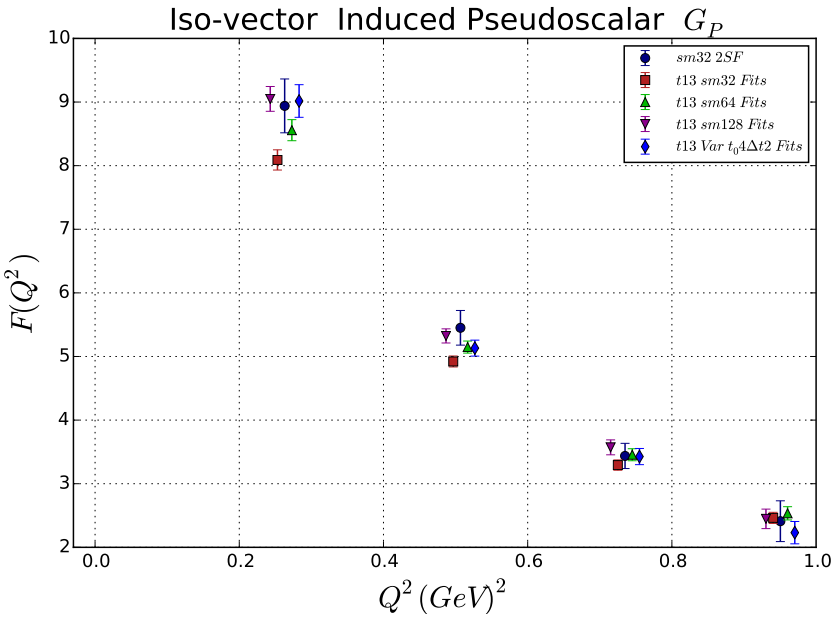

Figure 8.12: Induced pseudoscalar form factor G_P plotted as a function of the physical transfer momentum Q^2.

8.3 Summary

In general, the one-exponential fit method shows quite close agreement with a standard plateau method for the 32 sweeps of smearing result, only showing the slight differences on quantities that are very susceptible to statistical noise. For example, the neutron G_E results shown in of Figure 8.10 is highly susceptible to fluctuation as the nucleon has close to zero overall charge.

The main aim of this chapter is to demonstrate how controlling the excited-state contamination is a crucial part of form factor calculations. The excited-state contamination not only has an effect on the individual form factors at each Q^2, it also has the potential of increasing or decreasing the slope of the form factors with respect to Q^2. This last point is especially important, as the functional form of these form factors with respect to Q^2 plays an important role in not only experimental extrapolations from high momentum transfer results, but for

Method	Proton				Neutron	
	$\langle r^2 \rangle$	$\langle r_A^2 \rangle$	$\langle r_M^2 \rangle$	μ	$\langle r_M^2 \rangle$	μ
Fits	0.405(62)	0.22(18)	0.620(31)	2.259(35)	0.368(20)	1.370(24)
Var	0.300(26)	0.15(13)	1.224(87)	2.797(66)	0.767(60)	1.738(48)
TSF	0.417(21)	0.267(84)	0.93(11)	2.51(12)	0.524(65)	1.492(77)

Table 8.2: Table showing the extracted values for the proton charge radius $\langle r^2 \rangle$ and axial charge radius $\langle r_A^2 \rangle$ in units of fm^2 as well as the magnetic moment μ and the magnetic charge radius $\langle r_M^2 \rangle$ in units of fm^2, for both the proton and neutron. The multiple values correspond to using the 32 sweeps of smearing (sm32) result at a source-sink separation of $t = 13$, the variational method (Var) at a source-sink separation of $t = 13$ and using the two-exponenital fit (TSF) method over all source-sink separated results t=10, 13, 16, 19 and 22, with 32 sweeps of smearing.

interesting physical properties as well.

We can see that excited-state contamination has caused both the electric and axial charge radii to be smaller than expected for the proton, as the slope at $Q^2 = 0$ has increased when moving to the variational method in Figures 8.5 and 8.11. These figures demonstrates how important the excited-state systematics are to the determination of radii, as small excited-state effects in the individual Q^2 form factor values can lead to large shifts in the shape of the fit function used to find the slope at $Q^2 = 0$.

A similar sensitivity is observed when exploring how excited-state contamination effects the determination of the magnetic moment for the proton and neutron. In both Figures 8.5 and 8.11 we observed a "crossing over" effect of the extracted form factor points, which had a very large impact on the dipole fit extrapolation to $Q^2 \to 0$.

We display all the extracted radii and magnetic moments in Table 8.2 and all the numerical values plotted in this section can be found in Appendix C.2.

Chapter 9

Summary

To understand the structure of the proton and neutron, we began with a brief overview of Quantum Chromodynamics and looked at some experimental processes used to extract useful quantities. The simplest was neutron β-decay, occurring at the limit of zero momentum transfer, then moving onto elastic scattering processes at small transfer momentum producing the vector and axial form factors. Lastly we looked at large momentum transfer collisions creating in-elastic scattering processes. The quark momentum fraction $\langle x \rangle$ shows us, in the parton mode view of a nucleon, the fractional momentum carried by the up/down quark in the proton or neutron. After defining the quantities to analyse, the lattice approach to calculating these said quantities was developed. Beginning with the discretisation of space-time, the gluon and fermion actions are then defined. Once randomly generated gauge fields are generated, particles are introduced into the system by inverting the Dirac matrix to from the *two-point propagator*. These propagators are then the building blocks for calculating useful quantities associated with nucleons.

The *two-point correlator* is the spatial Fourier transform of an appropriate combination of two-point propagators, which gives us access to the masses, energies and useful scaling properties. To probe the structure of the nucleon, we utilised the *three-point correlator*, in which a third insertion point is added to the two-point correlator on a single quark in the nucleon. Although these constructs are enough to extract quantities by fitting a plateau to the *ratio function*, this naive approach is highly susceptible to excited-state contamination effects which can severely alter the fitted values. This motivates us to employ the variational method to the two- and three-point correlation functions, which utilises multiple nucleon interpolating fields (commonly achieved through the use of smearing operators). Another more common approach is to employ the two-exponential fit methods to the two- and three-point correlation functions to attempt to parameterise the ground and first excited-states.

The results presented in Chapter 7 clearly shows how excited-state contami-

nation is an important systematical effect and must be controlled to extract any meaningful quantities. It is worth noting, that the comparisons to follow still do not consider finite lattice spacing effects, renormalisation determination effects and larger pion mass effects.

The variational method produced a value for the axial-vector current of $g_A = 1.157(11)$, which still undershoots the experimental determination of $g_A = 1.270(3)$ [2–21], but we did see an improvement when removing excited-states (which caused the value to increase).

A tensor charge value of $g_T = 0.8^{+0.35}_{-0.44}$ has been calculated experimentally using the transfer momentum dependant (TMD) distribution method [132–134] and this is in agreement with the dihadron method [135, 136]. The variational method employed here to our lattice result produced a value of $g_T = 1.0734(78)$ which agrees to the experimental determination within the current statistical uncertainties.

For the quark momentum fraction, the variational method has the largest effect of removing excited-states, producing a smaller value of $\langle x \rangle = 0.1874(23)$, which still over-evaluates compared to the experimental estimate of $\langle x \rangle^{MRST} = 0.157(9)$ [125], but again, we have employed a heavier quark mass.

The preceding Chapter 8 shows that excited-state contamination effects are still prevalent when moving to non-zero momentum transfer. The vector Sachs form factor combination G_E/G_M for the proton and neutron shows a clear distinction between results with excited-states present and the variational method with its reduced excited-state contamination. We looked into some key properties of proton and neutron by analysing the charge and axial charge radius of the proton, as well as their magnetic moments. Large sensitivity was discovered for the radii $\langle r^2 \rangle$ and $\langle r_A^2 \rangle$ with respect to excited-state contamination, due to the dipole fit function changing shape when effected by excited-states. A similar sensitivity was discovered for the magnetic moment, as the extrapolated dipole fit functions to $Q^2 \to 0$ changed shape when excited-states were suppressed. As experimental form factor data [21] is undertaken at large Q^2, the ideal range to work in lattice QCD would also be at large Q^2. However, this is problematic as firstly, the signal to noise drastically reduces as we increase Q^2 and secondly, the excited-state contamination is more prevalent. Along with this, the other aforementioned systematics need to be brought under-control.

The pencil of function method outlined in Section 5.2.2 hinted at a potential method for improving the excited-state extraction process for zero momentum transfer results. The problem demonstrated in Chapter 7 is the signal to noise ratio is greatly decreased when applying the method. In Appendix A.3, we outline a potential cause for the such weak signal to noise ratio.

Lastly, so that the results presented in Chapter 7 and Chapter 8 have physical meaning, we formalised the standard non-perturbative renormalisation scheme

$RI'-MOM$ and demonstrated how we use perturbative constants to convert these renormalisation constants to the $\overline{MS}$ scheme in Chapter 4. The main value calculated in this thesis that had not been calculated previously, was $Z_{\langle x \rangle}^{\overline{MS}} = 1.104(23)$.

As we increase computing power, we can brute force the extraction of hadron matrix elements that have highly suppressed excited-state contamination by utilising multi-state fitting methods. But the only current way we can improve the excited-state determination from a physics standpoint, is by constructing optimal interpolating fields that have high overlap with the ground-state or excited-state in question. I would argue that the latter approach is a more computationally cost-effective and robust in achieving the goal of extracting hadron matrix elements with suppressed excited-state contamination.

Appendix A

Lattice QCD

A.1 Sakurai Representation

Here we display our chosen gamma matrix basis, the *Sakurai Representation*, in Euclidean space. These will co-inside with the results when a suitable O has been chosen for the three-point correlation function in Section 3.4.2.

$$\gamma_0 = \gamma_4 = \begin{bmatrix} 1 & 0 & 0 & 0 \\ 0 & 1 & 0 & 0 \\ 0 & 0 & -1 & 0 \\ 0 & 0 & 0 & -1 \end{bmatrix}, \gamma_1 = \begin{bmatrix} 0 & 0 & 0 & -i \\ 0 & 0 & -i & 0 \\ 0 & i & 0 & 0 \\ i & 0 & 0 & 0 \end{bmatrix},$$
$$\gamma_2 = \begin{bmatrix} 0 & 0 & 0 & -1 \\ 0 & 0 & 1 & 0 \\ 0 & 1 & 0 & 0 \\ -1 & 0 & 0 & 0 \end{bmatrix}, \gamma_3 = \begin{bmatrix} 0 & 0 & -i & 0 \\ 0 & 0 & 0 & i \\ i & 0 & 0 & 0 \\ 0 & -i & 0 & 0 \end{bmatrix}, \gamma_5 = \begin{bmatrix} 0 & 0 & -1 & 0 \\ 0 & 0 & 0 & -1 \\ -1 & 0 & 0 & 0 \\ 0 & -1 & 0 & 0 \end{bmatrix} \tag{A.1}$$

In this representation, we have the σ tensor being

$$\sigma_{\mu\nu} = -i\gamma_\mu\gamma_\nu. \tag{A.2}$$

A.2 Bootstrap and Jackknife Ensembles of Correlation Functions

For the analysis of correlation functions described in Chapter 6, we note that the quantities calculated per gauge field are correlated. This means that we can either

use *Bootstrap* or *Jackknife* statistical analysis methods of the correlation functions, which enables us to construct combinations and create fits.

For this thesis, we undergo bootstrap analysis. For some quantity O calculated on the gauge field $U_i \in \mathcal{U}_N$, we create the bootstrapped set by

$$O_b = \sum_{i=1}^{N_A} \frac{1}{N_A} O[U_{r(i)}], \tag{A.3}$$

where N_A is the size of the averaging process, and $r(i)$ is the i'th a random index from a list of N_A randomly generated indices spanning $1, \ldots, N$.

Then we can estimate the mean and standard deviation using the same equations, but applied to the bootstrapped configurations

$$\overline{O} = \sum_{b=1}^{N_b} \frac{1}{N_b} O_b, \qquad \sigma_O = \sqrt{\sum_{b=1}^{N_b} \frac{1}{N_b} (O_b - \overline{O})^2}. \tag{A.4}$$

For Jackknife, we use the following similar construction

$$O_j = \sum_{i \neq j}^{N} \frac{1}{N-1} O[U_i], \tag{A.5}$$

then we can estimate the mean and standard deviation using the similar equations, but applied to the jackknifed configurations

$$\overline{O} = \sum_{j=1}^{N} \frac{1}{N} O_j, \qquad \sigma_O = \sqrt{\sum_{j=1}^{N} \frac{N-1}{N} (O_j - \overline{O})^2}. \tag{A.6}$$

This technique of replacing the individual gauge field quantities with the bootstrap or jackknife configuration versions must be done once the two- and three-point correlation functions have been calculated. After this construction, we manipulate our correlators by undergoing the operation on a per-bootstrap configuration level or per-jackknife configuration level. For example, multiplication of two bootstrap quantities is achieved by

$$O = O_1 O_2 \to O_b = O_{1b} O_{2b}, \quad \forall b = 1, ..., N_b. \tag{A.7}$$

This technique applies to the ratio function construction in Eq.(3.68) or Eq.(3.69), the iso-vector, proton or neutron combinations created from the quark contributions to the three-point correlation function discussed in Section 6.4, the summation method in Section 6.3 and solving the form factor system of equations outlined in Section 6.26.

Moreover, when fitting a bootstrapped quantity, we fit the individual bootstrapped values which results in bootstrapped fit parameters. This is done in the one-exponential, two-exponential and plateau fit methods described in Chapter 6.

For testing the "goodness" of a fit, we use the χ^2_{PDF} which is defined as

$$\chi^2_{PDF}(O,F) = \frac{\chi^2(O,F)}{D} = \frac{1}{D}\sum_{t=1}^{n}\frac{(F(t)-\overline{O}(t))^2}{\sigma^2_{O(t)}}, \tag{A.8}$$

for some set of quantities O over some values (usually time values) t and some fit function F. We use $\sigma_{O(t)}$ due to the fact that all fitting done are weighted by the standard deviation of the sink time result $O(t)$. The quantity D is the number of degrees of freedom that are unconstrained

$$D = n - \text{fit parameters in function } F \tag{A.9}$$

It is common practice when analysing fits of correlation functions to reject any fit range with $\chi^2_{PDF} > 1$. In fact this value is generally used as a parameter to find an appropriate fit range that satisfies some large time approximation (e.g. two-point correlation functions with $t \gg 0$).

A.3 Pencil of Function De-correlation

As demonstrated in Chapter 7, the pencil of function construction outlined in Section 5.2.2 seems to demonstrate greatly improved excited-state suppression, but as a downside, has significantly smaller signal to noise ratios. One potential cause for this effect could be due to a de-correlation in the statistical analysis due to different source locations within the matrix of correlators.

Analysing the time translation definition

$$\begin{aligned}\chi^{\delta}(\vec{x},t) &\equiv e^{\hat{H}\delta}\chi(\vec{x},t)\,e^{-\hat{H}\delta} = \chi(\vec{x},t+\delta)\\ \overline{\chi}^{\delta}(\vec{x},t) &\equiv e^{-\hat{H}\delta}\overline{\chi}(\vec{x},t)\,e^{\hat{H}\delta} = \overline{\chi}(\vec{x},t-\delta)\end{aligned} \tag{5.25}$$

on a per gauge field basis, the correct way may be to express Eq.(5.29) without shifting the time in Eq.(5.25). When we analyse from some source time to t_0, the basis of two-point correlation functions becomes

$$(G_2)_{ij}(\Gamma;\vec{p},t,t_0) = \begin{bmatrix} G_2(\Gamma;\vec{p},t_0) & G_2(\Gamma;\vec{p},t+\delta,t_0) \\ G_2(\Gamma;\vec{p},t,t_0-\delta) & G_2(\Gamma;\vec{p},t+\delta,t_0-\delta)\end{bmatrix}, \tag{A.10}$$

where the bottom row is a new set of correlation functions constructed at a shifted source time $t_0 - \delta$. This correction can be extended to three-point correlation functions by correcting Eq.(5.32) to

$$(G_3)_{ij}\,(\vec{p}',t;\vec{q},\tau;t_0) = \begin{bmatrix} G_3(\vec{p}',t;\vec{q},\tau;t_0) & G_3(\vec{p}',t+\delta;\vec{q},\tau;t_0) \\ G_3(\vec{p}',t;\vec{q},\tau;t_0-\delta) & G_3(\vec{p}',t+\delta;\vec{q},\tau;t_0-\delta) \end{bmatrix}, \quad \text{(A.11)}$$

where, once again, a new row of correlation functions on the second line need to be constructed from a source time $t_0 - \delta$.

Appendix B

Perturbative Renormalisation Parameters

In Section 4.2.3, we utilise perturbatively expanded coefficients β_i and γ_i and this appendix, we defines these quantities and show their numerical value.

The *anomalous dimension* in some scheme $\mathcal{S}$ is defined and expanded as

$$\gamma^{\mathcal{S}} \equiv -\mu \frac{d}{d\mu} \log\left(Z_{\mathcal{S}}\right) = \gamma_0 \frac{g^{\mathcal{S}}(\mu)^2}{16\pi^2} + \gamma_1^{\mathcal{S}} \left(\frac{g^{\mathcal{S}}(\mu)^2}{16\pi^2}\right)^2 + \gamma_2^{\mathcal{S}} \left(\frac{g^{\mathcal{S}}(\mu)^2}{16\pi^2}\right)^2 \ldots, \tag{B.1}$$

where again, $\mathcal{S}$ is the current scheme. Analogously, the β-function is defined as

$$\beta^{\mathcal{S}} \equiv -\mu \frac{d}{d\mu} g^{\mathcal{S}}(\mu) = -\beta_0 \frac{g^{\mathcal{S}}(\mu)^3}{16\pi^2} - \beta_1 \frac{g^{\mathcal{S}}(\mu)^5}{(16\pi^2)^2} - \beta_2^{\mathcal{S}} \frac{g^{\mathcal{S}}(\mu)^7}{(16\pi^2)^3} \ldots, \tag{B.2}$$

The coefficients β_i up to three loops are equivalent for $\mathcal{S} = \overline{MS}$ and $RI' - MOM$, with values [78]

$$\begin{aligned} \beta_0 &= 11 - \frac{2}{3} N_f, \\ \beta_1 &= 102 - \frac{38}{3} N_f, \\ \beta_2 &= \frac{2857}{2} - \frac{5033}{18} N_f + \frac{325}{54} N_f^2, \end{aligned} \tag{B.3}$$

where N_f is the number of flavours. The anomalous dimension is operator dependant, with the vector and pseudo-vector values being $\gamma = 0$. The scalar and pseudo-scalar values are

$$
\begin{aligned}
\gamma_0 &= -8, \\
\gamma_1^{\overline{MS}} &= -\frac{404}{3} + \frac{40}{9} N_f, \\
\gamma_1^{RI'-MOM} &= -252 + \frac{104}{9} N_f, \\
\gamma_2^{\overline{MS}} &= -2498 + \left(\frac{4432}{27} + \frac{320}{3} \zeta_3 \right) N_f + \frac{280}{81} N_f^2, \\
\gamma_2^{RI'-MOM} &= -\frac{40348}{3} + \frac{6688}{3} \zeta_3 + \left(\frac{35176}{27} - \frac{256}{9} \zeta_3 \right) N_f + \frac{1712}{81} N_f^2,
\end{aligned}
\tag{B.4}
$$

where the zeta function $\zeta_3 = 1.20206\ldots$. The tensor values are

$$
\begin{aligned}
\gamma_0 &= \frac{8}{3}, \\
\gamma_1 &= \frac{724}{9} - \frac{104}{27} N_f, \\
\gamma_2^{\overline{MS}} &= \frac{105110}{81} - \frac{1856}{27} \zeta_3 - \left(\frac{10480}{81} + \frac{320}{9} \zeta_3 \right) N_f - \frac{8}{9} N_f^2, \\
\gamma_2^{RI'-MOM} &= \frac{359012}{81} - \frac{26144}{27} \zeta_3 + \left(-\frac{39640}{81} - \frac{512}{27} \zeta_3 \right) N_f + \frac{2288}{243} N_f^2,
\end{aligned}
\tag{B.5}
$$

and the $\langle x \rangle$ or $v_{2,b}$ values are

$$
\begin{aligned}
\gamma_0 &= \frac{64}{9}, \\
\gamma_1^{\overline{MS}} &= \frac{23488}{243} - \frac{512}{81} N_f, \\
\gamma_2^{\overline{MS}} &= \frac{11028416}{6561} + \frac{2560}{81} \zeta_3 - \left(\frac{334400}{2187} + \frac{2560}{27} \zeta_3 \right) N_f - \frac{1792}{729} N_f^2,
\end{aligned}
\tag{B.6}
$$

The values for $\gamma^{RI'-MOM}$ were only calculated the whole function $\Delta Z^{RGI}_{RI'-MOM}$ for the quark momentum fraction $\langle x \rangle$, which is summarised over the momenta scale μ^2 in Table B.1

μ^2	$\Delta Z^{RGI}_{RI'-MOM}$	μ^2	$\Delta Z^{RGI}_{RI'-MOM}$	μ^2	$\Delta Z^{RGI}_{RI'-MOM}$
0.15421	1.40463	0.03855	1.35984	0.00964	1.10353
0.61685	1.08859	0.34698	1.34455	0.24096	1.08374
1.38791	1.22120	0.96383	1.13380	0.78070	1.05920
2.46740	1.32251	1.88910	1.27893	1.62887	1.25240
3.85531	1.38676	3.12280	1.35753	2.78546	1.34088
5.55165	1.43366	4.66493	1.41180	4.25048	1.39973
7.55642	1.47039	6.51548	1.45302	6.02393	1.44362
9.86960	1.50045	8.67446	1.48610	8.10580	1.47843
12.49122	1.52580	11.14186	1.51362	10.49609	1.50717
		13.91768	1.53711	13.19481	1.53155

Table B.1: Table showing the calculated quantity $\Delta Z^{RGI}_{RI'-MOM}$ for the quark momentum fraction $\langle x \rangle$ at every momenta scale used in Chapter 4

Appendix C

Tabulated Results

In this appendix, we present the tabulated results which correspond to the mass parameters extracted in Section 7.2 as well as the values presented in the summary Figures 7.42, 7.43, 7.44 and 7.45 in Chapter 7. In addition, this appendix includes tabulated results for all the form factor values presented in Chapter 8.

C.1 Zero Momentum

calculation type	fit type	fit range	$m^{[0]}$	$\Delta m^{[0]}$	χ^2_{PDF}
sm32	OSF	12-19	0.4618	0.0045	0.07486
sm64	OSF	12-19	0.4599	0.0042	0.02868
sm128	OSF	12-19	0.4595	0.0046	0.04725
variational method	OSF	8-19	0.4617	0.0038	0.08476
pencil of function	OSF	3-16	0.4630	0.0036	0.62055
sm32, 64, 128	TSF	4-19	0.4581	0.0043	0.08361

Table C.1: Table showing all the extracted masses $m^{[0]}$ in lattice units from the one-exponential fit (OSF) and the two-exponential fit (TSF).

Methods	g_A	g_S	$\langle x \rangle$	g_T
Fit t=10, sm32	1.0359(64)	0.748(12)	0.2484(18)	1.0610(53)
Fit t=13, sm32	1.0858(95)	0.837(22)	0.2223(23)	1.0571(89)
Fit t=16, sm32	1.112(16)	0.901(36)	0.2009(33)	1.047(14)
Fit t=19, sm32	1.114(29)	0.956(58)	0.1865(46)	1.030(25)
Fit t=22, sm32	1.136(53)	0.97(10)	0.1802(78)	1.044(46)
Fit t=13, sm32	1.0858(95)	0.837(22)	0.2223(23)	1.0571(89)
Fit t=13, sm64	1.1108(92)	0.879(22)	0.2111(22)	1.0655(82)
Fit t=13, sm128	1.1389(92)	0.931(23)	0.1977(22)	1.0734(78)
Var CM t=13, t_0=4 Δt=2	1.157(11)	0.978(26)	0.1874(23)	1.0787(82)
Var CM t=16, t_0=2 Δt=2	1.150(20)	0.970(51)	0.1851(45)	1.084(17)
1exp t=10, sm32	1.099(16)	0.793(16)	0.2636(39)	1.126(16)
1exp t=13, sm32	1.0793(91)	0.827(21)	0.2218(22)	1.0532(86)
1exp t=16, sm32	1.100(15)	0.885(34)	0.2044(31)	1.045(14)
1exp t=19, sm32	1.125(27)	0.955(58)	0.1928(44)	1.047(22)
1exp t=22, sm32	1.160(54)	0.99(12)	0.1870(82)	1.072(41)

Table C.2: Summary of results as displayed in Figures 7.42, 7.43, 7.44, 7.45 for the fits and half the one-exponential fits.

Methods	g_A	g_S	$\langle x \rangle$	g_T
1exp PoF t=13, t_0=4Δt=2	1.135(49)	0.982(62)	0.1876(100)	1.047(44)
1exp PoF t=16, t_0=2Δt=2	1.128(55)	0.963(75)	0.185(11)	1.031(49)
1exp t=13, sm32	1.0793(91)	0.827(21)	0.2218(22)	1.0532(86)
1exp t=13, sm64	1.1039(91)	0.869(21)	0.2105(21)	1.0614(80)
1exp t=13, sm128	1.1334(98)	0.921(23)	0.1975(22)	1.0703(80)
1exp CM t=13, t_0=4 Δt=2	1.153(16)	0.963(27)	0.1878(28)	1.075(13)
2exp t=13, sm32 δt=2	1.148(23)	0.944(39)	0.2001(52)	1.064(16)
2exp t=13, sm32 δt=3	1.148(23)	0.953(41)	0.2060(76)	1.060(18)
2exp t=13, sm32 δt=4	1.151(24)	0.971(47)	0.221(14)	1.053(19)
2exp t=13, sm64 δt=2	1.144(17)	0.959(35)	0.1910(49)	1.050(12)
2exp t=13, sm64 δt=3	1.144(18)	0.965(37)	0.1947(70)	1.049(14)
2exp t=13, sm64 δt=4	1.145(19)	0.971(41)	0.208(12)	1.041(16)
2exp t=13, sm128 δt=2	1.160(16)	0.998(35)	0.1836(50)	1.051(12)
2exp t=13, sm128 δt=3	1.159(17)	1.000(36)	0.1834(72)	1.050(14)
2exp t=13, sm128 δt=4	1.158(19)	0.993(39)	0.188(13)	1.044(18)
2exp All sm32 δt=2	1.140(26)	0.957(58)	0.1771(63)	1.034(25)
2exp All sm32 δt=3	1.149(33)	0.976(70)	0.1753(72)	1.039(30)
2exp All sm32 δt=4	1.157(45)	1.005(92)	0.1736(87)	1.046(37)
2exp t$\neq$10,13 sm32 δt=2	1.155(45)	1.013(93)	0.1728(83)	1.041(37)
2exp t$\neq$10,13 sm32 δt=3	1.157(47)	1.012(97)	0.1723(86)	1.043(39)
2exp t$\neq$10,13 sm32 δt=4	1.157(51)	1.01(10)	0.1730(91)	1.047(41)
2exp t$\neq$16,19,22 sm32 δt=2	1.129(17)	0.948(42)	0.1816(59)	1.030(16)
2exp t$\neq$16,19,22 sm32 δt=3	1.138(19)	0.958(47)	0.1819(65)	1.034(18)
2exp t$\neq$16,19,22 sm32 δt=4	1.152(25)	0.972(58)	0.1800(78)	1.042(23)
Sum All δt=0	1.179(28)	1.026(80)	0.1542(64)	1.041(26)
Sum All δt=1	1.170(27)	1.009(74)	0.1596(57)	1.041(25)
Sum All δt=2	1.160(25)	0.987(67)	0.1671(50)	1.041(23)
Sum All δt=3	1.147(22)	0.959(60)	0.1767(43)	1.043(20)
Sum t$\neq$10,13 δt=0	1.16(11)	1.24(24)	0.138(20)	1.000(96)
Sum t$\neq$10,13 δt=1	1.15(11)	1.19(22)	0.142(19)	0.998(93)
Sum t$\neq$10,13 δt=2	1.15(10)	1.15(21)	0.143(17)	1.001(88)
Sum t$\neq$10,13 δt=3	1.148(96)	1.11(19)	0.147(15)	1.006(82)

Table C.3: Summary of results as displayed in Figures 7.42, 7.43, 7.44, 7.45 for half the one-exponential fits, the two-exponential fits and summation method results.

C.2 Form Factors

Iso-Vector
Two-Exponential Fit Form Factors

Q^2(GeV)^2	G_A	G_P
0.0	1.149(33)	NA
0.26295	0.915(24)	8.94(42)
0.50674	0.775(25)	5.45(27)
0.73503	0.650(29)	3.44(20)
0.95045	0.577(35)	2.41(32)

Table C.4: Table showing the iso-vector form factors using the two-exponential fit method over all 32 sweeps of smearing results, tabulated over the physical transfer momentum Q^2.

Iso-Vector 32 Smearing
Plateau Form Factors

Q^2(GeV)^2	G_A	G_P
0.0	1.0858(95)	NA
0.26295	0.9214(79)	8.09(16)
0.50674	0.8072(73)	4.922(86)
0.73503	0.7144(89)	3.293(81)
0.95045	0.653(11)	2.463(87)

Iso-Vector 32 Smearing
One-Exponential Fit Form Factors

Q^2(GeV)^2	G_A	G_P
0.0	1.0793(91)	NA
0.26295	0.9209(79)	8.21(15)
0.50674	0.8097(71)	5.041(86)
0.73503	0.7165(84)	3.368(78)
0.95045	0.650(10)	2.487(82)

Table C.5: Tables showing the iso-vector form factors using the 32 sweeps of smearing calculation with a plateau fit (left) and one-exponential fit (right), tabulated over the physical transfer momentum Q^2.

Iso-Vector Variational Method
Plateau Form Factors

Q^2(GeV)^2	G_A	G_P
0.0	1.157(11)	NA
0.26295	0.9283(89)	9.02(26)
0.50674	0.7630(99)	5.13(13)
0.73503	0.651(15)	3.43(13)
0.95045	0.561(21)	2.23(18)

Iso-Vector Variational Method
One-Exponential Fit Form Factors

Q^2(GeV)^2	G_A	G_P
0.0	1.153(16)	NA
0.26295	0.935(12)	9.15(25)
0.50674	0.779(11)	5.40(14)
0.73503	0.666(14)	3.56(13)
0.95045	0.580(20)	2.41(15)

Table C.6: Tables showing the iso-vector form factors using the variational method calculation with a plateau fit (left) and one-exponential fit (right), tabulated over the physical transfer momentum Q^2.

Proton Two-Exponential Fit Form Factors

Q^2(GeV)^2	Vector		Sachs Vector		
	F_1	F_2	G_E	G_M	G_E/G_M
0.0	1.000(17)	NA	1.000(17)	NA	NA
0.26295	0.695(16)	1.006(45)	0.652(16)	1.700(52)	0.384(11)
0.50674	0.540(16)	0.748(34)	0.478(15)	1.288(43)	0.372(11)
0.73503	0.429(17)	0.554(33)	0.363(16)	0.984(43)	0.370(15)
0.95045	0.387(21)	0.472(36)	0.314(20)	0.858(47)	0.367(23)

Neutron Two-Exponential Fit Form Factors

Q^2(GeV)^2	Vector		Sachs Vector		
	F_1	F_2	G_E	G_M	G_E/G_M
0.0	0.00000(32)	NA	0.00000(32)	NA	NA
0.26295	0.0254(61)	1.015(33)	0.0177(60)	1.041(35)	0.0171(60)
0.50674	0.0398(62)	0.751(27)	0.0218(59)	0.791(30)	0.0276(78)
0.73503	0.0411(66)	0.550(26)	0.0243(59)	0.591(30)	0.041(11)
0.95045	0.0510(81)	0.480(28)	0.0227(80)	0.531(31)	0.043(15)

Table C.7: Tables showing the data for the two-exponential fit methods for all the proton and neutron form factors.

Proton 32 Smearing Plateau Form Factors

$Q^2(\text{GeV})^2$	Vector		Sachs Vector		
	F_1	F_2	G_E	G_M	G_E/G_M
0.0	1.00000(23)	NA	1.00000(23)	NA	NA
0.26295	0.7602(30)	0.943(16)	0.7201(28)	1.703(18)	0.4228(42)
0.50674	0.6224(42)	0.710(12)	0.5642(38)	1.332(15)	0.4235(40)
0.73503	0.5305(57)	0.559(12)	0.4641(52)	1.090(16)	0.4258(53)
0.95045	0.4799(73)	0.468(14)	0.4079(66)	0.948(18)	0.4302(76)

Neutron 32 Smearing Plateau Form Factors

$Q^2(\text{GeV})^2$	Vector		Sachs Vector		
	F_1	F_2	G_E	G_M	G_E/G_M
0.0	0.00000(13)	NA	0.00000(13)	NA	NA
0.26295	0.0366(16)	1.004(12)	0.0061(15)	1.041(13)	0.0058(14)
0.50674	0.0532(19)	0.7653(95)	0.0095(18)	0.818(10)	0.0116(22)
0.73503	0.0614(23)	0.6055(97)	0.0106(21)	0.667(11)	0.0159(32)
0.95045	0.0681(23)	0.509(11)	0.0102(21)	0.578(12)	0.0176(36)

Table C.8: Tables showing the data for the 32 sweeps of smearing result using the plateau method for extracting the proton and neutron form factors.

Proton 32 Smearing One-Exponential Fit Form Factors

$Q^2(\text{GeV})^2$	Vector		Sachs Vector		
	F_1	F_2	G_E	G_M	G_E/G_M
0.0	1.0000(19)	NA	1.0000(19)	NA	NA
0.26295	0.7490(34)	0.957(17)	0.7083(32)	1.706(18)	0.4152(42)
0.50674	0.6174(40)	0.725(12)	0.5580(37)	1.342(14)	0.4157(40)
0.73503	0.5274(52)	0.574(12)	0.4592(47)	1.101(15)	0.4172(52)
0.95045	0.4732(66)	0.478(14)	0.3998(61)	0.951(17)	0.4206(75)

Neutron 32 Smearing One-Exponential Fit Form Factors

$Q^2(\text{GeV})^2$	Vector		Sachs Vector		
	F_1	F_2	G_E	G_M	G_E/G_M
0.0	0.00000(11)	NA	0.00000(11)	NA	NA
0.26295	0.0338(17)	1.009(12)	0.0091(15)	1.043(13)	0.0087(15)
0.50674	0.0516(20)	0.7727(91)	0.0117(18)	0.824(10)	0.0142(23)
0.73503	0.0603(23)	0.6126(90)	0.0125(22)	0.673(10)	0.0186(33)
0.95045	0.0675(25)	0.512(10)	0.0112(23)	0.579(11)	0.0193(39)

Table C.9: Tables showing the data for the 32 sweeps of smearing result using the one-state fit method for extracting the proton and neutron form factors.

Proton Variational Method Plateau Form Factors

$Q^2(\text{GeV})^2$	Vector		Sachs Vector		
	F_1	F_2	G_E	G_M	G_E/G_M
0.0	1.00000(35)	NA	1.00000(35)	NA	NA
0.26295	0.7067(40)	1.072(20)	0.6611(38)	1.779(22)	0.3717(43)
0.50674	0.5405(60)	0.770(17)	0.4774(54)	1.310(21)	0.3644(47)
0.73503	0.4359(91)	0.586(19)	0.3662(81)	1.022(25)	0.3583(75)
0.95045	0.375(13)	0.473(25)	0.303(11)	0.849(34)	0.357(12)

Neutron 32 Variational Method Form Factors

$Q^2(\text{GeV})^2$	Vector		Sachs Vector		
	F_1	F_2	G_E	G_M	G_E/G_M
0.0	0.00000(19)	NA	0.00000(19)	NA	NA
0.26295	0.0339(16)	1.071(16)	0.0116(16)	1.104(16)	0.0105(14)
0.50674	0.0466(20)	0.769(13)	0.0164(20)	0.816(13)	0.0201(23)
0.73503	0.0500(25)	0.587(15)	0.0198(23)	0.637(16)	0.0311(37)
0.95045	0.0565(34)	0.465(20)	0.0149(33)	0.521(22)	0.0286(61)

Table C.10: Tables showing the data for the variational method result using the plateau method for extracting the proton and neutron form factors.

Proton Variational Method One-Exponential Fit Form Factors

Q^2(GeV)^2	Vector		Sachs Vector		
	F_1	F_2	G_E	G_M	G_E/G_M
0.0	1.000(11)	NA	1.000(11)	NA	NA
0.26295	0.7050(76)	1.077(23)	0.6592(71)	1.782(28)	0.3701(46)
0.50674	0.5441(71)	0.787(18)	0.4796(64)	1.331(23)	0.3603(49)
0.73503	0.4408(86)	0.608(20)	0.3686(78)	1.048(25)	0.3517(81)
0.95045	0.381(11)	0.493(25)	0.3057(92)	0.874(33)	0.350(12)

Neutron Variational Method One-Exponential Fit Form Factors

Q^2(GeV)^2	Vector		Sachs Vector		
	F_1	F_2	G_E	G_M	G_E/G_M
0.0	0.00000(12)	NA	0.00000(12)	NA	NA
0.26295	0.0335(19)	1.073(18)	0.0121(18)	1.107(19)	0.0110(16)
0.50674	0.0459(23)	0.786(13)	0.0185(23)	0.832(14)	0.0222(28)
0.73503	0.0503(30)	0.602(14)	0.0213(28)	0.652(16)	0.0327(45)
0.95045	0.0573(38)	0.487(19)	0.0175(33)	0.544(22)	0.0322(61)

Table C.11: Tables showing the data for the variational method result using the one-state fit method for extracting the proton and neutron form factors.

Bibliography

[1] Nicola Serra. *Standard Model*. [Online; accessed August 31, 2016]. 2015. URL: http://www.physik.uzh.ch/groups/serra/StandardModel.html.

[2] P. Liaud et al. "The measurement of the beta asymmetry in the decay of polarized neutrons". In: *Nucl. Phys.* A612 (1997), pp. 53–81. DOI: 10.1016/S0375-9474(96)00325-9.

[3] H. Abele et al. "A measurement of the beta asymmetry A in the decay of free neutrons". In: *Phys. Lett.* B407 (1997), pp. 212–218. DOI: 10.1016/S0370-2693(97)00739-9.

[4] H. Abele et al. "Is the unitarity of the quark mixing CKM matrix violated in neutron beta decay?" In: *Phys. Rev. Lett.* 88 (2002), p. 211801. DOI: 10.1103/PhysRevLett.88.211801. arXiv: hep-ex/0206058 [hep-ex].

[5] M. Schumann et al. "Measurement of the Proton Asymmetry Parameter C in Neutron Beta Decay". In: *Phys. Rev. Lett.* 100 (2008), p. 151801. DOI: 10.1103/PhysRevLett.100.151801. arXiv: 0712.2442 [hep-ph].

[6] B. Plaster et al. "Measurement of the neutron β-asymmetry parameter A_0 with ultracold neutrons". In: *Phys. Rev.* C86 (2012), p. 055501. DOI: 10.1103/PhysRevC.86.055501. arXiv: 1207.5887 [nucl-ex].

[7] D. Mund et al. "Determination of the Weak Axial Vector Coupling from a Measurement of the Beta-Asymmetry Parameter A in Neutron Beta Decay". In: *Phys. Rev. Lett.* 110 (2013), p. 172502. DOI: 10.1103/PhysRevLett.110.172502. arXiv: 1204.0013 [hep-ex].

[8] M. P. Mendenhall et al. "Precision measurement of the neutron β-decay asymmetry". In: *Phys. Rev.* C87.3 (2013), p. 032501. DOI: 10.1103/PhysRevC.87.032501. arXiv: 1210.7048 [nucl-ex].

[9] Yu. A. Mostovoi et al. "Experimental value of G(A)/G(V) from a measurement of both P-odd correlations in free-neutron decay". In: *Phys. Atom. Nucl.* 64 (2001). [Yad. Fiz.64,2040(2001)], pp. 1955–1960. DOI: 10.1134/1.1423745.

[10] H. Abele et al. “Is the Unitarity of the Quark-Mixing CKM Matrix Violated in Neutron β-Decay?” In: *Phys. Rev. Lett.* 88 (21 May 2002), p. 211801. DOI: 10.1103/PhysRevLett.88.211801. URL: http://link.aps.org/doi/10.1103/PhysRevLett.88.211801.

[11] J. Liu et al. “Determination of the Axial-Vector Weak Coupling Constant with Ultracold Neutrons”. In: *Phys. Rev. Lett.* 105 (2010), p. 181803. DOI: 10.1103/PhysRevLett.105.181803. arXiv: 1007.3790 [nucl-ex].

[12] B. Erozolimsky et al. “Corrigendum: Corrected value of the beta-emission asymmetry in the decay of polarized neutrons measured in 1990”. In: *Phys. Lett.* B412 (1997), pp. 240–241. DOI: 10.1016/S0370-2693(97)01004-6.

[13] K. Schreckenbach et al. “A New measurement of the beta emission asymmetry in the free decay of polarized neutrons”. In: *Phys. Lett.* B349 (1995), pp. 427–432. DOI: 10.1016/0370-2693(95)00228-D.

[14] B. G. Erozolimsky et al. “New measurements of the electron - neutron spin asymmetry”. In: *Phys. Lett.* B263 (1991), pp. 33–38. DOI: 10.1016/0370-2693(91)91703-X.

[15] P. Bopp et al. “The Beta Decay Asymmetry of the Neutron and g_A/g_V”. In: *Phys. Rev. Lett.* 56 (1986). [Erratum: Phys. Rev. Lett.57,1192(1986)], p. 919. DOI: 10.1103/PhysRevLett.56.919.

[16] Yu. A. Mostovoi. “DETERMINATION OF G(A) / G(V) FROM THE SET OF THREE ANGULAR CORRELATION COEFFICIENTS OBSERVED IN THE DECAY OF THE FREE NEUTRON”. In: *JETP Lett.* 37 (1983). [Pisma Zh. Eksp. Teor. Fiz.37,564(1983)], pp. 196–197.

[17] C. Stratowa, R. Dobrozemsky, and P. Weinzierl. “Ratio G(a)/G(v) Derived from the Proton Spectrum in Free Neutron Decay”. In: *Phys. Rev.* D18 (1978), pp. 3970–3979. DOI: 10.1103/PhysRevD.18.3970.

[18] B. G. Erozolimsky et al. “New Measurements of Spin electron Angular Correlation in Polarized Neutron Decay”. In: *JETP Lett.* 23 (1976). [Pisma Zh. Eksp. Teor. Fiz.23,720(1976)], p. 663.

[19] R. Dobrozemsky et al. “Electron-neutrino angular correlation coefficient a measured from free-neutron decay”. In: *Phys. Rev.* D11 (1975), pp. 510–512. DOI: 10.1103/PhysRevD.11.510.

[20] H. Kropf and E. Paul. “Least squares adjustment of the coupling constants in nuclear beta-decay”. In: *Z. Phys.* 267 (1974), pp. 129–133. DOI: 10.1007/BF01668639.

[21] J. Beringer et al. “Review of Particle Physics*”. In: *Phys. Rev. D* 86 (1 July 2012), p. 010001. DOI: 10.1103/PhysRevD.86.010001. URL: http://link.aps.org/doi/10.1103/PhysRevD.86.010001.

[22] M. N. Rosenbluth. “High Energy Elastic Scattering of Electrons on Protons”. In: *Phys. Rev.* 79 (1950), pp. 615–619. DOI: 10.1103/PhysRev.79.615.

[23] R. Hofstadter and R. W. McAllister. “Electron Scattering From the Proton”. In: *Phys. Rev.* 98 (1955), pp. 217–218. DOI: 10.1103/PhysRev.98.217.

[24] M. R. Yearian and Robert Hofstadter. “Magnetic Form Factor of the Neutron”. In: *Phys. Rev.* 110.2 (1958), p. 552. DOI: 10.1103/PhysRev.110.552.

[25] J. Arrington, C. D. Roberts, and J. M. Zanotti. “Nucleon electromagnetic form-factors”. In: *J. Phys.* G34 (2007), S23–S52. DOI: 10.1088/0954-3899/34/7/S03. arXiv: nucl-th/0611050 [nucl-th].

[26] J. C. Bernauer et al. “High-precision determination of the electric and magnetic form factors of the proton”. In: *Phys. Rev. Lett.* 105 (2010), p. 242001. DOI: 10.1103/PhysRevLett.105.242001. arXiv: 1007.5076 [nucl-ex].

[27] M. K. Jones et al. “G(E(p)) / G(M(p)) ratio by polarization transfer in polarized e p —¿ e polarized p”. In: *Phys. Rev. Lett.* 84 (2000), pp. 1398–1402. DOI: 10.1103/PhysRevLett.84.1398. arXiv: nucl-ex/9910005 [nucl-ex].

[28] G. Ron et al. “Low Q^2 measurements of the proton form factor ratio mu_pG_E/G_M”. In: *Phys. Rev.* C84 (2011), p. 055204. DOI: 10.1103/PhysRevC.84.055204. arXiv: 1103.5784 [nucl-ex].

[29] X. Zhan et al. “High-Precision Measurement of the Proton Elastic Form Factor Ratio μ_pG_E/G_M at low Q^2”. In: *Phys. Lett.* B705 (2011), pp. 59–64. DOI: 10.1016/j.physletb.2011.10.002. arXiv: 1102.0318 [nucl-ex].

[30] C. Alexandrou et al. “Axial Nucleon and Nucleon to Delta form factors and the Goldberger-Treiman Relations from Lattice QCD”. In: *Phys. Rev.* D76 (2007). [Erratum: Phys. Rev.D80,099901(2009)], p. 094511. DOI: 10.1103/PhysRevD.80.099901,10.1103/PhysRevD.76.094511. arXiv: 0706.3011 [hep-lat].

[31] C. Alexandrou et al. “The Nucleon electromagnetic form factors from Lattice QCD”. In: *Phys. Rev.* D74 (2006), p. 034508. DOI: 10.1103/PhysRevD.74.034508. arXiv: hep-lat/0605017 [hep-lat].

[32] M. Gockeler et al. “Nucleon electromagnetic form-factors on the lattice and in chiral effective field theory”. In: *Phys. Rev.* D71 (2005), p. 034508. DOI: 10.1103/PhysRevD.71.034508. arXiv: hep-lat/0303019 [hep-lat].

[33] Ph. Hagler et al. “Nucleon Generalized Parton Distributions from Full Lattice QCD”. In: *Phys. Rev.* D77 (2008), p. 094502. DOI: 10.1103/PhysRevD.77.094502. arXiv: 0705.4295 [hep-lat].

[34] Huey-Wen Lin et al. “Nucleon structure with two flavors of dynamical domain-wall fermions”. In: *Phys. Rev.* D78 (2008), p. 014505. DOI: 10.1103/PhysRevD.78.014505. arXiv: 0802.0863 [hep-lat].

[35] K. F. Liu et al. “Pi N N and pseudoscalar form-factors from lattice QCD”. In: *Phys. Rev. Lett.* 74 (1995), pp. 2172–2175. DOI: 10.1103/PhysRevLett.74.2172. arXiv: hep-lat/9406007 [hep-lat].

[36] Shoichi Sasaki and Takeshi Yamazaki. “Nucleon form factors from quenched lattice QCD with domain wall fermions”. In: *Phys. Rev.* D78 (2008), p. 014510. DOI: 10.1103/PhysRevD.78.014510. arXiv: 0709.3150 [hep-lat].

[37] Ph. Hagler. “Hadron structure from lattice quantum chromodynamics”. In: *Phys. Rept.* 490 (2010), pp. 49–175. DOI: 10.1016/j.physrep.2009.12.008. arXiv: 0912.5483 [hep-lat].

[38] S. Boinepalli et al. “Precision electromagnetic structure of octet baryons in the chiral regime”. In: *Phys. Rev.* D74 (2006), p. 093005. DOI: 10.1103/PhysRevD.74.093005. arXiv: hep-lat/0604022 [hep-lat].

[39] Takeshi Yamazaki et al. “Nucleon form factors with 2+1 flavor dynamical domain-wall fermions”. In: *Phys. Rev.* D79 (2009), p. 114505. DOI: 10.1103/PhysRevD.79.114505. arXiv: 0904.2039 [hep-lat].

[40] S. Collins et al. “Dirac and Pauli form factors from lattice QCD”. In: *Phys. Rev.* D84 (2011), p. 074507. DOI: 10.1103/PhysRevD.84.074507. arXiv: 1106.3580 [hep-lat].

[41] Huey-Wen Lin and Kostas Orginos. “Strange Baryon Electromagnetic Form Factors and SU(3) Flavor Symmetry Breaking”. In: *Phys. Rev.* D79 (2009), p. 074507. DOI: 10.1103/PhysRevD.79.074507. arXiv: 0812.4456 [hep-lat].

[42] P. Wang et al. “Chiral extrapolation of octet-baryon charge radii”. In: *Phys. Rev.* D79 (2009), p. 094001. DOI: 10.1103/PhysRevD.79.094001. arXiv: 0810.1021 [hep-ph].

[43] P. E. Shanahan et al. “Magnetic form factors of the octet baryons from lattice QCD and chiral extrapolation”. In: *Phys. Rev.* D89 (2014), p. 074511. DOI: 10.1103/PhysRevD.89.074511. arXiv: 1401.5862 [hep-lat].

[44] P. E. Shanahan et al. “Electric form factors of the octet baryons from lattice QCD and chiral extrapolation”. In: *Phys. Rev.* D90 (2014), p. 034502. DOI: 10.1103/PhysRevD.90.034502. arXiv: 1403.1965 [hep-lat].

[45] Huey-Wen Lin et al. “Lattice Calculations of Nucleon Electromagnetic Form Factors at Large Momentum Transfer”. In: (2010). arXiv: 1005.0799 [hep-lat].

[46] Huey-Wen Lin et al. “First Lattice Study of the N - P(11)(1440) Transition Form Factors”. In: *Phys. Rev.* D78 (2008), p. 114508. DOI: 10.1103/PhysRevD.78.114508. arXiv: 0803.3020 [hep-lat].

[47] Dmitri Diakonov et al. “Nucleon parton distributions at low normalization point in the large N(c) limit”. In: *Nucl. Phys.* B480 (1996), pp. 341–380. DOI: 10.1016/S0550-3213(96)00486-5. arXiv: hep-ph/9606314 [hep-ph].

[48] Andreas W. Schreiber et al. “The Pion cloud of the nucleon and its effect on deep inelastic structure”. In: *Phys. Rev.* D45 (1992), pp. 3069–3078. DOI: 10.1103/PhysRevD.45.3069.

[49] Leonard P. Gamberg, Gary R. Goldstein, and Karo A. Oganessyan. “Novel transversity properties in semiinclusive deep inelastic scattering”. In: *Phys. Rev.* D67 (2003), p. 071504. DOI: 10.1103/PhysRevD.67.071504. arXiv: hep-ph/0301018 [hep-ph].

[50] I. C. Cloet, Wolfgang Bentz, and Anthony William Thomas. “Nucleon quark distributions in a covariant quark-diquark model”. In: *Phys. Lett.* B621 (2005), pp. 246–252. DOI: 10.1016/j.physletb.2005.06.065. arXiv: hep-ph/0504229 [hep-ph].

[51] I. C. Cloet, Wolfgang Bentz, and Anthony William Thomas. “Transversity quark distributions in a covariant quark-diquark model”. In: *Phys. Lett.* B659 (2008), pp. 214–220. DOI: 10.1016/j.physletb.2007.09.071. arXiv: 0708.3246 [hep-ph].

[52] Alessandro Bacchetta, Francesco Conti, and Marco Radici. “Transverse-momentum distributions in a diquark spectator model”. In: *Phys. Rev.* D78 (2008), p. 074010. DOI: 10.1103/PhysRevD.78.074010. arXiv: 0807.0323 [hep-ph].

[53] Cedric Lorce, Barbara Pasquini, and Marc Vanderhaeghen. “Unified framework for generalized and transverse-momentum dependent parton distributions within a 3Q light-cone picture of the nucleon”. In: *JHEP* 05 (2011), p. 041. DOI: 10.1007/JHEP05(2011)041. arXiv: 1102.4704 [hep-ph].

[54] Hung-Liang Lai et al. “New parton distributions for collider physics”. In: *Phys. Rev.* D82 (2010), p. 074024. DOI: 10.1103/PhysRevD.82.074024. arXiv: 1007.2241 [hep-ph].

[55] C. Adloff et al. "Measurement and QCD analysis of neutral and charged current cross-sections at HERA". In: *Eur. Phys. J.* C30 (2003), pp. 1–32. DOI: 10.1140/epjc/s2003-01257-6. arXiv: hep-ex/0304003 [hep-ex].

[56] Richard D. Ball et al. "A Determination of parton distributions with faithful uncertainty estimation". In: *Nucl. Phys.* B809 (2009). [Erratum: Nucl. Phys.B816,293(2009)], pp. 1–63. DOI: 10.1016/j.nuclphysb.2008.09.037,10.1016/j.nuclphysb.2009.02.027. arXiv: 0808.1231 [hep-ph].

[57] A. D. Martin et al. "Update of parton distributions at NNLO". In: *Phys. Lett.* B652 (2007), pp. 292–299. DOI: 10.1016/j.physletb.2007.07.040. arXiv: 0706.0459 [hep-ph].

[58] R. Horsley et al. "Charge Symmetry Breaking in Parton Distribution Functions from Lattice QCD". In: *Phys. Rev.* D83 (2011), p. 051501. DOI: 10.1103/PhysRevD.83.051501. arXiv: 1012.0215 [hep-lat].

[59] William Detmold, W. Melnitchouk, and Anthony William Thomas. "Moments of isovector quark distributions from lattice QCD". In: *Phys. Rev.* D66 (2002), p. 054501. DOI: 10.1103/PhysRevD.66.054501. arXiv: hep-lat/0206001 [hep-lat].

[60] Gunnar S. Bali et al. "$< x >^{u-d}$ from lattice QCD at nearly physical quark masses". In: *Phys. Rev.* D86 (2012), p. 054504. DOI: 10.1103/PhysRevD.86.054504. arXiv: 1207.1110 [hep-lat].

[61] I. C. Cloet et al. "Charge Symmetry Breaking in Spin Dependent Parton Distributions and the Bjorken Sum Rule". In: *Phys. Lett.* B714 (2012), pp. 97–102. DOI: 10.1016/j.physletb.2012.06.041. arXiv: 1204.3492 [hep-lat].

[62] J. Smit. "Introduction to quantum fields on a lattice: A robust mate". In: *Cambridge Lect. Notes Phys.* 15 (2002), pp. 1–271.

[63] Christof Gattringer and Christian B. Lang. "Quantum chromodynamics on the lattice". In: *Lect. Notes Phys.* 788 (2010), pp. 1–343. DOI: 10.1007/978-3-642-01850-3.

[64] Rajan Gupta. "Introduction to lattice QCD: Course". In: *Probing the standard model of particle interactions. Proceedings, Summer School in Theoretical Physics, NATO Advanced Study Institute, 68th session, Les Houches, France, July 28-September 5, 1997. Pt. 1, 2.* 1997, pp. 83–219. arXiv: hep-lat/9807028 [hep-lat]. URL: http://alice.cern.ch/format/showfull?sysnb=0284452.

[65] M. Luscher and P. Weisz. "On-Shell Improved Lattice Gauge Theories". In: *Commun. Math. Phys.* 97 (1985). [Erratum: Commun. Math. Phys.98,433(1985)], p. 59. DOI: 10.1007/BF01206178.

[66] W. Bietenholz et al. “Flavour blindness and patterns of flavour symmetry breaking in lattice simulations of up, down and strange quarks”. In: *Phys. Rev.* D84 (2011), p. 054509. DOI: 10.1103/PhysRevD.84.054509. arXiv: 1102.5300 [hep-lat].

[67] S. Itoh et al. “Renormalization Group Improved Lattice SU(3) Gauge Action and Hadron Spectrum in Quenched QCD on a 8**3 X 16 Lattice”. In: *Phys. Lett.* B148 (1984), pp. 153–156. DOI: 10.1016/0370-2693(84)91629-0.

[68] G. Peter Lepage and Paul B. Mackenzie. “On the viability of lattice perturbation theory”. In: *Phys. Rev.* D48 (1993), pp. 2250–2264. DOI: 10.1103/PhysRevD.48.2250. arXiv: hep-lat/9209022 [hep-lat].

[69] H. J. Rothe. “Lattice gauge theories: An Introduction”. In: *World Sci. Lect. Notes Phys.* 43 (1992). [World Sci. Lect. Notes Phys.82,1(2012)], pp. 1–381.

[70] *New Phenomena in Subnuclear Physics. Part A. Proceedings: First Half of the 1975 International School of Subnuclear Physics, Erice, Sicily, Jul 11-Aug 1 1975*. 1977.

[71] *New Phenomena in Subnuclear Physics. Part b. Proceedings, Second Half of the 1975 International School of Subnuclear Physics, Erice, Sicily, Jul 11-Aug 1 1975*. 1977.

[72] Herbert W. Hamber and Chi Min Wu. “Some Predictions for an Improved Fermion Action on the Lattice”. In: *Phys. Lett.* B133 (1983), pp. 351–358. DOI: 10.1016/0370-2693(83)90162-4.

[73] Mark G. Alford, T. R. Klassen, and G. P. Lepage. “Improving lattice quark actions”. In: *Nucl. Phys.* B496 (1997), pp. 377–407. DOI: 10.1016/S0550-3213(97)00249-6. arXiv: hep-lat/9611010 [hep-lat].

[74] N. Cundy et al. “Non-perturbative improvement of stout-smeared three flavour clover fermions”. In: *Phys. Rev.* D79 (2009), p. 094507. DOI: 10.1103/PhysRevD.79.094507. arXiv: 0901.3302 [hep-lat].

[75] Stephan Gusken. “Flavor singlet phenomena in lattice QCD”. In: (1999). arXiv: hep-lat/9906034 [hep-lat].

[76] A. Abdel-Rehim et al. “Disconnected quark loop contributions to nucleon observables in lattice QCD”. In: *Phys. Rev.* D89.3 (2014), p. 034501. DOI: 10.1103/PhysRevD.89.034501. arXiv: 1310.6339 [hep-lat].

[77] Tanmoy Bhattacharya et al. “Iso-vector and Iso-scalar Tensor Charges of the Nucleon from Lattice QCD”. In: *Phys. Rev.* D92.9 (2015), p. 094511. DOI: 10.1103/PhysRevD.92.094511. arXiv: 1506.06411 [hep-lat].

[78] M. Constantinou et al. In: *Phys. Rev.* D91.1 (2015), p. 014502. DOI: 10.1103/PhysRevD.91.014502. arXiv: 1408.6047 [hep-lat].

[79] J. M. Bell and J. A. Gracey. "Bilinear quark operator renormalization at generalized symmetric point". In: *Phys. Rev.* D93.6 (2016), p. 065031. DOI: 10.1103/PhysRevD.93.065031. arXiv: 1602.05514 [hep-ph].

[80] Martin Luscher et al. "The Schrodinger functional: A Renormalizable probe for nonAbelian gauge theories". In: *Nucl. Phys.* B384 (1992), pp. 168–228. DOI: 10.1016/0550-3213(92)90466-O. arXiv: hep-lat/9207009 [hep-lat].

[81] Martin Luscher et al. "Computation of the running coupling in the SU(2) Yang-Mills theory". In: *Nucl. Phys.* B389 (1993), pp. 247–264. DOI: 10.1016/0550-3213(93)90292-W. arXiv: hep-lat/9207010 [hep-lat].

[82] Stefan Sint. "One loop renormalization of the QCD Schrodinger functional". In: *Nucl. Phys.* B451 (1995), pp. 416–444. DOI: 10.1016/0550-3213(95)00352-S. arXiv: hep-lat/9504005 [hep-lat].

[83] Martin Luscher et al. "Chiral symmetry and O(a) improvement in lattice QCD". In: *Nucl. Phys.* B478 (1996), pp. 365–400. DOI: 10.1016/0550-3213(96)00378-1. arXiv: hep-lat/9605038 [hep-lat].

[84] Stefano Capitani et al. "Non-perturbative quark mass renormalization in quenched lattice QCD". In: *Nucl. Phys.* B544 (1999). [E: N. P.B582,762(2000)], pp. 669–698. DOI: 10.1016/S0550-3213(00)00163-2,10.1016/S0550-3213(98)00857-8. arXiv: hep-lat/9810063 [hep-lat].

[85] G. Martinelli et al. "A General method for nonperturbative renormalization of lattice operators". In: *Nucl. Phys.* B445 (1995), pp. 81–108. DOI: 10.1016/0550-3213(95)00126-D. arXiv: hep-lat/9411010 [hep-lat].

[86] M. Gockeler et al. "Perturbative and Nonperturbative Renormalization in Lattice QCD". In: *Phys. Rev.* D82 (2010). [Erratum: Phys. Rev.D86,099903(2012)], p. 114511. DOI: 10.1103/PhysRevD.82.114511,10.1103/PhysRevD.86.099903. arXiv: 1003.5756 [hep-lat].

[87] M. Constantinou et al. "Perturbatively improving regularization-invariant momentum scheme renormalization constants". In: *Phys. Rev.* D87.9 (2013), p. 096019. DOI: 10.1103/PhysRevD.87.096019. arXiv: 1303.6776 [hep-lat].

[88] C. T. Sachrajda and G. Villadoro. "Twisted boundary conditions in lattice simulations". In: *Phys. Lett.* B609 (2005), pp. 73–85. DOI: 10.1016/j.physletb.2005.01.033. arXiv: hep-lat/0411033 [hep-lat].

[89] S. Güsken. "A Study of smearing techniques for hadron correlation functions". In: *Nucl. Phys. Proc. Suppl.* 17 (1990), pp. 361–364. DOI: 10.1016/0920-5632(90)90273-W.

[90] Georg P. Engel et al., BGR [Bern-Graz-Regensburg]. In: *Phys. Rev.* D82 (2010), p. 034505. DOI: 10.1103/PhysRevD.82.034505. arXiv: 1005.1748 [hep-lat].

[91] Robert G. Edwards et al. In: *Phys. Rev.* D84 (2011), p. 074508. DOI: 10.1103/PhysRevD.84.074508. arXiv: 1104.5152 [hep-ph].

[92] M. Selim Mahbub et al. In: *Phys. Lett.* B707 (2012), pp. 389–393. DOI: 10.1016/j.physletb.2011.12.048. arXiv: 1011.5724 [hep-lat].

[93] Adrian L. Kiratidis et al. In: *Phys. Rev.* D91 (2015), p. 094509. DOI: 10.1103/PhysRevD.91.094509. arXiv: 1501.07667 [hep-lat].

[94] M. Selim Mahbub et al. In: *Phys. Rev.* D87.9 (2013), p. 094506. DOI: 10.1103/PhysRevD.87.094506. arXiv: 1302.2987 [hep-lat].

[95] Benjamin J. Menadue et al. In: *Phys. Rev. Lett.* 108 (2012), p. 112001. DOI: 10.1103/PhysRevLett.108.112001. arXiv: 1109.6716 [hep-lat].

[96] Benoit Blossier et al. "On the generalized eigenvalue method for energies matrix elements in lattice field theory". In: *JHEP* 04 (2009), p. 094. DOI: 10.1088/1126-6708/2009/04/094. arXiv: 0902.1265 [hep-lat].

[97] Benjamin J. Owen et al. In: *Phys. Rev.* D92.3 (2015), p. 034513. DOI: 10.1103/PhysRevD.92.034513. arXiv: 1505.02876 [hep-lat].

[98] Jonathan M. M. Hall et al. In: *Phys. Rev. Lett.* 114.13 (2015), p. 132002. DOI: 10.1103/PhysRevLett.114.132002. arXiv: 1411.3402 [hep-lat].

[99] Benjamin J. Owen et al. In: *Phys. Rev.* D91.7 (2015), p. 074503. DOI: 10.1103/PhysRevD.91.074503. arXiv: 1501.02561 [hep-lat].

[100] Benjamin J. Owen et al. In: *Phys. Lett.* B723 (2013), pp. 217–223. DOI: 10.1016/j.physletb.2013.04.063. arXiv: 1212.4668 [hep-lat].

[101] John Bulava, Michael Donnellan, and Rainer Sommer. "On the computation of hadron-to-hadron transition matrix elements in lattice QCD". In: *JHEP* 01 (2012), p. 140. DOI: 10.1007/JHEP01(2012)140. arXiv: 1108.3774 [hep-lat].

[102] Boram Yoon et al. "Controlling Excited-State Contamination in Nucleon Matrix Elements". In: (2016). arXiv: 1602.07737 [hep-lat].

[103] Derek B. Leinweber. "Nucleon properties from unconventional interpolating fields". In: *Phys. Rev.* D51 (1995), pp. 6383–6393. DOI: 10.1103/PhysRevD.51.6383. arXiv: nucl-th/9406001 [nucl-th].

[104] Fin M. Stokes et al. In: (2015). arXiv: 1302.4152v2 [hep-lat].

[105] Dale S. Roberts, Waseem Kamleh, and Derek B. Leinweber. "Nucleon Excited State Wave Functions from Lattice QCD". In: *Phys. Rev.* D89.7 (2014), p. 074501. DOI: 10.1103/PhysRevD.89.074501. arXiv: 1311.6626 [hep-lat].

[106] C. Aubin and K. Orginos. "An improved method for extracting matrix elements from lattice three-point functions". In: *PoS* LATTICE2011 (2011), p. 148.

[107] C. Aubin and K. Orginos. "A new approach for Delta form factors". In: *AIP Conf. Proc.* 1374 (2011), pp. 621–624. DOI: 10.1063/1.3647217. arXiv: 1010.0202 [hep-lat].

[108] K. Orginos. "Construction and Analysis of Two Baryon Correlation functions". In: *PoS* Lattice2010 (2010), p. 118.

[109] J. R. Green et al. In: *Phys. Rev.* D90 (2014), p. 074507. DOI: 10.1103/PhysRevD.90.074507. arXiv: 1404.4029 [hep-lat].

[110] Rainer W. Schiel. "Expanding the Interpolator Basis in the Variational Method to Explicitly Account for Backward Running States". In: *Phys. Rev.* D92.3 (2015), p. 034512. DOI: 10.1103/PhysRevD.92.034512. arXiv: 1503.02588 [hep-lat].

[111] Tanmoy Bhattacharya et al. "Axial, Scalar and Tensor Charges of the Nucleon from 2+1+1-flavor Lattice QCD". In: (2016). arXiv: 1606.07049 [hep-lat].

[112] S. Capitani et al. In: *Phys. Rev.* D92.5 (2015), p. 054511. DOI: 10.1103/PhysRevD.92.054511. arXiv: 1504.04628 [hep-lat].

[113] Gunnar S. Bali et al. In: *Phys. Rev.* D91.5 (2015), p. 054501. DOI: 10.1103/PhysRevD.91.054501. arXiv: 1412.7336 [hep-lat].

[114] Simon Dinter et al. In: *Phys. Lett.* B704 (2011), pp. 89–93. DOI: 10.1016/j.physletb.2011.09.002. arXiv: 1108.1076 [hep-lat].

[115] S. Capitani et al. In: *Phys. Rev.* D86 (2012), p. 074502. DOI: 10.1103/PhysRevD.86.074502. arXiv: 1205.0180 [hep-lat].

[116] Jack Dragos et al. "Nucleon matrix elements using the variational method in lattice QCD". In: (2016). arXiv: 1606.03195 [hep-lat].

[117] V. G. Bornyakov et al. "Wilson flow and scale setting from lattice QCD". In: (2015). arXiv: 1508.05916 [hep-lat].

[118] W. Bietenholz et al. In: *Phys. Lett.* B690 (2010), pp. 436–441. DOI: 10.1016/j.physletb.2010.05.067. arXiv: 1003.1114 [hep-lat].

[119] Tanmoy Bhattacharya et al. In: *Phys. Rev.* D89.9 (2014), p. 094502. DOI: 10.1103/PhysRevD.89.094502. arXiv: 1306.5435 [hep-lat].

[120] G. Jonkmans et al. "Radiative muon capture on hydrogen and the induced pseudoscalar coupling". In: *Phys. Rev. Lett.* 77 (1996), pp. 4512–4515. DOI: 10.1103/PhysRevLett.77.4512. arXiv: nucl-ex/9608005 [nucl-ex].

[121] Tim Gorringe and Harold W. Fearing. "Induced pseudoscalar coupling of the proton weak interaction". In: *Rev. Mod. Phys.* 76 (2004), pp. 31–91. DOI: 10.1103/RevModPhys.76.31. arXiv: nucl-th/0206039 [nucl-th].

[122] J. H. D. Clark et al. "Ortho-para transition rate in mu-molecular hydrogen and the proton's induced pseudoscalar coupling g(p)". In: *Phys. Rev. Lett.* 96 (2006), p. 073401. DOI: 10.1103/PhysRevLett.96.073401. arXiv: nucl-ex/0509025 [nucl-ex].

[123] V. A. Andreev et al. "Measurement of the rate of muon capture in hydrogen gas and determination of the proton's pseudoscalar coupling g(P)". In: *Phys. Rev. Lett.* 99 (2007), p. 032002. DOI: 10.1103/PhysRevLett.99.032002. arXiv: 0704.2072 [nucl-ex].

[124] Andrzej Czarnecki, William J. Marciano, and Alberto Sirlin. "Electroweak radiative corrections to muon capture". In: *Phys. Rev. Lett.* 99 (2007), p. 032003. DOI: 10.1103/PhysRevLett.99.032003. arXiv: 0704.3968 [hep-ph].

[125] A. D. Martin et al. "Uncertainties of predictions from parton distributions. 1: Experimental errors". In: *Eur. Phys. J.* C28 (2003), pp. 455–473. DOI: 10.1140/epjc/s2003-01196-2. arXiv: hep-ph/0211080 [hep-ph].

[126] Gunnar S. Bali et al. In: *Phys. Rev.* D90.7 (2014), p. 074510. DOI: 10.1103/PhysRevD.90.074510. arXiv: 1408.6850 [hep-lat].

[127] M. Anselmino et al. "Update on transversity and Collins functions from SIDIS and e+ e- data". In: *Nucl. Phys. Proc. Suppl.* 191 (2009), pp. 98–107. DOI: 10.1016/j.nuclphysbps.2009.03.117. arXiv: 0812.4366 [hep-ph].

[128] Markus Diefenthaler. "HERMES measurements of Collins and Sivers asymmetries from a transversely polarised hydrogen target". In: *Proceedings, 15th International Workshop on Deep-inelastic scattering and related subjects (DIS 2007). Vol. 1 and 2: Munich, Germany, April 16-20, 2007*. 2007, pp. 579–582. DOI: 10.3204/proc07-01/91. arXiv: 0706.2242 [hep-ex]. URL: https://inspirehep.net/record/753247/files/arXiv:0706.2242.pdf.

[129] M. Alekseev et al. "Collins and Sivers asymmetries for pions and kaons in muon-deuteron DIS". In: *Phys. Lett.* B673 (2009), pp. 127–135. DOI: 10.1016/j.physletb.2009.01.060. arXiv: 0802.2160 [hep-ex].

[130] R. Seidl et al. "Measurement of Azimuthal Asymmetries in Inclusive Production of Hadron Pairs in e+e- Annihilation at s**(1/2) = 10.58-GeV". In: *Phys. Rev.* D78 (2008). [Erratum: Phys. Rev.D86,039905(2012)], p. 032011. DOI: 10.1103/PhysRevD.78.032011, 10.1103/PhysRevD.86.039905. arXiv: 0805.2975 [hep-ex].

[131] I. C. Cloet et al. "Survey of nucleon electromagnetic form factors". In: *Few Body Syst.* 46 (2009), pp. 1–36. DOI: 10.1007/s00601-009-0015-x. arXiv: 0812.0416 [nucl-th].

[132] Zhong-Bo Kang et al. "Nucleon tensor charge from Collins azimuthal asymmetry measurements". In: *Phys. Rev.* D91 (2015), p. 071501. DOI: 10.1103/PhysRevD.91.071501. arXiv: 1410.4877 [hep-ph].

[133] M. Anselmino et al. "Transversity and Collins functions from SIDIS and e+e- data". In: ().

[134] M. Anselmino et al. "Simultaneous extraction of transversity and Collins functions from new SIDIS and e+e- data". In: *Phys. Rev.* D87 (2013), p. 094019. DOI: 10.1103/PhysRevD.87.094019. arXiv: 1303.3822 [hep-ph].

[135] Alessandro Bacchetta, A. Courtoy, and Marco Radici. "First extraction of valence transversities in a collinear framework". In: *JHEP* 03 (2013), p. 119. DOI: 10.1007/JHEP03(2013)119. arXiv: 1212.3568 [hep-ph].

[136] Alessandro Bacchetta, Aurore Courtoy, and Marco Radici. "First glances at the transversity parton distribution through dihadron fragmentation functions". In: *Phys. Rev. Lett.* 107 (2011), p. 012001. DOI: 10.1103/PhysRevLett.107.012001. arXiv: 1104.3855 [hep-ph].